

# Ultrasound-driven formation of porous metals for catalysis

---

Dissertation zur Erlangung des akademischen  
Grades des Doktors der Naturwissenschaften

- Dr. rer. nat. -

der Fakultät für Biologie, Chemie und  
Geowissenschaften der Universität Bayreuth

---

vorgelegt von

Diplom Ingenieurin

Jana Katharina Dulle, geborene Schäferhans

aus Blumenstein

Die vorliegenden Laborarbeiten wurde vom 1. November 2009 bis 1. November 2012 am Lehrstuhl für Physikalische Chemie II der Universität Bayreuth, unter der Leitung von Prof. Dr. Andreas Fery, in der Arbeitsgruppe Dr. Andreeva-Bäumler angefertigt. Teile der praktischen Arbeit wurden an der Universität Amsterdam, Van't Hoff Institute for Molecular Sciences, am Lehrstuhl Heterogeneous Catalysis and Sustainable Chemistry von Prof. Dr. Gadi Rothenberg durchgeführt.

Vollständiger Abdruck der von der Fakultät für Biologie, Chemie und Geowissenschaften der Universität Bayreuth genehmigten Dissertation zur Erlangung des akademischen Grades eines Doktors der Naturwissenschaften (Dr. rer. nat.).

Ermöglicht wurde die Arbeit durch finanzielle Unterstützung der Deutschen Forschungsgemeinschaft (SFB 840) und der Universität Bayreuth.

Promotionsgesuch eingereicht am: 20. April 2015

Zulassung durch die Promotionskommission: 29. April 2015

Wissenschaftliches Kolloquium: 16. Juli 2015

Amtierender Dekan: Prof. Dr. Rhett Kempe

Prüfungsausschuss:

Dr. Daria V. Andreeva- Bäumler (Erstgutachterin)

Prof. Dr. Rhett Kempe (Zweitgutachter)

Prof. Dr. Andreas Greiner (Vorsitz)

JProf. Dr. Markus Retsch

" Denn was man schwarz auf weiß besitzt,  
Kann man getrost nach Hause tragen."

von

- Johann Wolfgang von Goethe, Faust I –

Gewidmet meiner Familie, Martin, Sophia und Nico.

<b>ZUSAMMENFASSUNG .....</b>	<b>1</b>
<b>SUMMARY .....</b>	<b>3</b>
<b>DANKSAGUNG.....</b>	<b>5</b>
<b>LIST OF ABBREVIATIONS.....</b>	<b>6</b>
<b>LIST OF FIGURES .....</b>	<b>7</b>
<b>LIST OF TABLES .....</b>	<b>14</b>
<b>1 INTRODUCTION.....</b>	<b>15</b>
REFERENCES.....	19
<b>2 MECHANICAL AND CHEMICAL ASPECT OF HIGH INTENSITY ULTRASOUND.....</b>	<b>21</b>
2.1 GENERAL ASPECTS OF SONICATION .....	21
2.1.1 <i>Sonication</i> .....	21
2.1.2 <i>Cavitation</i> .....	21
2.2 CAVITATION IN AQUEOUS MEDIA .....	23
2.3 CAVITATION IN HETEROGENOUS SYSTEMS.....	25
2.3.1 <i>Interparticle collisions</i> .....	25
2.3.2 <i>Effects on particle size and morphology</i> .....	26
2.3.3 <i>Red/Ox reactions and structure formation in water</i> .....	27
REFERENCES.....	28
<b>3 OVERVIEW OF THE THESIS .....</b>	<b>29</b>
3.1 SONOCHEMICAL FORMATION OF METAL SPONGES .....	29
3.2 ULTRASOUND DRIVEN FORMATION OF METAL-SUPPORTED NANOCATALYSTS .....	31
3.3 SONOCHEMICAL ACTIVATION OF AL/Ni TOWARDS A HYDROGENATION CATALYST .....	33
3.4 SONOCHEMICAL ACTIVATION OF AL/CU TOWARDS A DEHYDROGENATION CATALYSTS .....	35
3.5 SONOCHEMICAL ACTIVATED CU/AL AS A CATALYST FOR A <sup>3</sup> COUPLING .....	37
3.6 SONONANOSTRUCTURING OF ZINC BASED MATERIAL .....	38
REFERENCES.....	40
<b>4 PUBLISHED ARTICLES IN PEER-REVIEWED JOURNALS .....</b>	<b>42</b>
4.1 SONOCHEMICAL FORMATION OF METAL SPONGES .....	42
4.1.1 <i>Contribution to the joint publication</i> .....	44
4.1.2 <i>Abstract</i> .....	44
4.1.3 <i>Introduction</i> .....	44
4.1.4 <i>Results and Discussion</i> .....	48
4.1.5 <i>Conclusion</i> .....	60
4.1.6 <i>Experimental</i> .....	61
Materials .....	61
Ultrasonication (US).....	62
Determination of the amount of superoxide.....	62
Preparation of polyelectrolyte film and loading with anticorrosion inhibitor .....	62
Formation of interpenetrating polypyrrole–aluminum composite.....	62
Synthesis and incorporation of gold, silver, and platinum nanoparticles in aluminum support.....	62
Experiments in ionic liquid.....	63
Scanning electron microscopy (SEM).....	63
Transmission electron microscopy (TEM).....	63
Confocal scanning fluorescence microscopy (CSFM) .....	63
Scanning vibrating electrode technique (SVET) .....	63

X-ray diffraction (XRD) .....	63
BET analysis.....	63
Three-dimensional atom probe analyses.....	63
4.1.7 Acknowledgements .....	64
REFERENCES.....	64
4.2 ULTRASOUND DRIVEN FORMATION OF METAL-SUPPORTED NANOCATALYSTS .....	67
4.2.1 Contribution to the joint publication .....	67
4.2.2 Abstract.....	67
4.2.3 Introduction.....	67
4.2.4 Results and discussion .....	68
Material properties.....	68
Catalytic properties.....	75
4.2.5 Conclusion .....	76
4.2.6 Experimental .....	77
Materials and methods.....	77
Synthesis of Ag, Au, and Pt nanoparticles.....	77
Ultrasonication .....	78
Catalytic reaction .....	78
4.2.7 Acknowledgement.....	78
REFERENCES.....	78
4.3 SONOCHEMICAL ACTIVATION OF Al/Ni HYDROGENATION CATALYST .....	80
4.3.1 Contribution to the joint publication .....	80
4.3.2 Abstract.....	80
4.3.3 Introduction.....	81
4.3.4 Results and discussion .....	83
Catalyst activation and characterization.....	83
Catalytic Performance.....	90
4.3.5 Conclusion .....	92
4.3.6 Experimental .....	93
Materials.....	93
Preparation of Al/Ni catalyst.....	93
Scanning electron microscopy .....	93
Powder X-ray diffraction.....	93
<sup>27</sup> Al MAS NMR.....	94
Surface area and pore size distribution .....	95
Pulse titration analysis .....	95
Inductively coupled plasma .....	95
X-ray photoelectron spectroscopy.....	95
Confocal scanning fluorescence microscopy .....	95
Catalytic application of the modified Al/Ni material .....	95
Reusability .....	96
4.3.7 Acknowledgment.....	96
REFERENCES.....	96
4.4 NOVEL AND EFFECTIVE COPPER - ALUMINUM PROPANE DEHYDROGENATION CATALYSTS.....	99
4.4.1 Contribution to the joint publication .....	99
4.4.2 Abstract.....	99
4.4.3 Introduction.....	100
4.4.4 Results and discussion .....	100
4.4.5 Conclusion .....	104
4.4.6 Experimental .....	104
Materials and Instrumentation.....	104
Procedure for preparing the Al-Cu alloy .....	105
Procedure for catalyst preparation.....	105

General procedure for propane dehydrogenation .....	105
Procedure for synthesising the Pt-Sn/Al <sub>2</sub> O <sub>3</sub> reference catalyst .....	106
4.4.7 Acknowledgments .....	106
REFERENCES.....	106
<b>4.5 EFFICIENT THREE-COMPONENT COUPLING CATALYSED BY MESOPOROUS COPPER-ALUMINUM BASED NANOCOMPOSITE.....</b>	<b>108</b>
4.5.1 Contribution to the joint publication .....	108
4.5.2 Abstract.....	108
4.5.3 Introduction.....	109
4.5.4 Results and discussion .....	110
4.5.5 Conclusion .....	118
4.5.6 Experimental .....	118
Materials and instrumentation .....	118
Procedure for catalyst preparation.....	119
General procedure for Cu/Al-catalysed A <sup>3</sup> coupling .....	119
4.5.7 Acknowledgment.....	120
REFERENCES.....	120
<b>4.6 SONONANOSTRUCTURING OF ZINC BASED MATERIAL .....</b>	<b>123</b>
4.6.1 Contribution to the joint publication .....	123
4.6.2 Abstract.....	123
4.6.3 Introduction.....	124
4.6.4 Results and discussion .....	126
Sonication of Zn particles: formation of the Zn based core-shell “hedgehogs” .....	126
Mechanism of formation of core-shell Zn based “hedgehogs” .....	127
Photocatalytic activity.....	132
4.6.5 Conclusion .....	135
4.6.6 Experimental .....	136
Formation of core-shell “hedgehogs” from Zn particles.....	136
Characterisation methods .....	136
Photocatalytic experiments .....	136
4.6.7 Acknowledgments .....	137
REFERENCES.....	137
<b>5 EXCERPT OF PUBLISHED ABSTRACTS AT NATIONAL AND INTERNATIONAL CONFERENCES .....</b>	<b>140</b>
5.1 COPS 2012 – POSTER AWARD .....	140
5.2 CPM-6 – POSTER AWARD.....	140
5.3 DPG FRÜHJAHRTAGUNGEN .....	140
5.4 ECIS 2010 .....	140
5.5 KATALYTIKER 2011 .....	141
5.6 EUCHEMS 2010 .....	141
<b>ERKLÄRUNG .....</b>	<b>142</b>

## Zusammenfassung

Vom Bösewicht zum Freund und Helfer. Kavitation wurde u.a. von Lord Rayleigh im 19. Jahrhundert dafür verantwortlich gemacht, die Schiffsschrauben bei zu hoher Geschwindigkeit zu zerstören. Diese zerstörerische Eigenschaft wurde für diese Arbeit herangezogen, um poröse Metalle herzustellen. Die Faszination von porösen Materialien liegt in der Vielfalt ihrer Anwendungen. Ihr Einsatz hat sich in den letzten Jahren immer weiter verbreitet, angefangen bei Katzenstreu bis hin zu hoch komplexen Katalysatoren. Jedoch gestaltet sich die Herstellung dieser porösen Materialien schwierig. Diese ist z.T. kostenaufwendig und mit viel Abfall verbunden und stellt daher eine Herausforderung dar. Genau hier setzt diese Arbeit an. Kavitation, die mittels hoch intensiven Ultraschalls erzeugt wird, macht aus den eingesetzten pulverigen Metallen poröse Materialien.

In dieser Arbeit wurde zuerst untersucht, welche Parameter Einfluss auf die Modifizierung der Metallpulver haben. Die Hauptrolle spielen hierbei der Schmelzpunkt und die Oxidationsfähigkeit des Metalls, sowie die Dauer und Intensität der Ultraschallbehandlung. Während der Implosion der Kavitationsblase kommt es, nach der „Hot-Spot Theorie“, zu Temperaturen von 5000 K und Drücken bis zu 500 bar, sowie der thermolytischen Spaltung von Wasser. Diese Einflüsse sorgen dafür, dass das Metall aufgesprengt und aufgeschmolzen wird und die neu entstandene Struktur anschließend mit einer Oxidschicht stabilisiert wird.

Nach vielfältigen Vorversuchen mit unterschiedlichen Metallen wurde der Fokus auf das Metall Aluminium gelegt. Mittels Ultraschall wurde in Wasser poröses Aluminium hergestellt, welches im nächsten Arbeitsschritt als Matrix für die Einbringung von Platin-Nanopartikeln durch Ultraschall verwendet wurde. Diese katalytisch hochaktiven Nanopartikel wurden dann für die Reduktion von Ferricyanid mit Thiosulfat verwendet. Nanopartikel anderer Metalle, wie Silber und Gold, können mit dieser Methode ebenso in die poröse Aluminium-Matrix ebenfalls eingelagert werden. Die Ultraschallmethode ermöglicht demzufolge die schnelle und saubere Herstellung heterogener Katalysatoren.

Aus dieser Erkenntnis heraus wurde nun eine handelsübliche Aluminium/Nickel-Legierung in Pulverform ebenfalls mit hoch intensivem Ultraschall behandelt. Die spezifische Oberfläche, dieser ca. 10 µm großen Partikel, konnte durch 50 minütige Ultraschallbehandlung bei 140 W cm<sup>-2</sup> um das 625 fache auf 120 m<sup>2</sup> g<sup>-1</sup> gesteigert werden. Diese poröse Metalllegierung ist ein hervorragender heterogener Katalysator für die Hydrierung von Acetophenon. Im Gegensatz zum konventionellen, durch chemisches Dealloying, hergestelltes „Raney®-Nickel“, ist dieses Material nicht pyrophor.

Aufbauend auf den positiven Erfahrungen mit der Al/Ni-Legierung wurde eine Aluminium/Kupfer-Legierung im eigenen Labor hergestellt. Diese wurde durch Ultraschallbehandlung porös und katalytisch aktiv. Diese neue poröse Al/Cu-Legierung stellte sich als weitaus effektiverer Katalysator für die Dehydrierung von Propan heraus, als die üblicherweise eingesetzten, sehr teuren Pt-Sn/Al<sub>2</sub>O<sub>3</sub>-Katalysatoren. Abgesehen von geringeren Materialkosten, ist auch die Reaktionstemperatur um 200 °C niedriger als bei den zuvor genannten Pt-Sn/Al<sub>2</sub>O<sub>3</sub>-Katalysatoren.

Diese neuartige poröse Al/Cu-Legierung wurde anschließend zur Synthese von Propargylaminen eingesetzt. Die innovative "A<sup>3</sup> Kupplungsreaktion" wurde angewendet, um ein Alkin, ein Aldehyd und ein Amin zusammen zu kuppeln. Diese Reaktion läuft üblicherweise durch Katalyse an homogenen Goldsalzen, Organogold-Komplexen oder Silbersalzen ab. Diese homogenen Katalysatoren sind jedoch teuer und schwierig zu separieren. Das Ergebnis ist, dass auch hier die günstig hergestellten porösen, katalytisch aktiven Al/Cu Pulver, den Standardkatalysatoren Konkurrenz machen.

Abschließend wurde der Fokus auf die Herstellung von Zink-Katalysatoren für die Photokatalyse gelegt. Zink wurde mittels Ultraschall behandelt. Es oxidiert und formt dabei igelförmige Kern-Schale-Strukturen mit einer großen Oberfläche, die katalytisch aktiv ist.

Die Anwendung von hoch intensivem Ultraschall in Wasser, in Verbindung mit pulverförmigen Metallen und Metalllegierungen, ergibt eine ressourcenschonende Methode. Diese ermöglicht es in einem Einschnittverfahren katalytisch höchst aktive und stabile Katalysatoren herzustellen. Diese innovative Methode öffnet die Tür für die Herstellung vieler weiterer heterogener Katalysatoren.

## Summary

From a foe to a friend – Cavitation. Lord Raleigh and others first described the phenomenon known as cavitation, when they investigated the destruction of ship propellers at high travelling speeds. Exactly this property was utilized in this thesis to produce porous metals. The fascination of porous materials lies in the many ways they can be used. Their use covers a wide range of applications reaching from cat litter to highly complex catalysts. But the production of, for example, such a catalyst is very sophisticated and expensive, usually involving many steps and producing a lot of waste. To remedy this was the motivation behind the work presented here. Cavitation, produced by high intensity ultrasound, transforms sonicated metals to porous materials.

As a first step, the parameters which had the most influence on the modification of the used metallic powders were investigated. The melting point and redox potential of the metals as well as the duration and intensity of the ultrasound treatment are the most important factors. When such a cavitation bubble implodes according to the “hot-spot theory” temperatures of up to 5000 K and pressures up to 500 atmospheres are reached, and water is thermolytically cleaved and yields radicals that can react with the present metal. These conditions lead to the cracking and melting of metals as well as an oxide layer stabilizing the newly formed structures.

After a lot of experiments utilizing different metals the focus was laid on aluminum. Porous aluminum, which was obtained after sonication in water, was used as matrix material for platinum nanoparticles which were incorporated using also ultrasound. These catalytically active nanoparticles were used for the reduction of ferricyanide with thiosulfate. The same method can also be used to incorporate silver and gold nanoparticles into the porous aluminum matrix. We showed that with ultrasound it is possible to produce heterogeneous catalysts in a fast and clean way.

These insights lead us to experiments on a commercially available Al/Ni alloy in powdered form with high intensity ultrasound. The specific surface area of these ca. 20  $\mu\text{m}$  particles was increased by a factor of 625 to 120  $\text{m}^2 \text{g}^{-1}$  after a 50 minute long ultrasound treatment at 140  $\text{W cm}^{-2}$ . The resulting porous material is very well suited as catalyst for the hydrogenation of acetophenone. In contrast to the conventionally employed “Raney®-Nickel”, which is made by chemical dealloying, our material is not pyrophoric and indefinitely stable at ambient conditions.

The promising results obtained with the Al/Ni alloy lead to the production of an Al/Cu alloy powder in our lab. This alloy was made porous and catalytically active via ultrasound treatment. In comparison to the very expensive Pt–Sn/ $\text{Al}_2\text{O}_3$  catalysts this, new porous material could dehydrate propane much

more efficiently. But not only the material is much cheaper also the reaction can be performed at temperatures 200 °C lower than usually necessary when using the Pt–Sn/Al<sub>2</sub>O<sub>3</sub> catalysts.

We used this fascinating porous Al/Cu alloy for the synthesis of propargylamines. A new method in the form of a so-called “A<sup>3</sup> coupling” reaction was used to couple an alkyne, an aldehyde, and an amine together. This reaction is typically performed with homogeneous gold salts, organogold complexes, or silver salts. However, these homogeneous catalysts are expensive and difficult to separate. The result is that also for this reaction the porous and catalytically active Al/Cu powder competes with the common catalysts.

Finally, the focus was placed on the preparation of zinc catalysts for photocatalysis. Zinc was sonicated in water for various durations. It oxidizes and forms thereby hedgehog–like core–shell structures with a large surface area that is catalytically active.

The application of high intensity ultrasound in water in connection with powdered metals and metal alloys is a resource-conserving method to produce, by a simple process, very active and stable catalysts. This innovative method opens the door for many other applications in heterogeneous catalysis.

## Danksagung

An erster Stelle bedanke ich mich bei meinen Freunden Kathi, Toffi, Krake und Dr. Maxi. Ohne Sie wäre ich nicht so weit gekommen, wie ich es jetzt bin. Danke! Mein Dank braucht keine vielen Worte, ihr wisst sicher, wie sehr ich euch schätze!

Meiner Mutter Erika danke ich ganz herzlich, dass sie mich immer unterstützt hat, in jeder Lebenslage.

Volodymyr Kutznetsov und Christoph Hanske danke ich für das klasse Arbeitsklima bei uns im Büro. Es war immer spannend. Pavel, unsere gemeinsame Zeit im Labor war leider viel zu kurz, schade!

Sybille Zimmermann weiß am besten, welcher große spezielle Dank ihr gebührt. Danke Sybille für die Zeit, die begann, als ich den ersten Fuß in den Lehrstuhl gesetzt habe, bis heute fortlaufend.

Daria danke ich für das gute Dissertationsthema. Forschungsaufenthalte und die Teilnahme an Konferenzen waren immer selbstverständlich.

Prof. Fery danke ich für die Möglichkeit an seinem Lehrstuhl zu promovieren und mir den Einblick in die Naturwissenschaften aus Sicht eines Ingenieurs ermöglichen zu haben.

Gadi und Shiju sage ich „Thank you very much“ für die tolle Zeit in Amsterdam! In so kurzer Zeit zwei Publikationen zu veröffentlichen, war spitze. Und nicht nur das, ich habe sehr viel von Gadi zum Thema „Write it Right“ gelernt! Danke an euch beide!

Torsten Irrgang danke ich für die gute Zusammenarbeit, die immer Zeit für eine Schmah lies.

Mein Dank gilt Prof. Kempe, Prof. Breu und Prof. Senker, sowie Prof. Papastavrou für Ihre Beiträge zu meinen Publikationen.

Dr. Milius, Herrn Putz und Lena Geiling danke ich für Ihre Unterstützung bei allen XRD und BET Fragen und Messungen.

Dr. Häfner, Carmen K., Petra Z. und Markus Hund danke ich für die technische Unterstützung in allen Wissenschaftslagen, betreffend TEM, SEM, AFM, IT, Sicherheit, usw..

Meinem lieben und besten Ehemann danke ich von ganzem Herzen für seine bedingungslose Liebe, Unterstützung, Motivation und für unsere einmaligen Kinder, Tochter Sophia Teresa und Sohn Nico Sebastian. Danke mein Liebster! Du weißt, wie dankbar ich dir bin.

## List of Abbreviations

<b>BDDT</b>	Branuer, Deming, Deming, and Teller theory
<b>BET</b>	Brunauer, Emmett, and Teller theory
<b>BJH</b>	Barrett–Joyner–Halenda method
<b>CSFM</b>	Confocal scanning fluorescence microscopy
<b>EDS</b>	Electron diffraction spectroscopy
<b>GC</b>	Gas chromatography
<b>ICP</b>	Inductively coupled plasma mass spectrometry
<b>h</b>	Hour(s)
<b>IL</b>	Ionic liquid
<b>min</b>	Minute(s)
<b>MO</b>	Methyl orange
<b>MP</b>	Melting point
<b>NMR</b>	Nuclear magnetic resonance
<b>NP</b>	Nanoparticle
<b>PPy</b>	Polypyrrole
<b>PXRD</b>	Powder X-ray diffraction
<b>RSF</b>	Relative sensitivity factors
<b>RT</b>	Room temperature
<b>SEM</b>	Scanning electron microscopy
<b>SVET</b>	Scanning vibrating electrode technique
<b>US, USHI</b>	High intensity ultrasound
<b>US-Zn</b>	High intensity ultrasound modified zinc
<b>UV–Vis/near-IR</b>	Ultraviolet–visible/near infrared spectroscopy
<b>XAES</b>	X-ray excited Auger electron spectroscopy
<b>XPS</b>	Photoelectron spectroscopy
<b>XRD</b>	X-ray diffraction

## List of Figures

Fig. 1-1 A plug-flow catalytic reactor at various zoom-in levels. Gadi Rothenberg: Catalysis: Concepts and Green Applications. 130. 2008. Copyright Wiley-VCH Verlag GmbH & Co. KGaA. Reproduced with permission. ....	16
Fig. 1-2 Formation of porous metal particles by ultrasonication. Adapted from Green Chem., 15, J. Dulle, et al., Efficient three-component coupling catalysed by mesoporous copper-aluminum based nanocomposite, 1238 – 1243, Copyright (2013), with permission from The Royal Society of Chemistry. ....	18
Fig. 2-1 Schematic representation of transient acoustic cavitation. Reprinted from J. H. Bang, K. S. Suslick, Applications of Ultrasound to the Synthesis of Nanostructured Materials, Advanced Materials 2010, 22, 1039–1059, Copyright (2010), with permission from John Wiley and Sons. ....	22
Fig. 2-2 The cavitation bubble as a chemical microreactor. Adapted from G. Cravotto et. al., Forcing and Controlling Chemical Reactions with Ultrasound, Angew. Chem. Int. Ed. 2007, 46, 5476 – 5478, Copyright (2007), with permission from John Wiley and Sons. ....	24
Fig. 3-1 Sonochemical modification of metal particles: (I) initial particles; (II) chemical aspect surface oxidation (A) and physical aspects (B) interparticle collisions; (III) formation of mesoporous metals. Reprinted from Adv. Funct. Mater. 22, J. Dulle, et al., Sonochemical Activation of Al/Ni Hydrogenation Catalyst, 3128 – 3135, Copyright (2012), with permission from John Wiley and Sons.....	29
Fig. 3-2 Schematic presentation of the effect of acoustic cavitation on modification of metal particles. Metals with low (Zn) melting point exhibit transformation into oxide, and with high (Ni, Ti) melting points exhibit surface modification under sonication. Al and Mg form mesoporous sponge-like structures. Noble metals are resistant to ultrasound irradiation due to the stability against oxidation. The time of modification was chosen to be 60 min as an optimum for aluminum sponge metal particle formation. Reprinted from Nanoscale, 3, E.V. Skorb, et al., Sonochemical formation of metal sponges, 985 – 993, Copyright (2011), with permission from The Royal Society of Chemistry.....	30
Fig. 3-3 Digital photographs of Au, Ag, and Pt nanoparticle suspensions (A, B, and C respectively) before (left) and after (right) the ultrasound-assisted loading in Al nanostructures. The particles sediment due to their incorporation into the Al particles. TEM image of microtomed mesoporous bimetallic (Al–Au) particle (D). The linear dependence of the Au intake in the Al particles vs. the sonication time. In 50 min of sonication the saturation is achieved (E). Reprinted from Microporous Mesoporous Mater., 154, N. Pazos-Peréz, et al., Ultrasound driven formation of metal-supported nanocatalysts, 164 – 169, Copyright (2012), with permission from Elsevier.....	32
Fig. 3-4 SEM images and the aluminum (Al), nickel (Ni), and oxygen (O) ratio measured by EDS (inserts) of Al/Ni particles: A–initial; B–after 5 min; C–30 min and D–50 min of sonication at 140 W cm <sup>-2</sup> . 3D confocal microscopy reconstruction of the Al/Ni nanostructure loaded with fluorescein: (E) the alloy particle after 3 min (the reconstruction of both transmission and fluorescent mode) and (F) 50 min of sonochemical exposure at 140 W cm <sup>-2</sup> . Reprinted from Adv. Funct. Mater., 22, J. Dulle, et al., Sonochemical Activation of Al/Ni Hydrogenation Catalyst, 3128 – 3135, Copyright (2012), with permission from John Wiley and Sons. ....	34
Fig. 3-5 Graphical abstract. Reprinted from Chem. Eur. J., 17, J. Schäferhans, et al., Novel and Effective Copper - Aluminum Propane Dehydrogenation Catalysts, 12254 – 12256, Copyright (2012), with permission from John Wiley and Sons. ....	36
Fig. 3-6 Graphical abstract. Adapted from Green Chem., 15, J. Dulle, et al., Efficient three-component coupling catalysed by mesoporous copper-aluminum based nanocomposite, 1238 – 1243, Copyright (2013), with permission from The Royal Society of Chemistry. ....	37

Fig. 3-7 PXRD pattern (E), the insert (e) shows the magnified part of the PXRD patterns with the ZnO attributed peaks, and SEM image of the zinc particles treated for 10 min by ultrasound. Reprinted from RSC Advances, 2, J. Dulle, et al., Sononanostructuring of zinc based material, 12460 – 1246, Copyright (2012), with permission from The Royal Society of Chemistry. ....	38
Fig. 3-8 Reaction rate constant $k$ is shown in dependence of ultrasound treatment duration. We used 10 mg of the US modified zinc particles. Reprinted from RSC Advances, 2, J. Dulle, et al., Sononanostructuring of zinc based material, 12460 – 1246, Copyright (2012), with permission from The Royal Society of Chemistry. ....	39
Fig. 4-1 Coverletter. Reprinted from Nanoscale, 3, Copyright (2011), with permission from The Royal Society of Chemistry. ....	43
Fig. 4-2 Sonochemical modification of metal particles: (I) initial particles; (II) chemical aspect (a) surface oxidation, physical aspects (b) interparticle collisions, surface impinging by high velocity microjets; (III) formation of mesoporous metals. Reprinted from Nanoscale, 3, E.V. Skorb, et al., Sonochemical formation of metal sponges, 985 – 993, Copyright (2011), with permission from The Royal Society of Chemistry. ....	45
Fig. 4-3 Schematic presentation of the effect of acoustic cavitation on modification of metal particles. Metals with low (Zn) melting point exhibit transformation into oxide and with high (Ni, Ti) melting points exhibit surface modification under sonication. Al and Mg form mesoporous sponge-like structure. Noble metals are resistant to ultrasound irradiation due to the stability against oxidation. The time of modification was chosen to be 60 min as an optimum for aluminum sponge metal particle formation. Reprinted from Nanoscale, 3, E.V. Skorb, et al., Sonochemical formation of metal sponges, 985 – 993, Copyright (2011), with permission from The Royal Society of Chemistry. ....	47
Fig. 4-4 SEM and TEM (insets) images of aluminum particles initially (a) and after sonication at 57 W cm <sup>-2</sup> for (b) 1 min, (c) 3 min, (d) 60 min, and (e) 120 min.). Reprinted from Nanoscale, 3, E.V. Skorb, et al., Sonochemical formation of metal sponges, 985 – 993, Copyright (2011), with permission from The Royal Society of Chemistry. ....	48
Fig. 4-5 Adsorption–desorption isotherms for aluminum particles after different sonication times (a) and increase of the surface area of the aluminum particles vs. sonication time (b). Reprinted from Nanoscale, 3, E.V. Skorb, et al., Sonochemical formation of metal sponges, 985 – 993, Copyright (2011), with permission from The Royal Society of Chemistry. ....	50
Fig. 4-6 3D confocal microscopy reconstruction of the metal sponge loaded with doxorubicin hydrochloride: (1) the metal particle after 3 min (the reconstruction of both transmission and fluorescent mode) and (2) 60 min of sonochemical exposure at 57 W cm <sup>-2</sup> (fluorescent mode, transmission mode reconstruction is not possible due to microscope resolution). Reprinted from Nanoscale, 3, E.V. Skorb, et al., Sonochemical formation of metal sponges, 985 – 993, Copyright (2011), with permission from The Royal Society of Chemistry. ....	51
Fig. 4-7 Three dimensional field ion microscopy reconstruction of the atom positions of aluminum. Reprinted from Nanoscale, 3, E.V. Skorb, et al., Sonochemical formation of metal sponges, 985 – 993, Copyright (2011), with permission from The Royal Society of Chemistry. ....	52
Fig. 4-8 (a) SEM, TEM images, (c) XRD patterns and (d) adsorption–desorption isotherm for magnesium particles after 20 min sonication at 57 W cm <sup>-2</sup> in aqueous solution. Reprinted from Nanoscale, 3, E.V. Skorb, et al., Sonochemical formation of metal sponges, 985 – 993, Copyright (2011), with permission from The Royal Society of Chemistry. ....	53
Fig. 4-9 SEM images of Zn particles sonicated at 57 W cm <sup>-2</sup> for (a) 3 min and (b) 90 min; (c) XRD patterns of the initial particles and particles sonicated for 90 min and (d) adsorption–desorption isotherm for 15 and 30 min treated zinc particles. Reprinted from Nanoscale, 3, E.V. Skorb, et al., Sonochemical	

formation of metal sponges, 985 – 993, Copyright (2011), with permission from The Royal Society of Chemistry. ....	54
Fig. 4-10 SEM images of (a) the initial nickel, (b) after 60 min sonication at $57 \text{ W cm}^{-2}$ , and (c) XRD patterns of the initial and the sonicated nickel; (d) initial titanium particles, (e) after 60 min sonication, and (f) their XRD patterns. Reprinted from <i>Nanoscale</i> , 3, E.V. Skorb, et al., Sonochemical formation of metal sponges, 985 – 993, Copyright (2011), with permission from The Royal Society of Chemistry. 55	
Fig. 4-11 (a) Efficiency of $\text{O}_2^{\bullet -}$ sonogeneration at 14, 28, $57 \text{ W cm}^{-2}$ ; (b) relationship between ultrasound output power and quantity of generated hydrogen peroxide. Reprinted from <i>Nanoscale</i> , 3, E.V. Skorb, et al., Sonochemical formation of metal sponges, 985 – 993, Copyright (2011), with permission from The Royal Society of Chemistry. ....	56
Fig. 4-12 TEM images of the catalysts formed by (a) one-step sonochemical method of AlNi alloy particle treatment (inset shows the initial AlNi untreated alloy); (b) sonochemical assisted intercalation of gold particle inside mesoporous aluminum support (inset shows the solution containing aluminum mesoporous support particles and gold nanoparticles before and after intercalation). Reprinted from <i>Nanoscale</i> , 3, E.V. Skorb, et al., Sonochemical formation of metal sponges, 985 – 993, Copyright (2011), with permission from The Royal Society of Chemistry. ....	58
Fig. 4-13 Schematic illustration of the structure of metal–polymer composite synthesized in one step (a); and TEM image providing an evidence of complete filling of pores in metal matrix with polymer (polypyrrole): aluminum particles 15 min sonication at $57 \text{ W cm}^{-2}$ in ethanol solution (b); ethanol + pyrrole solution (c). Reprinted from <i>Nanoscale</i> , 3, E.V. Skorb, et al., Sonochemical formation of metal sponges, 985 – 993, Copyright (2011), with permission from The Royal Society of Chemistry. ....	59
Fig. 4-14 Schematic representation of the self-healing corrosion protection layer at the surface of the aluminum plate. The corrosion inhibitor is encapsulated in the pores at the metal surface by applying polyelectrolyte multilayer. The corrosion process initiates the release of corrosion inhibitor (1). The current density maps obtained by SVET for aluminum plates immersed in 0.1 M NaCl for 12 h (2 and 3). Before measurements the sample (2) was exposed at $57 \text{ W cm}^{-2}$ ultrasound for 30 min; (3) exposed at $57 \text{ W cm}^{-2}$ ultrasound for 30 min, soaked in the mercaptobenzothiazole solution and modified by deposition of polyelectrolyte multilayer; the complete suppression of corrosion is observed in the latter case. Reprinted from <i>Nanoscale</i> , 3, E.V. Skorb, et al., Sonochemical formation of metal sponges, 985 – 993, Copyright (2011), with permission from The Royal Society of Chemistry.....	60
Fig. 4-15 Schematic illustration of the sonochemical production of aluminum-supported nanocatalysts. A – The $160\text{-}\mu\text{m}$ -Al particles; B – Pre-treatment by sonication of initial Al particles for 30 min at $57 \text{ W cm}^{-2}$ ; C – The porous Al frameworks; D – Sonication of the mixture of the pre-treated Al particles and the noble NPs (Au, Ag, or Pt); E – The desired Al-supported nanocatalysts consisted of mesoporous aluminum support and homogeneously distributed NPs of Au, Ag or Pt. Reprinted from <i>Microporous Mesoporous Mater.</i> , 154, N. Pazos-Peréz, et al., Ultrasound driven formation of metal-supported nanocatalysts, 164 – 169, Copyright (2012), with permission from Elsevier.....	69
Fig. 4-16 TEM image of the ultramicrotomed mesoporous Al particle formed by 30-min-sonication at $57 \text{ W cm}^{-2}$ . Reprinted from <i>Microporous Mesoporous Mater.</i> , 154, N. Pazos-Peréz, et al., Ultrasound driven formation of metal-supported nanocatalysts, 164 – 169, Copyright (2012), with permission from Elsevier. ....	69
Fig. 4-17 Scanning electron microscopy (SEM) image of mesoporous aluminum particles after sonication (A). Low magnification SEM image of A (B). BET analysis (C) and BJH evaluation (D) of the mesoporous Al particles. Reprinted from <i>Microporous Mesoporous Mater.</i> , 154, N. Pazos-Peréz, et al., Ultrasound driven formation of metal-supported nanocatalysts, 164 – 169, Copyright (2012), with permission from Elsevier.....	70

Fig. 4-18 Digital photographs of Au, Ag and Pt nanoparticles suspensions (A, B, and C respectively) before (left) and after (right) the ultrasound-assisted loading in Al nanostructures. The particles sediment due to their incorporation into the Al particles. TEM image of microtomed mesoporous bimetallic (Al–Au) particle (D). The linear dependence of the Au intake in the Al particles vs. the sonication time. In 50 min of sonication the saturation is achieved (E). Reprinted from *Microporous Mesoporous Mater.*, 154, N. Pazos-Peréz, et al., Ultrasound driven formation of metal-supported nanocatalysts, 164 – 169, Copyright (2012), with permission from Elsevier. .... 72

Fig. 4-19 UV-Vis spectra of Au solution (red), and Al-Au mesoporous structure (blue). After incorporation of the nanoparticles within the Al support the intensity of the Plasmon resonance decreases because the Au particles adsorbed on the Al surface contribute to the signal, and big scattering is observed due to the Al particle size. Reprinted from *Microporous Mesoporous Mater.*, 154, N. Pazos-Peréz, et al., Ultrasound driven formation of metal-supported nanocatalysts, 164 – 169, Copyright (2012), with permission from Elsevier. .... 72

Fig. 4-20 PXRD spectrum of Al–Au system (A). Metallic Al is marked by triangles, aluminum oxides – Squares and Au – Circles. The calculated Au content from ICP is 1 wt.%. BJH (B) and BET (C) characterization of the mesoporous Al–Au systems. Pore size distribution for all cases was determined to be ~ 4 nm. Surface area: 110 m<sup>2</sup> g<sup>-1</sup>. Reprinted from *Microporous Mesoporous Mater.*, 154, N. Pazos-Peréz, et al., Ultrasound driven formation of metal-supported nanocatalysts, 164 – 169, Copyright (2012), with permission from Elsevier. .... 74

Fig. 4-21 Absorption spectra monitoring every 20 min the electron transfer reaction between hexacyanoferrate (III) and thiosulfate by using Al–Pt sponges with time (A). Plot showing the hexacyanoferrate (III) absorbance (concentration) as a function of the reaction time (B, squares). Relationship between the logarithmic scale of the normalized absorbance (against the absorbance at the beginning of the reaction) and the reaction time (B, circles). The calculated reaction rate constant (k) of Al–Pt nanostructures was 0.00775 min<sup>-1</sup>. Reprinted from *Microporous Mesoporous Mater.*, 154, N. Pazos-Peréz, et al., Ultrasound driven formation of metal-supported nanocatalysts, 164 – 169, Copyright (2012), with permission from Elsevier. .... 76

Fig. 4-22 Graphical abstract. Reprinted from *Adv. Funct. Mater.* 22, J. Dulle, et al., Sonochemical Activation of Al/Ni Hydrogenation Catalyst, 3128 – 3135, Copyright (2012), with permission from John Wiley and Sons. .... 81

Fig. 4-23 SEM images and the aluminum (Al), nickel (Ni) and oxygen (O) ratio measured by EDS (inserts) of Al/Ni particles: A–initial; B–after 5 min; C–30 min and D–50 min of sonication at 140 W cm<sup>-2</sup>. 3D confocal microscopy reconstruction of the Al/Ni nanostructure loaded with fluorescein: (E) the alloy particle after 3 min (the reconstruction of both transmission and fluorescent mode) and (F) 50 min of sonochemical exposure at 140 W cm<sup>-2</sup>. Reprinted from *Adv. Funct. Mater.* 22, J. Dulle, et al., Sonochemical Activation of Al/Ni Hydrogenation Catalyst, 3128 – 3135, Copyright (2012), with permission from John Wiley and Sons. .... 84

Fig. 4-24 N<sub>2</sub> Adsorption (–•–)–desorption (–●–) isotherms of Al/Ni particles prepared by 50 min of sonication at 140 W c<sup>-2</sup> (A). BJH pore size distribution (–●–) and pore volume (–•–) of the same particles (B). Reprinted from *Adv. Funct. Mater.* 22, J. Dulle, et al., Sonochemical Activation of Al/Ni Hydrogenation Catalyst, 3128 – 3135, Copyright (2012), with permission from John Wiley and Sons. .... 85

Fig. 4-25 PXRD (left) and <sup>27</sup>Al NMR (right) of Al/Ni -alloy particles: initial (A/B) and after 50 min of sonication at 140 W cm<sup>-2</sup> (C, D). <sup>27</sup>Al NMR spectra were recorded by using [Al(H<sub>2</sub>O)<sub>6</sub>]<sup>3+</sup> as a reference. ( \* ) indicates the spinning sidebands. Reprinted from *Adv. Funct. Mater.* 22, J. Dulle, et al.,

Sonochemical Activation of Al/Ni Hydrogenation Catalyst, 3128 – 3135, Copyright (2012), with permission from John Wiley and Sons. ....	87
Fig. 4-26 X-ray photoelectron (XPS) spectra of samples before (1) and after 50 min (2) of sonication treatment at 140 W cm <sup>-2</sup> intensity. Survey spectra (A), Ni2p peaks (B), Al2p peaks (C), and O1s peaks (D). Reprinted from <i>Adv. Funct. Mater.</i> 22, J. Dulle, et al., Sonochemical Activation of Al/Ni Hydrogenation Catalyst, 3128 – 3135, Copyright (2012), with permission from John Wiley and Sons. ....	88
Fig. 4-27 Sonochemical modification of metal particles: (I) initial particles; (II) chemical aspect surface oxidation (A) and physical aspects (B) interparticle collisions; (III) formation of mesoporous metals. Reprinted from <i>Adv. Funct. Mater.</i> 22, J. Dulle, et al., Sonochemical Activation of Al/Ni Hydrogenation Catalyst, 3128 – 3135, Copyright (2012), with permission from John Wiley and Sons.....	90
Fig. 4-28 Hydrogenation of acetophenone. Reprinted from <i>Adv. Funct. Mater.</i> 22, J. Dulle, et al., Sonochemical Activation of Al/Ni Hydrogenation Catalyst, 3128 – 3135, Copyright (2012), with permission from John Wiley and Sons. ....	90
Fig. 4-29 Reusability of Al/Ni catalyst under standard condition, namely 50 mg of USHI modified Al/Ni catalyst, 1 mL water as a solvent, reaction time 6 h at room temperature under 60 bar H <sub>2</sub> and stirring. Reprinted from <i>Adv. Funct. Mater.</i> 22, J. Dulle, et al., Sonochemical Activation of Al/Ni Hydrogenation Catalyst, 3128 – 3135, Copyright (2012), with permission from John Wiley and Sons.....	92
Fig. 4-30 Graphical abstract. Reprinted from <i>Chem. Eur. J.</i> , 17, J. Schäferhans, et al., Novel and Effective Copper - Aluminum Propane Dehydrogenation Catalysts, 12254 – 12256, Copyright (2012), with permission from John Wiley and Sons. ....	99
Fig. 4-31 Porous Al–Cu alloy D N <sub>2</sub> adsorption/desorption isotherms (a), pore size distributions (b), scanning electron micrographs (c) and transmission electron micrograph (d). Reprinted from <i>Chem. Eur. J.</i> , 17, J. Schäferhans, et al., Novel and Effective Copper - Aluminum Propane Dehydrogenation Catalysts, 12254 – 12256, Copyright (2012), with permission from John Wiley and Sons. ....	101
Fig. 4-32 X-ray diffraction patterns of the porous Al-Cu catalyst D before (a) and after (b) ultrasound treatment (the JCPDS-ICDD standards are also included for ease of comparison). Reprinted from <i>Chem. Eur. J.</i> , 17, J. Schäferhans, et al., Novel and Effective Copper - Aluminum Propane Dehydrogenation Catalysts, 12254 – 12256, Copyright (2012), with permission from John Wiley and Sons. ....	103
Fig. 4-33 Temporal propane conversion for catalyst D at 350 °C (●) and 550 °C (○). Inset: relationship between the catalyst space time (i.e. amount of catalyst per propane molar flow pass) and initial propane conversion. Note: the benchmark Pt–Sn/Al <sub>2</sub> O <sub>3</sub> catalyst (not shown) gives < 1% conversion at 550 °C. Reprinted from <i>Chem. Eur. J.</i> , 17, J. Schäferhans, et al., Novel and Effective Copper - Aluminum Propane Dehydrogenation Catalysts, 12254 – 12256, Copyright (2012), with permission from John Wiley and Sons. ....	104
Fig. 4-34 Graphical abstract. Adapted from <i>Green Chem.</i> , 15, J. Dulle, et al., Efficient three-component coupling catalysed by mesoporous copper-aluminum based nanocomposite, 1238 – 1243, Copyright (2013), with permission from The Royal Society of Chemistry. ....	109
Fig. 4-35 Sonochemical formation of mesoporous Cu/Al based particles. Intensive sonication of the initial alloy particles leads to fragmentation, porosity, and surface oxidation. Reprinted from <i>Green Chem.</i> , 15, J. Dulle, et al., Efficient three-component coupling catalysed by mesoporous copper-aluminum based nanocomposite, 1238 – 1243, Copyright (2013), with permission from The Royal Society of Chemistry.....	111
Fig. 4-36 Tentative mechanism of the A <sup>3</sup> coupling. The Cu(I) species activates the C–H bond of the alkyne to give a copper acetylide intermediate (a), which reacts with the immonium ion (b) generated in situ from the aldehyde and secondary amine to give the corresponding propargylamine (c).	

Reprinted from Green Chem., 15, J. Dulle, et al., Efficient three-component coupling catalysed by mesoporous copper-aluminum based nanocomposite, 1238 – 1243, Copyright (2013), with permission from The Royal Society of Chemistry. ....	114
Fig. 4-37 Scanning electron micrograph (a), 3D confocal microscopy reconstruction of the particle loaded with rhodamine B (picture taken in fluorescent mode) showing the porosity throughout the catalyst particle (b), transmission electron micrograph (c), and nitrogen adsorption isotherm (d) of the Cu/Al catalyst, showing the morphology and porous structure. Reprinted from Green Chem., 15, J. Dulle, et al., Efficient three-component coupling catalysed by mesoporous copper-aluminum based nanocomposite, 1238 – 1243, Copyright (2013), with permission from The Royal Society of Chemistry. ....	115
Fig. 4-38 PXRD patterns of the initial particles (a) and particles sonicated for 60 min (b). Reprinted from Green Chem., 15, J. Dulle, et al., Efficient three-component coupling catalysed by mesoporous copper-aluminum based nanocomposite, 1238 – 1243, Copyright (2013), with permission from The Royal Society of Chemistry. ....	116
Fig. 4-39 Cu 2p XP spectrum of Cu/Al; the inset shows the Cu LMM XAE spectrum (tabulated data are provided in Table 4-5). Reprinted from Green Chem., 15, J. Dulle, et al., Efficient three-component coupling catalysed by mesoporous copper-aluminum based nanocomposite, 1238 – 1243, Copyright (2013), with permission from The Royal Society of Chemistry. ....	117
Fig. 4-40 Catalyst recycling studies in the coupling of phenyl acetylene, benzaldehyde and piperidine. Reaction conditions: aldehyde (1.0 mmol), amine (1.2 mmol), and alkyne (1.3 mmol), Cu/Al (0.12 mmol Cu), toluene (1.7 ml), 100 °C, 22 h. After each cycle, the catalyst was filtered, washed with acetone and water and dried at 403 K. Reprinted from Green Chem., 15, J. Dulle, et al., Efficient three-component coupling catalysed by mesoporous copper-aluminum based nanocomposite, 1238 – 1243, Copyright (2013), with permission from The Royal Society of Chemistry. ....	118
Fig. 4-41 Graphical abstract. Reprinted from RSC Advances, 2, J. Dulle, et al., Sononanostructuring of zinc based material, 12460 – 1246, Copyright (2012), with permission from The Royal Society of Chemistry. ....	123
Fig. 4-42 A - Sonochemical modification of zinc particles: (I) initial particles; (II) (a) chemical aspect due to surface oxidation; (b) physical aspects are caused by interparticles collisions and surface impinging by high velocity microjets providing preferable directions of etching; (III) formation of “hedgdehog” zinc particles. B, C – TEM (B, 10 min US) and SEM (C, 15 min US) images of core-shell “hedgdehog” structure: metal core and the oxide nanorods attached to the core after US treatment. Reprinted from RSC Advances, 2, J. Dulle, et al., Sononanostructuring of zinc based material, 12460 – 1246, Copyright (2012), with permission from The Royal Society of Chemistry. ....	125
Fig. 4-43 XPS spectra of “hedgdehog” zinc particles (A) and the ZnO nanorods (C), and SEM image of the ultramicrotomed Zn/ZnO particle (B) and ZnO nanorods (D) after 15 min of US treatment. Reprinted from RSC Advances, 2, J. Dulle, et al., Sononanostructuring of zinc based material, 12460 – 1246, Copyright (2012), with permission from The Royal Society of Chemistry. ....	127
Fig. 4-44 PXRD patterns and SEM images of the initial zinc particles (A, B) and treated for 1 min (C, D), 10 min (E, F) and 60 min (G, H) by ultrasound. The inserts (a, c, e, g) show the magnified part of the PXRD patterns with the ZnO attributed peaks. Reprinted from RSC Advances, 2, J. Dulle, et al., Sononanostructuring of zinc based material, 12460 – 1246, Copyright (2012), with permission from The Royal Society of Chemistry. ....	129
Fig. 4-45 SEM images of ~ 4 µm and ~ 50 µm initial particle size after 5 (A, B), 15 (C, D) and 60 min (E, F) ultrasound treatment. Reprinted from RSC Advances, 2, J. Dulle, et al., Sononanostructuring of zinc	

based material, 12460 – 1246, Copyright (2012), with permission from The Royal Society of Chemistry.

..... 131

Fig. 4-46 Reaction rate constant  $k$  is shown in dependence of ultrasound treatment duration. We used 10 mg of the US-Zn (A). The SEM images of the samples prepared for 90 min of sonication: 0.01 g ml<sup>-1</sup> 50 μm Zn particles (B), 0.01 g ml<sup>-1</sup> 4 μm particles (C), 0.04 g ml<sup>-1</sup> 4 μm particles (D) and 0.1 g ml<sup>-1</sup> 4 μm particles (E). Reprinted from RSC Advances, 2, J. Dulle, et al., Sononanostructuring of zinc based material, 12460 – 1246, Copyright (2012), with permission from The Royal Society of Chemistry. ... 134

## List of Tables

Table 4-1 Conversion of acetophenone in dependence of H <sub>2</sub> -pressure, amount of catalyst, as well as amount of substrate for a reaction time of 24 h at RT, stirring, and 1 mL water as a solvent. ....	91
Table 4-2 NMR1. Refinement parameters for the <sup>27</sup> Al MAS spectra (Fig. 4-25B, D) of the Al/Ni alloy powder before and after 50 min of sonication. Reprinted from Adv. Funct. Mater. 22, J. Dulle, et al., Sonochemical Activation of Al/Ni Hydrogenation Catalyst, 3128 – 3135, Copyright (2012), with permission from John Wiley and Sons. ....	94
Table 4-3 Composition, surface area and initial dehydrogenation rate for Al–Cu catalysts A–D. Reprinted from Chem. Eur. J., 17, J. Schäferhans, et al., Novel and Effective Copper - Aluminum Propane Dehydrogenation Catalysts, 12254 – 12256, Copyright (2012), with permission from John Wiley and Sons. ....	102
Table 4-4 A <sup>3</sup> coupling catalyzed by Cu/Al. Reprinted from Green Chem., 15, J. Dulle, et al., Efficient three-component coupling catalysed by mesoporous copper-aluminum based nanocomposite, 1238 – 1243, Copyright (2013), with permission from The Royal Society of Chemistry. ....	112
Table 4-5 XPS data of the Cu/Al sample. Reprinted from Green Chem., 15, J. Dulle, et al., Efficient three-component coupling catalysed by mesoporous copper-aluminum based nanocomposite, 1238 – 1243, Copyright (2013), with permission from The Royal Society of Chemistry. ....	117

# 1 Introduction

Have you ever been climbing in the "Fränkische Schweiz", Margalef, or Gorges du Tarn and have asked yourself: What kind of wonderful material is it, which allows me to put my fingers inside its tiny holes and cracks? These rock "sponges" are porous materials.

Porous materials have brilliant properties. High surface area, low weight, great storage properties for water and hydrogen, catalyst support, to name just a few of them. These materials can be found everywhere in our daily life, even cat litter is made from porous materials.

However, porous materials can more than just store gases and liquids. Due to their high surface area they are highly popular for catalysis. Inside various porous materials, catalytic active hints and kinks can be produced or immobilized and used for catalytic reactions.

Power ultrasound, also named high intensity ultrasound (US) is a new tool for the formation of such catalytic active porous materials. In my work I focused on the formation of metals which get catalytically activated and porous by the power of US. The reason why US is such an interesting and unique tool for the modification is that it is an inexpensive, one-step, and "green chemistry" method to prepare porous materials compared to common methods like e.g. chemical dealloying. We can call our method "green chemistry" as some of the principles, announced 1998 by Anatas and Warner [1–3], apply for our system. Let's name just a few of them: Waste prevention instead of treatment, minimization of solvents and reagents, low operating costs, use of less hazardous materials, and a process with low accident risk.[1–3]

The application of US towards metal catalysts is very attractive. The materials we have produced fall into the category of heterogeneous catalyst. These dominate the petrochemical and bulk chemical industry [4] with sales over 2 billion Euro in 2005, having an expected annual growth of over 3 %.[3,5] Many reactions require a catalyst which contains noble metals like platinum, palladium, or gold. One of our aims was it to produce a heterogeneous catalyst, which performs the reaction without containing expensive and rare metals. Another aim was the immobilization of noble metal nanoparticles inside a porous aluminum matrix with the help of US.[6–11]

The following part will give a brief overview of the common methods to prepare porous materials and catalysts. Usually a catalyst consists of a carrier phase and a catalytically active phase (see Fig. 1-1).[3,12] The active phase should be evenly dispersed on the support and have the highest possible accessible surface area in order to transform as many guest compounds as possible. In order to achieve this, there are several preparation methods, which can be separated into two categories namely template assisted and template free.[12]

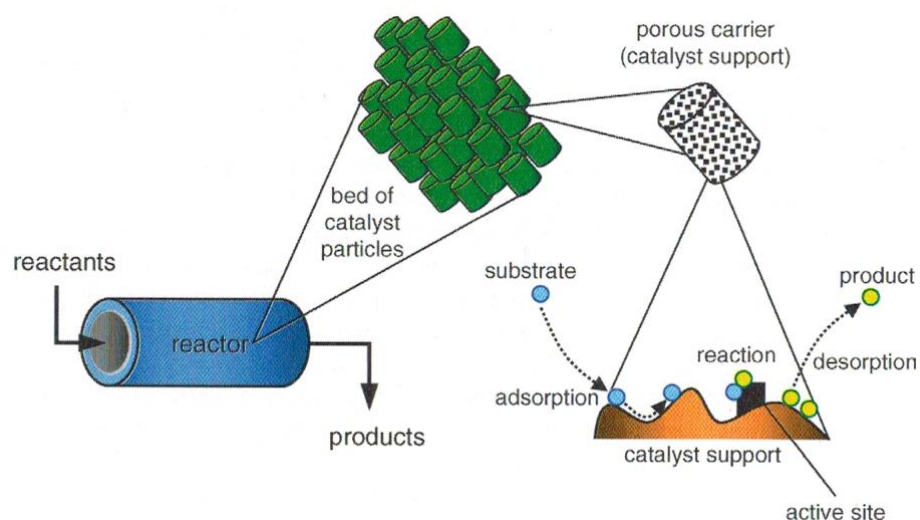


Fig. 1-1 A plug-flow catalytic reactor at various zoom-in levels. Gadi Rothenberg: *Catalysis: Concepts and Green Applications*. 130. 2008. Copyright Wiley-VCH Verlag GmbH & Co. KGaA. Reproduced with permission.

Template assisted methods require a preformed template, these templates are usually the product of self-assembly processes (liquid crystalline phases,[13] colloidal crystals,[14] porous block copolymers[15] etc.) which yield a scaffold onto which the catalytically active metal is bound. The resulting materials have a high surface area and narrow size distribution and are well suited for catalysis. This process is a multistage one and sometimes involves the exchange of the supporting phase. These facts make the materials cost intensive and wasteful, especially when the process is up scaled.[12]

Template-free methods depend on the principle of dealloying. Here one component of an alloy is removed through dissolution. If the alloy is monolithic, the resulting pores have a reasonably small size distribution. In the case that the alloy is not monolithic the resulting material has a wide range of pore sizes and is not well defined. The advantage of this method lies in its simplicity as it is only a one-step process.[12] The most prominent and important material made from such a template-free process is “Raney®-Nickel”, which is a widely used catalyst for hydrogenation reactions since the 1925s.[16] However, “Raney®-Nickel” has the big disadvantage that it is pyrophoric and not stable under ambient conditions. The main drawback of the template-free method is the limited number of systems that can yield well defined poresize distributions.[12]

In this thesis, we present a new and effective way to produce metal (Al, Mg) sponges via high intensity ultrasound. These sponges can act as a support for catalytically active species, which can range from incorporated noble metal nanoparticles to other metals like Cu or Ni. We investigated not only the catalytic properties of these materials but also the principles of formation and modification that are responsible for their structure and unique properties.[6–11]

Let us now come to the question of how US modifies metals in the way that they become porous and even active for catalysis. At high intensities above  $30 \text{ W cm}^{-2}$  and at a frequency of 20 kHz, soundwaves have the capability to chemically and physically modify metals.[17–25] Various processes are at work here. Particle collisions lead to break up of large particles. The collapse of cavitation bubbles leads to locally high temperatures of up to 5000 K and pressure of several hundred atmospheres and also produces liquid jets that impinge on the metal surface with very high velocity (so-called “hot-spot theory”).[23–27] Whenever a cavitation bubble is generated near a boundary, the asymmetry of the liquid particle motion during cavity collapse induces a deformation in the cavity. The potential energy of the expanded bubble is converted into kinetic energy of a liquid jet that extends through the bubble's interior and penetrates the opposite bubble wall. Because most of the available energy is transferred to the accelerating jet, rather than the bubble wall itself, this jet can reach velocities of hundreds of meters per second. Because of the induced asymmetry, the jet often impacts the local boundary and delivers enormous energy densities at the site of impact, especially for larger bubbles at lower frequency.[29] The second mechanism of cavitation-induced surface damage invokes shockwaves created by cavity collapse in the liquid. The impingement of microjets and shockwaves on the surface creates the localized erosion responsible for ultrasound cleaning and many of the sonochemical effects on heterogeneous reactions. The erosion of metals by cavitation generates newly exposed, highly heated surfaces. Such energy concentration can result in severe damage to the boundary surface; this is less true at higher (MHz) frequencies, simply because the cavitation bubbles are much smaller.[14] In order to induce substantial distortions during bubble collapse, the resonance bubble size has to be smaller than the solid surface (e.g. at 20 kHz the maximum size of a cavitation bubble is  $\sim 5 \mu\text{m}$  [30]). Whenever a microjet of liquid passes through the cavity it can impact the solid surface at speeds estimated at approximately  $100 \text{ m s}^{-1}$ . [31] However, this is only appearing for particles larger than  $\sim 200 \mu\text{m}$ , as this effect is not observed for smaller ones.[32] In the case of smaller particles, the cavitation-created shockwave induces high-velocity interparticle collisions.[29] Collisions and high shear forces break up bigger particles and increase the accessible surface area. The high temperature and pressure at cavitation sites are responsible for the emergence of radicals from the solvent.[17–27] All these phenomena are happening at the same time and have different influences on the sonicated material. Depending on the metal these radicals and the high kinetic forces as well as the temperature can have very different effects. In case of noble metals their high melting point as well their ability to withstand oxidation leads to hardly any structural change. Ni and Ti have high melting points and are only modified on the surface. Al and Mg form metal sponge phases with a stabilizing oxide layer on a metallic skeleton, and in case of Zn total oxidation occurs. The amount of oxide formed is mainly depended on the sonication time, please see our publications[17–22] further down for more details. When two metals are alloyed, this can lead to build-up of amorphous oxide in

one but not the other metal. This leads to a local phase segregation and improves the catalytic properties to a large degree due to the increase in accessible surface area and the number of active sites. We have found multiple examples of such behaviour and have investigated the catalytic properties of these systems in great detail.[17–22] For example, by mixing the right metals one can produce a highly active catalyst for hydrogenation reactions, which performs better in terms of stability and reactivity than the commercially available “Raney®-Nickel”, in a one-step one-pot process.[8] The ability of noble metals to withstand the effects of ultrasound can be used to incorporate noble metal nanoparticles into an already formed mesoporous support. An example of this is also given in the publications further down.[6,9] In this thesis, a number of new, exciting, and easy ways to produce mesoporous metals is brought forth. The materials obtained were tested mostly for their catalytic abilities as this is a field where even small improvements of existing and applied systems can have a big impact on a monetary and environmental scope. This is only one of many different possible applications for the produced materials.

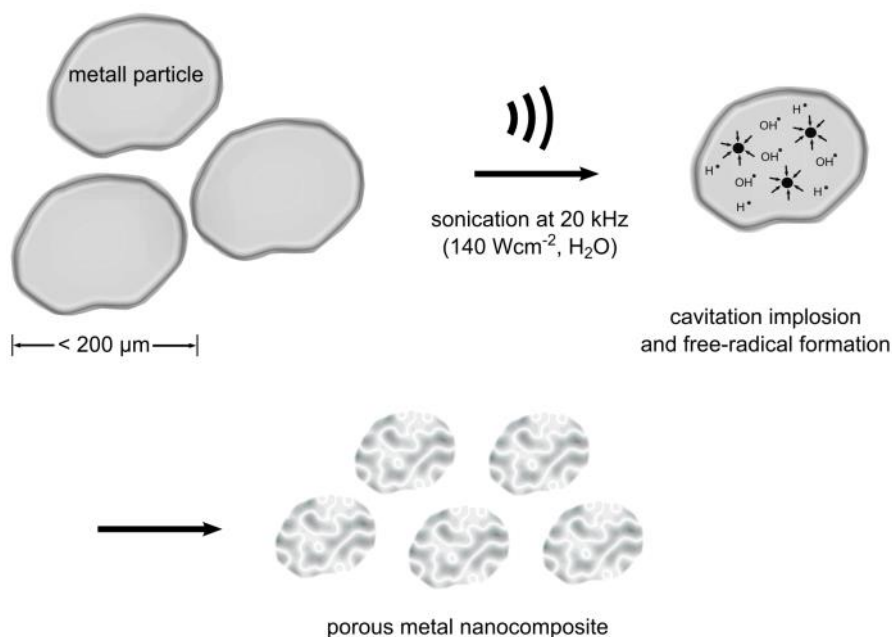


Fig. 1-2 Formation of porous metal particles by ultrasonication. Adapted from *Green Chem.*, 15, J. Dulle, et al., Efficient three-component coupling catalyzed by mesoporous copper-aluminum based nanocomposite, 1238 – 1243, Copyright (2013), with permission from The Royal Society of Chemistry.

Recent studies showed the US preparation method makes metals active for electrocatalyst and that they hold great potential for the hydrogen evolution reaction as well.[33,34] Furthermore the versatility of ultrasonication to produce various sponge phases with an array of different starting material is highlighted in a recent article in Ref. [35].

## References

- [1] P. T. Anastas, *Green Chemistry: Theory and Practice*, Oxford University Press, 2000.
- [2] P. T. Anastas and M. M. Kirchhoff, *Acc. Chem. Res.*, 2002, 35, 686.
- [3] Gadi Rothenberg: *Catalysis: Concepts and Green Applications*, Wiley-VCH Verlag GmbH & Co. KGaA, 2008.
- [4] J. H. Gary and G. E. Handwerk, *Petroleum Refining: Technology and economics*, CRC Press, Boca Ratan, 2001.
- [5] E M. Bryner and A. Scott, *Chem. Week*, 2006, 168, 19.
- [6] E.V. Skorb, D. Fix, D.G. Shchukin, H. Möhwald, D.V. Sviridov, R. Mousa, N. Wanderka, J. Schäferhans, N. Pazos-Pérez, A. Fery, D.V. Andreeva, *Nanoscale*, 2011, 3, 985.
- [7] J. Schäferhans, S. Gómez-Quero, D. V. Andreeva and G. Rothenberg, *Chem-Eur J*, 2011, 17, 12254–12256.
- [8] J. Schäferhans, S. Gomez-Quero, D. V. Andreeva, G. Rothenberg, *Chem.-Eur. J.* 2011, 17, 12254.
- [9] N. Pazos-Pérez, J. Schäferhans, E. V. Skorb, A. Fery, D. V. Andreeva, *Micropor. Mesopor. Mat.* 2012, 154, 164.
- [10] J. Dulle, S. Nemeth, E. V. Skorb, T. Irrgang, J. Senker, R. Kempe, A. Fery and D. V. Andreeva, *Adv. Funct. Mater.*, 2012, 22, 3128–3135.
- [11] J. Dulle, K. Thirunavukkarasu, M. Mittelmeijer-Hazeleger, D. V. Andreeva, N. R. Shiju, G. Rothenberg, *Green Chem.*, 2013, 15, 1238 – 1243.
- [12] A. Fürster, *Supporter metals in Active Metals*, VCH, 1996.
- [13] G. S. Attard, P. N. Bartlett, N. R. B. Coleman, J. M. Elliott, J. R. Owen, J. H. Wang, *Science* 1997, 278, 838.
- [14] O. D. Velev, P. M. Tessier, A. M. Lenhoff, E. W. Kaler, *Nature* 1999, 401, 548.
- [15] H. Maeda, Y. Kusunose, M. Terasaki, Y. Ito, C. Fujimoto, R. Fujii, T. Nakanishi, *Chem.-Asian J* 2007, 2, 350.
- [16] a) M. Raney, U.S. Patent 1,563,587, 1925; b) M. Raney, *Ind. Eng. Chem.*, 1940, 32, 1199 –1203; c) G. Ertl, H. Knözinger, (Eds.) 1997, *Preparation of Solid Catalysts*, Weinheim, Wiley.
- [17] L. A. Crum, *J. Acoust. Soc. Am.*, 1979, 66, S45.
- [18] M. Strasberg, *J. Acoust. Soc. Am.*, 1959, 31, 163–176.
- [19] E. N. Harvey, D. K. Barnes and W. D. Mc Elroy, A. H. Whitely, D. C. Pease and K. W. Cooper, *J. Cell. Comp. Physiol.*, 1944, 24, 1–22.
- [20] M. Strasberg, *J. Acoust. Soc. Am.*, 1957, 29, 177.
- [21] D. Y. Hsieh and M. S. Plesset, *J. Acoustic. Soc. Am.*, 1961, 33, 206–215.
- [22] A. I. Eller, *J. Acoust. Soc. Am.*, 1969, 46, 1246–1250.
- [23] R. K. Gould, *J. Acoust. Soc. Am.*, 1994, 56, 1740–1746.

- [24] L. A. Crum, *Ultrasonics*, 1984, 22, 215–223.
- [25] V. Kamath and A. Prosperetti, *J. Acoust. Soc. Am.*, 1991, 89, 1863.
- [26] C. E. Brennen, *Cavitation and Bubble Dynamics*, Cambridge University Press, 2013.
- [27] O. Louisnard and J. González-García, "Acoustic Cavitation," in *Ultrasound Technologies for Food and Bioprocessing*, Springer, 2011, 13–64.
- [28] G. Cravotto and P. Cintas, *Angew. Chem. Int. Ed.*, 2007, 46, 5476–5478.
- [29] K. S. Suslick and L. A. Crum, *Sonoluminescence and Sonochemistry*, *Encyclopedia of Physical Science and Technology*, 3rd ed., R. A. Meyers, Ed., San Diego,: Academic Press, 2001.
- [30] N. A. Tsochatzidis, P. Guiraud, A. M. Wilhelm and H. Delmas, *Chemical Engineering Science*, 2001, 56, 1831–1840.
- [31] N. V. Dezhkunov, V. I. Kuvshinov, G. I. Kuvshinov and P. P. Prokhorenko, *Soviet Physics Acoustics-Ussr*, 1980, 26, 392–395.
- [32] K. S. Suslick and G. J. Price, *Annual Review of Materials Science*, 1999, 29, 295–326.
- [33] P. V. Cherepanova, M. Ashokkumarb, and D. V. Andreevaa, *Ultrason. Sonochem.*, 2015, 23, 142–147.
- [34] P. V. Cherepanov, I. Melnyk, E. Skorb, P. Fratzl, E. Zolotoyabko, N. Dubrovinskaia, L. Dubrovinsky, Y. S. Avadhut, J. Senker, L. Leppert, S. Kummel and D. V. Andreeva, *Green Chem.*, 2015, doi = 10.1039/C5GC00047E.
- [35] E. Skorb and D. V. Andreeva, *J. Mater. Chem. A*, 2013, 1, 7547–7557.

## 2 Mechanical and chemical aspects of high intensity ultrasound

### 2.1 General aspects of sonication

#### 2.1.1 Sonication

Sonication is the treatment of a material (usually in a solvent) with high-intensity ( $> 1 \text{ W cm}^{-2}$ ) sound in the frequency range of 20 kHz to 200 kHz. The corresponding wave lengths are given by the speed of sound divided by the frequency and typically range from centimeters to micrometers, which is still orders of magnitude larger than molecular dimensions.[1] With such large wavelengths even a very strong sound wave could not interfere with or change any material on a molecular basis. But as sound waves are pressure waves they can induce what is called acoustic cavitation. The following paragraphs describe this phenomenon and also how it can be used to modify substances and materials on a molecular level.

#### 2.1.2 Cavitation

When a sound wave passes through a medium, like a liquid or a gas, it causes compressions and rarefactions in it. On the relevant atomic length scale, the wave is essentially an oscillation of pressure around its background value. In the compression phase the pressure is increased and in the rarefaction phase it is decreased. This change of pressure is dependent on the amplitude of the ultrasonic field. If the medium is a liquid and the amplitude of the sound wave is high enough, the pressure in the rarefaction phase can become lower than the vapor pressure of the liquid. Then the liquid does not withstand the rarefaction phase anymore and locally breaks up, forming small bubbles. These bubbles can either be stable or unstable. Blake derived a pressure threshold, from thermodynamic and interfacial considerations, below which only unstable bubbles are formed and cavitation must occur [2]. In this context, stable means that the bubbles are hardly influenced by an external force as they are mainly governed by surface tension. Stable bubbles are very small and their resonance frequency is much higher than the typical frequency for sonication. Unstable bubbles are bigger and have therefore lower resonance frequencies and can be influenced by sonication. Bubble formation depends on many parameters aside from intensity and frequency of the sound field, the most important ones are temperature, surface tension, and viscosity.[3] Gases and/or particles already present in the solvent also induce bubble formation by acting as nucleation sites as they weaken the cohesive force of the liquid.[4–7] After these bubbles are formed they either can vanish in the compression phase or start to oscillate in the acoustic field. We want to focus on the oscillating bubbles. These bubbles are expanding in the rarefaction phase and contract in the pressure phase. As the bubble expands, vapor of the surrounding medium fills the growing cavity. When the bubble is compressed, the vapor diffuses back in the medium again. As the interfacial area and hence the

amount of vapor that can be exchanged is bigger during the expansion phase the bubble is growing as it oscillates in the sound field. This process is called rectified diffusion.[8] This net inward flow of gas is opposed by the tendency of a gas bubble to dissolve in a gassy liquid due to the Laplace pressure. The Laplace pressure is the pressure difference between the bubble and the liquid. It mainly depends on the bubble radius and interfacial tension and can be several atmospheres for bubbles in the micrometer range. As the bubble grows to several hundred micrometers it will reach a critical radius and become unstable and collapse. The final size at which this transition takes place depends on the frequency of the sound field, when the response frequency of the bubble is close to the applied frequency resonance effects cause the bubble to violently collapse. This collapse results in very high local temperatures ( $\sim 5000$  K) and pressures ( $> 1000$  atm).[9] These conditions cause the formation of radicals and other reactive species in the medium and can induce many different chemical reactions.[10–13] A more detailed look at the sonochemistry in the aqueous system is given in the next section. The effects of cavitation are not limited to liquids, but can also be used to modify heterogeneous systems in exciting ways; this will be covered in the last section of this chapter.

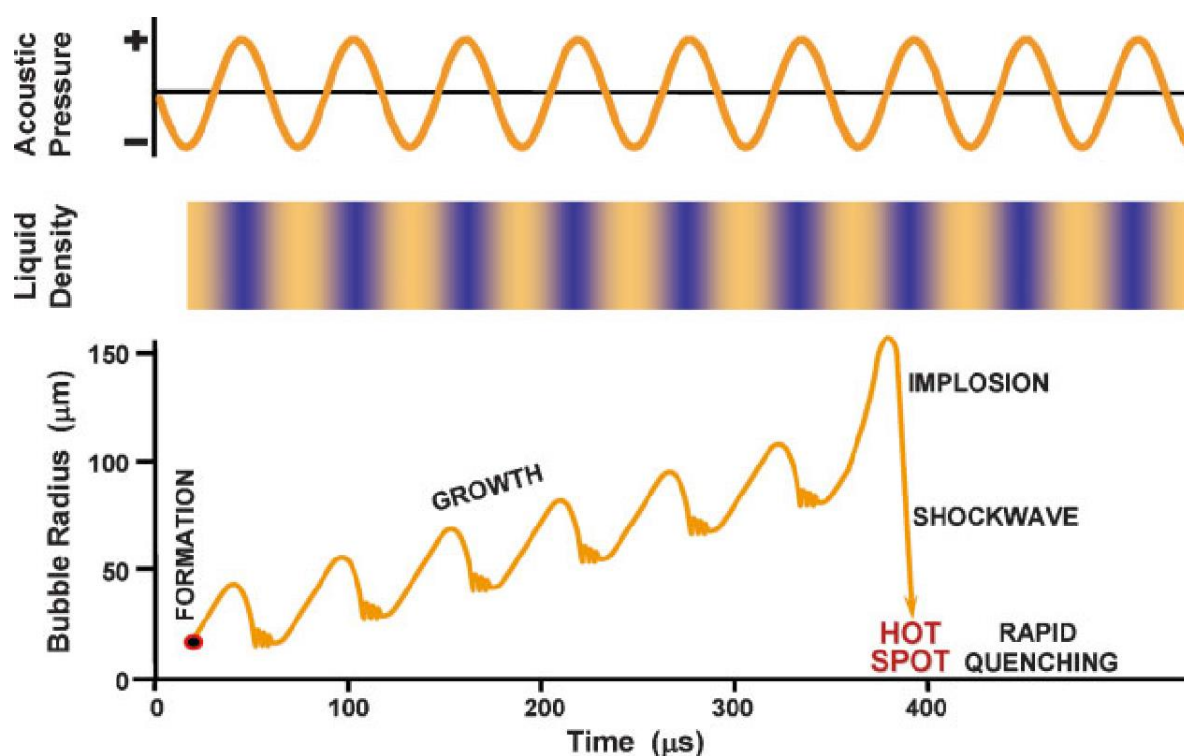
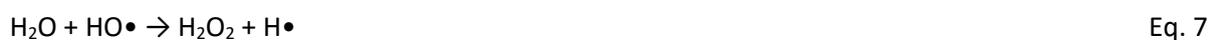
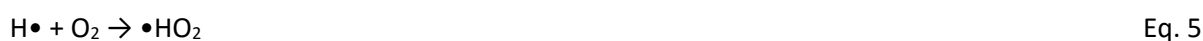


Fig. 2-1 Schematic representation of transient acoustic cavitation. Reprinted from J. H. Bang, K. S. Suslick, Applications of Ultrasound to the Synthesis of Nanostructured Materials, *Advanced Materials* 2010, 22, 1039–1059, Copyright (2010), with permission from John Wiley and Sons.

## 2.2 Cavitation in aqueous media

The extreme conditions arising with the collapse of the bubble lead to the dissociation of water molecules. The most important reactions involving radical formation and recombination upon sonication in water are the following.



Scheme 1: Sonolytic production and recombination of radical and reactive oxygen species.[14]

The distribution of these radical species in and around the bubble is highly inhomogeneous. There are three distinct regions where radicals are formed and react.[15] The first is the bubble interior where the highest temperatures and pressures occur and most of the radical species are found. The second is the bubble wall which plays a main role in the distribution of the formed species into the surrounding medium. The third one is the liquid around the collapsing bubble, which holds potential reaction partners for the formed radicals either in the form of water molecules or a specific substrate that should undergo transformation through sonochemistry. Inside the bubble the main reaction is the formation of  $\text{H}\cdot$  and  $\text{HO}\cdot$  according to Eq. 1 from water vapor. If any other molecules are present, they either are pyrolyzed due to the high temperature or they react with the  $\text{HO}\cdot$  radical. In the interfacial layer between the bubble interior and the bulk liquid the temperature is much lower and this layer can be considered as a supercritical liquid. Here the  $\text{HO}\cdot$  radicals can combine to  $\text{H}_2\text{O}_2$  according to Eq.4, which then can also react with present substrates besides the  $\text{HO}\cdot$  radicals. The region around the bubble is at ambient temperature. Here the reactive oxygen species that have formed inside the bubble mainly react with any present molecules like reaction partners in case of sonochemical synthesis or contaminants that should be removed from the solution.[16]

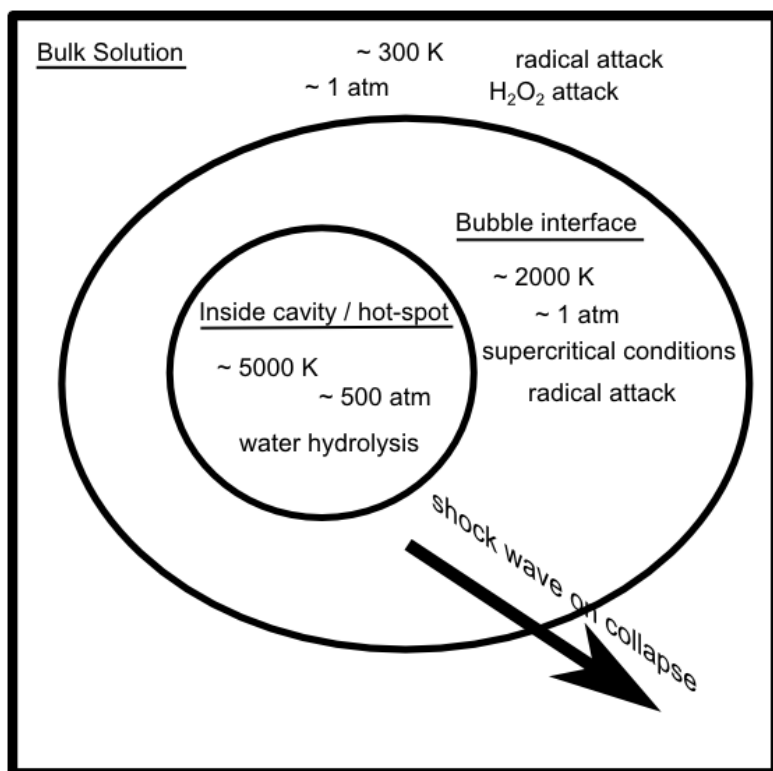


Fig. 2-2 The cavitation bubble as a chemical microreactor. Adapted from G. Cravotto et. al., Forcing and Controlling Chemical Reactions with Ultrasound, *Angew. Chem. Int. Ed.* 2007, 46, 5476 – 5478, Copyright (2007), with permission from John Wiley and Sons.

After the collapse, the distribution of radicals in and around the bubble follows a narrow Gaussian distribution with its maximum in the centre of the collapsing bubble. It was determined by Margulis[17] that radicals from one bubble can never react with the radicals from another bubble because they either recombine (Eq. 2-6) or react with water (Eq. 7) or a substrate molecule. The amount of free radicals that are produced during cavitation is directly related to the intensity of the bubble collapse. The main factor determining this is the maximum radius of the collapsing bubble. A bubble that has a larger radius when collapsing produces higher temperatures and therefore more free radicals.[18] This means that in order to produce a lot of radicals relatively low frequencies and high intensities have to be used.

There are various methods to determine the concentration of free radicals and other reactive oxygen species in and around the bubble. As radicals have a very short lifetime ( $\mu\text{s}$ ) they are hard to detect and quantify. In order to do so one has to trap the radical in a more stable state that can be quantitatively measured. In case of  $\text{HO}\bullet$  this can be done via spin trapping. The  $\text{HO}\bullet$  can be trapped for example with 5,5-dimethyl-pyrroline N-oxide and forms a nitrox-based spin adduct. This adduct can then be detected with electron paramagnetic resonance.[18] But this method also has its drawbacks as not all  $\text{HO}\bullet$  radicals will be trapped and can also react in other ways with the spin

trapping molecule. The concentration of  $\text{H}_2\text{O}_2$  however is much simpler to determine. One of the best described methods is iodometry,[19] but there are also other methods like the oxidation of luminol with horseradish peroxidase. Also  $\text{H}_2\text{O}_2$  in the presence of luminol at high pH ( $\text{pH} > 10$ ) gives rise to chemiluminescence. The intensity of the emitted light depends on the sound intensity as higher intensity produces more peroxides. The reason for this chemiluminescence lies in the production of superoxide anion radical  $\text{O}_2^{\bullet-}$  from  $\text{H}_2\text{O}_2$  under basic conditions.[20] The amount of superoxide can also be determined quantitatively with the use of tetranitromethane, a scavenger of superoxide.[21–23]

Apart from the formation of radicals water also represents a special case. Water has a very low vapour pressure and high surface tension. Both properties increase the cavitation threshold and lead to a more intense bubble collapse. This in turn means that the intensity of the bubble collapse can be easily tuned by lowering surface tension, by adding a small amount of surfactant for instance. Vapour pressure on the other hand is a function of temperature. Higher temperatures lead to a decrease of the cavitation threshold and to a less intense bubble collapse. Both properties can be utilized to tune the forces upon cavitation.

## 2.3 Cavitation in heterogeneous systems

The forces and reactive species which are produced through cavitation in liquid systems can, apart from the already mentioned sonochemistry, also be used to modify surfaces or particles. We will focus on the effects on metal particles which are at the heart of our investigations.

### 2.3.1 Interparticle collisions

When bubbles collapse they emit shockwaves into the surrounding medium. These shock waves are generated by the rebound of the bubble wall after the minimum radius is reached upon collapse. Pecha et al.[24] measured the initial velocity of these shockwaves to  $4000 \text{ m s}^{-1}$ . These shock waves accelerate the suspended particles. If the particle concentration is high enough, these particles will collide. At the points of collision immense energy is set free in the form of heat. The temperatures that can be reached at the point of impact are in between  $2600 \text{ }^\circ\text{C}$  and  $3400 \text{ }^\circ\text{C}$  [25] for  $10 \text{ }\mu\text{m}$  particles at velocities of several hundred meters per second. Doctys and Suslick [25] estimated the maximum velocity for  $10 \text{ }\mu\text{m}$  particles to be half the speed of sound in the respective medium so for water that would be  $\sim 740 \text{ m s}^{-1}$ . This can either lead to particle breakage, fragmentation, and an increase in roughness or to the fusion of smaller particles into bigger ones. The main factor influencing which behavior can be observed is the initial particle size. Prozorov et.al.[26] showed that for Zn particles in decane only a small size range ( $2.2 \text{ }\mu\text{m} \leq R \leq 38 \text{ }\mu\text{m}$ ) exists that allows for particle fusion to take place. In order to fuse a particle has to partially melt upon collision and for this to happen a certain critical velocity has

to be reached. The exact value for this velocity depends on the melting point of the particle material. The particle velocity that can be reached depends mainly on the particle cross section and the viscosity of the liquid. If the cross section is too small the particle will not be accelerated at a given viscosity to reach the critical velocity. If the particles are too large their viscous drag is too high in order to be accelerated to reach the critical velocity. Apart from fusion of particles melting can induce phase changes on the particle surface. Therefore, virtually all metals, except the highest-melting metals like tungsten are affected by interparticle collisions. If the velocity of the accelerated particles is not high enough to cause fusing the collisions can still break bigger particles apart and lead to deformation of the surface which improves the reactivity of sonicated metal particles.

Another form of mechanical force that is occurring when a bubble collapses is the so called liquid jet. This is formed when the site of cavitation is near a surface. The bubble cannot grow evenly and because of this becomes unstable, the bubble wall that faces away from the surface starts to implode and the bubble collapses. This collapse is accompanied by the impinging of a liquid jet on the near surface. The force this jet exercises on the surface leads to local erosion and in case of particles, if they are big enough, to breakage. Typically the jets have a speed of  $120 \text{ m s}^{-1}$  –  $150 \text{ m s}^{-1}$ . [27]

### **2.3.2 Effects on particle size and morphology**

The main factors influencing the effect of cavitation in water on a metal particles and surfaces are the melting point of the metal and its tendency to react with the free radicals that are emerging upon bubble collapse. We showed that metal particles that have a low melting point like Zn and are less resistant to oxidation can be totally oxidized upon treatment with high-intensity ultrasound. Particles made from metals with an intermediate melting point like Al, which is also not as easily oxidized as Zn, become porous and form a thin layer of oxide on their surface. With an even higher melting point, like for instance in the case of Ni, only slight surface oxidation is observed, and noble metals show no changes at all after US treatment. [28] The formation of the mesoporous structure when sonicating Al is the most interesting case, as here not only a surface modification occurs but also the internal structure of the metal particles is changed in a profound way. The accessible surface increases from  $< 1 \text{ m}^2 \text{ g}^{-1}$  up to  $80 \text{ m}^2 \text{ g}^{-1}$  and pores with a diameter of 4 nm are formed. In the next section we will go into more detail about the oxidation and reduction processes on the solid-liquid interface. The high temperatures that occur during cavitation lead also to partial melting of the metal particles. This can lead to phase separation in alloys and, in the case of pure metals, in separation into amorphous and crystalline phases. The particle size in case of Al decreased from  $160 \text{ }\mu\text{m}$  before sonication down to  $5 \text{ }\mu\text{m}$  –  $10 \text{ }\mu\text{m}$  after 60 minutes of sonication. Particles made of Zn are totally oxidized after 60 min sonication to ZnO which forms crystalline needles. In case of Ni the initial particles were already quite small ( $\sim 15 \text{ }\mu\text{m}$ ) and no significant effect on their size was found. For particles that are not fully oxidized

such behavior can be understood when considering the effects governing interparticle collisions and jet formation. As the particles get smaller during sonication they reach sizes where their velocity is not high enough to further break a small particle apart. The smaller size of the particles also prevents the formation of jets from collapsing bubbles. The mean size for such a bubble at the employed frequency is 150  $\mu\text{m}$  and therefore much too big to be influenced by a 5  $\mu\text{m}$  – 10  $\mu\text{m}$  particle.[28]

### **2.3.3. Red/Ox reactions and structure formation in water**

Apart from collisions and liquid jets high intensity ultrasound in aqueous media leads to oxidation processes which play a major role in the structure formation of mesoporous metal particles. Metals like Al and Zn for instance react with the formed free radicals in water to various oxides and hydroxides ( $\text{Al(OH)}$ ,  $\text{Al(OH)}_3$ , and  $\text{ZnO}$ ). Two factors influence the outcome of sonication for different metals, their ability to withstand oxidation and their melting point. Noble metals like Au, Pd, and Pt have a very high standard electrode potential and are therefore difficult to oxidize. Sonication of these noble metals in aqueous media has no effect on them. For metals that can be oxidized under these conditions (Zn, Al, Ti, Ni) their melting point is determining the extent of structural changes. Zn having the lowest melting point is completely oxidized and Ti having the highest shows only surface oxidation. The metals with an intermediate melting point like Al form a porous structure. Furthermore the mechanical forces like liquid jets and inter particle collisions during sonication lead to surface erosion. These mechanical and oxidation processes lead to structural changes of the particles by formation of macro as well as mesopores. These pores are stabilized by a thin oxide layer. For Al particles we found that the main oxidation products were  $\text{Al(OH)}_3$  and  $\text{AlO(OH)}$ . The concentration of oxidized metal increased with sonication time. Aluminum and its ability to form a mesoporous structure upon sonication that is stabilized by an oxide layer led us to the investigation of Al alloys. We found that metals like Ni and Cu, which are not made porous by ultrasound treatment, in case of Cu due to the resistance to oxidation and in case of Ni its high melting point, can be integrated in mesoporous structures of Al.[29,30] Sonication of such an alloy still leads to the aforementioned mesopores and high surface area. But it also leads to the formation of intermetallic compounds made of the present metals and oxygen. These intermetallic compounds can act as catalysts for hydrogenation[29] or  $\text{A}^3$  coupling reactions.[30] Sonication also makes the catalytic material more resistant to degradation by atmospheric oxygen because the catalytic sites are protected by a very thin layer of metal oxide. In order for such an intermetallic compound to be formed reduction processes must take place. We propose that inside the Al scaffold  $\text{H}_2$  is produced as a by-product of the Al oxidation. This  $\text{H}_2$  reduces already formed metal oxides in the presence of Al to give the catalytically active intermetallic compounds. The  $\text{H}_2$  plays also a role in the structure formation of sonicated Al particles. By reducing some of the Al oxide species that make up the mesoporous structure it is stabilized and can grow. The  $\text{H}_2$  counteracts oxidation processes and prevents the total oxidation of the metal.

## References

- [1] D.G. Shchukin, H. Möhwald, *Phys. Chem. Chem. Phys.*, 2006, 8, 3496.
- [2] F.G. Blake, Technical Memo 12, Acoustics Research Laboratory, Harvard University, Cambridge, MA, 1949.
- [3] J. P. L. Timothy and J. Mason, *Applied Sonochemistry*, Weinheim: Wiley-VCH, 2002.
- [4] W. Lauterborn and H. Bolle, *J. Fluid Mech.*, 1975, 72, 391–399.
- [5] A. K. Khurana, H. Chen and C. G. Wall, *Chem. Eng. Commun.*, 1998, 165, 199–215.
- [6] N. Bremond, M. Arora, C.–D. Ohi and D. Lohse, *J. Phys.: Condens. Matter*, 2005, 17, S3603–S3608.
- [7] D. G. Shchukin, E. Skorb, V. Belova and H. Möhwald, *Adv. Mater.*, 2011, 23, 1922–1934.
- [8] T. Leighton, *The Acoustic Bubble*, London: Academic Press Inc, 1997.
- [9] B.E. Noltingk, E.A. Neppiras, *Proc. Phys. Soc. B*, 1950, 63, 674.
- [10] Y. G. Adewuyi, *Ind. Eng. Chem. Res.*, 2001, 40, 4681–4715.
- [11] P. Riesz, D. Berdahl, and L. C. Christman, *Environ. Health Perspect.*, 1985, 64, 233.
- [12] E. B. Flint and K. S. Suslick, *Science*, 1991, 253, 1397.
- [13] K. S. Suslick, *Science*, 1990, 247, 1439.
- [14] G. Cravotto, P. Cintas, *Chem Soc Rev.*, 2006, 35, 180–196.
- [15] P. Chowdhury, T. Viraraghavan, *Sci. Total Environ.*, 2009, 407, 2474–2492.
- [16] T.Y. Wu, N. Guo, C.Y. Teh, J.X.W. Hay, *Advances in Ultrasound Technology for Environmental Remediation*, Springer, 2013, DOI: 10.1007/978-94-007-5533-8.
- [17] M. A. Margulis, *Russ. J. Phys. Chem.*, 1976, 50, 534–537.
- [18] P. Riesz, D. Berdahl, and L. C. Christman, *Environ. Health Perspect.*, 1985, 64, 233.
- [19] C. Kormann, D.W. Bahnemann, M.R. Hoffmann, *Environ. Sci. Technol.*, 1988, 22, 798–806.
- [20] H.N. Mc Murray, B.P. Wilson, *J. Phys. Chem. A*, 1999, 103, 3955–3962.
- [21] C. Petrier, M.-F. Lamy, A. Francony, A. Benahcene, B. David, V. Renaudin and N. Gondrexon, *J. Phys. Chem.*, 1994, 98, 10514.
- [22] A. Henglein, D. Herburger and M. Gutierrez, *J. Phys. Chem.*, 1992, 96, 1126.
- [23] D. J. Flannigan, S. D. Hopkins and K. S. Suslick, *J. Organomet. Chem.*, 2005, 690, 3513.
- [24] R. Pecha, B. Gompf *Phys. Rev. Lett.*, 2000, 84, 1328
- [25] S. J. Doktycz, K. S. Suslick, *Science*, 1990, 247, 1067.
- [26] T. Prozorov, R. Prozorov and K. S. Suslick, *J. Am. Chem. Soc.*, 2004, 126, 13890
- [27] A. Phillip, W. Lauterborn *J. Fluid Mech.*, 1998, 362, 75
- [28] E. V. Skorb et.al., *Nanoscale*, 2011, 3, 985–993.
- [29] J. Dulle, et. al., *Adv. Func. Mat.*, 2012, 22, 3128–3135.
- [30] J. Dulle, et. al., *Green Chem.*, 2013, 15, 1238–1243.

### 3 Overview of the thesis

#### 3.1 Sonochemical formation of metal sponges

The high intensity ultrasound treatment of particles shows, that the reaction towards the US differs between the different kinds of materials. The modification of the material depends on its tendency to undergo oxidation and its melting point. The main effects of ultrasound are (i) particle collisions with high velocity that lead to particle breakage (ii) modification of outer surface due to cavitation and oxidation (iii) generation of inner porous structure with high surface area (see Fig. 3-1).[1–3]

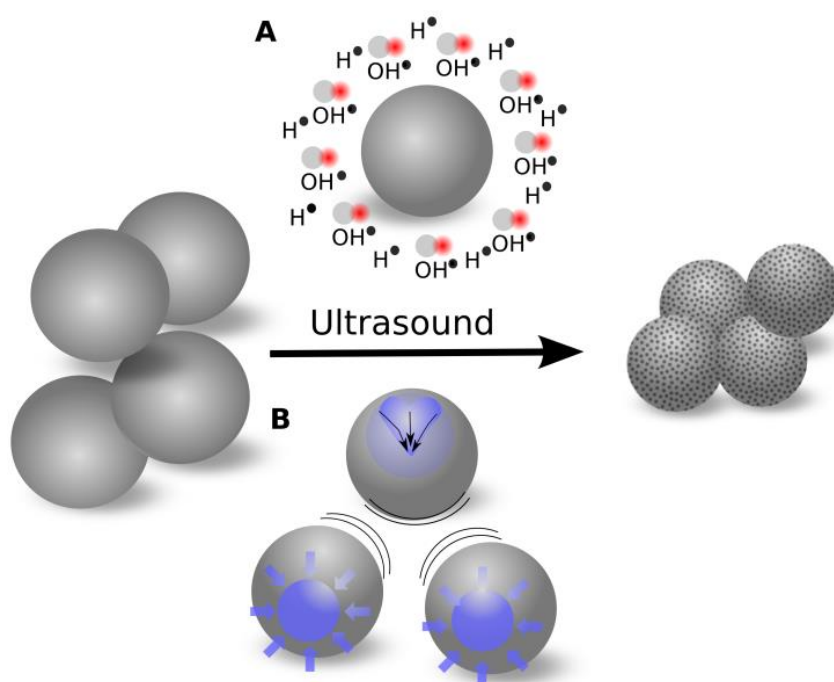


Fig. 3-1 Sonochemical modification of metal particles: (I) initial particles; (II) chemical aspect surface oxidation (A) and physical aspects (B) interparticle collisions; (III) formation of mesoporous metals. Reprinted from *Adv. Funct. Mater.* 22, J. Dulle, et al., Sonochemical Activation of Al/Ni Hydrogenation Catalyst, 3128 – 3135, Copyright (2012), with permission from John Wiley and Sons.

We found that for aluminum and magnesium ultrasonication leads to the formation of metal sponges. These sponges possess a huge surface area compared to the particles before the sonication. The sponges consist of a metallic skeleton that is mesoporous with an average pore size of 4 nm. The local high temperatures (5000 K) and pressure (several hundreds of bars) during sonication lead to a melting and recasting of the metal as well as oxidation, which leads to the porous structure.[1–8] The highest surface areas were found for a sonication time of 60 min. But already after 3 min of sonication time, the outer layer of the Al particles becomes mesoporous and further sonication leads to modification of inner structure by the formation of 200 nm thick metal lamellae stabilized by a 2 nm oxide layer.[3] This was determined by BET[9] measurements and SEM images, taken after different sonication times.

For sonication times longer than 60 min, we observed a decrease of surface area due to a decrease in porosity as well as smoothing and the fusion of particles. Magnesium behaves in a very similar way to the treatment with ultrasound; the main difference is that the pores formed have a diameter of 14 nm instead of 4 nm. Metals that have oxidation potentials similar to Al like Zn, Ti and Ni show very different structures after sonication, depending on their melting points. Zn having a melting lower than aluminum is totally transformed into ZnO which crystallizes on the Zn particles and yields a “hedgehog” structure. Ti and Ni have much higher melting points. Here, only the outer surface of the sonicated particles is oxidized but no sponge formation was observed. We also sonicated noble metals (Au, Pd, Pt, and Ag), but these undergo no structural or chemical changes under sonication. This in turn can be utilized to homogeneously distribute noble-metal colloids in an Al sponge in a one-step process.[3]

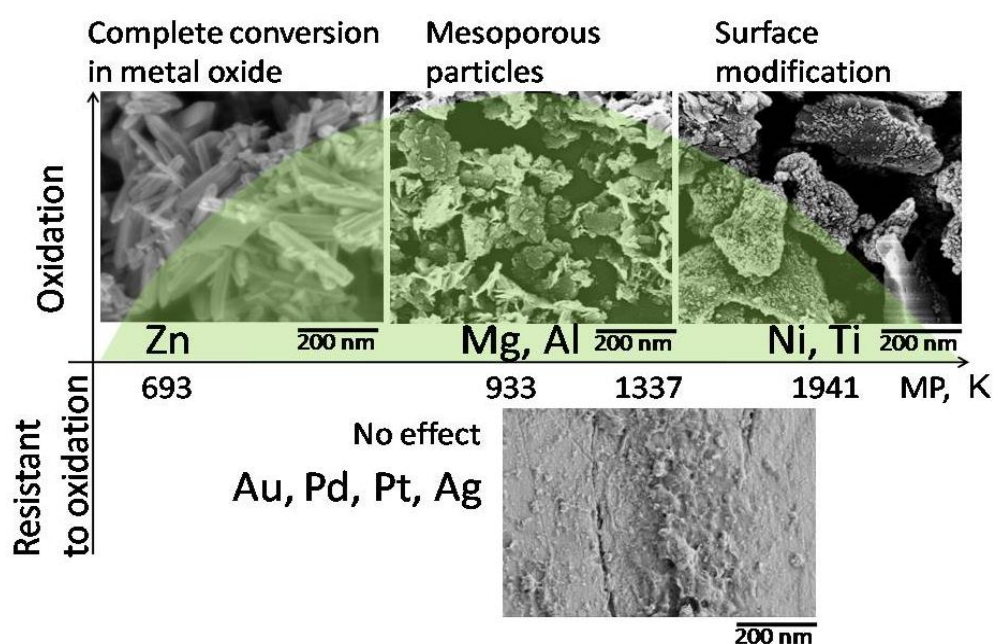


Fig. 3-2 Schematic presentation of the effect of acoustic cavitation on modification of metal particles. Metals with low (Zn) melting point exhibit transformation into oxide, and with high (Ni, Ti) melting points exhibit surface modification under sonication. Al and Mg form mesoporous sponge-like structures. Noble metals are resistant to ultrasound irradiation due to the stability against oxidation. The time of modification was chosen to be 60 min as an optimum for aluminum sponge metal particle formation. Reprinted from Nanoscale, 3, E.V. Skorb, et al., Sonochemical formation of metal sponges, 985 – 993, Copyright (2011), with permission from The Royal Society of Chemistry.

### 3.2 Ultrasound driven formation of metal-supported nanocatalysts

Taking into account that the effect of ultrasonication on metals depends on the metal's oxidation potential and melting point, we prepared a nanocatalyst consisting of an Al matrix featured with noble nanoparticles loading of up to 1 wt.%. Therefore we used aluminum particles (200  $\mu\text{m}$ ) which underwent a profound structural and chemical change due to their ultrasound treatment. They broke up into smaller particles (10  $\mu\text{m}$  – 20  $\mu\text{m}$ ) and formed a metal sponge with an average pore size of 4 nm and a high surface area of 60  $\text{m}^2 \text{g}^{-1}$ . We then took advantage of the fact that noble metals like Au or Pt don't get modified by sonication. We utilized this behavior by using ultrasound on a dispersion containing already sonicated porous Al particles and 4 nm sized Pt particles. This process yielded an Al supported nanocatalyst consisting of the mesoporous Al and homogeneously distributed nanoparticles within. We found a linear dependence of the amount of noble-metal particles incorporated with the sonication time, reaching a plateau after 60 min. It is important to note that even after 120 min total sonication time the Al particles are not totally oxidized but still exhibit their mesoporous structure with an Al skeleton. The TEM image (Fig. 3-3) clearly shows that the noble-metal particles are evenly distributed in the Al matrix and are not aggregated. Nitrogen adsorption isotherms show that the surface area of the nanocatalyst is increased compared to the mesoporous Al and the change of the adsorption isotherm to H-3 type indicates that the nanoparticles are located in the pores of the porous aluminum.[10]

The reactivity of the new nanocatalyst with incorporated Pt NPs was tested with the reduction of ferricyanid with thiosulfate. By following the absorbance of hexacyanoferrate we were able to determine the reaction rate of the reduction catalyzed by nanocatalyst. Our catalyst showed a very high efficiency, good recyclability, as well as high stability.[10]

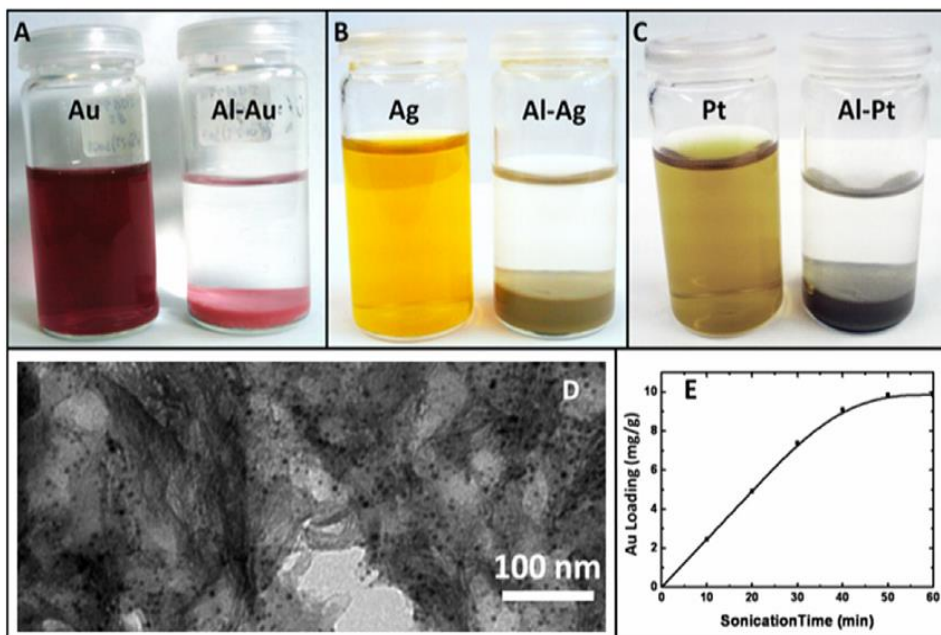


Fig. 3-3 Digital photographs of Au, Ag, and Pt nanoparticle suspensions (A, B, and C respectively) before (left) and after (right) the ultrasound-assisted loading in Al nanostructures. The particles sediment due to their incorporation into the Al particles. TEM image of microtomed mesoporous bimetallic (Al–Au) particle (D). The linear dependence of the Au intake in the Al particles vs. the sonication time. In 50 min of sonication the saturation is achieved (E). Reprinted from *Microporous Mesoporous Mater.*, 154, N. Pazos-Peréz, et al., Ultrasound driven formation of metal-supported nanocatalysts, 164 – 169, Copyright (2012), with permission from Elsevier.

### 3.3 Sonochemical activation of Al/Ni towards a hydrogenation catalyst

The finding of the previous work[3,11] that the reaction of different metals towards ultrasound treatment is not equal, lead to the treatment of an Al/Ni alloy powder. In this case, nickel is less sensitive to the US treatment than the aluminum. We used nickel because it plays an important role in the hydrogenation, partial oxidation of methane, and hydrogenolysis. The most common process to get a catalyst containing nickel is the “Raney® process”, patented by Murray Raney in 1925.[12] The disadvantage of this chemical dealloying process is that the produced so-called “Raney®-Nickel” is pyrophoric and not long-term stable at ambient conditions.[13] With our way of nickel catalyst preparation we produced a material that has all the benefits of Raney®-Nickel but is stable under ambient conditions, catalytically active for the hydrogenation of acetophenone, and can be easily handled and reused after the hydrogenation is finished. The ultrasound-driven formation of porous metals for catalysis is therefore a promising tool for the preparation of metal catalysts.[14]

For the preparation of the Al/Ni catalyst, we used Al/Ni (50/50) alloy powder, consisting of intermetallic  $\text{Al}_3\text{Ni}_2$  and  $\text{Al}_3\text{Ni}$  with a particle size of 100  $\mu\text{m}$ . The resulting particles have a diameter of 10  $\mu\text{m}$  – 20  $\mu\text{m}$  and are porous with a narrow pore size distribution of around 4 nm and a surface area of 120  $\text{m}^2 \text{g}^{-1}$ . What we found was that when an Al/Ni alloy is sonicated due to their different behavior towards the sonication, microphase separation occurs. This means that a metal sponge of unmodified Al/Ni is formed that is stabilized by a thin aluminum oxide layer including active reduced nickel. This layer stabilizes the structure formed by ultrasound and has no negative effect on the catalytic properties.[14,15]

But this alone would not give a catalytically active material. In order to be able to catalyze hydrogenation reactions, Ni has to be in its metallic form ( $\text{Ni}^0$ ). We found by varying the sonication times that upon longer sonication the amount of this species was increasing. Most likely the sonication of Al is the key to this activation. It is proposed that the sonochemical activation of the Al/Ni powder is due to generation of  $\text{H}_2$  [16] during partial oxidation of the aluminum matrix. To achieve high catalytic efficiency, the time and intensity of sonication, as well as the catalyst composition are the parameters to optimize.[14]

The hydrogenation of acetophenone was performed for 24 hours at room temperature, under 60 bar  $\text{H}_2$  pressure, and with water as solvent. We found that under these conditions the catalyst produced more than 99.9% 1-phenylethanol for the first five runs. The fact that the catalyst remained effective after 8 runs proved its high reusability.[14]

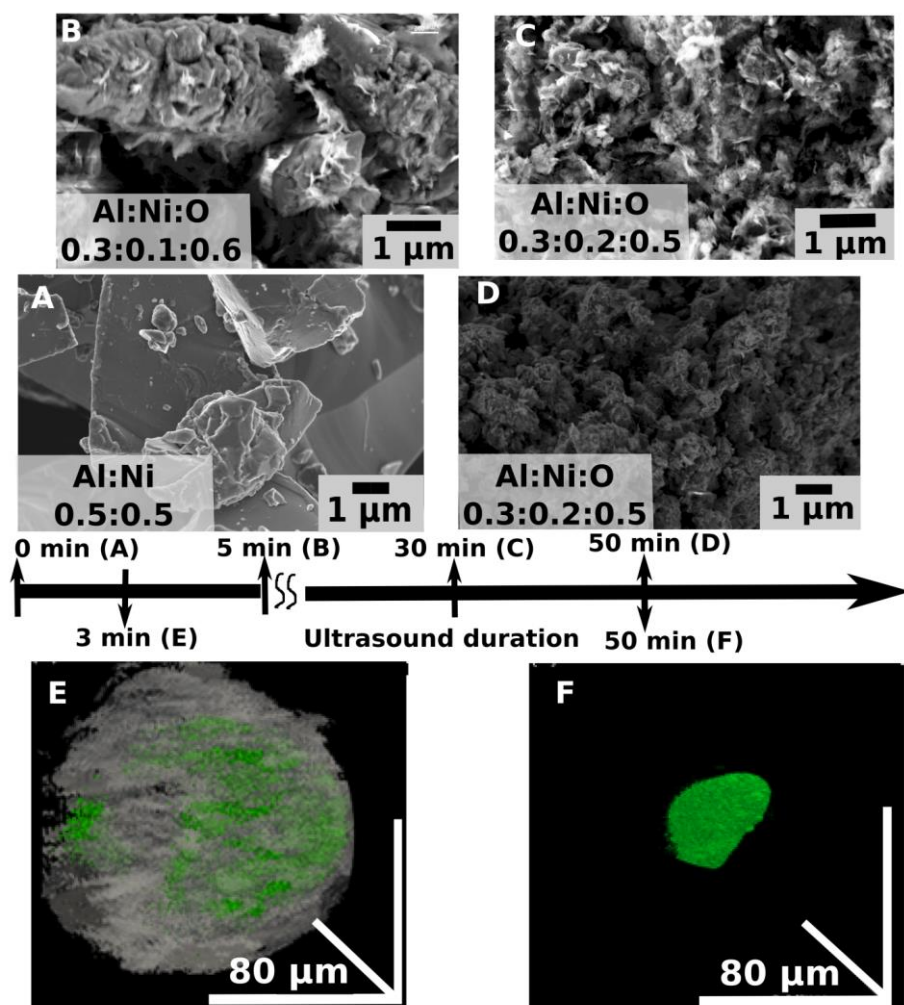


Fig. 3-4 SEM images and the aluminum (Al), nickel (Ni), and oxygen (O) ratio measured by EDS (inserts) of Al/Ni particles: A–initial; B–after 5 min; C–30 min and D–50 min of sonication at  $140 \text{ W cm}^{-2}$ . 3D confocal microscopy reconstruction of the Al/Ni nanostructure loaded with fluorescein: (E) the alloy particle after 3 min (the reconstruction of both transmission and fluorescent mode) and (F) 50 min of sonochemical exposure at  $140 \text{ W cm}^{-2}$ . Reprinted from *Adv. Funct. Mater.*, 22, J. Dulle, et al., Sonochemical Activation of Al/Ni Hydrogenation Catalyst, 3128 – 3135, Copyright (2012), with permission from John Wiley and Sons.

### 3.4 Sonochemical activation of Al/Cu towards a dehydrogenation catalysts

The sonochemical activation of Al/Ni encouraged us to further investigate the ultrasound-driven formation of metal alloys for catalysis.

We wanted to find an alternative to commonly used dehydrogenation catalysts, supported Cr oxides[17] and Pt based[18] systems, which are either rare and costly, or hazardous.[19] Additionally, due to thermodynamic limitations[20] they perform well only at high temperatures[21] (typically at 500 °C – 600 °C). In contrast to this, we wanted to produce in an inexpensive and solvent-free procedure a catalyst which consists of cheap and hazard-free components. In this we were successful, we have not only achieved the above mentioned aims, we could even perform the propane dehydrogenation reaction at temperatures 200 °C lower than for the Pt–Sn/Al<sub>2</sub>O<sub>3</sub> benchmark.[19]

The high intensity ultrasound treatment of the Al/Cu alloy was the main key to this novel and efficient propane dehydrogenation catalyst. We produced by arc-melting several Al/Cu beads with different Al/Cu ratios. After milling the alloy beads, the obtained powder was ultrasonicated in water for one hour and dried afterwards. The received mesoporous metal particles with 10 – 50 µm in diameter showed an average pore size of about 4 nm. These pores were covered and stabilized by an ultra-thin oxide layer. This oxide layer was estimated to be less than 2.0 nm in thickness.[3] At the same time due to the surface area of 34 m<sup>2</sup> g<sup>-1</sup> a lot of copper was made available as catalyst. Of the different compositions that we used during our study the one comprising 25 wt.% Cu and 75 wt.% Al was the best. On catalysts with this composition we tried activation procedures at various temperatures under different activation atmospheres (O<sub>2</sub>, Ar, H<sub>2</sub>). As we did this it became clear that at the standard temperatures we used to activate the material it was already starting to partly melt and particles were fusing. This led to a decrease in available surface area and lowered the catalytic activity. Also the reaction was done at a temperature of 550 °C as this is the best temperature for the benchmark material, but at this temperature our material was near its melting point. Therefore, we decided to perform the activation in O<sub>2</sub> atmosphere as well as the reaction at temperatures 200 °C lower than for the benchmark. The result was better performance than the benchmark.[19]

This one example shows that these new materials have a lot of potential when it comes to low temperature dehydrogenation reactions without the use of noble metals.

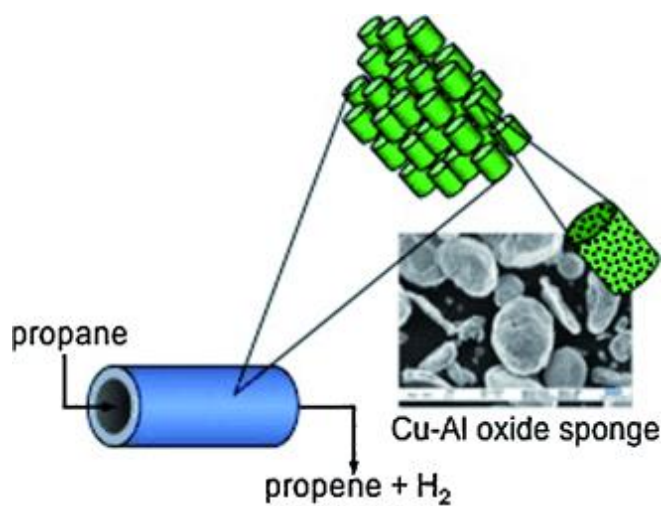


Fig. 3-5 Graphical abstract. Reprinted from Chem. Eur. J., 17, J. Schäferhans, et al., Novel and Effective Copper - Aluminum Propane Dehydrogenation Catalysts, 12254 – 12256, Copyright (2012), with permission from John Wiley and Sons.

### 3.5 Sonochemical activated Cu/Al as a catalyst for A<sup>3</sup> coupling

Apart from the application for dehydrogenation, we wanted to investigate further, if our porous Al/Cu alloy is also catalytically active for the “A<sup>3</sup> coupling” (detailed explanation see chap. 3.5) to produce propargylamines.[22–24] The reason was the same as before, we wanted to find an inexpensive and “green” prepared catalyst to replace commonly used expensive homogenous catalysts containing gold.[22,25,26]

The catalyst is made by sonication of small particles (~ 120 μm) consisting of an alloy (Al 75 wt.% and Cu 25 wt.%). The sonication leads to the formation of smaller particles (10 – 50 μm) that have a mesoporous structure and offer a large catalytically active surface area. The sonication process and how it affects the surface properties of the particles have been described in another publication.[3,11] We tested the catalyst for a lot of different A<sup>3</sup> coupling reactions and for most of these reactions the yields and the selectivity were comparable or even better than with already established catalysts.[22]

The reason for the high yields and selectivity obtained with this material lies in the structure of the surface. The catalytically active metal is Cu in particular the Cu<sup>+</sup> species which makes up the bulk of Cu present at the surface. Tests with pure Cu<sub>2</sub>O as catalyst showed only intermediate yields this together with results from the XPS analysis lead us to the conclusion that also the Al support plays a big part as it influences the electronic environment of the Cu<sup>+</sup> in just the right way. We also tested the material for its reusability and found no degradation after five consecutive reaction and retrieval cycles.[22]

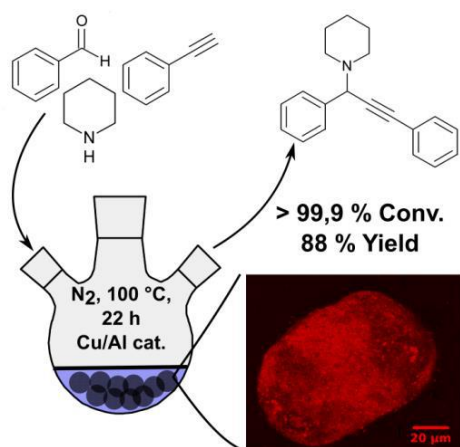


Fig. 3-6 Graphical abstract. Adapted from Green Chem., 15, J. Dulle, et al., Efficient three-component coupling catalyzed by mesoporous copper-aluminum based nanocomposite, 1238 – 1243, Copyright (2013), with permission from The Royal Society of Chemistry.

### 3.6 Sononanostructuring of zinc based material

In a previous study[3] we used ultrasound to modify Al and Mg particles to yield a mesoporous material that can be used as a scaffold for other components and act as a high surface area support. During these studies we also used Zn and found that instead of making a porous material it forms “hedgehog” like structures with a metallic Zn core covered by ZnO nanorods. As ZnO also has a wide range of applications, for instance as a semiconductor or photocatalyst we made an in depth investigation of the material and its photocatalytic abilities.[27]

What we found was that when the sonication time of Zn particle is short, the Zn is not totally converted to ZnO but spikes of ZnO form on the surface of the sonicated particles (Fig. 3-7).[27]

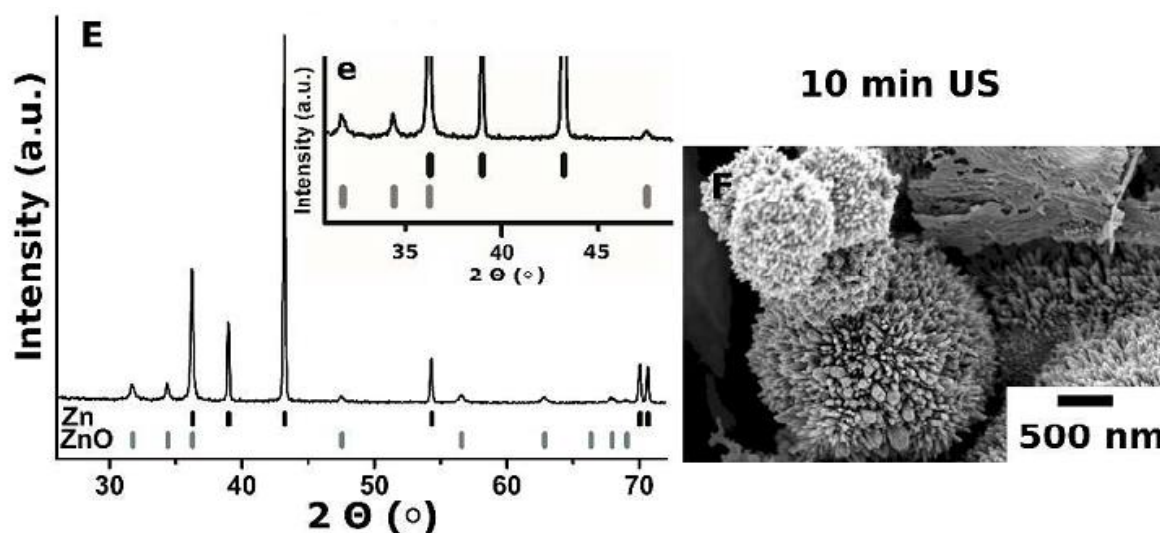


Fig. 3-7 PXRD pattern (E), the insert (e) shows the magnified part of the PXRD patterns with the ZnO attributed peaks, and SEM image of the zinc particles treated for 10 min by ultrasound. Reprinted from RSC Advances, 2, J. Dulle, et al., Sononanostructuring of zinc based material, 12460 – 12466, Copyright (2012), with permission from The Royal Society of Chemistry.

The length of these spikes is dependent on the sonication time and concentration of particles. After a certain time the spikes get too long and are sheared off due to the sonication but when the sonication is continued new spikes grow as the now plain surface is oxidized again. Also a too high concentration limits the length of the spikes as interparticle collisions hinder their further growth. We used two different Zn particle sizes for the photocatalytic degradation of methyl orange, which was the reaction we decided to test our material on. The rate constants of the degradation of methyl orange are plotted in Fig. 3-8 for the different particles and concentrations we studied.[27]

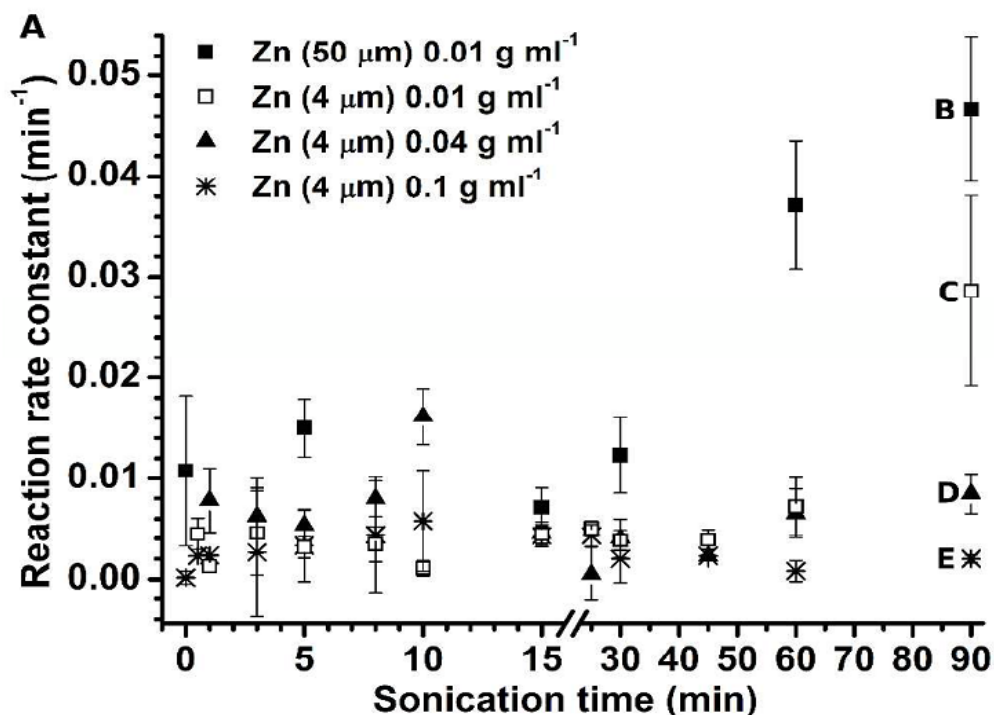


Fig. 3-8 Reaction rate constant  $k$  is shown in dependence of ultrasound treatment duration. We used 10 mg of the US modified zinc particles. Reprinted from RSC Advances, 2, J. Dulle, et al., Sononanostructuring of zinc based material, 12460 – 1246, Copyright (2012), with permission from The Royal Society of Chemistry.

What we found was that the structure of the ZnO spikes is also dependent on the size of Zn particles used. When the particles are small (4  $\mu\text{m}$ ) the spikes are all perpendicular to the surface and the catalytic activity is there but not too high. But the bigger particles (50  $\mu\text{m}$ ) have spikes that are lying on the surface and therefore have a much larger surface area that is catalytically active. These particles gave the highest conversion rates and present a very good material for the green photodegradation of water pollutants.[27]

## References

- [1] E. V. Skorb, D. G. Shchukin, H. Möhwald and D. V. Andreeva, *Langmuir*, 2010, 26, 16973.
- [2] E. V. Skorb, D. G. Shchukin, H. Möhwald and D. V. Andreeva, *Nanoscale*, 2010, 2, 722.
- [3] E.V. Skorb, D. Fix, D.G. Shchukin, H. Möhwald, D.V. Sviridov, R. Mousa, N. Wanderka, J. Schäferhans, N. Pazos-Pérez, A. Fery, D.V. Andreeva, *Nanoscale*, 2011, 3, 985.
- [4] R. K. Gould, *J. Acoust. Soc. Am.*, 1994, 56, 1740–1746.
- [5] L. A. Crum, *Ultrasonics*, 1984, 22, 215–223.
- [6] V. Kamath and A. Prosperetti, *J. Acoust. Soc. Am.*, 1991, 89, 1863.
- [7] C. E. Brennen, *Cavitation and Bubble Dynamics*, Cambridge University Press, 2013.
- [8] O. Louisnard and J. González-García, "Acoustic Cavitation", in *Ultrasound Technologies for Food and Bioprocessing*, Springer, 2011, 13–64.
- [9] S. Brunauer, P.H. Emmett, E.J. Teller, *J. Am. Chem. Soc.*, 1938, 60, 309.
- [10] N. Pazos-Pérez, J. Schäferhans, E. V. Skorb, A. Fery, D. V. Andreeva, *Micropor. Mesopor. Mat.* 2012, 154, 164.
- [11] E. V. Skorb., H. Möhwald, T. Irrgang, A. Fery, D. V. Andreeva, *Chem. Commun.*, 2010,46, 7897–7899.
- [12] a) M. Raney, U.S. Patent 1,563,587, 1925; b) M. Raney, *Ind. Eng. Chem.*, 1940, 32, 1199 –1203; c) G. Ertl, H. Knözinger, (Eds.) 1997, *Preparation of Solid Catalysts*, Weinheim: Wiley.
- [13] J. Masson, P. Cividino and J. Court, *Appl. Catal., A*, 1997, 161, 191; P. Mars, T. V. D. Mond and J. J. Scholten, *Ind. Eng. Chem. Prod. Res. Dev.*, 1962, 1, 161.
- [14] J. Dulle, S. Nemeth, E. V. Skorb, T. Irrgang, J. Senker, R. Kempe, A. Fery and D. V. Andreeva, *Adv. Funct. Mater.*, 2012, 22, 3128–3135.
- [15] E. Skorb and D. V. Andreeva, *J. Mater. Chem. A*, 2013, 1, 7547–7557.
- [16] E. V. Skorb, D. V. Andreeva, H. Möhwald, *Angew. Chem. Int. Ed.* 2012, 51, 5138–5142.
- [17] M. Santhosh Kumar, N. Hammer, M. Rønning, A. Holmen, D. Chen, J. C. Walmsley, G. Øye, *J. Catal.*, 2009, 261, 116.
- [18] D. Akporiaye, S. F. Jensen, U. Olsbye, F. Rohr, E. Rytter, M. Ronnekleiv, A. I. Spjelkavik, *Ind. Eng. Chem. Res.*, 2001, 40, 4741 –4748.
- [19] J. Schäferhans, S. Gomez-Quero, D. V. Andreeva, G. Rothenberg, *Chem.-Eur. J.* 2011, 17, 12254.
- [20] M. S. Voronetskii, L. P. Didenko, V. I. Savchenko, *Russ. J. Phys. Chem. B*, 2009, 3, 216.
- [21] S. R. Schmidt, *Top. Catal.*, 2010, 53, 1114 –1120.
- [22] J. Dulle, K. Thirunavukkarasu, M. Mittelmeijer-Hazeleger, D. V. Andreeva, N. R. Shiju, G. Rothenberg, *Green Chem.*, 2013, 15, 1238 – 1243.
- [23] T. Naota, H. Takaya and S.-I. Murahashi, *Chem. Rev.*, 1998, 98, 2599–2660.

- [24] G. Dyker, *Angew. Chem., Int. Ed.*, 1999, 111, 1808–1822.
- [25] C. Wei and C.-J. Li, *J. Am. Chem. Soc.*, 2003, 125, 9584–9585.
- [26] V. K.-Y. Lo, Y. Liu, M.-K. Wong and C.-M. Che, *Org. Lett.*, 2006, 8, 1529–1532.
- [27] J. Dulle, S. Nemeth, E. V. Skorb, T. Irrgang, J. Senker, R. Kempe, A. Fery and D. V. Andreeva, *Adv. Funct. Mater.*, 2012, 22, 3128–3135.

## **4 Published articles in peer-reviewed journals**

### **4.1 Sonochemical formation of metal sponges**

Ekaterina V. Skorb, Dmitri Fix, Dmitry G. Shchukin, Helmuth Möhwald, Dmitry V. Sviridov, Rami Mousa, Nelia Wanderka, Jana Schäferhans, Nicolas Pazos-Peréz, Andreas Fery and Daria V. Andreeva\*

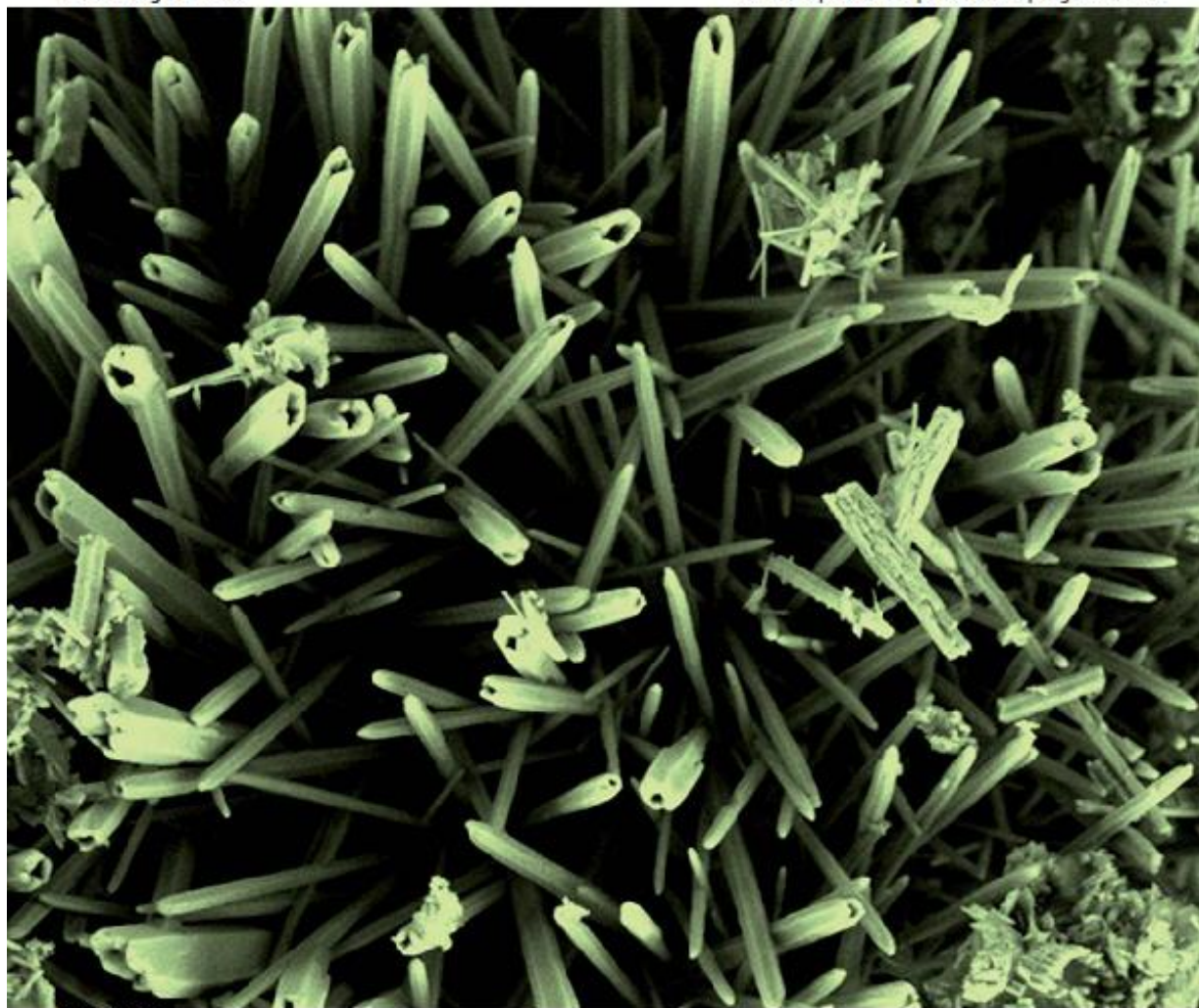
This work is published in *Nanoscale* 2011, 3, 985 – 993.

This article is reprinted from *Nanoscale*, 3, E.V. Skorb, et al., Sonochemical formation of metal sponges, 985 – 993, Copyright (2011), with permission from The Royal Society of Chemistry.

# Nanoscale

www.rsc.org/nanoscale

Volume 3 | Number 3 | March 2011 | Pages 753–1276



ISSN 2040-3364

**RSC Publishing**

**COVER ARTICLE**  
Andreeva *et al.*  
Sonochemical formation of metal  
sponges

**HOT ARTICLE**  
Jiang and Liu  
Metallic surfaces with special wettability

Fig. 4-1 Cover letter. Reprinted from *Nanoscale*, 3, Copyright (2011), with permission from The Royal Society of Chemistry.

#### **4.1.1 Contribution to the joint publication**

I prepared the metal sponges loaded with doxorubicin hydrochloride and made the 3D confocal microscopy reconstruction images of them. Also, I performed the sonochemical assisted intercalation of gold, platinum, and silver nanoparticle inside the mesoporous aluminum support. I repeated the experiments for the modification of Al, Mg, and Zn for my own research.

#### **4.1.2 Abstract**

A novel sonochemical method for formation of mesoporous metal sponges is developed. Systematic investigation of ultrasound effects on various types of metal particles reveals the cavitation-induced oxidation of metal surface and etching of metal matrix as main factors in the ultrasound-driven metal modification. Beyond the specific examples, the findings provide guidelines for expansion of the concept towards a broad variety of metal systems and allow development of the sonochemical approaches to manipulation of the metal surface and inner structure.

#### **4.1.3 Introduction**

Metal sponges with tunable structures have gained interest for a wide range of applications from filters to reservoirs for energy conversion and storage.[1–3] Porous metals are designed to exhibit specific characteristics combining the beneficial properties of the base metal and sponge scaffold: resistance to corrosion,[4] mechanical strength,[3,5] high-temperature performance,[6] and thermal and electrical characteristics.[6] Through a process of casting, powder metallurgy, and sputter deposition, porous materials with large pores (200  $\mu\text{m}$  to 2 mm) can be produced.[1–6] The approaches to fabricate mesoporous metals with controlled porosity are based on electroplating into the self-assembled liquid crystal surfactants,[7] colloidal crystals,[8] porous block copolymers[9] or anodic porous alumina.[10] Nanoporous metals have been synthesized by chemical reduction,[11] plasma spraying,[12] electrodeposition[13] followed by template decomposition, etc.[14–17] Some of these methods have the advantage of precise control over the size and structure of the final metal sponge, however, they are multistage, expensive and time-consuming to implement. Thus, it is very important to develop a novel, general, energy effective and environmentally friendly approach for porous metal structure formation with pore size in the nanometer scale which can be applied to a broad range of metals and alloys. Here, we apply a novel method of manipulation of metal structure by using a high power ultrasound.

High power ultrasound has been used in the industry for 60 years, in applications such as cleaning and more recently, in the processing of materials for waste remediation and pharmaceutical manufacture. Beyond these claims intensive ultrasound can provide highly non-equilibrium conditions for synthetic chemistry.[18–21] The effect of ultrasound on matter occurs through acoustic cavitation: generation, growth, and collapse of bubbles.

Sonochemistry can be described in terms of the “hot-spot theory”:[22] volatile solutes undergo thermal cleavage with the formation of radical or excited species within a cavitation bubble.[23] These species may induce subsequent reactions with less-volatile substrates at the bubble shell.

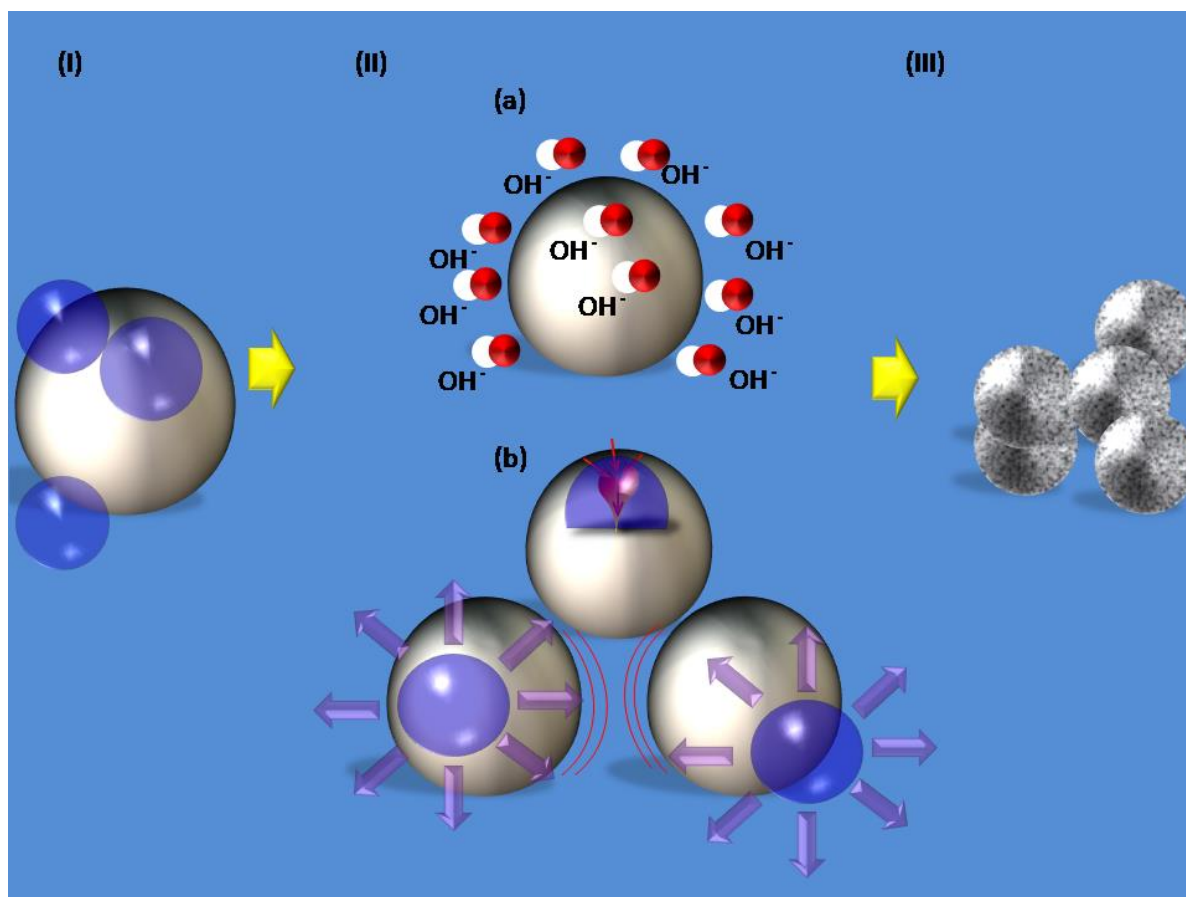


Fig. 4-2 Sonochemical modification of metal particles: (I) initial particles; (II) chemical aspect (a) surface oxidation, physical aspects (b) interparticle collisions, surface impinging by high velocity microjets; (III) formation of mesoporous metals. Reprinted from *Nanoscale*, 3, E.V. Skorb, et al., Sonochemical formation of metal sponges, 985 – 993, Copyright (2011), with permission from The Royal Society of Chemistry.

The chemical effect of the intense ultrasound is based on generation of free radicals during cavitation. Application of ultrasound to chemical synthesis allows acceleration of a reaction or permits use of less aggressive conditions, reduces the number of steps which are required using normal methodology (initiation of reaction, the need for additives), and opens up possibilities for alternative reaction pathways.[22,23] The interfacial region around cavitation bubbles has very high temperature, pressure, and (possibly) electric field gradients.[24,25] Liquid motion in this vicinity also generates very large shear and strain gradients. These are caused by the very rapid streaming of solvent molecules around the cavitation bubble, as well as by the intense shock waves emanating upon collapse. The physical effects include: (a) the improvement of mass transport from turbulent mixing and acoustic streaming, (b) the generation of surface damage at liquid–solid interfaces by shock waves and

microjets, (c) the generation of high-velocity interparticle collisions in slurries, and (d) the fragmentation of solids to increase the surface area.[26,27] However, sonochemistry of solids and a quantitative understanding of their sonochemical modification are emerging only now. Thus the effect of ultrasound irradiation on the structure and morphology of metals and alloys is a developing research area.[28–30] To date, studies on application of ultrasound to metal particles have been mostly focused on general enhancement of the reactivity of metals as stoichiometric reagents[28,29] and interparticle collisions driven by ultrasound.[26,30] In our recent publications[31,32] we applied a high intensity ultrasound to modification of metal surfaces. We demonstrated that effect of cavitation on the metal surface is other than pure surface oxidation and causes formation of up to 200 nm thick porous layer on the surface of a metal plate. We also showed that ultrasound treatment of metal plates provides them with novel properties (superhydrophobic, anticorrosion). In the current research we expand application of ultrasound to metals and focus on ultrasound-assisted formation of nanostructured metal sponges with tunable porosity. The novel metal sponges formed by ultrasonication could be useful elements in conceptual design of smart coatings, delivery systems, nanocatalysts and nanocomposite materials. Moreover we studied the kinetics of metal particle modification in aqueous medium.

The mechanism of the modification of metal structure under ultrasound irradiation is complex and involves a variety of aspects related to melting,[30] recrystallization,[31–36] solidification of metals,[37] selective etching[38] and oxidation of metal surfaces.[39] Main effects of ultrasound on metal particles illustrated in Fig. 4-2 are the reactions between metal and sonogenerated species (Fig. 4-2a), interparticle collisions and mechanical imprinting of metal surfaces by liquid jets of high velocity (Fig. 4-2b). Therefore, the nature of the used metals determines structures, morphology and properties of metal particles after ultrasound treatment. We suggest that metals with relatively low melting point should be promptly modified by ultrasound than the metals with higher melting point.

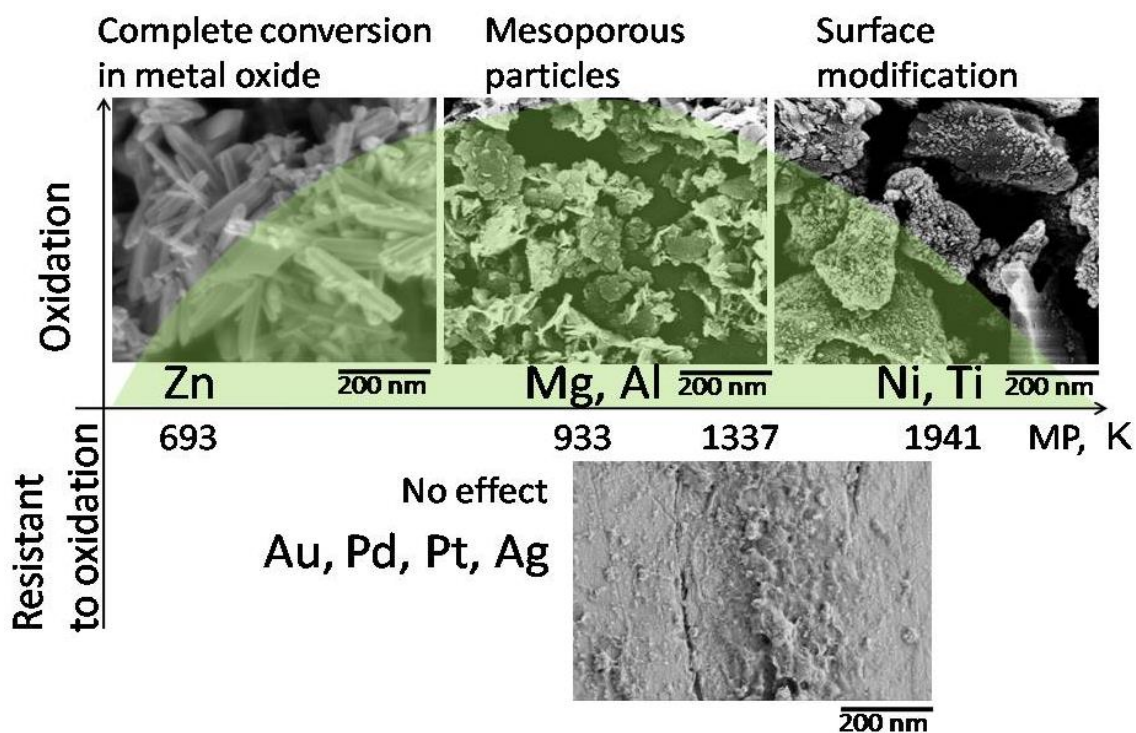


Fig. 4-3 Schematic presentation of the effect of acoustic cavitation on modification of metal particles. Metals with low (Zn) melting point exhibit transformation into oxide and with high (Ni, Ti) melting points exhibit surface modification under sonication. Al and Mg form mesoporous sponge-like structure. Noble metals are resistant to ultrasound irradiation due to the stability against oxidation. The time of modification was chosen to be 60 min as an optimum for aluminum sponge metal particle formation. Reprinted from *Nanoscale*, 3, E.V. Skorb, et al., Sonochemical formation of metal sponges, 985 – 993, Copyright (2011), with permission from The Royal Society of Chemistry.

Since surface oxidation (Fig. 4-2a) during ultrasound irradiation is an important aspect in formation and stabilization of porous metal structures, we suggest that the tendency to oxidation is another key characteristic of metals for ultrasound modification. In this work, we report on systematic investigation of ultrasound effects on various types of metal particles: zinc, aluminum, magnesium, titanium, nickel, gold, silver, and platinum and their alloys. Structural and morphological changes of ultrasound modified metals were studied in order to reveal the mechanism of formation of mesoporous metal sponges via ultrasound. The influence of sonication parameters (intensity and duration) as well as the nature of metals and ultrasonic liquid was studied by using a combination of microscopy, spectroscopy and structural analysis. Furthermore, the here proposed novel metal sponges formed by a “green” method of ultrasonication are applicable in different fields of nanotechnology and nanoengineering. We demonstrated (i) one-step formation of metal polymer interpenetrating nanocomposite, (ii) one-step formation of heterogenic nanocatalysts by using initial metal alloys and by incorporation of metal nanoparticles into sponge matrix and (iii) formation of mm thick sponge like surface structure on metal plates to enhance their properties (here shown by the example of corrosion resistance).

#### 4.1.4 Results and Discussion

The general concept of ultrasound driven modification of metal particles in water is schematically shown in Fig. 4-3.

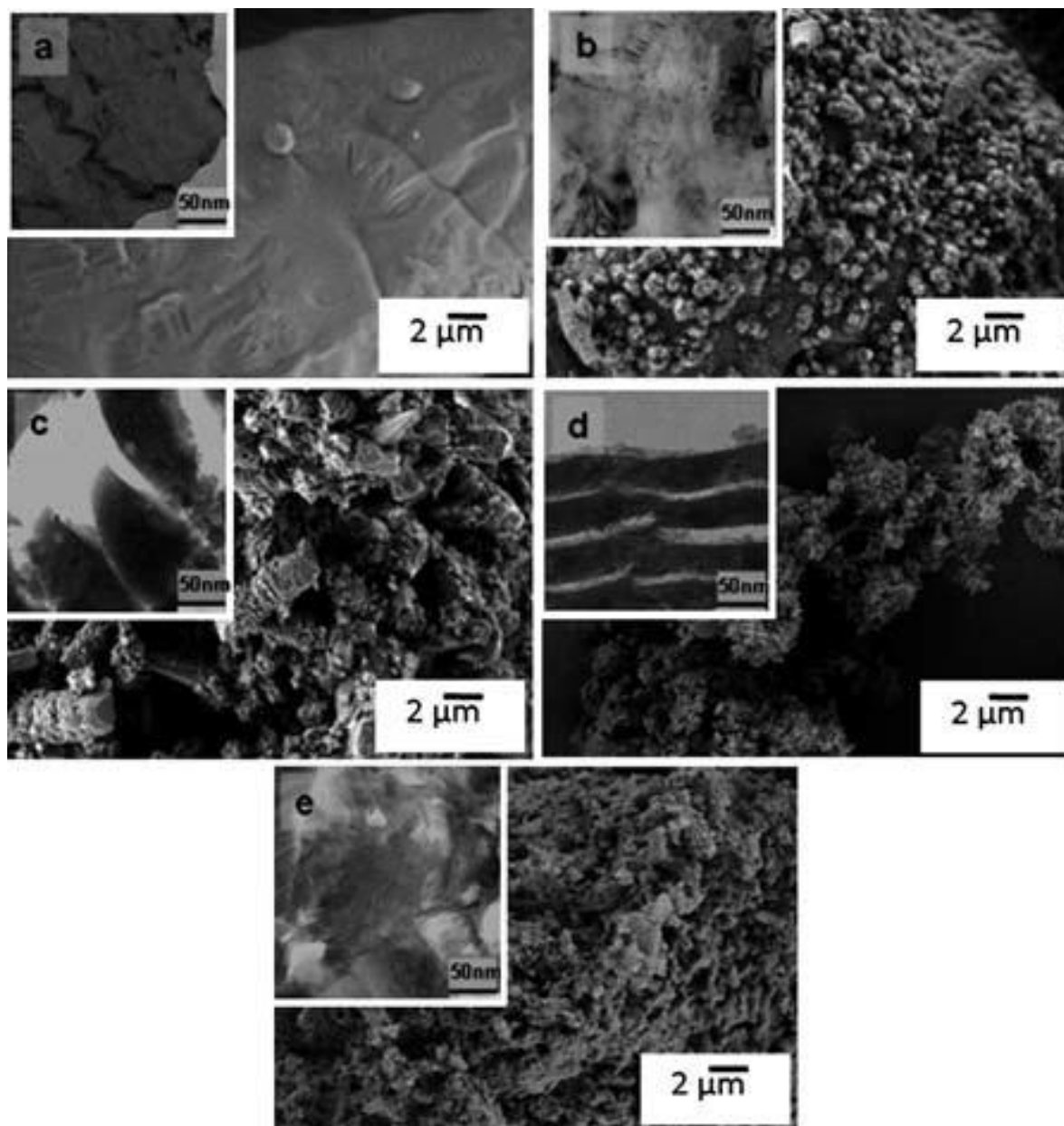


Fig. 4-4 SEM and TEM (insets) images of aluminum particles initially (a) and after sonication at  $57 \text{ W cm}^{-2}$  for (b) 1 min, (c) 3 min, (d) 60 min, and (e) 120 min.). Reprinted from *Nanoscale*, 3, E.V. Skorb, et al., Sonochemical formation of metal sponges, 985 – 993, Copyright (2011), with permission from The Royal Society of Chemistry.

In order to clarify the underlying ultrasound driven physical and chemical processes in liquid–metal system, we investigated several groups of metals at different sonication conditions (solvent, duration of sonication). We divided metals chosen for investigation (zinc, aluminum, magnesium, nickel, titanium, noble metals) into the following groups according to their chemical and physical properties relevant to ultrasound modification: difference in ability to oxidation (y-axis in the sketch Fig. 4-3) and

difference in melting point (MP) (x-axis in the sketch Fig. 4-3): Zn—693 K, Al—933 K, Mg— 923 K, Au—1337 K, Ni—1728 K, and Ti—1941 K. SEM images (Fig. 4-4) of the initial Al particles (a) and after sonication for 1 (b), 3 (c), 60 (d) and 120 (e) min in water shows that ultrasound treatment changes the size and the surface of the particles. Increasing the specific surface area of the particles (the isotherms (Fig. 4-5a) and the graph (Fig. 4-5a)) claims that together with surface modification the inner structure is affected. The surface areas could reach  $80 \text{ m}^2 \text{ g}^{-1}$  in 60 min sonication. Formation of porous inner structure was also studied by monitoring the distribution of a fluorescent dye inside porous metals prepared at different sonication times. Fig. 4-6 shows the 3D reconstructions of the transmission and fluorescence images of confocal scanning fluorescence microscopy (CSFM) of the aluminum particles loaded with a water-soluble antibiotic doxorubicin hydrochloride. Based on microscopy and BET study we can claim that the ultrasound-driven modification of aluminum particles results in three directions: (i) particle breakage (160  $\mu\text{m}$  initial particles are broken into 5  $\mu\text{m}$  – 10  $\mu\text{m}$  pieces after 60 min of sonication), (ii) formation of a porous outer surface (the rough surface can be observed even in 3 min of sonication (Fig. 4-6 (1)), and (iii) modification of the inner structure of the particles (increasing the specific surface area (Fig. 4-6 (2))). The BET isotherms of Al particles (Fig. 4-5a) show the formation of mesopores in the first 5 min of sonication. The type of isotherms (Fig. 4-5a) could be classified between Type II and Type IV general isotherms according to BDDT (Branauer, Deming, Deming, and Teller) theory. At the relative pressure values of around 0.08, especially in the case of long time ultrasound treatment, there is an inflection point, which indicates the completion of monolayer coverage and the starting point of multilayer  $\text{N}_2$  adsorption.

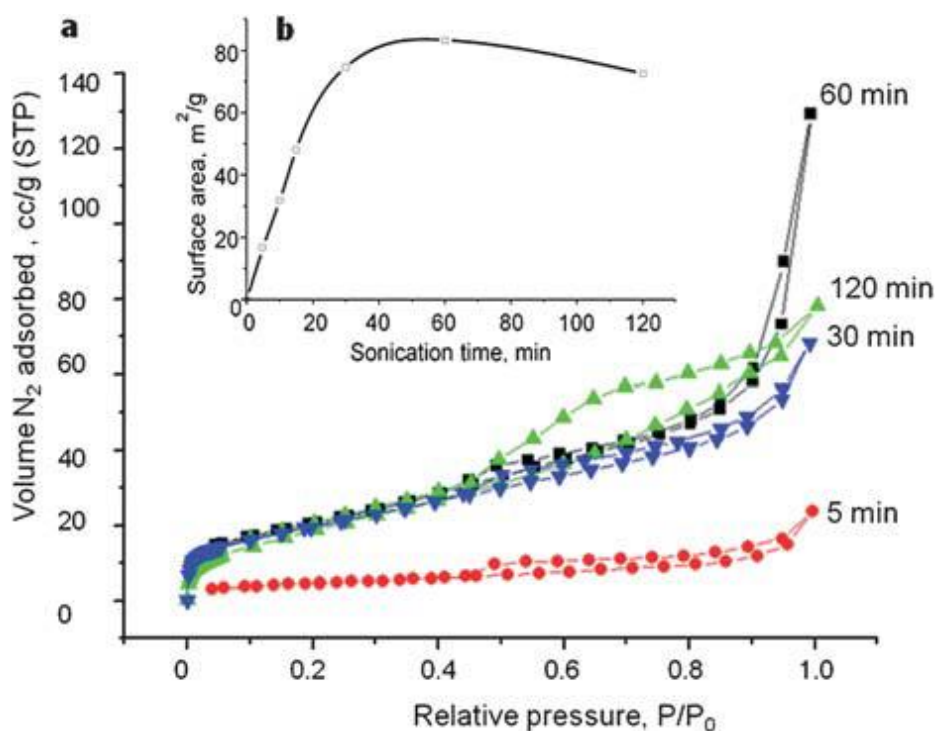


Fig. 4-5 Adsorption–desorption isotherms for aluminum particles after different sonication times (a) and increase of the surface area of the aluminum particles vs. sonication time (b). Reprinted from *Nanoscale*, 3, E.V. Skorb, et al., Sonochemical formation of metal sponges, 985 – 993, Copyright (2011), with permission from The Royal Society of Chemistry.

Between the relative pressure values of 0.08 and 0.45, all the isotherms are almost linear indicating the presence of micropores along with the mesopores. The presence of micropores also was confirmed by adsorption of argon. After the relative pressure value of 0.45, the amount of adsorbed N<sub>2</sub> starts to increase sharply. This is due to the continuous progression from multilayer adsorption to capillary condensation, in which the smaller pores become completely filled with liquid nitrogen. This occurs because the saturation vapor pressure in a small pore is reduced, according to the Kelvin equation, by the effect of surface tension.

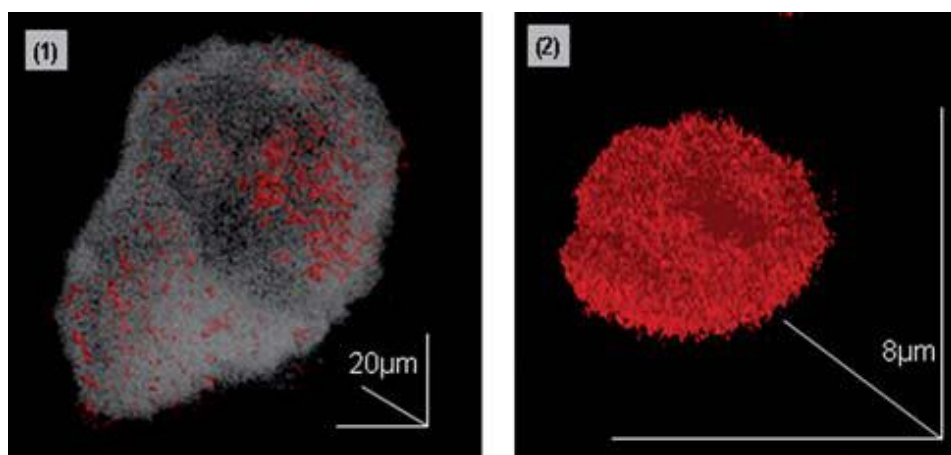


Fig. 4-6 3D confocal microscopy reconstruction of the metal sponge loaded with doxorubicin hydrochloride: (1) the metal particle after 3 min (the reconstruction of both transmission and fluorescent mode) and (2) 60 min of sonochemical exposure at  $57 \text{ W cm}^{-2}$  (fluorescent mode, transmission mode reconstruction is not possible due to microscope resolution). Reprinted from *Nanoscale*, 3, E.V. Skorb, et al., Sonochemical formation of metal sponges, 985 – 993, Copyright (2011), with permission from The Royal Society of Chemistry.

Thus at the early stages of ultrasound treatment, the sample contains mesopores in which capillary condensation occurs when the relative pressure reaches a value corresponding to the radius of the pore by the Kelvin equation. After a longer sonication time microporous structures are produced and at low relative pressures larger amounts of micropores are filled by  $\text{N}_2$ . Thus, at the initial stage the formation of mesopores takes place. After 10 min of ultrasound treatment both micropores and mesopores are formed. The average pore diameter is about 4 nm for the 60 min treated particles. The maximum porosity was observed for the 60 min sonicated particles (Fig. 4-5b). A further increase of irradiation time leads to regression of structure development. SEM images (Fig. 4-4e) and BET analysis demonstrate a decrease of porosity, surface smoothing and fusion of the particles after 2 h sonication (Fig. 4-5). Thus, we can prepare particles of different sizes and porosities by varying the sonication time. The optimal treatment time, regarding the porosity of the resulting Al sponge, was estimated to be ca. 60 min. Moreover a three dimensional field ion microscopy study (Fig. 4-7) proves that the structure of the modified sample has the skeleton of metallic aluminum.

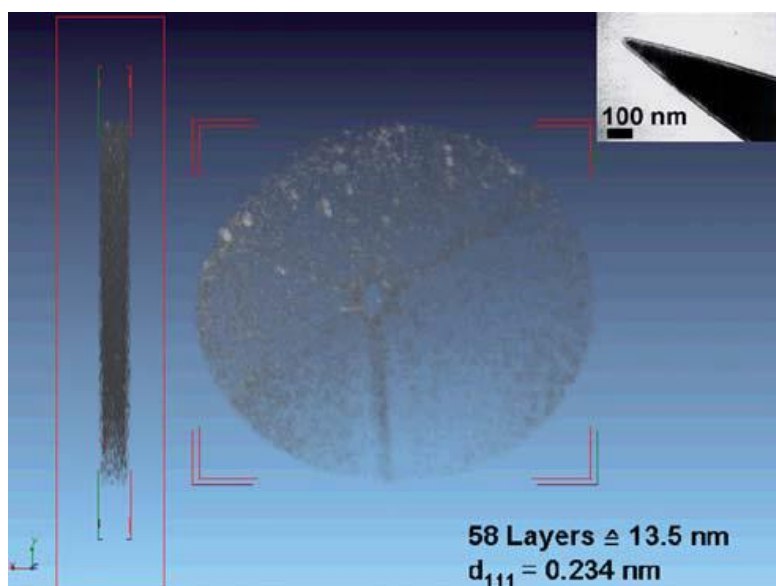


Fig. 4-7 Three dimensional field ion microscopy reconstruction of the atom positions of aluminum. Reprinted from *Nanoscale*, 3, E.V. Skorb, et al., Sonochemical formation of metal sponges, 985 – 993, Copyright (2011), with permission from The Royal Society of Chemistry.

Similar ultrasound driven behavior was exhibited by Mg and alloys containing Al and Mg. The SEM and TEM images of Mg (Fig. 4-8a, b) indicate significant size reduction of the particles and formation of the porous inner structure after 60 min sonication in water. Sonication of Mg (MP 923 K, less than for Al) leads to formation of a more porous structure with higher surface area. The surface area for 30 min sonicated Mg and Al is  $69 \text{ m}^2 \text{ g}^{-1}$  and  $54 \text{ m}^2 \text{ g}^{-1}$ , respectively. Furthermore, Mg sponges are characterized by larger pores than Al sponges: the average pore diameter is  $\sim 14 \text{ nm}$  in the case of Mg and  $\sim 4 \text{ nm}$  in the case of Al. XRD patterns (Fig. 4-8c) prove formation of magnesium hydroxide phase (Brucide, syn) after the first minute of ultrasonic irradiation. Adsorption/desorption isotherms for magnesium after 20 min of sonication (Fig. 4-8d) are very similar to the isotherms obtained for the porous aluminum. Thus, sonochemical modification of aluminum and magnesium (MP ca. 950 K) and their alloys results in formation of porous particles with high surface area and narrow pore size distribution.

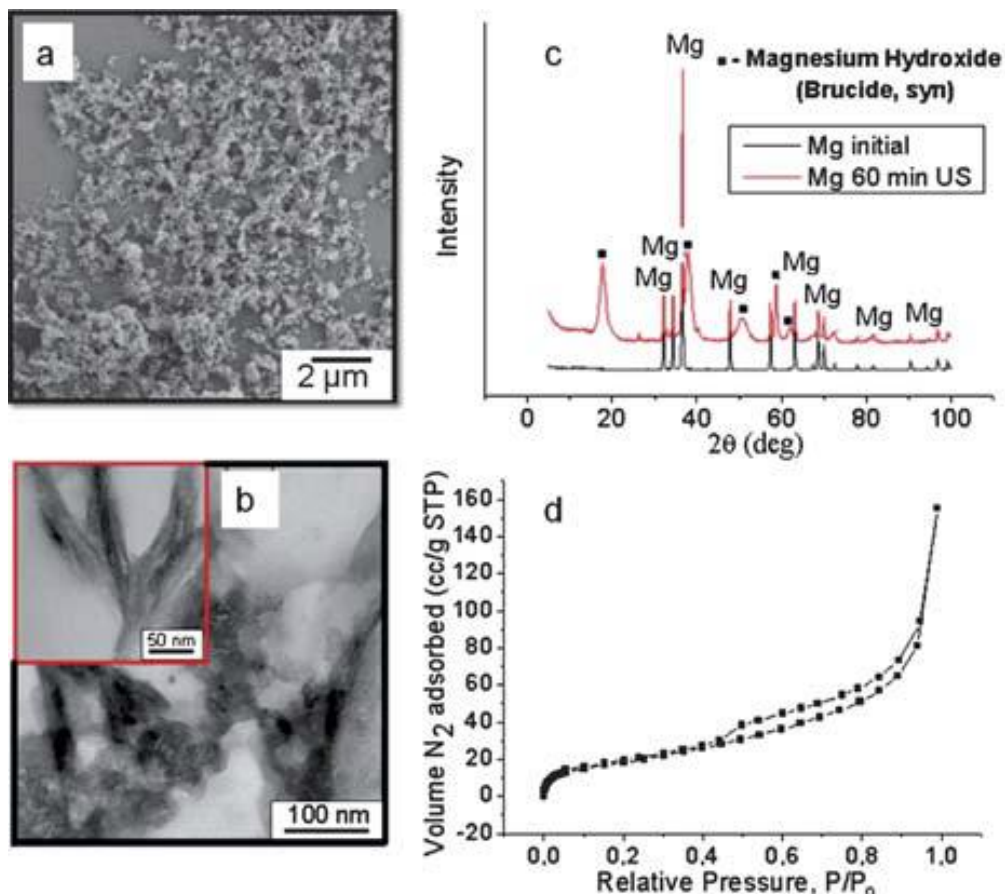


Fig. 4-8 (a) SEM, TEM images, (c) XRD patterns and (d) adsorption–desorption isotherm for magnesium particles after 20 min sonication at  $57 \text{ W cm}^{-2}$  in aqueous solution. Reprinted from *Nanoscale*, 3, E.V. Skorb, et al., Sonochemical formation of metal sponges, 985 – 993, Copyright (2011), with permission from The Royal Society of Chemistry.

When we apply ultrasound to modification of metals with higher and lower than aluminum and magnesium melting points we observed formation of absolutely different structures. As we see in Fig. 4-3 zinc particles have the lowest melting point (693 K) among the used metals.

Ultrasound treatment of Zn particles results in the complete conversion of Zn into Zn oxide. The ultrasound-stimulated formation of zinc oxide on the surface of zinc particles occurs already after short-term sonication yielding 2 mm zinc oxide crystals of tubular morphology (Fig. 4-9a). Probably due to their brittleness they are decomposed by further sonication. Long-term treatment ( $> 30 \text{ min}$ ) stimulates formation of stable nanorods with length  $\approx 100 \text{ nm}$  and diameter approximately 20 nm (Fig. 4-9b). This structure is stable and is able to resist the impact of ultrasound cavitation. The XRD spectra (Fig. 4-9c) show that ultrasonic treatment leads to fast conversion of Zn into ZnO. However, even after 90 min of sonication we observe the XRD patterns of Zn oxide and metallic Zn. In particular during the modification we form a “hedgehog” like structure consisting of a Zn metal core and ZnO rods attached to the Zn core. The porosity of the sonicated Zn (Fig. 4-9d) is rapidly decreased with sonication time due to transformation of tubular ZnO into ZnO nanorods.

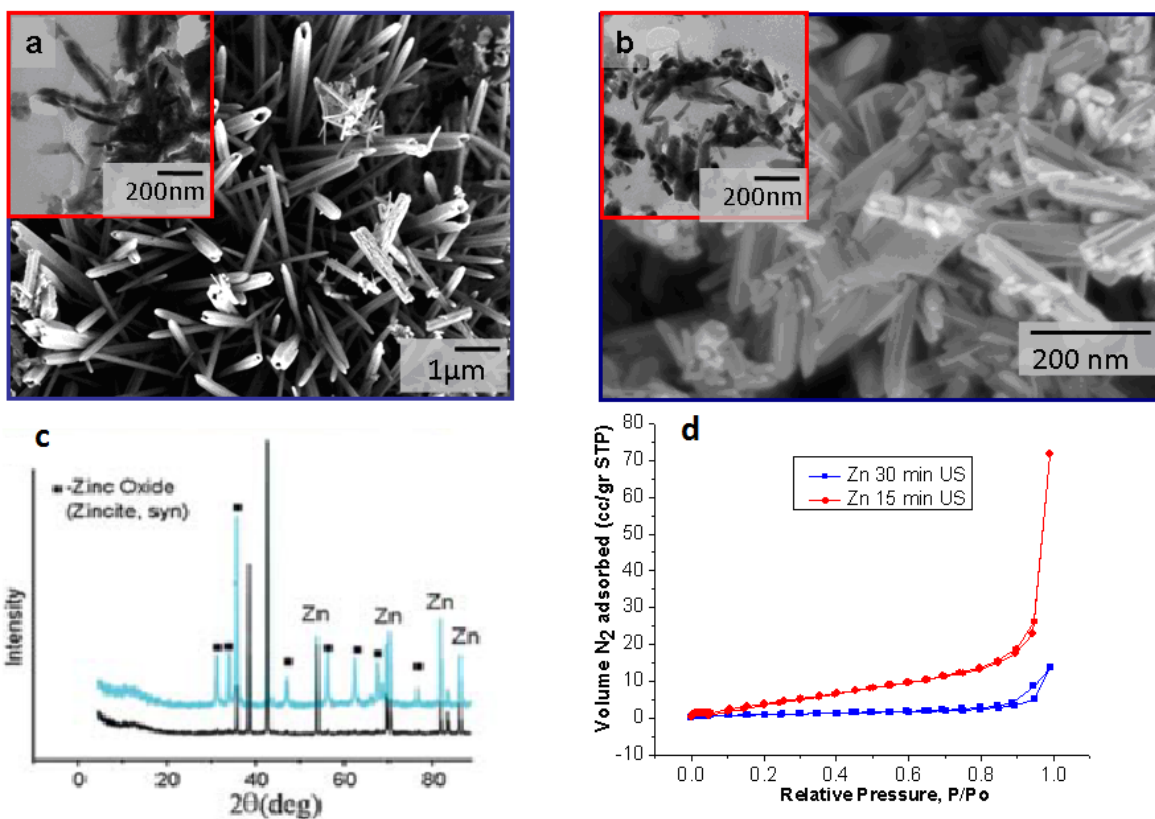


Fig. 4-9 SEM images of Zn particles sonicated at  $57 \text{ W cm}^{-2}$  for (a) 3 min and (b) 90 min; (c) XRD patterns of the initial particles and particles sonicated for 90 min and (d) adsorption–desorption isotherm for 15 and 30 min treated zinc particles. Reprinted from Nanoscale, 3, E.V. Skorb, et al., Sonochemical formation of metal sponges, 985 – 993, Copyright (2011), with permission from The Royal Society of Chemistry.

The metals with higher (compared to Mg and Al) MPs (Ni, 1723 K, and Ti, 1941 K) exhibit changes in interfacial layer only in 60 min of sonication, Ni and Ti particles demonstrate a slight increase in surface roughness (Fig. 4-10). The BET and TEM data have no evidence of formation of porous inner structure for all these metals. We also fail to prove the surface oxidation by the XRD analysis (Fig. 4-10c, f) due to the negligible part of metal oxide in non-porous metal particles.

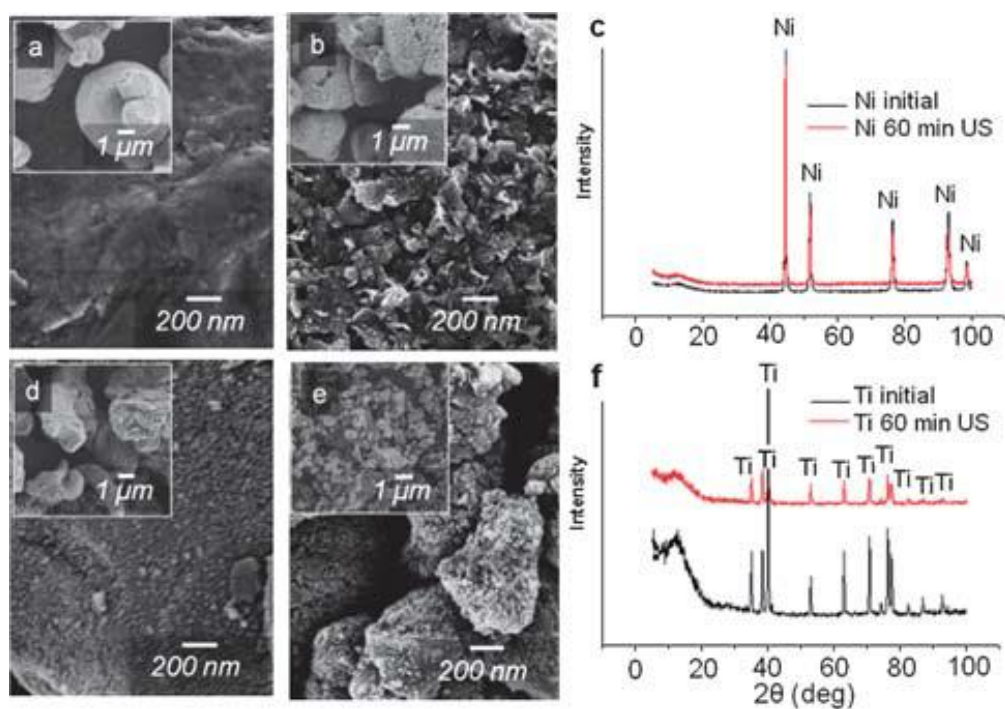


Fig. 4-10 SEM images of (a) the initial nickel, (b) after 60 min sonication at  $57 \text{ W cm}^{-2}$ , and (c) XRD patterns of the initial and the sonicated nickel; (d) initial titanium particles, (e) after 60 min sonication, and (f) their XRD patterns. Reprinted from *Nanoscale*, 3, E.V. Skorb, et al., Sonochemical formation of metal sponges, 985 – 993, Copyright (2011), with permission from The Royal Society of Chemistry.

Finally, the noble metals (Au, Ag, Pt) that have a special place in Fig. 4-3 due to their low tendency to oxidation exhibit the highest resistance to ultrasound irradiation (among the metals investigated here) and form neither porous structure nor rough surface after sonication, even in cases where their MP is actually lower than that of metals that can be modified slightly (like Ni or Ti). Therefore, surface oxidation should have a crucial role in stabilization of the metal structure developed under ultrasound irradiation.

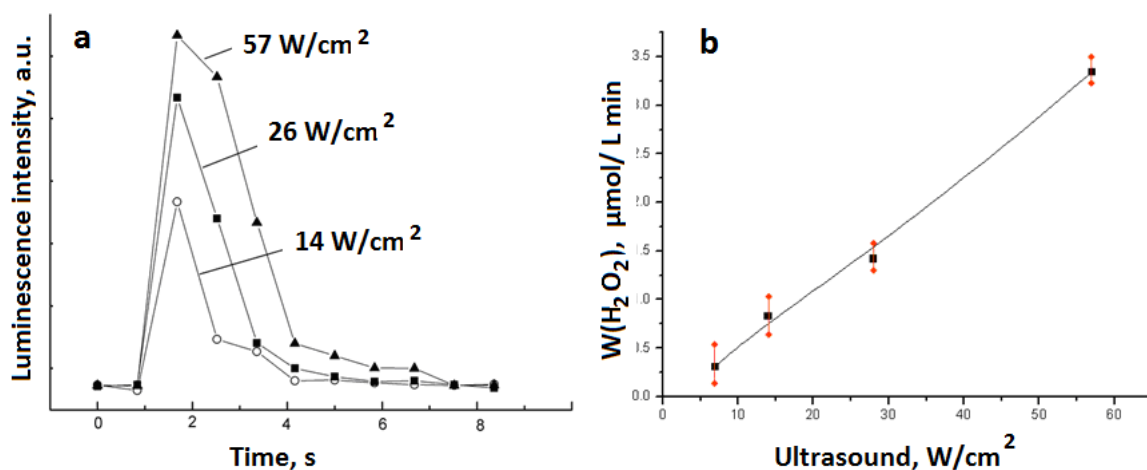


Fig. 4-11 (a) Efficiency of  $O_2^{\bullet-}$  sonogeneration at 14, 28, 57  $W\ cm^{-2}$ ; (b) relationship between ultrasound output power and quantity of generated hydrogen peroxide. Reprinted from *Nanoscale*, 3, E.V. Skorb, et al., Sonochemical formation of metal sponges, 985 – 993, Copyright (2011), with permission from The Royal Society of Chemistry.

We summarize characteristic aspects of ultrasound modification of the used metals and detail the particular features of each of them. Commonly, ultrasound modification of metal particles starts with oxidation of the surface of a metal and formation of a rough metal oxide (hydroxide) layer. The surface of the metal particles after 1 min of sonication has a rough morphology of metal oxide (except noble metals). In 3 min of sonication decomposition of particles and formation of a channel-like structure take place. The initial hundred micron metal particles change into 200 nm thick lamellae (shown in TEM images of Al and Mg). The surface of lamellae is covered by a smooth thin metal oxide. The behavior of metals under ultrasound irradiation is rather determined by the structure of crystal grains. Therefore, melting point is a reasonable property for describing the behavior of metals under ultrasound irradiation. Special conditions provided by ultrasound of high intensity probably influence grain development processes. The analysis of XRD spectra of metal particles described above supports this suggestion. The XRD patterns given in Fig. 4-8, Fig. 4-9, Fig. 4-10 evidence that surface oxidation and formation of metal oxide layers have crucial role in modification of metal structure and formation of porous inner structure. Furthermore, the intensity of the signals is decreased and slightly shifted due to grain destruction under ultrasound irradiation. The quantity of Al (not shown here), Mg (Fig. 4-8, black squares) and Zn (Fig. 4-9, black squares) oxides increases during formation of the porous structure which corresponds to the formation of a high surface area. Neither formation of porous inner structure nor formation of significant amount of metal oxide was detected for “hard” (Ti, Ni (Fig. 4-10c, f)) and noble metals.

Modification of metal particles, surface oxidation and formation of porous inner structure can be controlled by intensity and duration of sonication. During sonochemical process in aqueous solution takes place a production of free radicals. The concentration of the free radicals depends on the

intensities of sonication. Experimentally the amount of superoxide generated in the system could be quantitatively determined using tetranitromethane, which is known to be a selective scavenger of  $O_2^{\bullet-}$ . [40–43, 45] We can see that the quantity of hydrogen peroxide significantly increases with the intensity of sonication (Fig. 4-11a, b).

Thus, formation of the mesoporous aluminum and magnesium particles for 60 min can be achieved at the intensity of  $57 \text{ W cm}^{-2}$  only. Sonication at lower intensities requires a longer treatment time due to lower concentration of active species generated by cavitation.

Moreover in order to test the importance of free radicals in structure formation, we tried to chemically reduce the amount of the free radicals in the system and performed sonication experiments in an ionic liquid [44] without any dissolved gas. Suppression of reactive free radical formation in the ionic liquid results in a drastic decrease of the sponge formation process. We suggest that in the process of ultrasound-driven formation of mesoporous metals free radicals are responsible for metal surface oxidation and stabilization of the porous structure formed during sonication. In order to demonstrate the importance of oxide layer in formation of porous metal structure we adjusted pH values of aqueous system (by 0.1 M solutions of HCl and NaOH) and therefore we suppress formation of a metal oxide layer. Ultrasonic treatment of aluminum particles at acidic and basic pH prevents sponge formation, as confirmed by SEM and BET. These experiments demonstrate that surface oxidation has a crucial role in formation of sponge-like structure.

The different behaviors of metal particles in ultrasound field could be used for formation of nanocomposites. [46] Thus, sonication of Al–Ni, Al–Cu–Pd, Al–Pd, and Al–Co–Fe alloys results in the formation of aluminum sponges consisting of mesoporous metal matrix with homogeneously distributed functional metals, Fig. 4-12a. We tested this idea for the Al/Ni (shown in Fig. 4-12a), Al/Pd, Al/Pd/Cu systems. Indeed the treatment of the aqueous alloy dispersions with highly intense ultrasound leads not only to the formation of porous structure but also results in phase segregation yielding ultrasound-resistant nickel, palladium and copper particles homogeneously distributed in the porous matrix as evidenced by the TEM micrographs given in Fig. 4-12a.

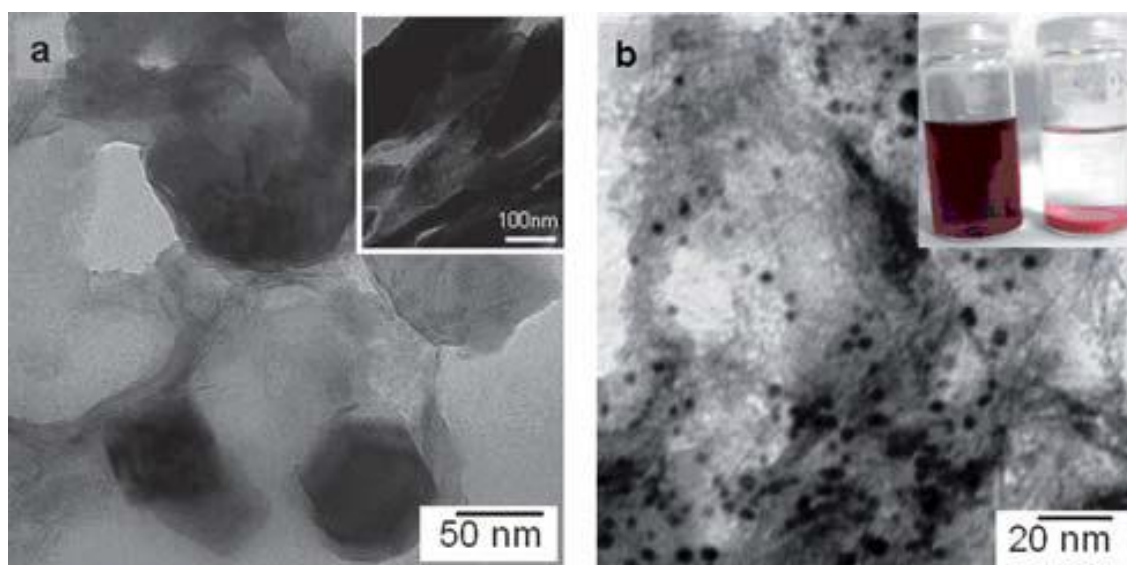


Fig. 4-12 TEM images of the catalysts formed by (a) one-step sonochemical method of AlNi alloy particle treatment (inset shows the initial AlNi untreated alloy); (b) sonochemical assisted intercalation of gold particle inside mesoporous aluminum support (inset shows the solution containing aluminum mesoporous support particles and gold nanoparticles before and after intercalation). Reprinted from *Nanoscale*, 3, E.V. Skorb, et al., Sonochemical formation of metal sponges, 985 – 993, Copyright (2011), with permission from The Royal Society of Chemistry.

BET analysis even shows the formation of a more porous structure in the case of nanocomposites. The surface area achieved in this case is  $280 \text{ m}^2 \text{ g}^{-1}$  and  $210 \text{ m}^2 \text{ g}^{-1}$  for those of Al/Pd/ Cu after 60 min of modification. Thus, phase segregation process in multi-metal systems stimulates formation of mesoporous structures by sonication.

Another type of nanocomposite materials was prepared by sonication of aluminum or magnesium particles in the presence of Au, Ag or Pt colloids. Fig. 4-12b is the TEM image of mesoporous Al particles with 1 wt.% Au particles incorporated by sonication. Combinations of different particles (for example, gold and platinum) are also possible.

The solid surfaces are fragmented and oxidized and the pores are formed deep inside, which requires material transport over mm dimensions within the short time of asymmetric bubble collapse ( $< \text{ms}$ ). In view of this it is also understandable that noble metal nanoparticles are incorporated and homogeneously distributed inside the porous matrix retaining their initial morphology, structure and properties. A great advantage in the use of sonochemical method for nanocomposite formation is the possibility to control the properties (porosity, distribution of active centers) of the resulting material varying the conditions of ultrasonic exposure (intensity, duration, solvent, the presence of additive).

Ultrasound can be applied in one step formation of organic– inorganic nanocomposites with tunable chemical and physical properties. It is possible to carry out radical polymerizations[23,46] without addition of initiators under ultrasound irradiation in situ metal sponges. We demonstrate the one step

formation of interpenetrating polymer–metal phase composites of polypyrrole (PPy) and aluminum sponge interconnected in three dimensions (Fig. 4-13). Such structures are very interesting because of a sponge skeleton formed by metal and unique properties of the polymer.[46–48]

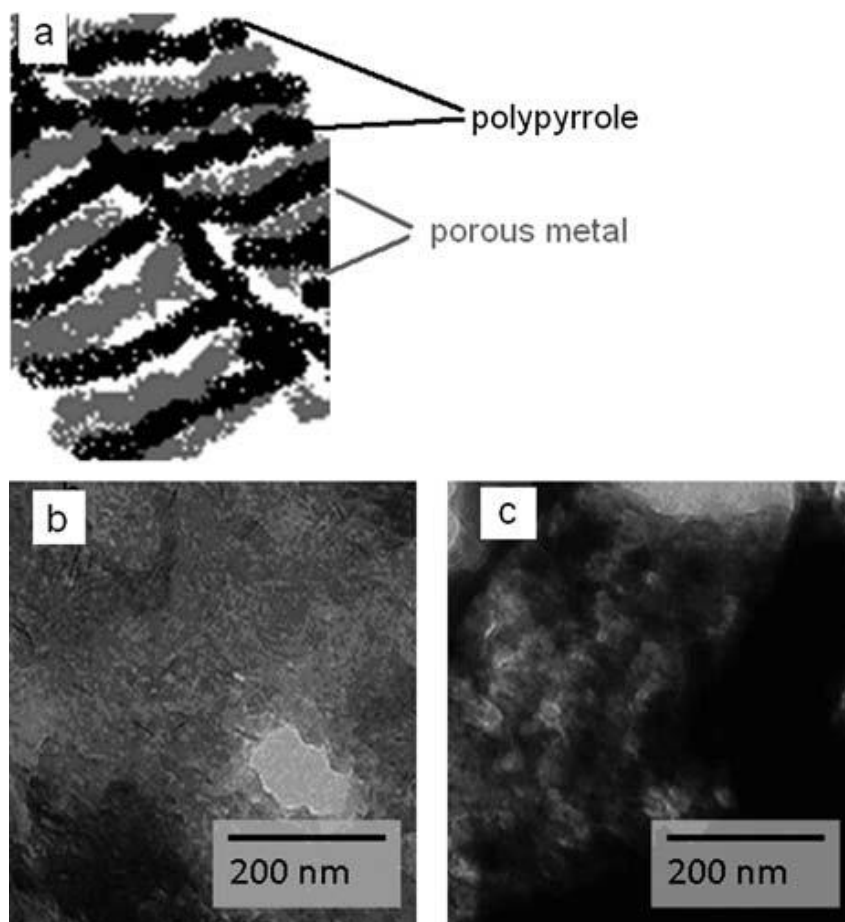


Fig. 4-13 Schematic illustration of the structure of metal–polymer composite synthesized in one step (a); and TEM image providing an evidence of complete filling of pores in metal matrix with polymer (polypyrrole): aluminum particles 15 min sonication at  $57 \text{ W cm}^{-2}$  in ethanol solution (b); ethanol + pyrrole solution (c). Reprinted from *Nanoscale*, 3, E.V. Skorb, et al., Sonochemical formation of metal sponges, 985 – 993, Copyright (2011), with permission from The Royal Society of Chemistry.

The CSFM image (Fig. 4-6) of microreservoirs loaded with a water-soluble antibiotic doxorubicin hydrochloride is an example of application of metal sponges as “smart” containers. Pore system of the sponges could be effectively loaded even with low molecular weight water soluble chemicals. Simultaneously the pore of the reservoirs should be closed by the procedure suggested in ref. [49–53]. Moreover it was shown that the developed approach permitting formation of metal sponges can be extended to flat metal surfaces that allow production of highly porous structures at the surface of the macroscopic metal samples. These structures represent a system of microreservoirs (Fig. 4-14(1)) which can be used for storage of different chemical agents (e.g., corrosion inhibitors in their interior). To prevent the leakage of chemicals stored in the pores, polyelectrolyte multilayers were deposited onto the pore surface via layer-by-layer adsorption of oppositely charged polyelectrolytes.[54–56] The

local change in pH accompanying the corrosion process results in conformational transitions in the polyelectrolyte multilayer releasing the corrosion inhibitor just in the vicinity of the corrosion pit.[54–56] This “self-healing” effect is clearly demonstrated by the scanning vibrating electrode technique (SVET) which allows measurement of the current density over selected areas of the sample thus monitoring local anodic activity in the corrosion zones.[51–58]

The SVET current density maps shown in Fig. 4-14(2, 3) evidence that a hybrid protective layer is formed at the surface of aluminum by sonication followed by loading of resultant pores with corrosion inhibitor (mercaptobenzothiazole), and deposition of polyelectrolyte layers ensures complete suppression of corrosion (Fig. 4-14).

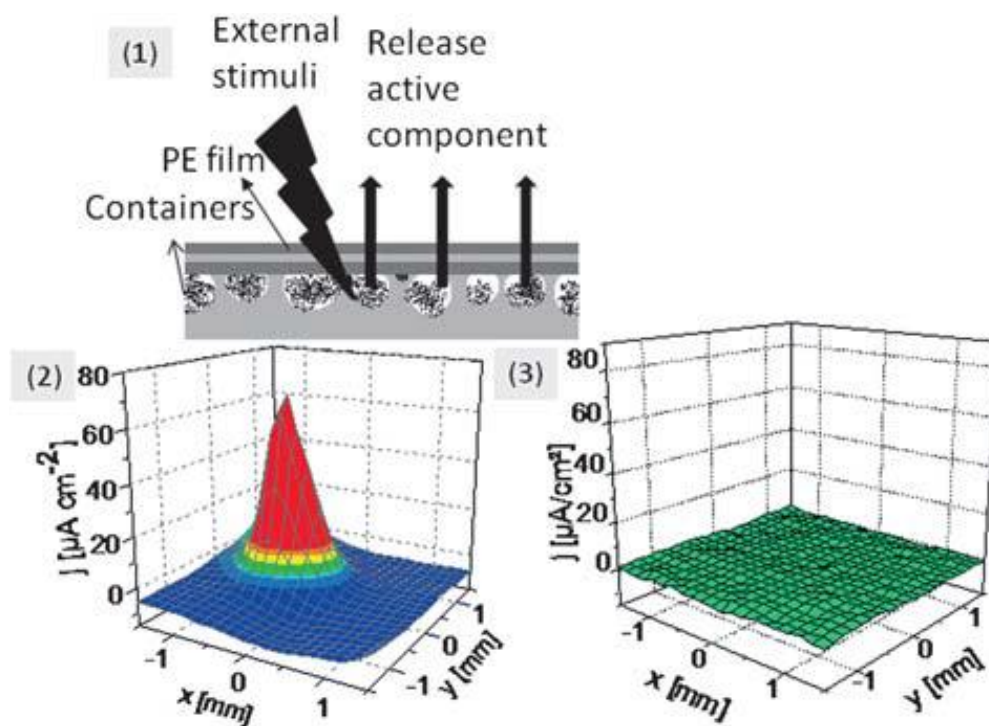


Fig. 4-14 Schematic representation of the self-healing corrosion protection layer at the surface of the aluminum plate. The corrosion inhibitor is encapsulated in the pores at the metal surface by applying polyelectrolyte multilayer. The corrosion process initiates the release of corrosion inhibitor (1). The current density maps obtained by SVET for aluminum plates immersed in 0.1 M NaCl for 12 h (2 and 3). Before measurements the sample (2) was exposed at  $57 \text{ W cm}^{-2}$  ultrasound for 30 min; (3) exposed at  $57 \text{ W cm}^{-2}$  ultrasound for 30 min, soaked in the mercaptobenzothiazole solution and modified by deposition of polyelectrolyte multilayer; the complete suppression of corrosion is observed in the latter case. Reprinted from *Nanoscale*, 3, E.V. Skorb, et al., Sonochemical formation of metal sponges, 985 – 993, Copyright (2011), with permission from The Royal Society of Chemistry.

#### 4.1.5 Conclusion

The high power of ultrasound results from the interplay of conceptually different mechanisms: (1) there is physical impact due to a pressure wave and a jet impinging on the surface of a particle and deep into it; while (2) the extreme temperatures and pressures create highly reactive radicals derived

from water and oxygen (see schematic representation in Fig. 4-2, Fig. 4-3). Obviously, the metal sponges demonstrated here rely on both mechanisms. Ultrasound-driven modification of metals results in several directions: (i) particle breakage (particle size is ca. 20 times reduced), (ii) formation of a developed outer surface, and (iii) modification of the inner structure of the particles increasing the specific surface area. Simultaneously metal surfaces are oxidized and the pore structures are stabilized. Modification of metals by ultrasound depends on the metal nature. We showed that metals with relatively high reactivity (e.g. Zn, Al, Mg) could be involved in oxidation during sonochemical process. The control over the oxidation process allows formation of porous metal structures consisting of metal skeleton stabilized with oxide layer. In view of this it is also understandable that noble metals do not form sponges mostly due to their low tendency to oxidation. In the case of alloys, the sonication is accompanied with phase segregation yielding nanoparticles of the metal with higher resistance to ultrasound treatment distributed in the pores of arising sponge-like structures.

We demonstrated application of novel metal sponges formed by a “green” method of ultrasonication in different fields of nanotechnology and nanoengineering: (i) one-step formation of metal polymer interpenetrating nanocomposite, (ii) one-step formation of heterogenic nanocatalysts by using initial metal alloys and by incorporation of metal nanoparticles into sponge matrix and (iii) formation of mm thick sponge like surface structure on metal plates to enhance their properties (here shown by the example of corrosion resistance).

The proposed novel method of ultrasound assisted modification of metal particles which is applicable to a large range of materials providing a basis for many types of applications in chemistry, materials science and medicine where the structure and properties of metal sponges can be easily controlled by ultrasound.

#### **4.1.6 Experimental**

##### ***Materials***

Aluminum powder (< 100  $\mu\text{m}$ , >99.5%, Roth), magnesium powder (325 mesh, 99.8%, Alfa Aesar), 1 : 1 aluminum–nickel alloy powder (Fluka), zinc (dust, < 50  $\mu\text{m}$ , 98%, Aldrich), nickel (15  $\mu\text{m}$ , 99.8%, Alfa Aesar), titanium (100 mesh, 99.5%, Acros organics), gold (powder, 99.99%, Fluka), platinum (powder, 99.99%, Aldrich), silver (powder, 99.9%, Aldrich), palladium– aluminum alloy (powder, 1% Pd,

Alfa Aesar), and copper– palladium–aluminum alloy (powder, 0.3% Cu, 1% Pd, Alfa Aesar) were used as received. The water was purified before use in a three stage Millipore Milli-Q Plus 185 purification system and had a resistivity higher than 18.2 M $\Omega$  cm<sup>-1</sup>.

### ***Ultrasonication (US)***

40 mL of 10 wt.% suspension of metals in purified water were sonicated in a thermostatted flow cell (FC100L1-1S) (at 65 °C temperature) with the VIP1000hd (Hielscher, Germany) operated at 20 kHz with a maximal output power of 1000 W ultrasonic horn BS2d22 (head area of 3.8 cm<sup>2</sup>) and equipped with a booster B2-1.2. The maximum intensity was calculated to be 57 W cm<sup>-2</sup> at a mechanical amplitude of 81 μm.

### ***Determination of the amount of superoxide***

The amount of superoxide generated during the sonochemical process was determined using luminol on the metal surface by the chemiluminescence measurement.[59] The cell was filled with luminol solution (to prepare this solution, 20 mg of luminol was dissolved in 0.5 ml of dimethyl sulfoxide and then diluted 1 : 10 with 0.1 M KOH). The integrated intensity of chemiluminescence emitted by luminol was used to compare the amount of the active oxygen species adsorbed at the surface of aluminum. The addition of mannitol (a selective scavenger of hydroxyl radicals) into the luminol solution did not result in the decrease of the chemiluminescence intensity evidencing that only superoxide species accumulated at the adsorption sites at the metal surface contribute to the detected chemiluminescent signal.[60]

### ***Preparation of polyelectrolyte film and loading with anticorrosion inhibitor***

Polyelectrolyte film was prepared by alternating adsorption of poly(ethyleneimine) (PEI, Mwz600–1000 kDa, Sigma-Aldrich) and poly(styrene sulfonate) sodium salt (PSS, Mw z 70 kDa, Sigma-Aldrich). This method is described in ref. 54–56. The corrosion inhibitor mercaptobenzothiazole (98%, Aldrich) was adsorbed from 10 wt.% solution in ethanol before the film preparation.

### ***Formation of interpenetrating polypyrrole–aluminum composite***

10 wt.% aluminum was added to 5 wt.% solution of pyrrole (98%, Aldrich) in purified water. The suspension was sonicated for 15 min at the intensity of 40 W cm<sup>-2</sup>.

### ***Synthesis and incorporation of gold, silver, and platinum nanoparticles in aluminum support***

To an aqueous solution 2.5 x 10<sup>-4</sup> M of sodium citrate (250 mL), the necessary volume of an aqueous metal salt solution (HAuCl<sub>4</sub>, AgNO<sub>3</sub>, or HPtCl<sub>6</sub>) was added in order to obtain a final metal salt concentration of 2.5 x 10<sup>-4</sup> M. The mixture was vigorously stirred meanwhile a fresh prepared ice-cold NaBH<sub>4</sub> solution (0.1 M, 7.5 mL) was quickly added.[39,41] The agitation was continued for 2 h. The bottle was left open in order to avoid overpressure during the NaBH<sub>4</sub> hydrogen release and to ensure its total decomposition. In order to incorporate nanoparticles in aluminum support 1 g of porous Al particles was mixed with 250 mL of the small noble metal nanoparticles dispersion. The mixture was

sonicated with the tip at a power of 57 W cm<sup>-2</sup> for 20 min. After that the solution comprising mesoporous Al particles filled with small noble metal nanoparticles was centrifuged (3500 rpm, 20 min), the supernatant discarded and dried in an oven at 85 °C for 24 h.

### ***Experiments in ionic liquid***

Experiments with room temperature ionic liquid, 1-butyl-3-methylimidazolium chloride (> 98%, Aldrich), were performed under argon flow. Sonication time was varied between 1 min and 90 min.

### ***Scanning electron microscopy (SEM)***

Scanning electron microscopy measurements were conducted with a Gemini Leo 1550 instrument at an operation voltage of 3 keV.

### ***Transmission electron microscopy (TEM)***

Transmission electron microscopy images were obtained on a Zeiss EM 912 Omega transmission electron microscope operating at 300 kV. The samples were ultramicrotomed (Leica EM FC6) and placed onto the copper grids coated with carbon film.

### ***Confocal scanning fluorescence microscopy (CSFM)***

A Leica TCS SP confocal laser scanning microscope (Leica, Germany) with a 100 x oil immersion objective, numerical aperture 1.4, was used.

### ***Scanning vibrating electrode technique (SVET)***

The SVET experiments were performed by using the equipment supplied by Applicable Electronics (Forestdale, MA, USA). The immersion solution was 0.1 M NaCl. Scans were initiated within 5 min of immersion and were collected every 30 min for the duration of the experiment, typically 16 h.

### ***X-ray diffraction (XRD)***

X-ray diffraction of the samples was studied on a Bruker AXS— D8 ADVANCE X-ray diffractometer and on a Nanostar Bruker AXS diffractometer.

### ***BET analysis***

The specific surface areas of the samples were determined by a Micromeritics ASAP 2000 surface area analyzer. All samples were outgassed under vacuum at 120 °C for 8 hours before N<sub>2</sub> adsorption.

### ***Three-dimensional atom probe analyses***

Three-dimensional atom probe analyses were performed with a CAMECA instrument.[61] In order to prepare tips for 3D-AP investigations, small rods with a cross section of 0.2 x 0.2 mm<sup>2</sup> were cut. Sharp tips were prepared using standard techniques by electrolytical polishing as described in Ref. [62]. Samples after solution sonochemical treatment were investigated. All atom probe analyses were

performed at a temperature of 60 K with a pulse fraction ratio (pulse voltage to the standing tip voltage) of 0.2 and with a pulse repetition rate of 1 kHz in ultrahigh vacuum of  $1 \times 10^{-8}$  Pa.

#### 4.1.7 Acknowledgements

The research was supported by SFB840; the Nano-Futur program of the German Ministry for Education; EU FP7 project "MUST" NMP3-CP-IP 214261-2; Basic Research Foundation of Belarus and NATO grant CLG 984063. E.S. thanks Alexander von Humboldt Foundation. The authors thank S. Nemeth for assistance with the materials synthesis, C. Kunert, W. Milius, L. Geiling, and H. Partsch (University of Bayreuth) for microtoming, TEM, PXRD, BET, and ICP assistance and Prof. Rhett Kempe (University of Bayreuth) for the discussion on catalytic activity.

#### References

- [1] J. Banhart, *Prog. Mater. Sci.*, 2001, 46, 559.
- [2] G. J. Davies and S. J. Zhen, *J. Mater. Sci.*, 1983, 18, 1899.
- [3] Y. Sugimura, J. Meyer, M. Y. He, H. Bart-Smith, J. Grenstedt and A. G. Evans, *Acta Mater.*, 1997, 45, 5245.
- [4] O. Mizuno, T. Matsuura, S. Nakayama, K. Harad and A. Yamakawa, *SEI Tech. Rev.*, 2003, 55, 95.
- [5] H. Hakamada and M. Mabuchi, *Scr. Mater.*, 2007, 56, 1003.
- [6] V. V. Calmidi and R. L. Mahajan, *J. Heat Transfer*, 2000, 122, 557.
- [7] G. S. Attard, P. N. Bartlett, N. R. B. Coleman, J. M. Elliott, J. R. Owen and J. H. Wang, *Science*, 1997, 278, 838.
- [8] O. D. Velev, P. M. Tessier, A. M. Lenhoff and E. W. Kaler, *Nature*, 1999, 401, 548.
- [9] H. Maeda, Y. Kusunose, M. Terasaki, Y. Ito, C. Fujimoto, R. Fujii and T. Nakanishi, *Chem.–Asian J.*, 2007, 2, 350.
- [10] H. Masuda and K. Fukuda, *Science*, 1995, 268, 1466.
- [11] Y. Yusuke, M. Toshiyuki, Y. Tokihiko, K. Kazuyuki and O. J. Tetsuya, *J. Mater. Chem.*, 2005, 15, 1987.
- [12] A. Devasenapathi, H. W. Ng, C. M. S. Yu and S. W. Lim, *J. Mater. Sci.*, 2005, 40, 5463.
- [13] H. M. Luo, L. Sun, Y. F. Lu and Y. S. Yan, *Langmuir*, 2004, 20, 10218.
- [14] J. Erlebacher, M. J. Aziz, A. Karma, N. Dimitrov and K. Sieradzki, *Nature*, 2001, 410, 450.
- [15] J. R. C. Newman, S. G. Corcoran, J. Erlebacher, M. J. Aziz and K. Sieradzki, *MRS Bull.*, 1999, 24, 24.
- [16] J. Erlebacher and K. Sieradzki, *Scr. Mater.*, 2003, 49, 991.
- [17] K. Sieradzki, R. R. Corderman, K. Shukla and R. C. Newman, *Philos. Mag. A*, 1989, 59, 713.
- [18] J. P. Lorimer and T. J. Mason, *Chem. Soc. Rev.*, 1987, 16, 239.
- [19] K. S. Suslick and G. J. Price, *Annu. Rev. Mater. Sci.*, 1999, 29, 295.
- [20] T. Prozorov, R. Prozorov and K. S. Suslick, *J. Am. Chem. Soc.*, 2004, 126, 13890.
- [21] J. H. Bang and K. S. Suslick, *Adv. Mater.*, 2010, 22, 1039.

- [22] G. Cravotto and P. Cintas, *Angew. Chem., Int. Ed.*, 2007, 46, 5476.
- [23] J. Lindlay and T. Meson, *Chem. Soc. Rev.*, 1987, 16, 275.
- [24] K. S. Suslick, S. J. Doktycz and E. B. Flint, *Ultrasonics*, 1990, 28, 280.
- [25] A. Margulis, *Ultrasonics*, 1985, 23, 157.
- [26] S. J. Doktycz and K. S. Suslick, *Science*, 1990, 247, 1067.
- [27] J.-L. Luche, *Ultrason. Sonochem.*, 1994, 1, S11.
- [28] M. M. Mdeleleni, T. Hyeon and K. S. Suslick, *J. Am. Chem. Soc.*, 1998, 120, 6189.
- [29] K. S. Suslick, S.-B. Choe, A. Cichowlas and M. W. Grinstaff, *Nature*, 1991, 353, 414.
- [30] K. S. Suslick, D. J. Casadonte and S. J. Doktycz, *Chem. Mater.*, 1989, 1, 6.
- [31] E. V. Skorb, D. G. Shchukin, H. Möhwald and D. V. Andreeva, *Langmuir*, 2010, 26, 16973.
- [32] E. V. Skorb, D. G. Shchukin, H. Möhwald and D. V. Andreeva, *Nanoscale*, 2010, 2, 722.
- [33] B. Langenecker, C. W. Fountain and O. V. Janes, *Metal Prog.*, 1964, 85, 97.
- [34] B. A. Shenoj, K. S. Indira and R. Subramanian, *Met. Finish.*, 1979, 77, 41.
- [35] O. V. Abramov, *Ultrasonics*, 1987, 25, 73.
- [36] A. P. Kupustin, *Effect of Ultrasound on the Kinetics of Crystallization*, Consultants Bureau, New York, 1963.
- [37] W. Kurz and D. J. Fisher, *Fundamentals of Solidification*, Trans Tech Publication, Switzerland, Germany, UK, USA, 1986.
- [38] L. N. Solovieva, *Kolloidn. Zh.*, 1939, 5, 289.
- [39] K. R. Lawless, *Rep. Prog. Phys.*, 1974, 37, 231.
- [40] E. V. Skorb, L. I. Antonouskaja, N. A. Belyasova, D. G. Shchukin and D. V. Sviridov, *Appl. Catal., B*, 2008, 84, 94.
- [41] C. Petrier, M.-F. Lamy, A. Francony, A. Benahcene, B. David, V. Renaudin and N. Gondrexon, *J. Phys. Chem.*, 1994, 98, 10514.
- [42] A. Henglein, D. Herburger and M. Gutierrez, *J. Phys. Chem.*, 1992, 96, 1126.
- [43] H. N. McMurray and B. P. Wilson, *J. Phys. Chem. A*, 1999, 103, 3955.
- [44] W. R. Seitz and D. M. Hercules, in *Chemiluminescence and Bioluminescence*, ed. M. J. Cormier, D. M. Hercules and L. Lee, Plenum Press, New York, 1973, p. 427.
- [45] D. J. Flannigan, S. D. Hopkins and K. S. Suslick, *J. Organomet. Chem.*, 2005, 690, 3513.
- [46] E. V. Skorb, H. Möhwald, T. Irrgang, A. Fery and D. V. Andreeva, *Chem. Commun.*, 2010, 7897.
- [47] S. A. Meenach, J. Burdick, A. Kunwar and J. Wang, *Small*, 2007, 3, 239.
- [48] D. L. Burris and W. G. Sawyer, *Wear*, 2008, 264, 374.
- [49] R. B. Grubbs, *J. Polym. Sci., Part A: Polym. Chem.*, 2005, 43, 4323.
- [50] E. V. Skorb, D. Fix, D. V. Andreeva, D. G. Shchukin and H. Möhwald, *Adv. Funct. Mater.*, 2009, 19, 2373.

- [51] E. V. Skorb, D. V. Sviridov, H. Möhwald and D. G. Shchukin, *Chem. Commun.*, 2009, 6041.
- [52] E. V. Skorb, A. Skirtach, D. V. Sviridov, D. G. Shchukin and H. Möhwald, *ACS Nano*, 2009, 3, 1753.
- [53] E. V. Skorb, D. G. Shchukin, H. Möhwald and D. V. Sviridov, *J. Mater. Chem.*, 2009, 19, 4931.
- [54] D. O. Grigoriev, K. Köhler, E. V. Skorb, D. G. Shchukin and H. Möhwald, *Soft Matter*, 2009, 5, 1426.
- [55] D. V. Andreeva, D. Fix, D. G. Shchukin and H. Möhwald, *J. Mater. Chem.*, 2008, 18, 1738.
- [56] D. V. Andreeva, D. Fix, H. Möhwald and D. G. Shchukin, *Adv. Mater.*, 2008, 20, 2789.
- [57] D. V. Andreeva, E. V. Skorb and D. G. Shchukin, *ACS Appl. Mater. Interfaces*, 2010, 2, 1954.
- [58] R. Akid and M. Garma, *Electrochim. Acta*, 2004, 49, 2871.
- [59] K. Ishibashi, A. Fujishima, T. Watanabe and K. Hashimoto, *J. Phys. Chem. B*, 2000, 104, 4934.
- [60] J. Rabani, W. A. Mulac and M. S. Maseson, *J. Phys. Chem.*, 1965, 69, 53.
- [61] D. Blavette, B. Deconihout, A. Bostel, J. M. Sarrau, M. Bouet and A. Menand, *Rev. Sci. Instrum.*, 1993, 64, 2911.
- [62] H. Leitner, H. Clemens, S. Horing, N. Wanderka, J. Banhart, P. Staron and B. Jamnig, *Z. Metallkd.*, 2004, 95, 644.

## 4.2 Ultrasound driven formation of metal-supported nanocatalysts

Nicolas Pazos-Peréz, Jana Schäferhans, Ekaterina V. Skorb, Andreas Fery, and Daria V. Andreeva\*

This work is published in *Microporous and Mesoporous Materials* 2012, 154, 164 – 169

This article is reprinted from *Microporous Mesoporous Mater.*, 154, N. Pazos-Peréz, et al., Ultrasound driven formation of metal-supported nanocatalysts, 164 – 169, Copyright (2012), with permission from Elsevier.

### 4.2.1 Contribution to the joint publication

I carried out the material preparation, evaluated the physisorption data and processed and evaluated the powder x-ray diffraction measurements, and performed the catalytic experiments. I partly prepared the manuscript, the main part was written by Nicolas Pazos-Peréz. Andreas Fery corrected the manuscript. Daria Andreeva corrected the manuscript and supervised the project.

### 4.2.2 Abstract

Bimetal nanocatalysts with a narrow pore size distribution and high surface area were prepared using a fast, easy, and “green” method of ultrasound irradiation in water. The concept is demonstrated for the case of aluminum – gold, silver or platinum, but applicable to a large range of nanoparticles. The application as effective nanocatalysts is shown.

### 4.2.3 Introduction

The application of ultrasound to nanocomposite preparation has raised much interest in recent years [1–3]. First of all the reduction of metal salts in the presence of ultrasound has been widely used in the preparation of heterogeneous catalysts.[4] Metal nanoparticles were prepared by the sonication of a corresponding metal salt in the presence of stabilizers.[5] However, the direct sonochemical reduction of metals does not allow the control over the morphology, monodispersity, and size of the nanoparticles even in presence of stabilizers.[6] Recently, we proposed a novel up–bottom method for the ultrasound-assisted formation of multimetal composites from metal alloys particles.[7] We showed that ultrasonic processes could cause phase segregation in metal alloys, for example, aluminum/palladium (1% Pd) due to the crystallization of one of the components (Pd) of the alloy. This very promising method is, however, restricted by a number of the available metal alloy particles. Another bottom–up method of formation of composite materials by sonication is ultrasound-assisted intercalation of molecules into layered inorganic solids.[8] It was shown that high temperatures (up to 5000 K) and high pressures (hundreds of bars) together with a shock wave generated by ultrasound [9,10] could enhance the penetration of inorganic species into the interlayer spacing of solids. The sonochemical insertion of nanoparticles (NP) into two-dimensional mesoporous alumina sheets has

been demonstrated,[11] where the silver NPs were spread homogeneously in the predesigned mesoporous alumina matrix. High-intensity ultrasound dramatically increases the rates of intercalation of a wide range of compounds into various layered inorganic solids, such as  $ZrO_2$  [12] and clays[13]. The adsorption of organic or inorganic compounds between the atomic sheets of layered solids permits the systematic change of optical, electronic, and catalytic properties.

Here we propose a novel bottom-up method of formation of nanocomposites consisting of the mesoporous metal frameworks as a support and noble nanoparticles (NPs). In our previous works[14,15] we already demonstrated the successful preparation of mesoporous metal frameworks from  $\mu\text{m}$ -size aluminum (Al), magnesium (Mg), and zinc (Zn) particles in aqueous media by using ultrasound. The ultrasonically formed mesoporous metal frameworks exhibit relatively high surface area (up to  $80 \text{ m}^2 \text{ g}^{-1}$ ) and narrow pore size distribution (2 – 4 nm). In this study ultrasound is applied to both the formation of the support frameworks and the incorporation of metal NPs. We demonstrated that the novel procedure allows an easy, fast and surfactant free approach to produce high quantities of stable bimetallic particles with a narrow pore size distribution and high surface areas. High local energy provided by ultrasound leads to formation of very stable composite materials where metal active phase is supported by another metal phase. The novel composite materials can be directly used as nanocatalyst and exhibit an enhanced catalytic rate constant.

#### 4.2.4 Results and discussion

##### *Material properties*

The schematic illustration of the formation of functional nanostructures consisting of mesoporous aluminum frameworks with incorporated Au, Ag, or Pt NPs is in Fig. 4-15. Fig. 4-15 illustrates the steps of the formation of Al-supported nanocatalysts. At the beginning, the  $160\text{-}\mu\text{m}$ -Al particles are pre-sonicated for 30 min at  $57 \text{ W cm}^{-2}$  in order to form porous metal frameworks (Fig. 4-15A–C). Then, the mixture of the pre-treated (sonicated) aluminum particles (Fig. 4-15C) and the noble NPs (Au, Ag, or Pt) synthesized as described in Refs. [18–20] was sonicated for the additional time at the same intensity (Fig. 4-15D). Fig. 4-15E demonstrates the desired metal-supported nanocatalysts consisted of mesoporous aluminum support and homogeneously distributed NPs of Au, Ag, or Pt.

In particular, the preparation procedure of metal-supported nanocatalysts begins with ultrasound-assisted pre-treatment of the support (here Al) particles. The initial  $160\text{-}\mu\text{m}$ -Al particles were pre-sonicated for 30 min.

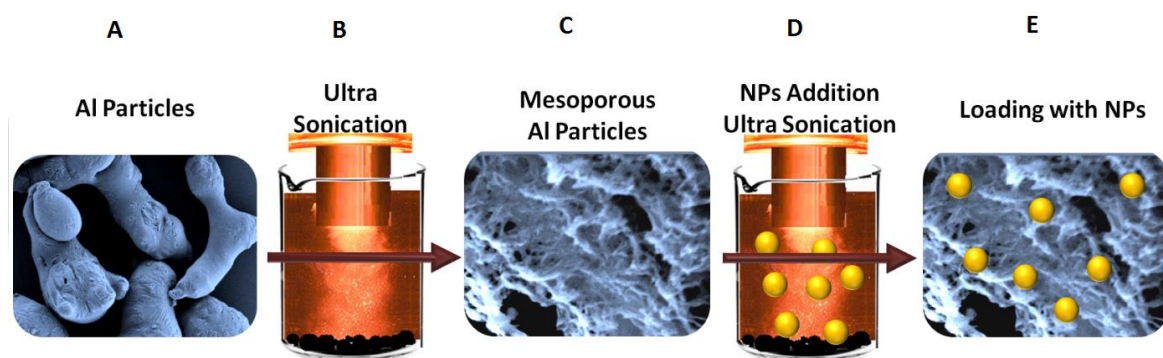


Fig. 4-15 Schematic illustration of the sonochemical production of aluminum-supported nanocatalysts. A – The 160- $\mu\text{m}$ -Al particles; B – Pre-treatment by sonication of initial Al particles for 30 min at  $57 \text{ W cm}^{-2}$ ; C – The porous Al frameworks; D – Sonication of the mixture of the pre-treated Al particles and the noble NPs (Au, Ag, or Pt); E – The desired Al-supported nanocatalysts consisted of mesoporous aluminum support and homogeneously distributed NPs of Au, Ag or Pt. Reprinted from *Microporous Mesoporous Mater.*, 154, N. Pazos-Peréz, et al., Ultrasound driven formation of metal-supported nanocatalysts, 164 – 169, Copyright (2012), with permission from Elsevier.

As we showed previously[14,15], sonication of aluminum particles results in particle breakage (approximately 160  $\mu\text{m}$  initial particles are broken into 10 – 20  $\mu\text{m}$  ones, shown in Fig. 4-17A, B) and formation of a porous structure (Fig. 4-16).

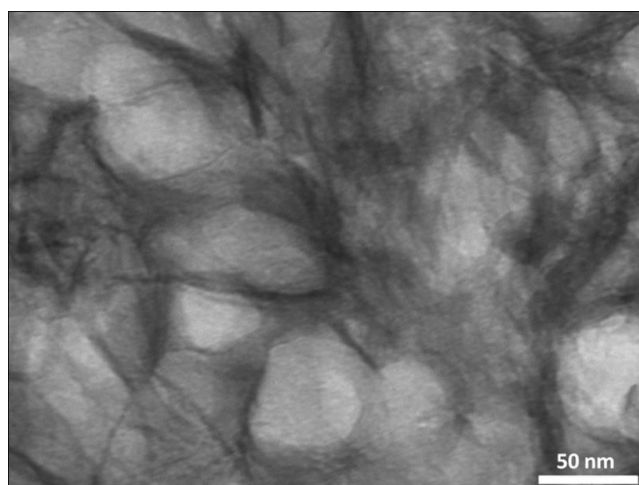


Fig. 4-16 TEM image of the ultramicrotomed mesoporous Al particle formed by 30-min-sonication at  $57 \text{ W cm}^{-2}$ . Reprinted from *Microporous Mesoporous Mater.*, 154, N. Pazos-Peréz, et al., Ultrasound driven formation of metal-supported nanocatalysts, 164 – 169, Copyright (2012), with permission from Elsevier.

The BJH and BET (Fig. 4-17C, D) reveals formation of mesoporous structure with a pore size distribution between 1 nm – 4 nm and a surface area of  $60 \text{ m}^2 \text{ g}^{-1}$  after 30 minutes of sonication at  $57 \text{ W cm}^{-2}$ . [14] The surface of the aluminum oxide was explored by means of nitrogen adsorption measurements,  $\text{N}_2$  (77 K) (Fig. 4-17C). The adsorption–desorption isotherm cannot be rigorously classified into any IUPAC group. [21,22] The initial part corresponds to type II, typical of nonporous or macroporous materials, and represents a process of unrestricted monolayer–multilayer adsorption. The observed hysteresis

loop in the multilayer range, associated with capillary condensation in mesopores, is characteristic of type IV isotherms. However, it is possible to classify this isotherm as group Ib if the new classification system proposed by Rouquerol et al.[22] is considered. The hysteresis loop can be classified into type H-4, according to IUPAC classification standards.[22] This is typical of particles with narrow openings. The point of closure ( $p/p_0 = 0.42$ ) is attributed to the surface tension of the liquid adsorbate reaching an unstable state at a specific pressure. The surface area value, obtained by applying the BET method[16] is  $60 \text{ m}^2 \text{ g}^{-1}$ . The BJH[17] pore distribution for adsorption of  $\text{N}_2$  at 77 K (Fig. 4-17D), shows a maximum at 4 nm. Based on these results, this material can be classified as mesoporous. The surface area of the initial Al particles was  $0.12 \text{ m}^2 \text{ g}^{-1}$  therefore; the surface area is increased by a factor of 500 after the ultrasound treatment. Thus, pre-treatment results in formation of the Al frameworks characterized by high surface area and a narrow pore size distribution. We used these frameworks for incorporation of NPs and achieve their homogeneous distribution inside of the Al frameworks.

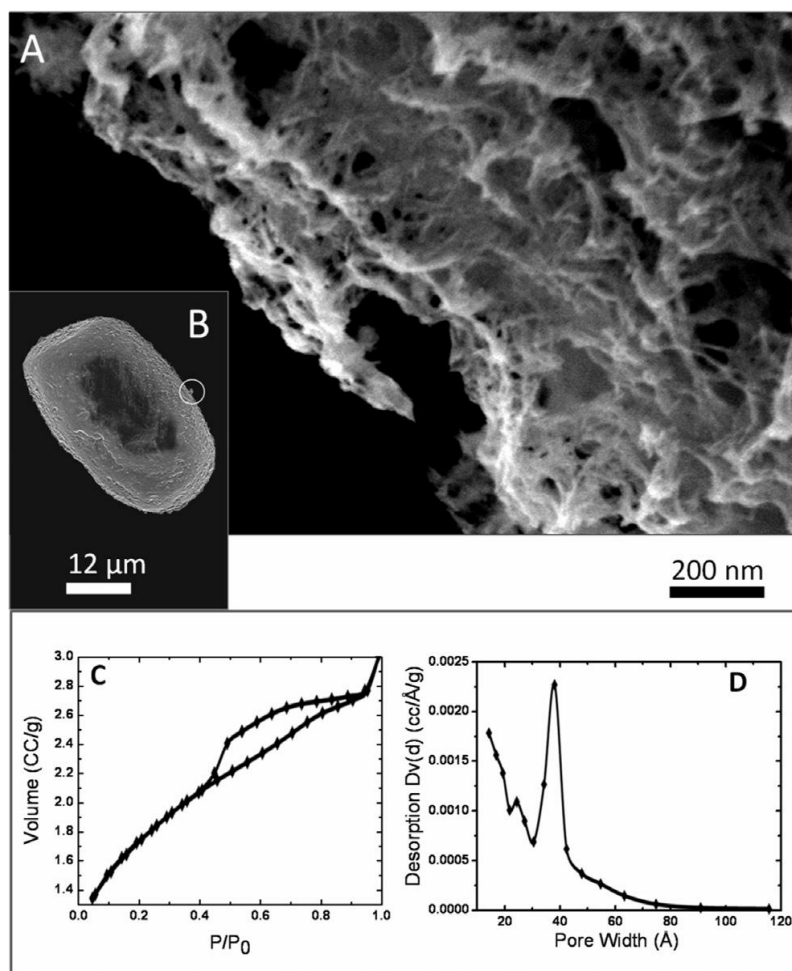


Fig. 4-17 Scanning electron microscopy (SEM) image of mesoporous aluminum particles after sonication (A). Low magnification SEM image of A (B). BET analysis (C) and BJH evaluation (D) of the mesoporous Al particles. Reprinted from *Microporous Mesoporous Mater.*, 154, N. Pazos-Peréz, et al., Ultrasound driven formation of metal-supported nanocatalysts, 164 – 169, Copyright (2012), with permission from Elsevier.

It is very important that in our previous works[14,15] we showed that the sonication up to 120 min does not lead to complete oxidation of the metals. The  $^{27}\text{Al}$  MAS NMR and PXRD spectra exhibit the signals and picks that were assigned to Al and aluminum oxides.[15] The high local temperature generated by acoustic cavitation has been found to cause phase transitions (amorphous  $\leftrightarrow$  crystalline) resulting in increased surface area of metal systems. Free radicals produced during cavitation oxidize the metal surface and stabilize the porous metal skeleton by formation of a thin oxide layer. Thus, the aluminum frameworks consist on porous aluminum structure covered by a thin oxide layer.

These porous metal frameworks were used for ultrasound-assisted incorporation of the metal NPs. For this propose the mixture of the Al framework particles and the noble NPs were further sonicated. The formation of nanocomposites was proved by the color test (Fig. 4-18A, B, C). Digital photographs (Fig. 4-18) clearly show the color changes of the aluminum frameworks after sonication in presence of the aqueous suspensions of Au, Ag and Pt NPs. The TEM image of the microtomed mesoporous bimetallic (Al–Au) particle (Fig. 4-18D) proved the homogeneous distribution of NPs within the frameworks. The perfect distribution of the monodisperse particle within the frameworks was also observed for Ag and Pt loaded samples. The linear dependence of the Au intake in Al frameworks vs. the sonication time (Fig. 4-18E) allows the precise control over the amounts of noble metal NPs incorporated in the system. The UV–Vis spectral characterization of Au and Al–Au are shown in Fig. 4-19, after loading the Al frameworks the intensity of the plasmonic band considerably decrease due to that the contribution to the signal comes only from the Au particles adsorbed on the Al surface, and also because of the big scattering observed due to the Al particle size. An important point concerning this procedure is the formation of a stable, surfactant free system, which could be an effective alternative to existing nanocatalyst.

The ICP analysis discloses the maximal loading up to 1 wt.% of Au, 0.72 wt.% of Ag and 1 wt.% of Pt into the Al frameworks (the Ag and Pt contents were calculated from the concentrations and volumes used). The lower Ag weight content in respect to the Au and Pt arises from the lower molecular weight of the Ag.

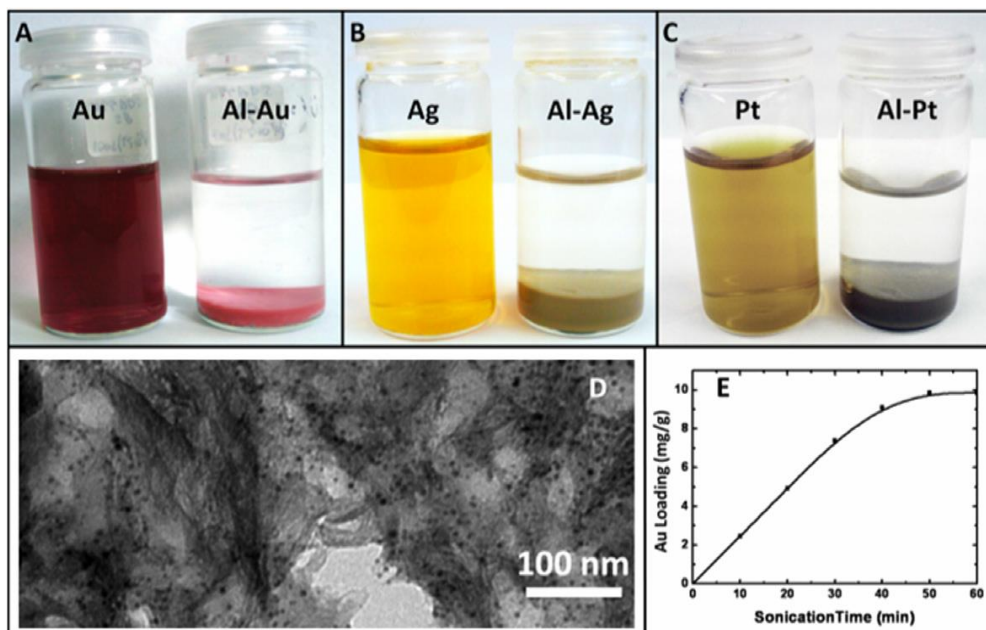


Fig. 4-18 Digital photographs of Au, Ag and Pt nanoparticles suspensions (A, B, and C respectively) before (left) and after (right) the ultrasound-assisted loading in Al nanostructures. The particles sediment due to their incorporation into the Al particles. TEM image of microtomed mesoporous bimetallic (Al-Au) particle (D). The linear dependence of the Au intake in the Al particles vs. the sonication time. In 50 min of sonication the saturation is achieved (E). Reprinted from *Microporous Mesoporous Mater.*, 154, N. Pazos-Peréz, et al., Ultrasound driven formation of metal-supported nanocatalysts, 164 – 169, Copyright (2012), with permission from Elsevier.

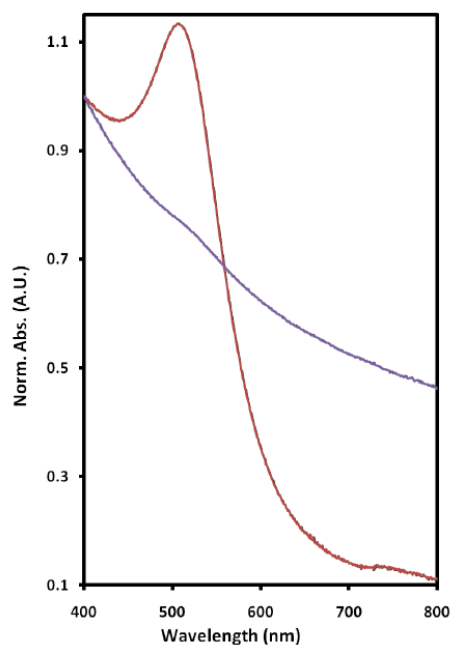


Fig. 4-19 UV-Vis spectra of Au solution (red), and Al-Au mesoporous structure (blue). After incorporation of the nanoparticles within the Al support the intensity of the Plasmon resonance decreases because the Au particles adsorbed on the Al surface contribute to the signal, and big scattering is observed due to the Al particle size. Reprinted from *Microporous Mesoporous Mater.*, 154, N. Pazos-Peréz, et al., Ultrasound driven formation of metal-supported nanocatalysts, 164 – 169, Copyright (2012), with permission from Elsevier.

The structure of the NPs within the Al frameworks was analyzed by powder X-ray diffraction (PXRD). The PXRD analysis (Fig. 4-20A) reveals the presence of crystalline NPs in the metal system. Since the PXRD method cannot indicate if the NPs are located within the mesopores or deposited on the surface, the distribution of NPs within the mesoporous matrix can be proved by the TEM image of the ultramicrotomed samples (Fig. 4-18D). The aluminum frameworks consists on the aluminum covered by bayerite  $\text{Al}(\text{OH})_3$  and boehmite  $\text{AlO}(\text{OH})$  oxide layer.[23] The quantity of bayerite increases during formation of the porous structure, which corresponds to the formation of the higher surface areas of the samples. The formation of mesoporous metal composites with high surface area (the surface area for the Al–Au system achieves  $110 \text{ m}^2 \text{ g}^{-1}$ ) and the narrow pore size distribution is proved by the analysis of the nitrogen adsorption isotherms (Fig. 4-20B, C). It is interesting that the micropores ( $< 3 \text{ nm}$ ) formed in pre-treated Al particles are blocked by the NPs. As in the case of the bare mesoporous aluminum the isotherms can be classified into the group IIb.[22] However, the hysteresis loops clearly changes to H-3 type.[22] This is typical of aggregated particles that form plates and give rise to formations such as rifts or wedges. These isotherms show unlimited adsorption within a large range. The closure of the loop is gradual and this confirms the existence of mesopores formed by parallel plates or wedge-shaped sites where desorption occurs due to capillary evaporation. The presence of narrow openings, which implies sharp desorption, can be discarded. This points towards the retention of the nanoparticles into the initial aluminum pores while generating a new porous surface.

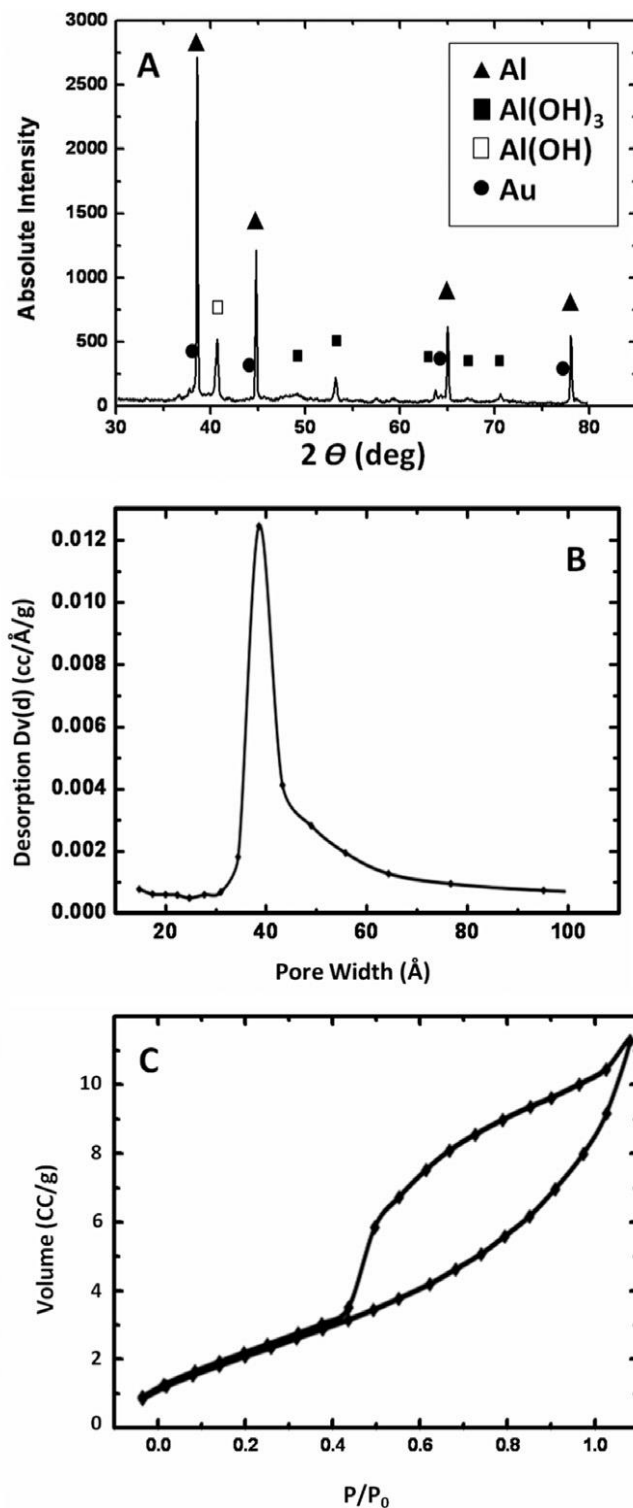


Fig. 4-20 PXRD spectrum of Al–Au system (A). Metallic Al is marked by triangles, aluminum oxides – Squares and Au – Circles. The calculated Au content from ICP is 1 wt.%. BJH (B) and BET (C) characterization of the mesoporous Al–Au systems. Pore size distribution for all cases was determined to be  $\sim 4$  nm. Surface area:  $110 \text{ m}^2 \text{ g}^{-1}$ . Reprinted from Microporous Mesoporous Mater., 154, N. Pazos-Peréz, et al., Ultrasound driven formation of metal-supported nanocatalysts, 164 – 169, Copyright (2012), with permission from Elsevier.

It is remarkable that 60 min ultrasound treatment of suspension of different metal particles results in formation of the nanocomposites with high surface area, narrow pore size distribution and

homogeneous spreading of the functional centers. Ultrasound-assisted formation of mesoporous bimetal structures is based on specific interactions of cavitation bubble and metal particles. In heterogeneous solid–liquid systems[24–26] cavitation could have three main effects: (1) surface damage at the liquid–solid interface by symmetric bubble collapse (shock waves and subsequent microstreaming) and (2) asymmetric bubble collapse (microjets occur at the surface several orders of magnitude larger than the cavitation bubble size, e.g. at 20 kHz the maximum size of a cavitation bubble is approximately 5  $\mu\text{m}$  [27]), and interface effects are observed with solids from ca. 200  $\mu\text{m}$ ; 3) chemical surface modification/stabilization due to ultrasonic induced formation of free radicals.[28] Thus, the asymmetric collapse of bubble and surface imprinting by high speed microjets are observed for “large” particle. This result in the formation of the metal frameworks, namely, particle fragmentation and surface area increase. The “small” particles (here,  $\sim 4$  nm particles of noble metals) are moved violently within shock waves generated by the symmetric collapse of cavitation bubbles in bulk and incorporated in porous support. Nature of the metal particles (melting point and tendency to oxidation by free radicals produced by sonication) determines the surface morphology of the particles after sonication. In our previous works[14,15,29–31] we demonstrated that the surface of Al is oxidized immediately by highly reactive radicals derived from water and oxygen (active oxygen species). On the contrary, the noble metals exhibit very low tendency to oxidation and have relatively high melting points. Due to their nature NPs are resistant to ultrasound irradiation and remain their initial properties in the ultrasonically prepared bimetal nanostructures.

### ***Catalytic properties***

As a proof of principle we performed a model catalytic reaction on Pt NPs because of their multiple catalytic applications.[32] The kinetic of the reduction of ferricyanide by thiosulfate[33] was investigated by monitoring the intensity of the hexacyanoferrate (III) absorption peak at 420 nm as a function of time via UV–Vis absorption spectroscopy.

We can clearly see (Fig. 4-21A) from the decrease of the maximum absorbance related to hexacyanoferrate (III) the  $>70\%$  conversion is observed after 1.7 h at ambient conditions. As shown in Fig. 4-21B, the absorbance maximum decays logarithmically with the time (black squares) indicating a first order kinetics for the hexacyanoferrate (III) decomposition. Thus, plotting the  $\ln(\text{Abs})$  vs. the reaction time demonstrates a linear relationship. Based on this linear dependence the reaction rate constant ( $k$ ) can be calculated. This reaction rate constant of Al–Pt nanostructures was calculated to  $0.0077 \text{ min}^{-1}$ , which is much higher to the value reported by Maitra et al.[34] for the same reaction using Pt nanoparticles of different sizes. This is probably due to the fact that by using ultrasound we could manipulate by smaller surfactant-free particles. Thus, higher surface area is available to the catalytic reaction. Moreover, the similar high value was obtained by El-Sayed et al.[35] ( $0.0076 \text{ min}^{-1}$ )

for the same reaction but with gold nanocages. However, the rate of the reported in Ref. [35] reaction was accelerated by surface plasmon resonance. Based on our experiments and the literature we can conclude that the novel catalytic system developed here exhibit high efficiency, good recyclability, easy handling and high stability.

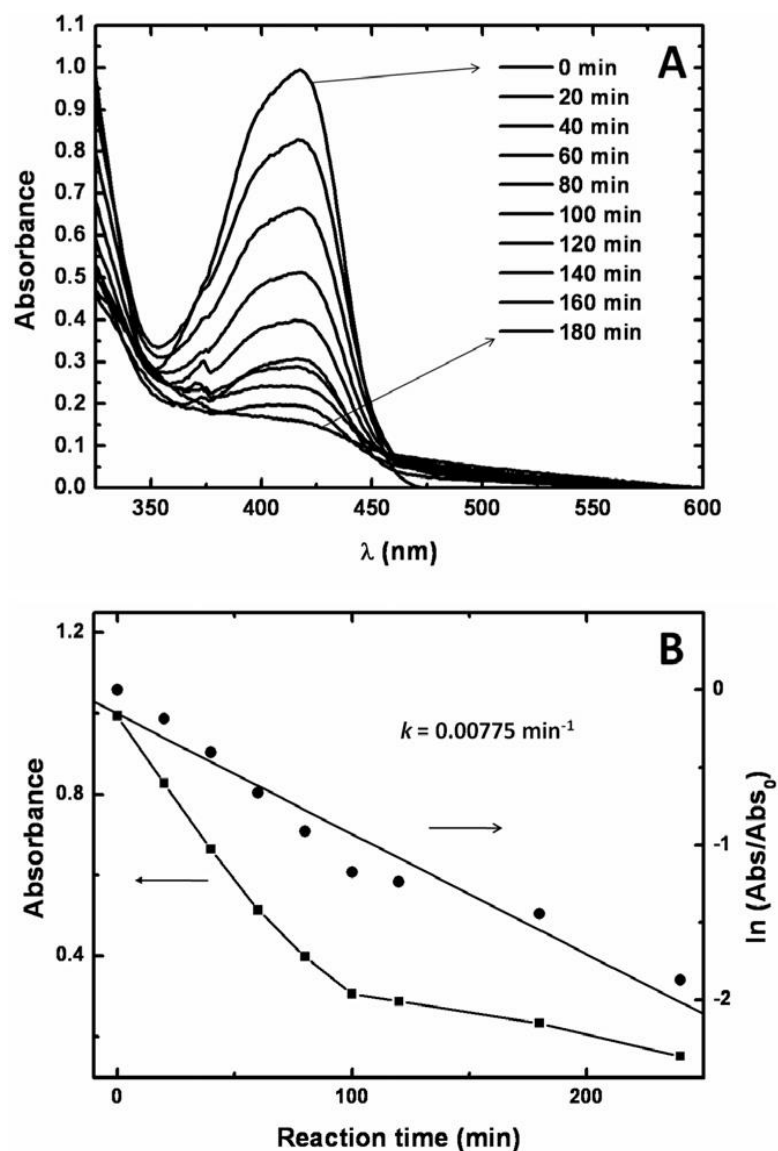


Fig. 4-21 Absorption spectra monitoring every 20 min the electron transfer reaction between hexacyanoferrate (III) and thiosulfate by using Al-Pt sponges with time (A). Plot showing the hexacyanoferrate (III) absorbance (concentration) as a function of the reaction time (B, squares). Relationship between the logarithmic scale of the normalized absorbance (against the absorbance at the beginning of the reaction) and the reaction time (B, circles). The calculated reaction rate constant ( $k$ ) of Al-Pt nanostructures was  $0.00775 \text{ min}^{-1}$ . Reprinted from Microporous Mesoporous Mater., 154, N. Pazos-Peréz, et al., Ultrasound driven formation of metal-supported nanocatalysts, 164 – 169, Copyright (2012), with permission from Elsevier.

#### 4.2.5 Conclusion

In summary, we propose a novel concept of ultrasound driven formation of bimetal nanocatalysts. We showed that sonochemical manipulation of structure and properties of metals depends on the size and

nature of metal particles. The “large” solid surfaces are fragmented, oxidized, and pores are formed deep inside. Simultaneously, the “small” metal nanoparticles are incorporated and homogeneously distributed inside the porous matrix remaining their initial morphology, structure and properties. This novel procedure allows an easy, fast and surfactant free approach to production of high quantities of stable bimetallic particles with a narrow pore size distribution and high surface areas. The successful application as nanocatalysts demonstrated a higher rate constant for catalytic conversion than previously reported. The concept is applicable on a large range of materials providing a basis for many types of applications in chemistry, materials science and medicine where the structure and properties of metal nanocomposites can be easily controlled by ultrasound.

#### **4.2.6 Experimental**

##### ***Materials and methods***

Al powder (< 160  $\mu\text{m}$ , Roth), trisodium citrate dehydrate, silver nitrate (99.9%  $\text{AgNO}_3$ ), tetrachloroauric acid ( $\text{HAuCl}_4 \cdot 3\text{H}_2\text{O}$ ), hexachloroplatinate ( $\text{HPtCl}_6$ ) and sodiumborohydride ( $\text{NaBH}_4$ ) were purchased from Sigma–Aldrich. All reactants were used without further purification. Milli-Q water ( $18 \text{ M}\Omega \text{ cm}^{-1}$ ) was used in all aqueous solutions.

UV–Vis/near-IR spectroscopy (PerkinElmer, 65 Lambda 19), transmission and scanning electron microscopy (TEM, LEO 922 EFTEM operating at 200 kV and LEO 1530 FE-SEM, Zeiss, respectively), in combination with an ultra-microtome (Ultracut E Reichert Jung, thickness 50 nm) were applied to characterize the optical response, structure, and size of the nanoparticles. Powder X-ray diffraction (PXRD) ( $\Theta$ – $\Theta$  mode using a Stoe STADI P X-ray Transmission diffractometer:  $\text{Cu K}\alpha_1$  irradiation, room temperature,  $2^*\Theta = 5^\circ - 90^\circ$ ), inductive coupled plasma (ICP) (PerkinElmer plasma 400 with Ar plasma), the Brunauer–Emmett–Teller method[16] and the Barrett–Joyner–Halenda[17] (Quantachrom) evaluation of the adsorption branch of the isotherm, were used to characterize the composition, surface area and pore size distribution of the samples.

##### ***Synthesis of Ag, Au, and Pt nanoparticles***

To an aqueous solution  $2.5 \times 10^{-4} \text{ M}$  of sodium citrate (250 mL), the necessary volume of an aqueous metal salt solution ( $\text{HAuCl}_4$ ,  $\text{AgNO}_3$ , or  $\text{HPtCl}_6$ ) was added in order to obtain a final metal salt concentration of  $2.5 \times 10^{-4} \text{ M}$ . The mixture was vigorously stirred meanwhile a fresh prepared ice-cold  $\text{NaBH}_4$  solution (0.1 M, 7.5 mL) was quickly added.[18–20] The agitation was continued during 2 h. The bottle was left open in order to avoid overpressure during the  $\text{NaBH}_4$  hydrogen release and to ensure its total decomposition.

### ***Ultrasonication***

Forty milliliter of a 10 wt.% suspension of aluminum particles in purified water were pre-sonicated during 30 min with an ultrasonic horn operated at 20 kHz with a maximal output power of 1000 W in an ice-cold flask (at 65 °C temperature). The maximum intensity was calculated to 57 W cm<sup>-2</sup> at a mechanical amplitude of 81µm (described in detail in Refs. [14,15]). Then 1 g of pre-sonicated dried (an oven at 85 °C during 24 h) Al particles was mixed with 250 mL of the noble metal nanoparticles dispersion. The mixture was sonicated at 57 W cm<sup>-2</sup> during 5 – 50 min. After that the solution, comprising mesoporous Al particles filled with small noble metal nanoparticles, was centrifuged (3500 rpm, 20 min), the supernatant discarded and dried in an oven at 85 °C during 24 h.

### ***Catalytic reaction***

The electron transfer reaction between hexacyanoferrate (III) and thiosulfate was carried out by mixing potassium hexacyanoferrate (III) (150 µL, 0.1 M) and sodium thiosulfate (300 µL, 0.1 M) into 15 mL water. The mixture was magnetically stirred at room temperature meanwhile 150 mg of porous aluminum particles filled with platinum were added. Aliquots at different reaction times were investigated previous centrifugation (3000 rpm, 1 min) via UV–Vis-spectroscopy in order to follow the electron transfer reaction.

### **4.2.7 Acknowledgement**

The authors thank to S. Nemeth for assistance with the materials synthesis, C. Kunert, W. Milius, L. Geiling, and H. Partsch for microtoming, TEM, PXRD, BET, and ICP assistance. This work was supported by SFB840.

### **References**

- [1] K.S. Suslick, D.J. Casadonte, *J. Am. Chem. Soc.*, 1987, 109, 3459.
- [2] K.S. Suslick, R.E. Johnson, *J. Am. Chem. Soc.*, 1984, 106, 6856.
- [3] J.H. Bang, K.S. Suslick, *Advanced Materials*, 2010, 22, 1039.
- [4] K. Chatakondur, M.L.H. Green, M.E. Thompson, K.S. Suslick, *Chem. Commun.*, 1987, 900.
- [5] K. Okitsu, Y. Mizukoshi, H. Bandow, Y. Maeda, T. Yamamoto, Y. Nagata, *Ultrason. Sonochem.*, 1996, 3, S249.
- [6] W. Chen, W. Cai, *J. Colloid Interface Sci.*, 2001, 238, 291.
- [7] D.V. Andreeva, *Intern. J. Mater. Res.*, 2011, 102, 597.
- [8] K.S. Suslick, D.J. Casadonte, M.L.H. Green, M.E. Thompson, *Ultrasonics*, 1987, 25, 56.
- [9] H. Endo, *Journal of the Acoustical Society of America*, 1994, 95, 2409.
- [10] T.A. Weber, E. Helfland, *J. Chem. Phys.*, 1980, 72, 4014.
- [11] S. Bhattacharyya, A. Gabashvili, N. Perkas, *J. Phys. Chem. B*, 2007, 111, 11161.
- [12] V. Singh, V. Sapehiya, L.K. Goverdhan, *J. Mol. Catal. A: Chem.*, 2004, 210, 124.

- [13] S. Swain, A.I. Isayev, *Polymer*, 2007, 48, 289.
- [14] E.V. Skorb, D. Fix, D.G. Shchukin, H. Möhwald, D.V. Sviridov, R. Mousa, N. Wanderka, J. Schäferhans, N. Pazos-Pérez, A. Fery, D.V. Andreeva, *Nanoscale*, 2011, 3, 985.
- [15] E.V. Skorb, H. Möhwald, T. Irrgang, A. Fery, D.V. Andreeva, *Chem. Commun.*, 2010, 46, 7897.
- [16] S. Brunauer, P.H. Emmett, E.J. Teller, *J. Am. Chem. Soc.*, 1938, 60, 309.
- [17] E.P. Barrett, L.G. Joyner, P.P. Halenda, *J. Am. Chem. Soc.*, 1951, 73, 373.
- [18] N.R. Jana, L. Gearheart, C.J. Murphy, *J. Phys. Chem. B*, 2001, 105, 4065.
- [19] N.R. Jana, L. Gearheart, C.J. Murphy, *Chem. Commun.*, 2001, 6, 17.
- [20] J. Zeng, J.Y. Lee, W. Zhou, *Appl. Catal., A: General*, 2006, 308, 99.
- [21] K.S.W. Sing, D.H. Everett, R.A.W. Haul, L. Moscou, R.A. Pierotti, J. Rouquerol, T. Siemieniowska, *Pure Appl. Chem.*, 1985, 57, 603.
- [22] F. Rouquerol, J. Rouquerol, K.S.W. Sing, Eds., *Adsorption by powders and Porous Solids*, Academic Press, London, 1999.
- [23] R. Schoen, C.E. Roberson, *Am. Mineral.*, 1970, 55, 43.
- [24] K.S. Suslick, *Science*, 1990, 247, 1439.
- [25] J.P. Lorimer, T.J. Mason, *Journal of the Chemical Society Reviews*, 1987, 16, 239.
- [26] K.S. Suslick, G.J. Price, *Annual Review of Material Science*, 1999, 29, 295.
- [27] N.A. Tsochatzidis, P. Guiraud, A.M. Wilhelm, H. Delmas, *Chem. Eng. Sci.*, 2001, 56, 1831.
- [28] A. Weissler, *J. Am. Chem. Soc.*, 1957, 81, 1077.
- [29] D.V. Andreeva, D. Fix, H. Möhwald, D.G. Shchukin, *J. Adv. Mater.*, 2008, 20, 2789.
- [30] E.V. Skorb, D.G. Shchukin, H. Möhwald, D.V. Andreeva, *Langmuir*, 2010, 26, 16973.
- [31] E.V. Skorb, D.G. Shchukin, H. Möhwald, D.V. Andreeva, *Nanoscale*, 2010, 2, 722.
- [32] A.D. Taylor, M. Michel, R.C. Sekol, J.M. Kizuka, N.A. Kotov, L.T. Thompson *Adv. Funct. Mater.*, 2008, 18, 3003.
- [33] R. Narayanan, M.A. El-Sayed, *J. Phys. Chem. B*, 2003, 107, 12416.
- [34] R.K. Sharma, P. Sharma, A. Maitra, *J. Colloid Interface Sci.*, 2003, 265, 134.
- [35] C.W. Yen, M.A. El-Sayed, *J. Phys. Chem. C*, 2009, 113, 19585.

### 4.3 Sonochemical Activation of Al/Ni Hydrogenation Catalyst

Jana Dulle, Silke Nemeth, Ekaterina V. Skorb, Torsten Irrgang, Jürgen Senker, Rhett Kempe,\* Andreas Fery, and Daria V. Andreeva\*

This work is published in *Advanced Functional Materials* 2012, 22, 3128 – 3135.

This article is reprinted from *Adv. Funct. Mater.*, 22, J. Dulle, et al., Sonochemical Activation of Al/Ni Hydrogenation Catalyst, 3128 – 3135, Copyright (2012), with permission from John Wiley and Sons.

#### 4.3.1 Contribution to the joint publication

I wrote main part of the manuscript and evaluated the physisorption isotherms and PXRD patterns. I prepared a part the porous Al/Ni and performed a part of the catalytic experiments. Together with the people from University of Erlangen I measured ICP. Silke Nemeth prepared some porous Al/Ni. Ekaterina Skorb was responsible for the 3D confocal images and the XPS including writing. Torsten Irrgang performed further catalytic experiments. Jürgen Senker carried out the solid state NMR measurements including simulations and wrote the NMR part. Daria Andreeva made SEM images including EDS and supervised the project. Daria Andreeva, Ekatarina Skorb, Andreas Fery, and Rhett Kempe corrected the manuscript.

#### 4.3.2 Abstract

This paper proposes a sonochemical approach to the nanostructuring of Al/Ni catalyst with high content of accessible Ni centers and a high reusability. The surface and bulk composition as well as pore size distribution of this catalyst are controlled synergistically by adjusting the ultrasound intensity in aqueous solution. Sonochemical activation of Al/Ni alloy leads to formation of mesoporous Al/Ni metallic based frameworks with surface area up to  $125 \text{ m}^2 \text{ g}^{-1}$ , and regular distribution of nickel active center in the porous matrix. One of the opportunities of porous Al/Ni catalyst is that due to a time-resolved controllable formation of protective oxide layer it can be stored and handled under air in comparison to traditional Raney<sup>®</sup>-Nickel catalysts which need inert conditions. The Al/Ni catalyst is characterized by scanning electron microscopy (SEM), electron diffraction spectroscopy (EDS), X-ray photoelectron spectroscopy (XPS), confocal scanning fluorescence microscopy (CSFM), solid-state NMR experiments, and powder X-ray diffraction analysis (PXRD). The catalytic activity was investigated for the hydrogenation of acetophenone.

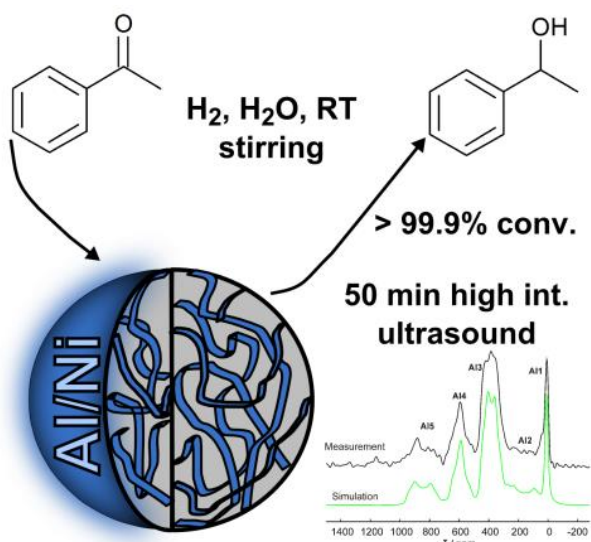


Fig. 4-22 Graphical abstract. Reprinted from *Adv. Funct. Mater.* 22, J. Dulle, et al., Sonochemical Activation of Al/Ni Hydrogenation Catalyst, 3128 – 3135, Copyright (2012), with permission from John Wiley and Sons.

### 4.3.3 Introduction

In recent years attention has been devoted to nanostructured metals because of their unique properties and potential applications in a variety of fields.[1–5] Especially their use as a support material and/or active agent for heterogeneous catalyst became more important.[6–8] Approaches towards the fabrication of porous metals are based on both template-free and template-assisted methods. Typical template-free methods are chemical or electrochemical dealloying procedures.[9] Mesoporous gold, platinum, and palladium can be formed by the dealloying process.[10] The formation of a uniform porosity after the dealloying process is possible if an alloy system is a monolithic phase because the nanoporosity is formed by a self-assembly process through surface diffusion and not by the simple dissolution of one phase from a multiphase system. For example, mesoporous gold prepared by dealloying from gold–silver alloys has disordered mesostructures, and the wide pore-size distributions of these mesostructures are not suited for the selective transport and adsorption of catalyzed species. A typical example of chemical dealloying is the preparation of “Raney®-Nickel”. [11] Raney®-Nickel is produced when a block of a nickel-aluminum alloy is treated with concentrated sodium hydroxide. However, the dissolution of aluminum ions during the catalyst formation step could accelerate the formation of catalytically inactive surface nickel aluminate species.

The template methods are based on electroplating,[12] chemical reduction,[13] or plasma spraying [14] techniques. These methods require the use of preformed templates, such as self-assembled liquid-crystal surfactants,[15] colloidal crystals,[16] porous block copolymers,[17] or anodic porous alumina.[18] By using mesoporous silica as a template, mesoporous metals with highly ordered networks and a narrow pore-size distribution can be obtained. Because fluoric acid or sodium

hydroxide is used to remove silica, the metals prepared using this method are limited to those unaffected by the dissolution agents (e.g. gold, platinum, and silver).[19] The template methods also have some disadvantages. These methods are multistage and involve a sacrificial second phase, which increases production costs because of the formation of the template and its subsequent removal, combined with the waste generation, especially when up-scaling the procedure.

Supported nickel catalysts play an important role in heterogeneous catalysis such as hydrogenation, hydrogenolysis, and partial oxidation of methane. One of the most successful methods of the activation of Al/Ni systems is the so-called Raney<sup>®</sup> process, patented by the American engineer Murray Raney in 1925.[11,20] This process based on oxidation of aluminum to aluminum oxide and partial dissolution of aluminum component by using a strong base solution. However, the hydrolysis rate of alumina precursor in Raney<sup>®</sup> process is difficult to control. The final outcome is pyrophoric and sensitive to storage conditions.[21,22] These facts encouraged us to apply an ultrasound of high intensity (USHI) for the activation of the Al/Ni alloy, where the output is a catalytic active Al/Ni catalyst, which can be stored and handled under ambient conditions.

Recently[23–28] we have found that ultrasound treatment had dramatic effects on the morphology of aluminum particles. In particular, surface areas of the sonicated colloidal particles could be significantly increased when compared with untreated colloids. Intensive etching and oxidation of aluminum by ultrasound leads to formation of a sponge like metal matrix stabilized by a thin metal oxide layer.[25] These metal sponges could be a perfect support for a heterogeneous catalyst. Based on the known physical and chemical effects of the high-intensity ultrasound outlined in Ref. [23–39] we expect that properties of metals such as resistance to oxidation and melting point could determine their behavior in the ultrasonic field and the final surface morphology, composition and properties of a catalyst. The dramatically different ability of the metals to respond to ultrasound irradiation can be exploited for the formation of nanoscale composites; thus, if alloy particles consisting of resistant and sponge-forming compounds are treated, a microphase separation could be expected under ultrasound irradiation. We tested this idea for the aluminum/nickel (1:1) system and generated an Al/Ni alloy catalyst stabilized by a thin oxide layer. Herein, we present the results of the catalyst characterization of the sonochemically prepared/activated Al/Ni alloy powder and its application for the hydrogenation of acetophenone as a model reaction.

#### 4.3.4 Results and discussion

##### *Catalyst activation and characterization*

The sonochemical nanostructuring of metal alloys is based on microphase separation in an alloy due to different phase response to ultrasonic effects. The initial 1:1 Al/Ni alloy consists of  $\text{Al}_3\text{Ni}_2$  and  $\text{Al}_3\text{Ni}$  intermetallides. Collapse of cavitation bubbles generated by ultrasound is followed by high local ( $\mu\text{m}^2$  area) temperature (up to 5000 K) and a high heating/cooling rate. Thus, ultrasound of high intensity provides unique conditions for metal treatment and should affect the microstructure of an alloy. Moreover, recently it was shown that aluminum could be not just oxidized itself during ultrasonic treatment in aqueous solution, but also could serve as an effective donor of reducing agent ( $\text{H}_2$ ).<sup>[40]</sup> The finding is extremely important for Al/Ni catalysts in situ activation during preparation. The catalyst activation in  $\text{H}_2$  could be expected during the catalyst formation without the total transformation of metallic nickel to oxide. We could expect even reduction process during sonication,<sup>[40]</sup> also in the porous metal matrix. The aluminum/nickel (1:1) alloy powder was treated in a 10 wt.% aqueous suspension with USHI at  $140 \text{ W cm}^{-2}$  from 30 sec to 50 min. The USHI driven interparticle collisions result in continuous breakage of 100  $\mu\text{m}$  initial particles. It was shown that at surfaces several times larger than the resonance cavity size (e.g., at 20 kHz the maximum size of a cavitation bubble is approximately 5  $\mu\text{m}$ ) <sup>[41a]</sup> microjets of liquid can impact the solid surface.<sup>[41b]</sup> Thus, we choose 100  $\mu\text{m}$  initial particles in order to maximize this effect of cavitation. The scanning electron microscopy (SEM) images show that after 50 min of sonication the particles were broken into 10  $\mu\text{m}$  – 20  $\mu\text{m}$  species (Fig. 4-23A–D).

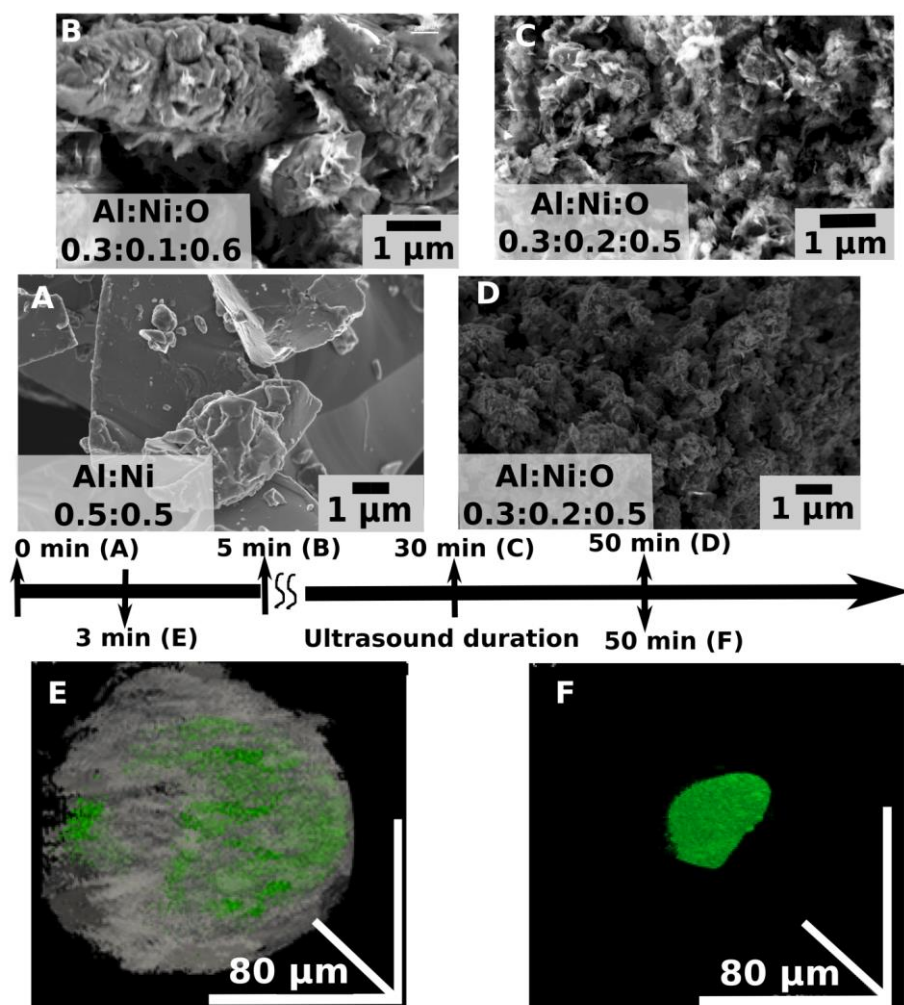


Fig. 4-23 SEM images and the aluminum (Al), nickel (Ni) and oxygen (O) ratio measured by EDS (inserts) of Al/Ni particles: A–initial; B–after 5 min; C–30 min and D–50 min of sonication at  $140 \text{ W cm}^{-2}$ . 3D confocal microscopy reconstruction of the Al/Ni nanostructure loaded with fluorescein: (E) the alloy particle after 3 min (the reconstruction of both transmission and fluorescent mode) and (F) 50 min of sonochemical exposure at  $140 \text{ W cm}^{-2}$ . Reprinted from *Adv. Funct. Mater.* 22, J. Dulle, et al., Sonochemical Activation of Al/Ni Hydrogenation Catalyst, 3128–3135, Copyright (2012), with permission from John Wiley and Sons.

The 3D reconstructions of the transmission and fluorescence images of the confocal scanning fluorescence microscopy (CSFM) of the sonicated Al/Ni particles loaded with the dye demonstrate the formation of porous inner structure. As longer sonication time of the particles as deeper the dye could penetrate into the matrix of the alloy particle (Fig. 4-23E, F). The 50-min-sonicated samples could be completely saturated by the dye. The detailed evaluation of porous structure was made by the Barrett–Joyner–Halenda method (BJH) and the Brunauer–Emmett–Teller method (BET).[42,43] The  $\text{N}_2$  adsorption/desorption isotherm (Fig. 4-24A) can be classified as group IIb if the new classification system proposed by Rouquerol et al. [44,45] is considered. The hysteresis loop corresponds to type H-1, according to IUPAC classification standards.[46] The pore size distribution, evaluated by BJH, proves the formation of mesopores with a pore size of about 4 nm for the Al/Ni alloy (Fig. 4-24B). The highest

surface area according to BET was found to be  $125 \text{ m}^2 \text{ g}^{-1}$  after 50 min of sonication at  $140 \text{ W cm}^{-2}$ . Initial Al/Ni alloy particles show a surface area of  $0.2 \text{ m}^2 \text{ g}^{-1}$  only. We increased by a factor of 625 the surface area for our modified samples. Compared to commercial Raney<sup>®</sup>-Nickel, which has a surface area of  $50 \text{ m}^2 \text{ g}^{-1}$ , [47] the sonochemically formed Al/Ni with a surface area of  $125 \text{ m}^2 \text{ g}^{-1}$  exhibits a clear advantage.

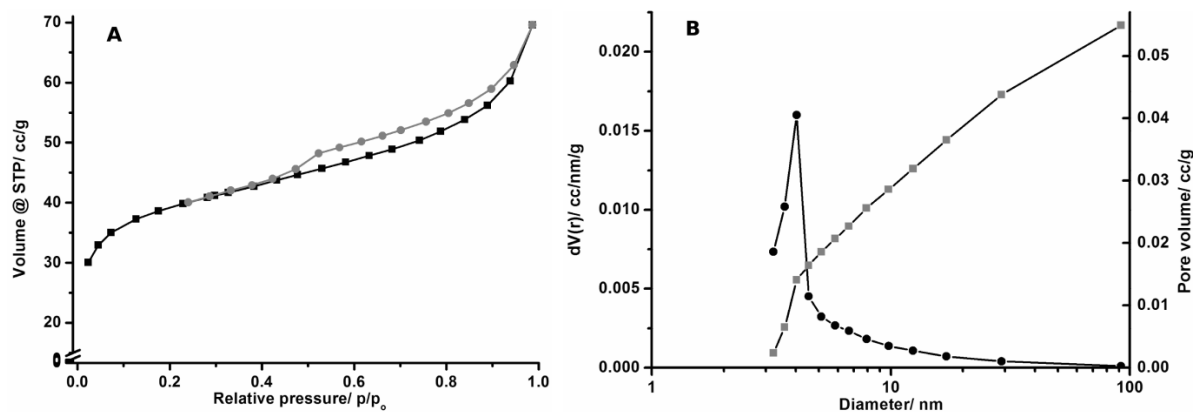


Fig. 4-24 N<sub>2</sub> Adsorption (—■—)–desorption (—●—) isotherms of Al/Ni particles prepared by 50 min of sonication at  $140 \text{ W cm}^{-2}$  (A). BJH pore size distribution (—●—) and pore volume (—■—) of the same particles (B). Reprinted from *Adv. Funct. Mater.* 22, J. Dulle, et al., Sonochemical Activation of Al/Ni Hydrogenation Catalyst, 3128 – 3135, Copyright (2012), with permission from John Wiley and Sons.

In order to estimate the concentration of high-energy kinks and breaks accessible for catalysis, we analyzed the metal surface area of the Al/Ni alloys via pulse titration. For the Al/Ni material we obtained  $1.14 \text{ m}^2 \text{ g}^{-1}$  metal surface of nickel, which gives a surface area per gram of nickel of  $3.78 \text{ m}^2 \text{ g}^{-1}$ .

The oxidation/reduction processes during sonication were monitored by the electron diffraction spectroscopy (EDS) (Fig. 4-23A–D, inserts). We observed increase of oxygen concentration on metal surface which indicates oxidation process and formation of a novel metal oxide layer on the increased surface area of the porous metal matrix. The thickness of the metal oxide sonochemically generated on the surface of the modified metal was previously estimated by field ion microscopy less than 2 nm. [25]

Having in mind that the catalytic properties of a material depend on its inner structure, morphology, and composition, a closer look to the sonochemically induced changes inside Al/Ni particles has been taken. The inductively coupled plasma mass spectrometry (ICP) method showed that the overall Al:Ni ratio in the samples did not change. For the sonicated Al/Ni alloy we determined a Ni content of 49.5% before and after ultrasonic treatment. Thus, treatment does not cause leakage of active metals from the samples.

The precise analysis of the powder X-ray diffraction (PXRD) of the sonicated Al/Ni alloy in comparison to the untreated alloy shows the formation of bayerite ( $\text{Al}(\text{OH})_3$ ) as a main oxidation product of the aluminum (Fig. 4-25A, C). The initial Al/Ni alloy consists mostly of intermetallic  $\text{Al}_3\text{Ni}_2$  with an admixture of  $\text{Al}_3\text{Ni}$ . Upon USHI treatment, bayerite appears as the main oxidation product, while the relative concentration of  $\text{Al}_3\text{Ni}_2$  exhibits the most pronounced decrease (the  $\text{Al}_3\text{Ni}$  phase remains untouched). Nickel metal is not evident in diffraction pattern. Although in an oxide form, nickel would be rather crystalline than amorphous. The absence of the characteristic patterns of NiO might be explained its low concentration in the system also due to its in situ reduction by hydrogen produced in sonogenerated pores. Nickel oxide was not detected probably due to mentioned reduction process and its negligible quantity per surface area. Nickel being amorphous also does not show pronounced peak in PXRD. Thus, beside cavitation induced oxidation process, we can expect the continuous reduction of the nickel particles due to formation of reducing agent (hydrogen).[40] We propose that ultrasound-driven activation of Al/Ni particles results in the formation of a Al/Ni mesoporous matrix stabilized by a thin oxide layer. In situ activated nickel centers by partial reduction of nickel particles are probably distributed in porous matrix. In order to prove this consideration we performed the detailed nuclear magnetic resonance (NMR) and X-ray photo electron spectroscopy (XPS) analysis of the novel material.

Solid state  $^{27}\text{Al}$  NMR experiments proved the presence of metallic and oxidized aluminum species. Due to the quadrupolar interaction the  $^{27}\text{Al}$  NMR resonances are usually broad and structured. Nevertheless, at least five different species can be distinguished. The sharp resonance at 10 ppm (Al1) appears significantly only in the spectrum of the sonicated sample, which can be assigned to aluminum oxide or hydroxide (Fig. 4-25B, D). All other four resonances (Al2-Al5 with  $\sigma_{\text{iso}} \approx 300$  ppm, 470 ppm, 670 ppm, and 980 ppm) are dominated by both the knight shift and the quadrupolar interaction, which demonstrates that they belong to different Al/Ni alloys with a low local symmetry for the Al sites. Details of the relevant refinement parameters are given in the experimental section. The  $^{27}\text{Al}$  MAS NMR spectra show that the metal particles are composed of the same alloy phases before and after the sonication. Although the intensities of the  $^{27}\text{Al}$  resonances might be hampered by different spin-spin relaxation times, the comparison between both data sets reveals that mainly alloy phase Al4 is affected during the sonication process.

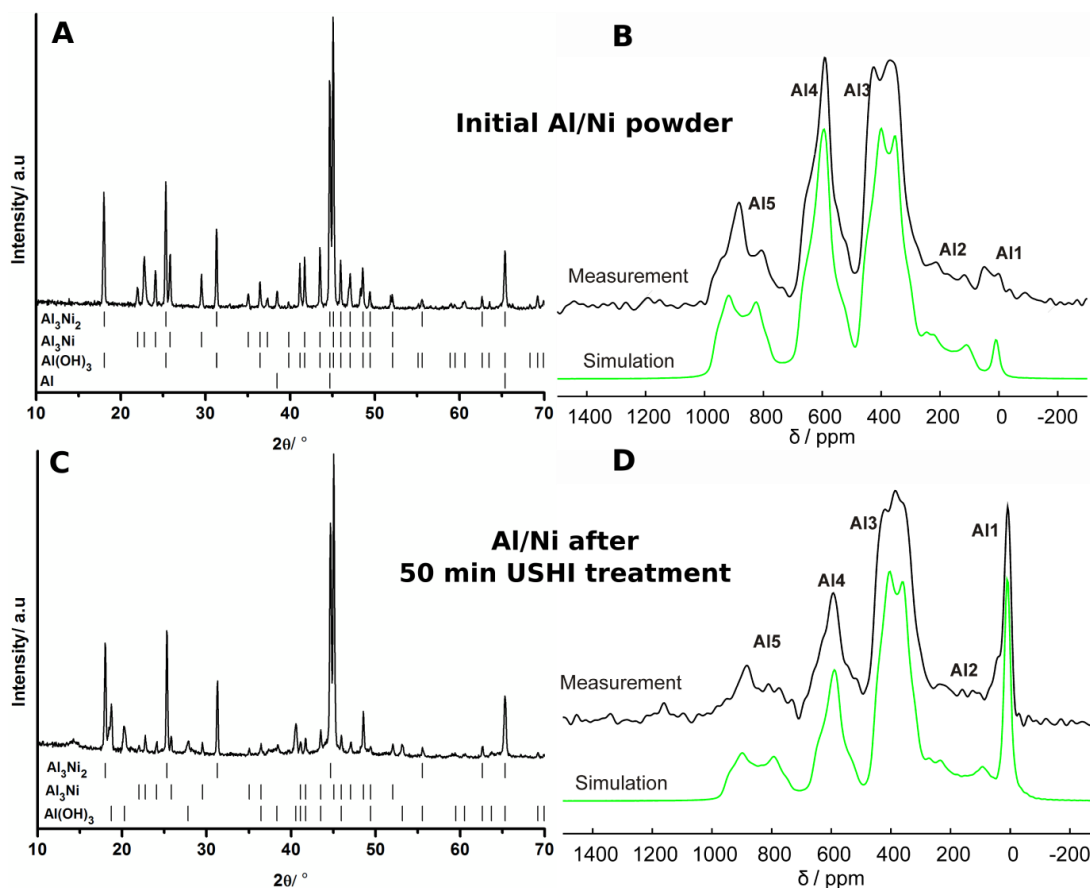


Fig. 4-25 PXR (left) and  $^{27}\text{Al}$  NMR (right) of Al/Ni -alloy particles: initial (A/B) and after 50 min of sonication at  $140\text{ W cm}^{-2}$  (C, D).  $^{27}\text{Al}$  NMR spectra were recorded by using  $[\text{Al}(\text{H}_2\text{O})_6]^{3+}$  as a reference. ( \* ) indicates the spinning sidebands. Reprinted from Adv. Funct. Mater. 22, J. Dulle, et al., Sonochemical Activation of Al/Ni Hydrogenation Catalyst, 3128 – 3135, Copyright (2012), with permission from John Wiley and Sons.

The XPS analysis is demonstrated in Fig. 4-26. The spectra were recorded before and after 50 min of ultrasonic treatment of the particles at  $140\text{ W cm}^{-2}$ . The components at 852.3 (shown in Fig. 4-26B) and 854.0 can be attributed to metallic Ni and NiO.[48,49] Peaks position indicates the partial reduction of Ni during the process. After 5-min-sonication we could observe in the spectra the peaks related to the metal oxides only. However after 50-min-sonication we could distinguish the peaks of metallic nickel in the XPS patterns. The fact of formation of metallic nickel could be explained due to in situ activation of catalyst centers (Ni) during sonication. Aluminum peaks can be attributed to both phases: metallic aluminum and the oxidized aluminum. The peaks of aluminum and nickel oxides indicate partial surface oxidation (see also PXR (Fig. 4-25)) of metals in the alloy. Thus, we can conclude that the sonochemical activation of the Ni/Al catalyst is probable due to generation of  $\text{H}_2$  [40] during partial oxidation of aluminum matrix. A conceptual novelty of the proposed ultrasound assisted Al/Ni activation is redox reactions controllable by sonication parameters and the material itself. The structure optimization for maximum catalytic efficiency can be done by adjustment of time and intensity of sonication and catalyst composition.

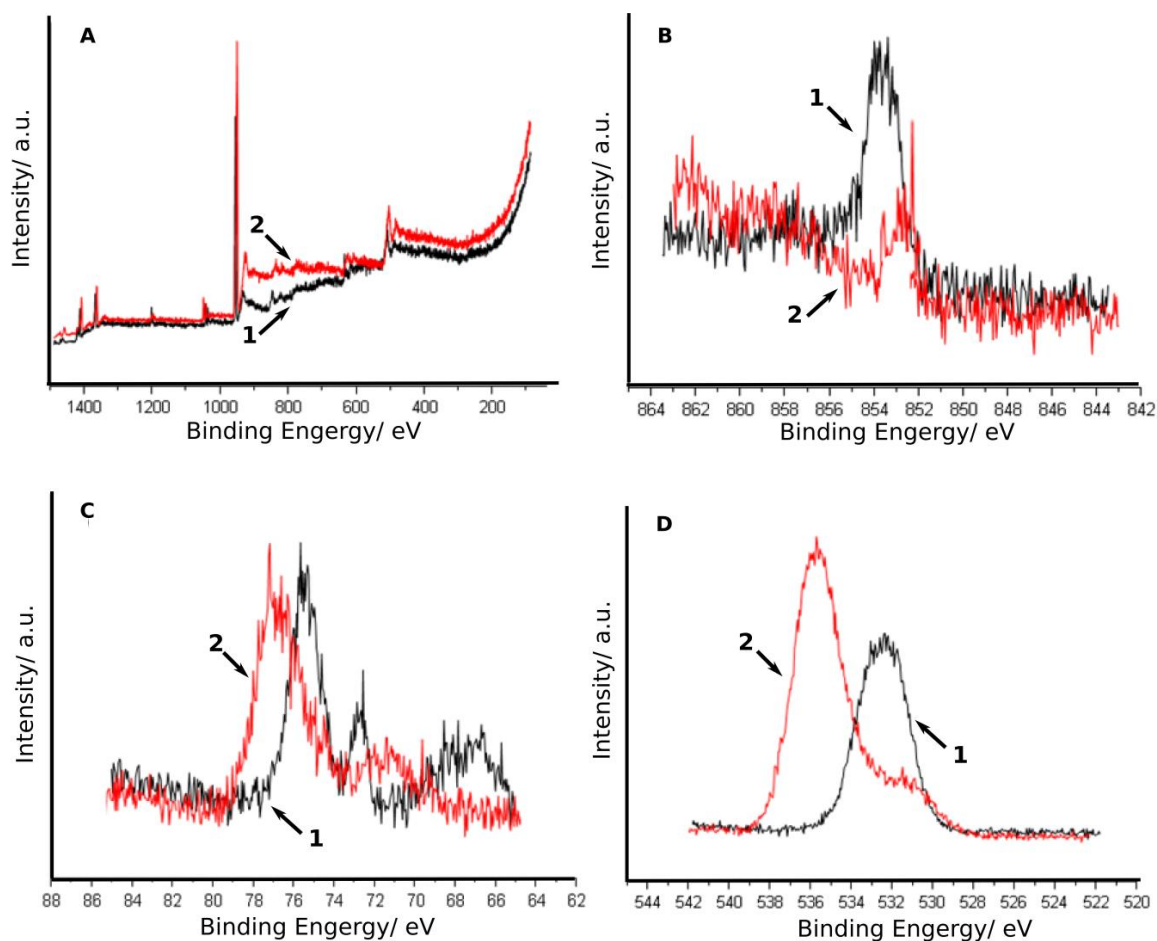


Fig. 4-26 X-ray photoelectron (XPS) spectra of samples before (1) and after 50 min (2) of sonication treatment at  $140 \text{ W cm}^{-2}$  intensity. Survey spectra (A), Ni2p peaks (B), Al2p peaks (C), and O1s peaks (D). Reprinted from *Adv. Funct. Mater.* 22, J. Dulle, et al., Sonochemical Activation of Al/Ni Hydrogenation Catalyst, 3128 – 3135, Copyright (2012), with permission from John Wiley and Sons.

By summarizing the results illustrated in the figures, we see that: (i) at the beginning stages of sonication of the alloy particles the increase of oxide phase could be attributed to partial oxidation of aluminum and nickel and the formation of porous structure with increased surface area; (ii) further sonication results in generation of metallic Ni detected by XPS due to possible reduction process[40] in the porous matrix. Thus, relying on the analytical methods we can assume that the sonochemically activated Al/Ni catalyst composed on unmodified Al/Ni skeleton with surface changed aluminum (oxidized) and catalytic active nickel centers regularly distributed in this matrix. The PXRD and  $^{27}\text{Al}$  MAS NMR experiments could detect the oxidation of Al during sonication. Our previous works[25] on ultrasound treatment of aluminum and nickel particles demonstrate that aluminum exhibits increase of surface area and formation of porous matrix after sonication stabilized by sonogenerated aluminum oxide. Nickel particles are relatively resistant to ultrasound irradiation and slight change in surface

morphology was detected. The SEM images demonstrate formation of a rough metal oxide on the surface of the modified Ni particles. Since the concentration of NiO is very low in the system we could detect it by using XPS only. Formation of a several-nm-thick metal oxide layer plays an important role in structure stabilization without negative effect to its catalytic activity. The importance of formation of metal oxide for the structure stabilization during sonication can be proved by the addition experiments in an inert solvent. It has been suggested that in ionic liquid the oxidation could be avoided. We performed the sonication of Al/Ni alloy in ionic liquid (IL) (1-butyl-3-methylimidazolium chloride), in order to see if the similar mesoporous structure could be formed without metal oxide stabilization. The sonication in ionic liquid did not lead to formation of porous structure. There were no other crystalline phases detected. Thus, the surface oxidation has a crucial role in stabilization of the modified metal matrix and formation of porous structure. Furthermore, the sonogenerated oxide layer provides excellent stability of the catalyst during its exploitation. The sonicated Al/Ni can be stored and used at ambient conditions in comparison to Raney<sup>®</sup>-Nickel that is pyrophoric and requires special storage conditions.[21,22]

Thus, sonochemical modification of metal particles schematically illustrated in Fig. 4-27 has the following effects generated by acoustic cavitation: sonochemical one - surface redox reactions by sonogenerated free radicals (A) and sonomechanical one - interparticle collisions (B). USHI induces particle breakage and increase of surface area of the material. Simultaneously depassivation of metal surface occurs due to cavitation stimulated breakage of initial oxide layer. Then the increased metal surface is stabilized by sonogenerated oxide layer. The generation of hydrogen during sonochemical oxidation of aluminum matrix plays an important role in catalyst activation. By adjustment of the sonication process we can avoid the complete material oxidation and achieve the particle reduction of nickel particles.

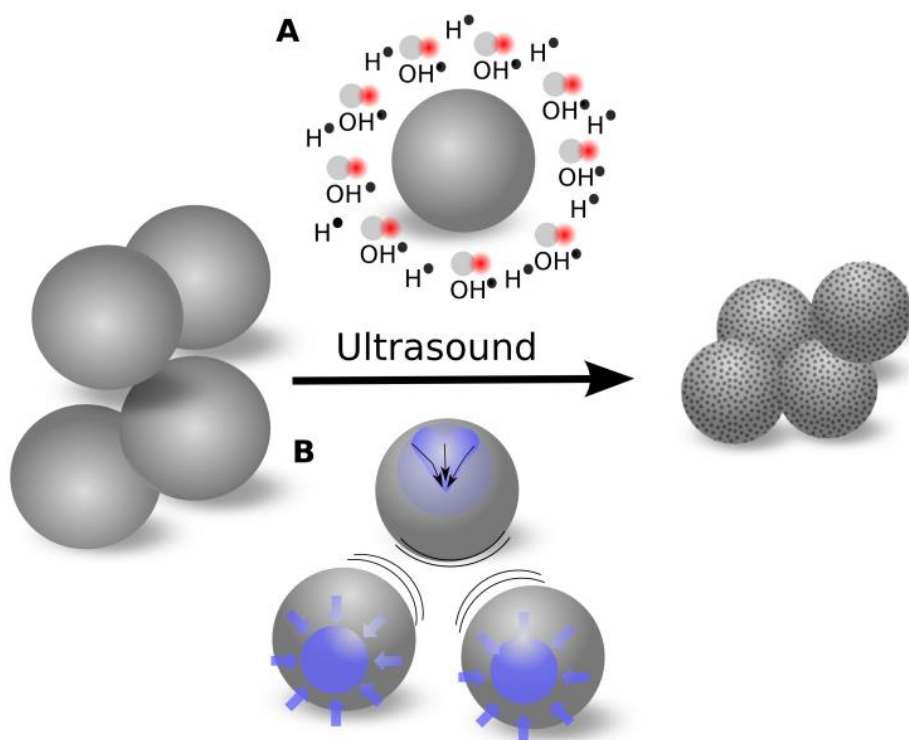


Fig. 4-27 Sonochemical modification of metal particles: (I) initial particles; (II) chemical aspect surface oxidation (A) and physical aspects (B) interparticle collisions; (III) formation of mesoporous metals. Reprinted from *Adv. Funct. Mater.* 22, J. Dulle, et al., Sonochemical Activation of Al/Ni Hydrogenation Catalyst, 3128 – 3135, Copyright (2012), with permission from John Wiley and Sons.

### **Catalytic Performance**

The central motivation for the investigation described here is the influence of an ultrasonic treatment on morphology, texture, and performance of a composite material. In this paper, we tested the catalyst for the model reaction of hydrogenation of acetophenone (Fig. 4-28). As a material of interest, Al/Ni alloy powder sonicated for 50 min with maximum surface area of  $125 \text{ m}^2 \text{ g}^{-1}$  was chosen. This material has previously shown its potential as catalyst.[24]

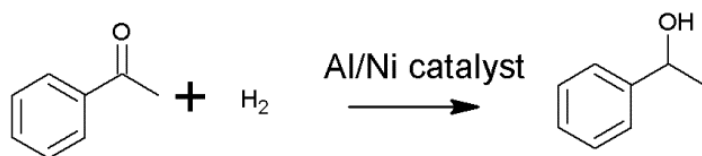


Fig. 4-28 Hydrogenation of acetophenone. Reprinted from *Adv. Funct. Mater.* 22, J. Dulle, et al., Sonochemical Activation of Al/Ni Hydrogenation Catalyst, 3128 – 3135, Copyright (2012), with permission from John Wiley and Sons.

The initial Al/Ni alloy particles show no catalytic activity in the hydrogenation of acetophenone under 60 bar  $\text{H}_2$  -pressure and stirring at room temperature (RT) and water as a solvent. No or poor catalytic activity for commercially available and untreated Al/Ni alloys have also been reported.[50,51] On a contrary the sonochemically activated Al/Ni material demonstrates catalytic activity. It is important,

that there were no side products observed during the hydrogenation of acetophenone under the used condition (RT, 60 bar of H<sub>2</sub>). The catalytic experiments are summarized in Table 4-2.

Table 4-1 Conversion of acetophenone in dependence of H<sub>2</sub>-pressure, amount of catalyst, as well as amount of substrate for a reaction time of 24 h at RT, stirring, and 1 mL water as a solvent.

Entry	Catalyst [mg]	Acetophenone [ $\mu$ L]	H <sub>2</sub> -pressure (bar)	Conversion of acetophenone [%]
1	25	300	60	36
	50	300	60	> 99.9
3	50	300	5	34
4	50	300	20	79
5	50	300	40	> 99.9
6	50	500	60	> 99.9
7	50	700	60	> 99.9
8	50	900	60	> 99.9
9	50	1100	60	> 99.9

The conversion of acetophenone to 1-phenylethanol was measured after 24 hours of reaction by gas chromatography (GC). The optimal conversion (> 99.9%) of acetophenone was observed when 50 mg of catalyst were used (Table 4-2, Entry 1-2). The pressure of the hydrogen applied during the catalytic reaction has its crucial influence on the conversion of acetophenone to 1-phenylethanol (Table 4-2, Entry 2-5). To avoid diffusion limitation we have chosen a pressure of 60 bar as the standard condition. It was observed that the yield of 1-phenylethanol decreases when the pressure is reduced. The maximum yield of 1-phenylethanol was observed at a hydrogen pressure of 40 bar, 5 bar hydrogen pressure gave a yield of 34%.

Using the optimal conditions of 50 mg of Al/Ni catalyst and a hydrogen pressure of 60 bar the conversion was studied based on the reaction time. Therefore, several catalytic runs were performed and stopped after a specific period of time. The complete consumption of the applied acetophenone was observed after the reaction time of 4 hours.

In addition the Al/Ni catalyst was tested under standard conditions (RT, 60 bar H<sub>2</sub>, water as the solvent, 50 mg Al/Ni catalyst, stirring, 24 h reaction time) with higher amounts of acetophenone, namely 300

mL up to 1.1 mL (9.57 mmol). One could see that performance of the catalyst has not changed (Table 4-2, Entry 2 and 6-9).

To investigate the catalyst reusability, we performed catalytic reactions under the conditions described above and the reaction time of 6 hours (Fig. 4-29). It was found that under these conditions the catalyst produces > 99.9% 1-phenylethanol within the first five runs. After 5 runs the yield slightly decreased upon reuse, but still remained effective after 8 runs. The consumption of the acetophenone is gone down to 78% after 8 runs.

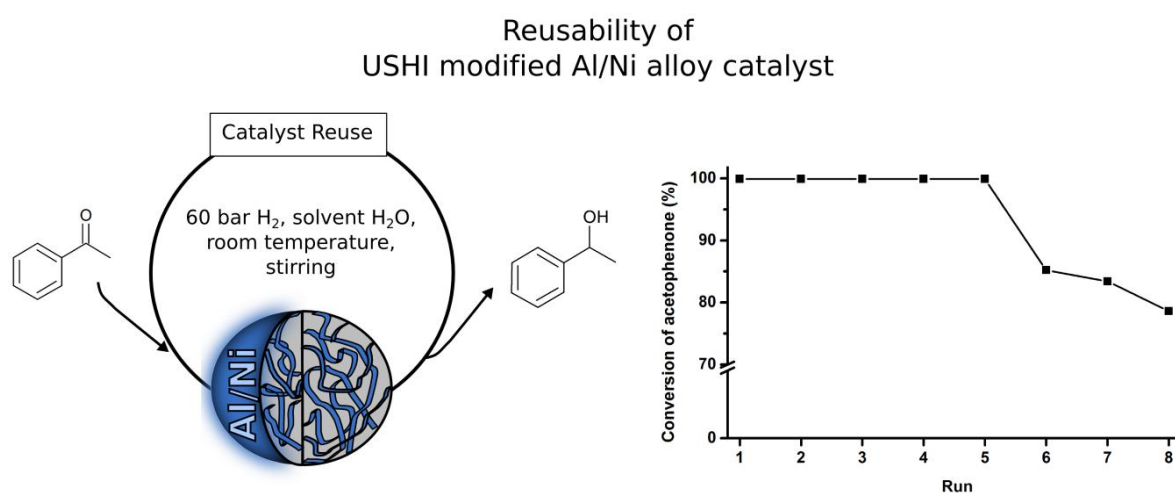


Fig. 4-29 Reusability of Al/Ni catalyst under standard condition, namely 50 mg of USHI modified Al/Ni catalyst, 1 mL water as a solvent, reaction time 6 h at room temperature under 60 bar H<sub>2</sub> and stirring. Reprinted from *Adv. Funct. Mater.* 22, J. Dulle, et al., Sonochemical Activation of Al/Ni Hydrogenation Catalyst, 3128 – 3135, Copyright (2012), with permission from John Wiley and Sons.

The unique morphology of our sonoactivated Al/Ni system (presence of metallic Ni and sonogenerated metal oxides) provides easy and efficient catalytic performance of the material. First of all the catalyst does not require preactivation stage before use. If the catalyst was preactivated for 24 h in a hydrogen atmosphere (solid catalyst material) no increase in catalytic activity was observed. Then, the sonoactivated Al/Ni can be a good alternative to the commercial Raney<sup>®</sup>-Nickel. The activity of sonochemically activated Al/Ni was compared with the commercial Raney<sup>®</sup>-Nickel catalyst. Similar activities were observed, conversion of acetophenone to 1-phenylethanol (60 bar H<sub>2</sub> pressure) at room temperature, for our best catalyst and commercial Raney<sup>®</sup>-Nickel catalyst.

#### 4.3.5 Conclusion

The sonochemical activation of Al/Ni particles results in nanostructuring of initial Al/Ni alloy and formation of an effective catalyst for the hydrogenation of acetophenone. The novel formation/activation method is based on the cavitation induced mechanochemical particle breakage and metal depassivation (breakage of initial oxide layer). The structure stabilization is achieved by

sonochemical formation of surface metal oxide layer. The self-regulated nickel reduction process (also in porous matrix of the catalyst) is responsible for formation of active centers of the catalysts. Thus, upon sonochemical activation the alloy species adopt a number of features attractive for catalytic applications: high surface area (up to  $125 \text{ m}^2 \text{ g}^{-1}$ ) and narrow pore size ( $\sim 4 \text{ nm}$ ) distribution, presence of metallic nickel. In addition, the easy storage and handling of the metal based stabilized by thin oxide layer Al/Ni catalyst is an advantage of our system. The ability to reuse the catalyst with little or no decrease of product yield makes the procedure of ultrasound activation for catalyst formation an attractive alternative to other preparation methods. Thus, the sonochemically activated Al/Ni alloy could become a great alternative to known Raney<sup>®</sup>-Nickel[20] and other heterogeneous hydrogenation catalysts. The findings presented here provide guidelines for the extension of the concept towards a broad variety of systems.

#### **4.3.6 Experimental**

##### ***Materials***

Aluminum-nickel alloy powder (Fluka) (composition: 50 wt.% Aluminum and 50 wt.% Nickel) was used with a particle size ca.  $100 \mu\text{m}$  as received. The water was purified before use in a three stage Millipore Milli-Q Plus 185 purification system and had a resistivity higher than  $18.2 \text{ M}\Omega \text{ cm}^{-1}$ .

##### ***Preparation of Al/Ni catalyst***

5 g of the commercial Al/Ni alloy were dispersed in purified water (50 mL) and sonicated up to 50 min with an ultrasound tip (VIP1000hd, Hielscher Ultrasonics GmbH, Germany) operated at 20 kHz with a maximum output power of 1000 W ultrasonic horn BS2d22 (head area of  $3.8 \text{ cm}^2$ ) and equipped with a booster B2-1.8. The maximum intensity was calculated to be  $140 \text{ W cm}^{-2}$  at mechanical amplitude of  $106 \mu\text{m}$ . To avoid the temperature increase during sonication the experiment was performed in a thermostatic cell. After the USHI treatment, the sample was dried under vacuum with a heat gun.

##### ***Scanning electron microscopy***

Scanning electron microscopy (LEO 1530 FE-SEM, Zeiss) was applied to characterize the optical response, structure, and size of the nanoparticles.

##### ***Powder X-ray diffraction***

Powder X-ray diffraction diagrams were collected at  $\Theta$ - $\Theta$  mode using a Stoe STADI P X-ray Transmission diffractometer: Cu  $\text{K}\alpha_1$  irradiation, room temperature,  $2*\Theta = 5^\circ - 90^\circ$ .

## **<sup>27</sup>Al MAS NMR**

The <sup>27</sup>Al MAS NMR spectra were recorded at room temperature with a Bruker Avance II 300 FT NMR spectrometer operating at 78.2 MHz for <sup>27</sup>Al. The samples were loaded into 2.5 mm ZrO<sub>2</sub> rotors and mounted in a commercial triple resonance MAS probe (Bruker). All spectra were collected using proton broadband decoupling with a spinal64 sequence and a nutation frequency of 70 kHz. The recycle delay and spinning speed were adjusted to 1 s and 30 kHz. To eliminate not desirable signals from the probe we applied a rotor-synchronized Hahn echo sequence with a 16 step phase cycle and a nutation frequency of 50 kHz. The first and second pulse of the echo was set to 1 μs and 2 μs, respectively, to ensure that the signal intensity becomes independent from the magnitude of the quadrupolar coupling. The chemical shift of the <sup>27</sup>Al resonance is given with respect to [Al(H<sub>2</sub>O)<sub>6</sub>]<sup>3+</sup>. The simulations of the MAS spectra were carried out with the program package SIMPSON.[52]

Table 4-2 NMR1. Refinement parameters for the <sup>27</sup>Al MAS spectra (Fig. 4-25B, D) of the Al/Ni alloy powder before and after 50 min of sonication. Reprinted from Adv. Funct. Mater. 22, J. Dulle, et al., Sonochemical Activation of Al/Ni Hydrogenation Catalyst, 3128 – 3135, Copyright (2012), with permission from John Wiley and Sons.

<b><sup>27</sup>Al Resonance</b>	<b>Parameter</b>	<b>0 min sonification</b>	<b>50 min sonification</b>
Al1	σ <sub>iso</sub> / ppm	10(2)	10(2)
	Δ <sub>aniso</sub> / MHz	--	--
	η	--	--
	Rel. Int / %	1(1)	11(2)
Al2	σ <sub>iso</sub> / ppm	280(10)	310(10)
	Δ <sub>aniso</sub> / MHz	1.6(2)	1.8(2)
	η	0.20(5)	0.20(5)
	Rel. Int / %	7(2)	10(2)
Al3	σ <sub>iso</sub> / ppm	475(5)	465(5)
	Δ <sub>aniso</sub> / MHz	1.4(2)	1.3(2)
	η	0.50(5)	0.45(5)
	Rel. Int / %	44(2)	46(2)
Al4	σ <sub>iso</sub> / ppm	680(5)	660(5)
	Δ <sub>aniso</sub> / MHz	1.2(2)	1.1(2)
	η	0.80(5)	0.80(5)
	Rel. Int / %	31(2)	18(2)
Al5	σ <sub>iso</sub> / ppm	990(5)	980(5)
	Δ <sub>aniso</sub> / MHz	1.6(2)	1.7(2)
	η	0.30(5)	0.30(5)
	Rel. Int / %	17(1)	14(2)

### ***Surface area and pore size distribution***

Surface area and pore size distribution based on physisorption (adsorption and desorption of gases) were measured by the BET (Brunauer–Emmett–Teller)[43] and BJH (Barrett–Joyner–Halenda)[42] method using N<sub>2</sub> at 77 K on a vacuum gas sorption NOVA 2000e (Quantachrome). The samples were dried under vacuum for 24 h at 300 °C.

### ***Pulse titration analysis***

Pulse Titration Analysis was performed by CHEMBET Pulsar TPD/TPR (Quantachrome) with hydrogen as the titration gas at a temperature of 300 K. Five hydrogen impulses were applied with a flow rate of 75 cm<sup>3</sup> min<sup>-1</sup> at an ambient pressure of 760.00 mmHg.

### ***Inductively coupled plasma***

Inductively Coupled Plasma by Perkin Elmer, Plasma 400 with Argon Plasma determined the nickel content.

### ***X-ray photoelectron spectroscopy***

XPS spectra were acquired with a SPECS hemispherical energy analyzer (Phoibus 100) and SPECS focus 500 X-ray monochromator using the Al K<sub>α</sub> (with energy of 1486.74 eV).

### ***Confocal scanning fluorescence microscopy***

A Leica TCS SP confocal laser scanning microscope (Leica, Germany) with a 100× oil immersion objective, numerical aperture 1.4 was used. The particles were loaded with a water-soluble fluorescent dye, Fluorescein. The pores of the particles were closed by the procedure suggested in [53–56].

### ***Catalytic application of the modified Al/Ni material***

The hydrogenation of ketones was studied as described in Ref. [58,59]. The hydrogenation experiments were carried out using a Parr Instrument stainless steel autoclave N-MT5 300 mL equipped with heating mantle and temperature controller. Gas chromatography analyses were performed on an Agilent 6890 N Network GC System using a Lipodex E column (25 m × 0.25 mm; Machery & Nagel). We placed 0.05 g of the catalyst and 1 mL water in a glass vial. Additionally acetophenone (300 μL, 0.31 g, 2.57 mmol) was transferred via sealed Fortuna-Pipette. The filled vial was put into the autoclave. Subsequently, the autoclave was purged three times with hydrogen. The reduction was carried out at room temperature under vigorous stirring by using a continuous pressure of 60 bar of hydrogen. The experiment was stopped after the hydrogen gas was released. The reaction mixture was worked up by the addition of dodecane (584 μL, 0.44 g, 2.57 mmol) as internal standard and 2.5 mL diethyl ether. The product was extracted from the organic layer. The catalytic reactions were all carried out twice and several runs were analyzed.

## ***Reusability***

For testing the reusability of the catalyst, the reaction mixture was extracted 5 times with 2.5 mL of ether and afterwards treated in a standard ultrasound bath for 5 min. To remove the ether, the mixture was heated in 90 °C water bath for 10 minutes. After that, the Al/Ni catalyst was used again for the hydrogenation under standard conditions.

### **4.3.7 Acknowledgment**

This work was supported by SFB840. We are grateful to Bernd Putz (Bayreuth University) for carrying out the PXRD as well as to Lena Geiling (Bayreuth University) for BET measurements. E. V. S. thanks to Alexander von Humboldt Foundation.

## **References**

- [1] R. Karmhag, T. Tesfamichael, E. Wackelgard, A. Niklasson, M. Nygren, *Sol. Energy* 2000, 68, 329.
- [2] T. Hyeon, *Chem. Commun.* 2003, 927.
- [3] K. Kim, S. C. Jeoung, J. Lee, T. Hyeon, J. I. Jin, *Macromol. Symp.* 2003, 201, 119.
- [4] I. S. Lee, N. Lee, J. Park, B. H. Kim, Y. W. Yi, T. Kim, T. K. Kim, I. H. Lee, S. R. Paik, T. Hyeon, *J. Am. Chem. Soc.* 2006, 128, 10658.
- [5] W. J. Tseng, C. N. Chen, *J. Mater. Sci.*, 2006, 41, 1213.
- [6] A. Houdayer, R. Schneider, D. Billaud, J. Ghanbaja, J. Lambert, *Synthetic Met.* 2005, 151, 165.
- [7] A. Saxena, A. Kumar, S. Mozumdar, *Appl. Catal. A-Gen.* 2007, 317, 210.
- [8] J. Banhart, *Prog. Mater. Sci.* 2001, 46, 559.
- [9] J. Erlebacher, M. J. Aziz, A. Karma, N. Dimitrov, K. Sieradzki, *Nature* 2001, 410, 450.
- [10] Y. Ding, J. Erlebacher, *J. Am. Chem. Soc.* 2003, 125, 7772.
- [11] M. Raney, USA Patent, US1563587, 1925.
- [12] H. M. Luo, L. Sun, Y. F. Lu, Y. S. Yan, *Langmuir* 2004, 20, 10218.
- [13] Y. Yamauchi, T. Momma, T. Yokoshima, K. Kuroda, T. Osaka, *J. Mater. Chem.* 2005, 15, 1987.
- [14] A. Devasenapathi, H. W. Ng, C. M. S. Yu, S. W. Lim, *J. Mater. Sci.* 2005, 40, 5463.
- [15] G. S. Attard, P. N. Bartlett, N. R. B. Coleman, J. M. Elliott, J. R. Owen, J. H. Wang, *Science* 1997, 278, 838.
- [16] O. D. Velev, P. M. Tessier, A. M. Lenhoff, E. W. Kaler, *Nature* 1999, 401, 548.
- [17] H. Maeda, Y. Kusunose, M. Terasaki, Y. Ito, C. Fujimoto, R. Fujii, T. Nakanishi, *Chem-Asian J* 2007, 2, 350.
- [18] H. Masuda, K. Fukuda, *Science* 1995, 268, 1466.
- [19] H. J. Shin, C. H. Ko, R. Ryoo, *J. Mater. Chem.* 2001, 11, 260.
- [20] M. Raney, *Ind. Eng. Chem.* 1940, 32, 1199.
- [21] J. Masson, P. Cividino, J. Court, *Appl. Catal. A-Gen.* 1997, 161, 191.

- [22] P. Mars, T. V. D. Mond, J. J. Scholten, *Ind. Eng. Chem. Prod. Rd.* 1962, 1, 161.
- [23] E. V. Skorb, D. G. Shchukin, H. Möhwald, D. V. Andreeva, *Nanoscale* 2010, 2, 722.
- [24] E. V. Skorb, H. Möhwald, T. Irrgang, A. Fery, D. V. Andreeva, *Chem. Commun.* 2010, 46, 7897.
- [25] E. V. Skorb, D. Fix, D. G. Shchukin, H. Möhwald, D. V. Sviridov, R. Mousa, N. Wanderka, J. Schäferhans, N. Pazos-Pérez, A. Fery, D. V. Andreeva, *Nanoscale* 2011, 3, 985.
- [26] J. Schäferhans, S. Gomez-Quero, D. V. Andreeva, G. Rothenberg, *Chem.-Eur. J.* 2011, 17, 12254.
- [27] N. Pazos-Peréz, J. Schäferhans, E. V. Skorb, A. Fery, D. V. Andreeva, *Micropor. Mesopor. Mat.* 2012, 154, 164.
- [28] N. Pazos-Peréz, T. Borke, D. V. Andreeva, R. A. Alvarez-Puebla, *Nanoscale* 2011, 3, 3265.
- [29] J. P. Lorimer, T. J. Mason, *Chem. Soc. Rev.* 1987, 16, 239.
- [30] K. S. Suslick, G. J. Price, *Annu. Rev. Mater. Sci.* 1999, 29, 295.
- [31] T. Prozorov, R. Prozorov, K. S. Suslick, *J. Am. Chem. Soc.* 2004, 126, 13890.
- [32] J. H. Bang, K. S. Suslick, *Adv. Mater.* 2010, 22, 1039.
- [33] G. Cravotto, P. Cintas, *Angew. Chem. Int. Edit.* 2007, 46, 5476.
- [34] J. Lindley, T. J. Mason, *Chem. Soc. Rev.* 1987, 16, 275.
- [35] K. S. Suslick, S. J. Doktycz, E. B. Flint, *Ultrasonics* 1990, 28, 280.
- [36] S. J. Doktycz, K. S. Suslick, *Science* 1990, 247, 1067.
- [37] J.-L. Luche, *Ultrason. Sonochem.* 1994, 1, S111.
- [38] D. V. Andreeva, D. V. Sviridov, A. Masic, H. Möhwald, E. V. Skorb, *Small* 2012, 6, 1679.
- [39] J. Gensel, T. Borke, N. Pazos-Peréz, A. Fery, D. V. Andreeva, E. Betthausen, A. Müller, H. Möhwald, E. V. Skorb, *Adv. Mater.* 2012, 24, 985.
- [40] E. V. Skorb, D. V. Andreeva, H. Möhwald, *Angew. Chem. Int. Ed.* 2012, 51, 5138–5142.
- [41] a) N. A. Tsochatzidis, P. Guiraud, A. M. Wilhelm, H. Delmas, *Chem. Eng Sci.* 2001, 56, 1831; b) G. I. Kuvshinov, N. V. Dezhkunov, V. I. Kuvshinov, P. P. Prokhorenko, *Inzh.-Fiz. Zh.* 1980, 39, 866.
- [42] E. P. Barrett, L. G. Joyner, P. P. Halenda, *J. Am. Chem. Soc.* 1951, 73, 373.
- [43] L. Brunauer, S. Deming, W. E. Deming, E. Teller, *J. Am. Chem. Soc.* 1940, 62, 1723.
- [44] K. S. W. Sing, D. H. Everett, R. A. W. Haul, L. Moscou, R. A. Pierotti, J. Rouquerol, T. Siemieniewska, *Pure Appl. Chem.* 1985, 57, 603.
- [45] F. Rouquerol, J. Rouquerol, K. S. W. Sing, Academic Press, London 1999, 467.
- [46] S. J. Gregg, K. S. W. Sing, Academic Press, London 1982, 303.
- [47] B. Zeifert, J. S. Blasquez, J. G. C. Moreno, H. A. Calderon, *Rev. Adv. Mater. Sci.* 2008, 18, 633.
- [48] S. R. Kirumakki, B. G. Shpeizer, G. V. Sagar, K. V. R. Chary, A. Clearfi eld, *J. Catal.* 2006, 242, 319.
- [49] J. Jun, M. Dhayal, J. H. Shin, Y. H. Han, N. Getoff, *Appl. Surf. Sci.* 2008, 254, 4557.
- [50] J. Petro, L. Hegedus, I. E. Sajo, *Appl. Catal. A-Gen.* 2006, 308, 50.
- [51] F. Alonso, P. Riente, J. A. Sirvent, M. Yus, *Appl. Catal. A-Gen.* 2010, 378, 42.

- [52] M. Bak, J. T. Rasmussen, N. C. Nielsen, *J. Magn. Reson.* 2000, 147, 296.
- [53] R. B. Grubbs, *J. Polym. Sci., Part A: Polym. Chem.* 2005, 43, 4323.
- [54] E. V. Skorb, D. Fix, D. V. Andreeva, H. Möhwald, D. G. Shchukin, *Adv. Funct. Mater.* 2009, 19, 2373.
- [55] E. V. Skorb, D. V. Sviridov, H. Möhwald, D. G. Shchukin, *Chem. Commun.* 2009, 6041.
- [56] E. V. Skorb, A. G. Skirtach, D. V. Sviridov, D. G. Shchukin, H. Möhwald, *ACS Nano* 2009, 3, 1753.
- [57] E. V. Skorb, D. G. Shchukin, H. Möhwald, D. V. Sviridov, *J. Mater. Chem.* 2009, 19, 4931.
- [58] Y. Mei, G. Sharma, Y. Lu, M. Ballauff, M. Drechsler, T. Irrgang, R. Kempe, *Langmuir* 2005, 21, 1 2229.
- [59] G. Sharma, Y. Mei, Y. Lu, M. Ballauff, T. Irrgang, S. Proch, R. Kempe, *J. Catal.* 2007, 246, 10.

## 4.4 Novel and Effective Copper - Aluminum Propane Dehydrogenation Catalysts

Jana Schäferhans, Santiago Gómez-Quero, Daria V. Andreeva,\* and Gadi Rothenberg\*

This work is published in Chemistry – An European Journal 2012, 17, 12254 – 12256

Keywords: heterogeneous catalysis, nanostructures, olefins, propylene, sonochemistry

This article is reprinted from Chem. Eur. J., 17, J. Schäferhans, et al., Novel and Effective Copper - Aluminum Propane Dehydrogenation Catalysts, 12254 – 12256, Copyright (2012), with permission from John Wiley and Sons.

### 4.4.1 Contribution to the joint publication

I prepared the alloys, treated them with ultrasound, and evaluated and analyzed the material characterization. Daria Andreeva had the supervision for the material preparation. I tested the porous Al/Cu for the dehydrogenation of propane under the supervision of Santiago Gómez-Quero and Gadi Rothenberg at the University of Amsterdam. I wrote the manuscript. Gadi Rothenberg, Santiago Gómez-Quero, and Daria Andreeva corrected the manuscript.

### 4.4.2 Abstract

No platinum needed! A Cu–Al bimetallic oxide “sponge” is reported that outperforms conventional noble metal catalysts in propane dehydrogenation. This catalyst gives higher conversions even when the temperature is 200 °C lower than the optimal temperature for the benchmark Pt–Sn/Al<sub>2</sub>O<sub>3</sub> catalyst.

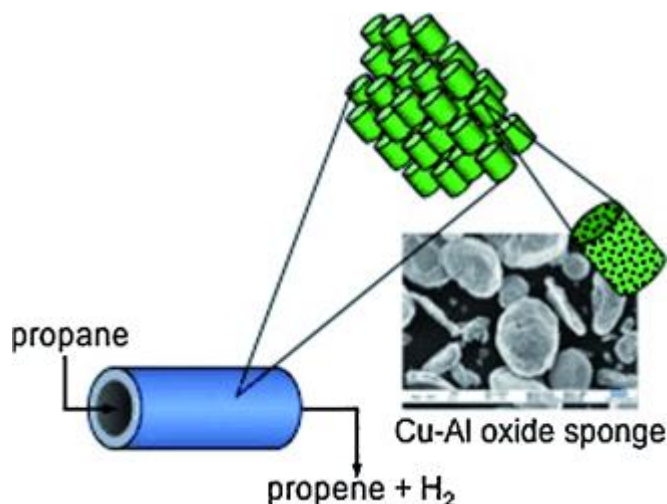


Fig. 4-30 Graphical abstract. Reprinted from Chem. Eur. J., 17, J. Schäferhans, et al., Novel and Effective Copper - Aluminum Propane Dehydrogenation Catalysts, 12254 – 12256, Copyright (2012), with permission from John Wiley and Sons.

### 4.4.3 Introduction

The importance of solid catalysts for converting petro and bulk chemicals is reflected in the sheer magnitude of their market size: catalysts' sales topped nine billion dollars in 2009.[1] This large value mirrors also the increasing academic interest in heterogeneous catalysis research.[2–4] As far as bulk chemicals (such as ethene, propene, and their derivatives) are concerned, there is a strong demand for clean and inexpensive catalysts and synthesis processes.[5,6] There are two types of commonly used dehydrogenation catalysts: supported Cr oxides[7] and Pt based[8] systems. The problem is that these catalysts are typically either rare and costly, or hazardous. Moreover, they perform well only at high temperatures[9] (typically at 500 °C – 600 °C) due to thermodynamic limitations.[10] Optimization studies have led to the inclusion of several promoters of which tin, especially in the combination with platinum as Pt–Sn/ Al<sub>2</sub>O<sub>3</sub> is one of the most popular.

We report here the discovery of a new alternative catalyst for propane dehydrogenation which does not contain noble or hazardous metals. It is an oxidized porous Cu–Al alloy with a structure that is similar to Raney®-type metals.[11] The Raney® process, patented by Murray Raney in 1925 and commercialized by W.R. Grace & Co.,[12] is one of the most successful routes for making porous metals. The problem is that this process requires extreme conditions that often restrict the final outcome at the nanometric scale. Here we opted for a different approach, applying a modified version of the ultrasound pore formation method that we have recently reported: high-power ultrasound.[13–17]

### 4.4.4 Results and discussion

In a typical synthesis, Cu and Al beads are melted by using an electric arc. The resulting cake is then pulverized and sonicated in water. This gives a highly porous material containing pores predominantly at the micro-scale (see Fig. 4-31a, b for a representative example; catalyst D).[11] Fig. 4-31c, d shows transmission and scanning electron micrographs of such a catalyst. We hypothesize that the sonication creates pores in the Al component followed by surface oxidation (compare the XRD profiles (a) and (b) in Fig. 4-32), whereas Cu supplies the active centers for the catalysis (*vide infra*). The thickness of the ultra-thin oxide layer was estimated by using 3D field ion microscopy as less than 2.0 nm.[13]

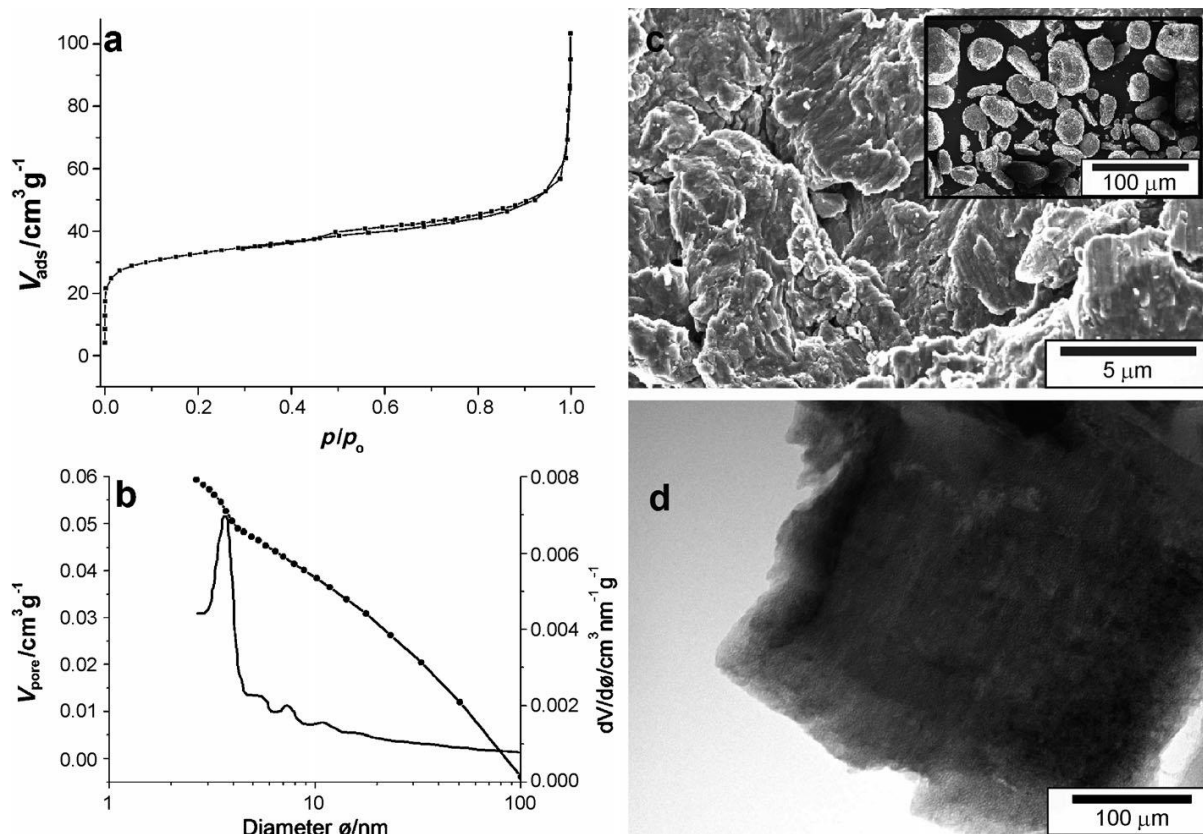


Fig. 4-31 Porous Al-Cu alloy D N<sub>2</sub> adsorption/desorption isotherms (a), pore size distributions (b), scanning electron micrographs (c) and transmission electron micrograph (d). Reprinted from Chem. Eur. J., 17, J. Schäferhans, et al., Novel and Effective Copper - Aluminum Propane Dehydrogenation Catalysts, 12254 – 12256, Copyright (2012), with permission from John Wiley and Sons.

We prepared a series of catalysts with different Cu content (Table 4-3, entries 1–4), and found that using 25 wt.% Cu (catalyst D) gave the most promising results. This catalyst was then activated under different conditions in an effort to optimize the preparation recipe (see entries 4–6). We see a reflecting some initial sintering and coke deposition (see Fig. 4-33).[10,19] After this short deactivation period, the catalyst maintains its steady-state activity (all values hereafter refer to the steady-state period). Our catalyst gave reasonable propane consumption rates already at 550 °C (see Table 4-3). Note that all the reactions gave very good reproducibility ( $\pm 7\%$  for different samples from the same catalyst batch).

Table 4-3 Composition, surface area and initial dehydrogenation rate for Al–Cu catalysts A–D. Reprinted from Chem. Eur. J., 17, J. Schäferhans, et al., Novel and Effective Copper - Aluminum Propane Dehydrogenation Catalysts, 12254 – 12256, Copyright (2012), with permission from John Wiley and Sons.

Entry	Catalyst	Cu (wt.%)	BET (m <sup>2</sup> g <sup>-1</sup> )	Initial rate (mol <sub>propane</sub> h <sup>-1</sup> g <sup>-1</sup> )	Activation atmosphere
1 <sup>a</sup>	A	5	48	1.35	O <sub>2</sub>
2 <sup>a</sup>	B	10	45	1.73	O <sub>2</sub>
3	C	15	42	0.20	O <sub>2</sub>
4	D	25	34	0.79	O <sub>2</sub>
5	D	25	34	0.54	H <sub>2</sub>
6	D	25	34	0.01	Ar
7 <sup>b</sup>	D	25	34	0.27	O <sub>2</sub>
8 <sup>c</sup>	D	25	34	3.39	O <sub>2</sub>

<sup>a</sup> Particle size >150 nm. <sup>b</sup> Reaction run without steam. <sup>c</sup> Catalyst activation at 400 °C, reaction at 350 °C.

However, if we look at the theoretical phase diagram of Al–Cu, we see that it shows an eutectic point at 548 °C.[20] True, our catalyst is not a pure Al–Cu alloy (since at least its surface is passivated with an oxide layer; see Fig. 4-32 ). Nevertheless, we hypothesized that a partial melting occurs during the pre-treatment at 600 °C (and possibly even during the reaction at 550 °C). Even if only part of the catalyst were melting, it would be perform the active part. This is because the first sites that would melt would be the high-energy kinks and breaks where catalysis usually happens.[21–23] Indeed, when we compared samples A and B that had less Cu but a larger particle size (typically > 150 nm), we saw that these were more active than those with more copper but smaller sizes.

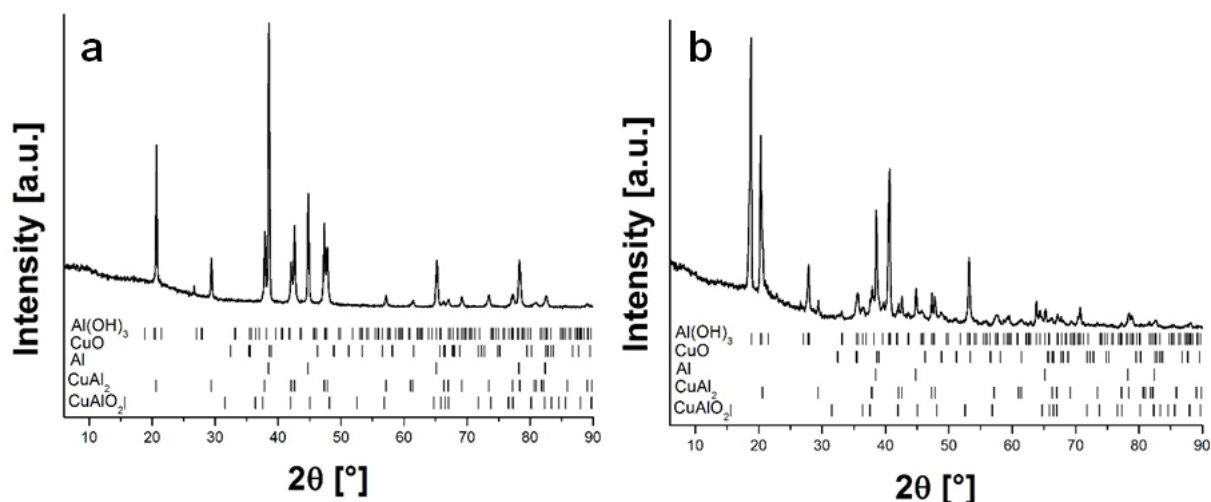


Fig. 4-32 X-ray diffraction patterns of the porous Al-Cu catalyst D before (a) and after (b) ultrasound treatment (the JCPDS-ICDD standards are also included for ease of comparison). Reprinted from Chem. Eur. J., 17, J. Schäferhans, et al., Novel and Effective Copper - Aluminum Propane Dehydrogenation Catalysts, 12254 – 12256, Copyright (2012), with permission from John Wiley and Sons.

To check this hypothesis, we prepared another batch of the same catalyst D, but this time activated at 400 °C (all other conditions identical). We then ran the dehydrogenation again, this time 200 degrees lower (i.e. at 350 °C). Excitingly, as Fig. 4-33 shows, this catalyst gave greater conversions, reaching a stable 4% on stream. This is equivalent to a constant rate of  $0.83 \text{ mol h}^{-1} \text{ g}^{-1}$ . This result is all the more remarkable considering the temperature difference: a 200 °C offset would be expected to slow down the reaction by approximately an order of magnitude (all other known catalysts are inactive under these conditions).

For comparison purposes, we tested a standard Pt–Sn/ $\text{Al}_2\text{O}_3$  catalyst under similar conditions. This catalyst has been shown in the available literature as the best in terms of activity/selectivity/stability for propane dehydrogenation.[24–27] Under the same reaction conditions, Pt–Sn/ $\text{Al}_2\text{O}_3$  was practically inactive at 350 °C and gave less than 1% conversion ( $< 0.2 \text{ mol h}^{-1} \text{ g}^{-1}$ ) at 550 °C. Searching the literature, we did not find any reports on propane dehydrogenation over Cu/  $\text{Al}_2\text{O}_3$ . But, we note the increase in rate quoted by Sokolova et al.[28] when adding Cu to Pt/ $\text{Al}_2\text{O}_3$ .

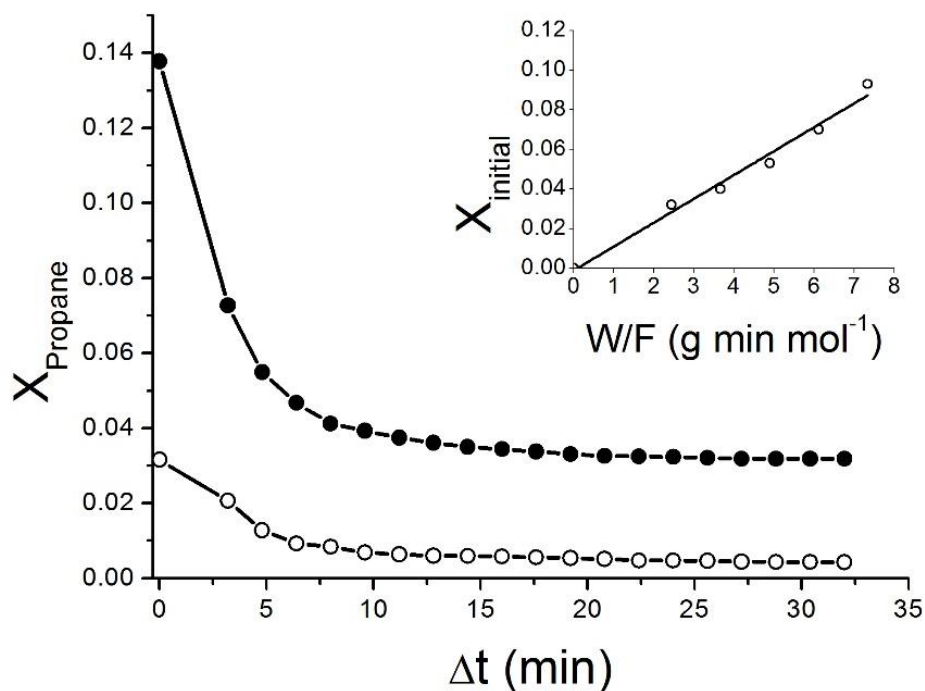


Fig. 4-33 Temporal propane conversion for catalyst D at 350 °C (●) and 550 °C (○). Inset: relationship between the catalyst space time (i.e. amount of catalyst per propane molar flow pass) and initial propane conversion. Note: the benchmark Pt–Sn/Al<sub>2</sub>O<sub>3</sub> catalyst (not shown) gives < 1% conversion at 550 °C. Reprinted from Chem. Eur. J., 17, J. Schäferhans, et al., Novel and Effective Copper - Aluminum Propane Dehydrogenation Catalysts, 12254 – 12256, Copyright (2012), with permission from John Wiley and Sons.

#### 4.4.5 Conclusion

In conclusion, we show here that high-power ultrasound is a green chemistry tool for the synthesis of porous copper– aluminum frameworks stabilized by metal oxide. Furthermore, this material is inexpensive (production expenses are approximately 3 E per liter) and the method can be easily scaled-up by using different sonotrodes (or a series of them), as these may vary widely in size and shape. These new porous materials (or “metal sponges”) have an alloy bulk and an oxidized surface, and can catalyze propane dehydrogenation at low temperatures. Thanks to their high activity and because they contain no noble metals, they open exciting opportunities in low-temperature dehydrogenation catalysis for making bulk chemicals.

#### 4.4.6 Experimental

##### *Materials and Instrumentation*

Transmission and scanning electron microscopy (TEM, Zeiss 922 EFTEM operating at 200 kV and LEO 1530 FE-SEM, Zeiss, respectively), in combination with an ultramicrotome (Ultracut E Reichert Jung, thickness 50 nm) were applied to characterize the optical response, structure, and size of the Al-Cu powder.

Powder X-ray diffraction diagrams were acquired using a Stoe STADI P X-ray Transmission diffractometer: Cu  $K\alpha_1$ , irradiation at ambient temperature, with  $2\theta = 5 - 90^\circ$ .

Surface area and pore size distribution based on physisorption (adsorption and desorption of gases) were measured by the BET[29] and BJH[30] methods using  $N_2$  at 77 K on the vacuum gas sorption Surfer (Thermo Scientific). All samples were dried under vacuum for 24 h at 300 °C prior to each measurement.

Al shots, irregular, 15 mm and down, 99.9% (metals basis) from Alfa Aesar and Cu beads, 2 – 8 mm, 99.9995% (trace metals basis) from Sigma Aldrich were used as received. The water was purified before use in a three stage Millipore Milli-Q Plus 185 purification system and had a resistivity higher than 18.2  $M\Omega \cdot m \cdot cm^{-1}$ . All gases were supplied by Praxair (= 99.995% pure). The  $H_2$ , Ar, and  $O_2$  streams were further purified over molecular sieves and/or BTS columns at 80 °C prior to use.

#### ***Procedure for preparing the Al-Cu alloy***

Commercial Al and Cu beads were alloyed by an arc melting device (Bühler) with a melt stream of 300 A. After reaching a vacuum of 10 – 5 mbar, 500 mbar Ar were transferred to the reactor. For homogenization, the melt of Cu and Al was turned around three times. Five different alloy samples (30 g each) were prepared. The Cu content in these samples was 25 wt.% (118 mmol), 20 wt.% (94 mmol), 15 wt.% (71 mmol), 10 wt.% (47 mmol), and 5 wt.% (24 mmol), respectively. The resulting solid was cut in pieces and then grounded by using a rotary mill (PULVERISETTE 14, Fritsch GmbH) with a sieve ring of 1.5 mm. After milling, the powder was sieved with a mesh of 14.

#### ***Procedure for catalyst preparation***

Five grams of the Al-Cu alloy powder were dispersed in ultrapure water (50 mL) and sonicated for 60 min with an ultrasound tip (Hielscher VIP1000 hd instrument; operated at 20 kHz with a maximum output power of 1000 W and a head area of 3.8  $cm^2$ , equipped with a booster B2-1.2). The maximum intensity was calculated to be 57  $W \cdot cm^{-2}$  at a mechanical amplitude of 81 mm. During the treatment the sample was cooled in an ice bath. After the treatment, the sample was dried at 120 °C for 24 h.

#### ***General procedure for propane dehydrogenation***

The catalyst was activated in situ before reaction in a flow of 77  $mL \cdot min^{-1}$  Ar and 3  $mL \cdot min^{-1}$   $O_2$  at 600 °C. The reactions were carried out at 1 atm and 550 °C in a continuous-flow fixed-bed vertical quartz reactor (4 mm i.d.), which was controlled with a fully automated system built in house.[23]. The partial pressures of  $C_3H_8$  and Ar were fixed at 0.5 atm where 2  $g \cdot h^{-1}$  of steam were supplied by means of Bronkhorst mass flow controllers (total flow = 80  $cm^3 \cdot min^{-1}$ ); the ratio of catalyst mass (W) to initial  $C_3H_8$  molar flow rate (F) spanned the range 0 – 9  $g \cdot min \cdot mol^{-1}$ . A quartz wool layer ( $\leq 3$  mm) above the catalyst served as a preheating zone and isothermal conditions were kept by diluting the catalyst bed

with ground glass; the reaction temperature was continuously monitored by a thermocouple at the catalyst bed. The reactor effluent was analyzed on-line by using an Interscience Compact GC equipped with two TCD detectors separating a) Ar, H<sub>2</sub>O, CO<sub>2</sub>, C<sub>2</sub>, and C<sub>3</sub> hydrocarbons on a Porabond Q column (helium as carrier gas); and b) H<sub>2</sub>, CO, CH<sub>4</sub>, and O<sub>2</sub> on a 5 Å molsieve column (argon as carrier gas). The measurement analytical repeatability was better than  $\pm 0.5\%$ . The fractional conversion of C<sub>3</sub>H<sub>8</sub> is defined in this study as  $XA = ((F - F_A)/F)$ , where F<sub>A</sub> represents the molar flow of C<sub>3</sub>H<sub>8</sub> at  $\Delta t$ . Repeated reactions with different samples from the same batch of catalyst delivered raw data that were reproducible to within  $\pm 7\%$ .

#### ***Procedure for synthesizing the Pt-Sn/Al<sub>2</sub>O<sub>3</sub> reference catalyst***

The bimetallic Pt-Sn/Al<sub>2</sub>O<sub>3</sub> was prepared by simultaneous addition of the precursor solutions (1 mol% loading of each metal). First, 13.0 cm<sup>3</sup> of an acidified 15 mM SnCl<sub>2</sub>•2H<sub>2</sub>O solution was added to 59.0 cm<sup>3</sup> of a 3 mM H<sub>2</sub>PtCl<sub>6</sub>•6H<sub>2</sub>O solution. Then, 2.0 g of support were added and the volume was adjusted to 200 cm<sup>3</sup>. The resulting slurry was heated to dryness at 80 °C (2 °C min<sup>-1</sup>) under an Ar purge. The solid residue was dried overnight in an Ar stream (60 cm<sup>3</sup> min<sup>-1</sup>) at 80 °C (heating ramp of 2 °C min<sup>-1</sup>), then cooled to room temperature and stored in a desiccator in the dark. Prior to catalysis, all catalyst samples were ground and sieved to < 200  $\mu$ m and activated in 80 cm<sup>3</sup> min<sup>-1</sup> 25% v/v H<sub>2</sub>/Ar to 600 °C (5 °C min<sup>-1</sup>) for 1 h.

#### **4.4.7 Acknowledgments**

We thank B. Putz and S. Koch (University of Bayreuth) for help with the PXRD analysis and the milling, Dr. M.C. Mittelmeijer-Hazeleger (University of Amsterdam) for technical assistance. J. S. and D. A. thank SFB840 for financial support.

#### **References**

- [1] M. B. A. Scott, Chem. Week, 2007, 169, 14– 18.
- [2] Z. Ma, F. Zaera in Encyclopedia of Inorganic Chemistry (Ed.: R. A. Scott, D. Atwood, C. M. Lukehart), Wiley, New York, 2006, DOI: 10.1002/0470862106.ia084.
- [3] N. B. McKeown, P. M. Budd, Chem. Soc. Rev., 2006, 35, 675 – 683.
- [4] A. Corma, H. Garcia, F. X. Llabres i Xamena, Chem. Rev., 2010, 110, 4606 –4655.
- [5] H. Oikawa, Y. Shibata, K. Inazu, Y. Iwase, K. Murai, S. Hyodo, G. Kobayashi, T. Baba, Appl. Catal. A, 2006, 312, 181 –185.
- [6] R. Gounder, E. Iglesia, Angew. Chem. 2010, 122, 820 –823; Angew. Chem. Int. Ed., 2010, 49, 808 – 811.
- [7] M. Santhosh Kumar, N. Hammer, M. Rønning, A. Holmen, D. Chen, J. C. Walmsley, G. Øye, J. Catal., 2009, 261, 116.

- [8] D. Akporiaye, S. F. Jensen, U. Olsbye, F. Rohr, E. Rytter, M. Ronnekleiv, A. I. Spjelkavik, *Ind. Eng. Chem. Res.*, 2001, 40, 4741–4748.
- [9] A. Virnovskaia, E. Rytter, U. Olsbye, *Ind. Eng. Chem. Res.*, 2008, 47, 7167–7177.
- [10] M. S. Voronetskii, L. P. Didenko, V. I. Savchenko, *Russ. J. Phys. Chem. B*, 2009, 3, 216.
- [11] S. R. Schmidt, *Top. Catal.*, 2010, 53, 1114–1120.
- [12] M. Raney, U.S. Patent 1,563,587, 1925; b) M. Raney, *Ind. Eng. Chem.*, 1940, 32, 1199–1203.
- [13] E. V. Skorb, D. Fix, D. G. Shchukin, H. Möhwald, D. V. Sviridov, R. Mousa, N. Wanderka, J. Schäferhans, N. Pazos-Peréz, A. Fery, D. V. Andreeva, *Nanoscale*, 2011, 3, 985–993.
- [14] E. V. Skorb, H. Möhwald, T. Irrgang, A. Fery, D. V. Andreeva, *Chem. Commun.*, 2010, 46, 7897–7899.
- [15] E. V. Skorb, D. G. Shchukin, H. Möhwald, D. V. Andreeva, *Nanoscale*, 2010, 2, 722–727.
- [16] K. S. Suslick, S. J. Doktycz, E. B. Flint, *Ultrasonics*, 1990, 28, 280–290.
- [17] M. Larsson, B. Andersson, O. A. Barias, A. Holmen, *Stud. Surf. Sci. Catal.*, 1994, 88, 233–240.
- [18] J.-P. Dacquin, J. Dhainaut, D. Duprez, S. Royer, A. F. Lee, K. Wilson, *J. Am. Chem. Soc.*, 2009, 131, 12896–12897.
- [19] S. M. K. Airaksinen, M. A. BaÇares, O. I. Krausea, *J. Catal.*, 2005, 230, 507–513.
- [20] M. F. Singleton, J. L. Murray, *Binary Alloys Phase Diagrams*, 2<sup>nd</sup> ed. (Eds.: T. B. Massalski, H. Okamoto), ASM International, Materials Park, 1990.
- [21] G. Rothenberg, *Catalysis: Concepts and Green Applications*, Wiley-VCH, Weinheim, 2008.
- [22] B. Blümich, L. B. Datsevich, A. Jess, T. Oehmichen, X. Ren, S. Stapf, *Chem. Eng. J.*, 2007, 134, 35–44.
- [23] J. H. Blank, J. Beckers, P. F. Collignon, F. Clerc, G. Rothenberg, *Chem. Eur. J.*, 2007, 13, 5121–5128.
- [24] O. A. Barias, A. Holmen, E. A. Blekkan, *J. Catal.*, 1996, 158, 1–12.
- [25] M. Santhosh Kumar, A. Holmen, D. Chen, *Microporous Mesoporous Mater.*, 2009, 126, 152.
- [26] B. K. Vu, S. M. Bok, I. Y. Ahn, E. W. Shin, *Catal. Lett.*, 2009, 133, 376.
- [27] C. Yu, H. Xu, Q. Ge, W. Li, *J. Mol. Catal. A: Chem.* 2007, 266, 80.
- [28] N. A. Sokolova, A. P. Barkova, D. B. Furman, V. Y. Borovkov, V. B. Kazansky, *Kinet. Catal.*, 1995, 36, 434.
- [29] S. Brunauer, L. S. Deming, W. E. Deming, E. Teller, *J. Am. Chem. Soc.*, 1940, 62, 1723–1732.
- [30] E. P. Barrett, L. G. Joyner, P. P. Halenda, *J. Am. Chem. Soc.*, 1951, 73, 373–380.

## 4.5 Efficient three-component coupling catalysed by mesoporous copper-aluminum based nanocomposite

Jana Dulle, K. Thirunavukkarasu, Marjo Mittelmeijer-Hazeleger, Daria V. Andreeva,\* N. Raveendran Shiju,\* and Gadi Rothenberg\*

This work is published in *Green Chemistry*, 2013, 15, 1238 – 1243

This article is reprinted from *Green Chem.*, 15, J. Dulle, et al., Efficient three-component coupling catalysed by mesoporous copper-aluminum based nanocomposite, 1238 – 1243, Copyright (2013), with permission from The Royal Society of Chemistry.

### 4.5.1 Contribution to the joint publication

I wrote the main part of the manuscript. I was responsible for the material preparation. Daria Andreeva had the supervision for it. I ran  $A^3$  coupling experiments with the porous Al/Cu at the University of Amsterdam and N. Raveendran Shiju did further ones. He also supervised the project. K. Thirunavukkarasu performed the XPS and XAES material analysis and wrote this part of the manuscript. Marjo Mittelmeijer-Hazeleger processed the physisorption measurements. N. Raveendran Shiju, Gadi Rothenberg, and Daria Andreeva corrected the manuscript.

### 4.5.2 Abstract

Traditional synthesis methods for propargylamines have several drawbacks. A recently developed alternative route is the so-called " $A^3$  coupling" in which an alkyne, an aldehyde, and an amine are coupled together. Typically, these reactions are catalyzed by homogeneous gold salts, organogold complexes, or silver salts. But these homogeneous catalysts are expensive and their separation is difficult. Here we report the discovery that solid Cu/Al/oxide mesoporous "sponges" are excellent  $A^3$  coupling catalysts. These materials are robust, inexpensive, and easy to make. They give well to excellent yields (87 – 97%) for a wide range of substrates. Being heterogeneous, these catalysts are also easy to handle and separate from the reaction mixture, and can be recycled with no loss of activity.

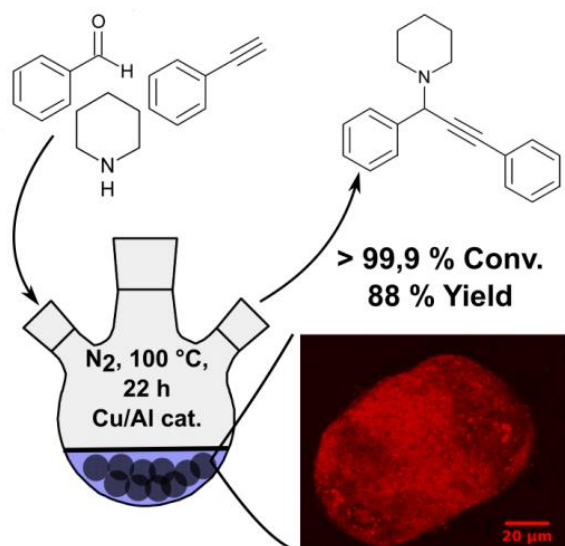


Fig. 4-34 Graphical abstract. Adapted from *Green Chem.*, 15, J. Dulle, et al., Efficient three-component coupling catalyzed by mesoporous copper-aluminum based nanocomposite, 1238 – 1243, Copyright (2013), with permission from The Royal Society of Chemistry.

### 4.5.3 Introduction

One of the biggest challenges in organic chemistry is mimicking the complexity of biosynthesis *in vitro*. Nature excels at matching multiple simple substrates in one-pot reactions that give complex molecules with high yields.[1–4] We chemists can also do this, but typically using a host of stoichiometric reagents and protecting groups, and often generating much waste in the process.

The synthesis of propargylic amines is a good example. These amines are key intermediates for making drugs and agrochemicals.[5–8] They are traditionally synthesized by nucleophilic attack of lithium acetylides or Grignard reagents on imines or their derivatives.[9,10] However, such reagents must be used stoichiometrically, causing large amounts of waste. They are also moisture-sensitive, and require strictly controlled reaction conditions.

An elegant alternative route is the so-called “A<sup>3</sup> coupling” (Equation 4-1). This catalytic reaction between an alkyne, an aldehyde, and an amine (hence the three A’s) gives water as the only by-product.[7,11] The reaction is run in a liquid phase, using homogeneous catalysts such as gold salts,[12] organogold complexes,[13] silver salts,[14–17] and  $Hg_2Cl_2$ . [18] Among these, the gold salts show the highest activity. The problem is that rapid reduction of cationic gold species to inactive metallic atoms is unavoidable when gold salts activate alkynes/alkenes.[19–21] Moreover, using homogeneous catalysts brings inherent complications in catalyst separation and reuse. The ideal solution, therefore, would be replacing the homogeneous gold salt with an effective, yet inexpensive, heterogeneous catalyst.[22–35] Many of the heterogeneous catalysts are supported/immobilized gold nanoparticles.[36] Zhang et al. reported that supported gold is active for the A<sup>3</sup> coupling reaction.[21]



several attractive features for heterogeneous catalysis: increased surface area, mesopores, and unique textural stability.

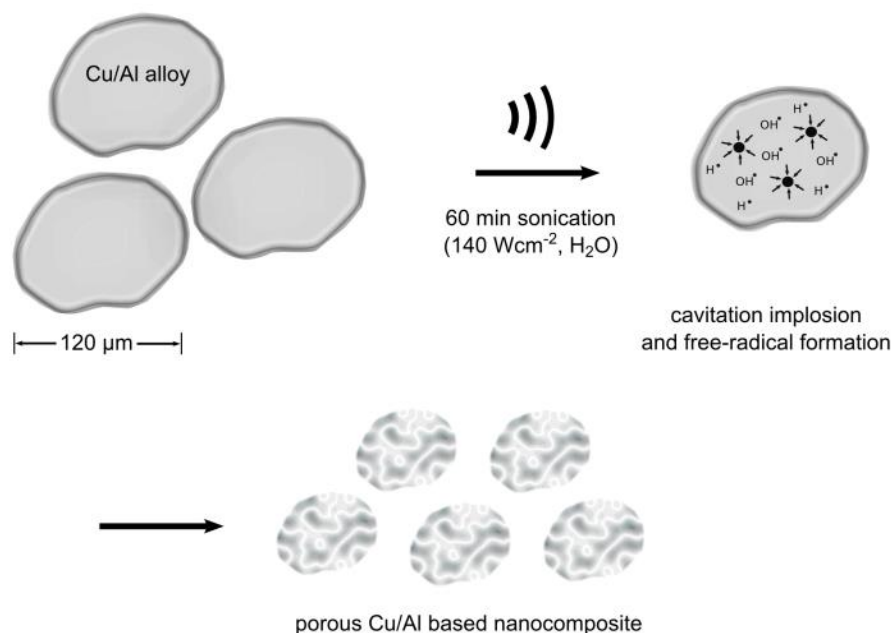
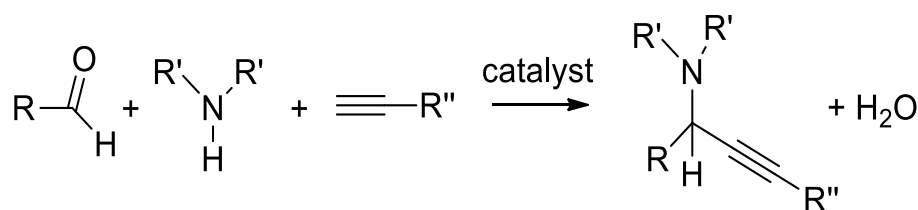


Fig. 4-35 Sonochemical formation of mesoporous Cu/Al based particles. Intensive sonication of the initial alloy particles leads to fragmentation, porosity, and surface oxidation. Reprinted from *Green Chem.*, 15, J. Dulle, et al., Efficient three-component coupling catalysed by mesoporous copper-aluminum based nanocomposite, 1238 – 1243, Copyright (2013), with permission from The Royal Society of Chemistry.

Benzaldehyde, piperidine, and phenylacetylene were used as model substrates to study the catalytic activity of the Cu/Al catalyst in A<sup>3</sup> coupling. Our catalyst gave high benzaldehyde conversion (~ 99%), as well as a high yield of the coupling product (see Table 4-4). Control experiments confirmed that no conversion was found in the absence of catalyst under otherwise identical conditions. Compared with commercial Cu<sub>2</sub>O (Cu<sup>+</sup> is predominant in our catalyst; see below the XPS characterization) the sample was not as active and selective to A<sup>3</sup> coupling, under the same conditions. Homocoupling of the alkyne was also observed in this case and selectivity to the A<sup>3</sup> coupled product was only 60%. Indeed, homogeneous copper salts were also reported to be active as catalysts, but again these gave only moderate conversions and selectivities.[48–51] Moreover, difficulties in recovering the catalyst from the reaction mixture limit their use.

To examine the scope of the A<sup>3</sup> coupling reaction, we studied different combinations of aldehydes, amines, and alkynes (see Table 4-4). Aromatic aldehydes as well as cyclohexanecarboxaldehyde (entry 3) gave high yields. The reactions with morpholine and pyrrolidine (entries 7 and 8) also gave > 90% yields of the A<sup>3</sup> coupled product.

Table 4-4 A<sup>3</sup> coupling catalyzed by Cu/Al. Reprinted from Green Chem., 15, J. Dulle, et al., Efficient three-component coupling catalyzed by mesoporous copper-aluminum based nanocomposite, 1238 – 1243, Copyright (2013), with permission from The Royal Society of Chemistry.



Entry	R <sup>a</sup> (aldehyde)	R' <sub>2</sub> NH (amine)	R'' (alkyne)	Yield (GC/Isolated) <sup>b</sup>
1	Ph	Piperidine	Ph	99/94
2	4-CH <sub>3</sub> C <sub>6</sub> H <sub>4</sub>	Piperidine	Ph	93/87
3	Cyclohexyl	Piperidine	Ph	97/90
4	3-ClC <sub>6</sub> H <sub>4</sub>	Piperidine	Ph	96
5	3-OHC <sub>6</sub> H <sub>4</sub>	Piperidine	Ph	92
6	3-NO <sub>2</sub> C <sub>6</sub> H <sub>4</sub>	Piperidine	Ph	88
7	Ph	Morpholine	Ph	94/88
8	Ph	Pyrrolidine	Ph	90
9	Ph	Piperidine	Hexyl	92
10	Ph	Piperidine	4-CH <sub>3</sub> C <sub>6</sub> H <sub>4</sub>	95
11	Ph	Piperidine	4-CH <sub>3</sub> OC <sub>6</sub> H <sub>4</sub>	90
12	4-OCH <sub>3</sub> C <sub>6</sub> H <sub>4</sub>	Piperidine	Ph	94
13	Ph	Piperidine	Ph	45 <sup>c</sup>
14	Ph	Piperidine	Ph	92 <sup>d</sup>
15	Ph	Piperidine	Ph	81 <sup>e</sup>

<sup>a</sup> Reaction conditions: aldehyde (1.0 mmol), amine (1.2 mmol), and alkyne (1.3 mmol), Cu/Al (0.12 mmol Cu), toluene (1.7 ml), 100 °C, 22 h; <sup>b</sup> mol% of A<sup>3</sup> coupling product yield based on aldehyde starting material (entries 1–12, complete conversion monitored by GC); <sup>c</sup> Cu<sub>2</sub>O catalyst, 75% conv.; <sup>d</sup> Cu/Al, 90 °C, 22 h (GC conv. 92%); <sup>e</sup> Cu/Al, 70 °C, 22 h (GC conv. 82%).

Kantam *et al.* showed that CuO nanoparticles gave a good yield for A<sup>3</sup> coupling, while commercially available bulk Cu<sub>2</sub>O and bulk CuO gave poor yields.[35] The yield was 82% using benzaldehyde, piperidine, and phenylacetylene using toluene as the solvent. The yield varied from 8% to 84% when

the substrates were changed. Recently, Albaladejo et al. reported that Cu<sub>2</sub>O on titania is a good catalyst for A<sup>3</sup> coupling.[52] The catalyst was prepared by supporting copper nanoparticles, made by the addition of CuCl<sub>2</sub> to a suspension of lithium and 4,4'-di-*tert*-butylbiphenyl in THF, on TiO<sub>2</sub>. They obtained 32% yield (using toluene as the solvent) and 98% yield (using neat substrate) starting from benzaldehyde, piperidine, and phenylacetylene. For other substrates, the yield of the A<sup>3</sup> coupled products varied, from 52% to 98%. Notwithstanding these results, our Cu/Al catalyst gives complete conversion to the A<sup>3</sup> product in toluene, as well as high activity for different substrates as well, with 88% – 99% yield. This matches and in some cases outperforms gold catalysts published elsewhere. Thus, Wei *et al.* reported that AuCl, AuI, AuBr<sub>3</sub>, and AuCl<sub>3</sub> showed good activities for A<sup>3</sup> coupling.[12] The yield of propargylamines ranged from 53% to 99%, depending on the substrates. Zhang *et al.* showed that Au/CeO<sub>2</sub> catalyses A<sup>3</sup> coupling and the yield varies from 25% – 99%, again depending on the substrates.[21] Another report shows that gold nanoparticles embedded in a mesoporous carbon nitride catalyzes the A<sup>3</sup> coupling, yielding 51% after 12 h and 62% after 24 h.[37]

We believe that the reaction mechanism (Fig. 4-36) involves the formation of copper acetylide, as was proposed for A<sup>3</sup> coupling with cationic gold under homogeneous conditions.[12,28] Recently, Albaladejo et al. demonstrated that A<sup>3</sup> coupling using heterogeneous Cu/TiO<sub>2</sub> also involves copper acetylide formation.[52] The same mechanism can be invoked in our system. Thus, the C–H bond of the alkyne is activated by a Cu(I) species to give a copper acetylide intermediate (a), which reacts with the immonium ion (b) generated *in situ* from the aldehyde and secondary amine to give the corresponding propargylamine (c) and regenerate the catalytically active site.

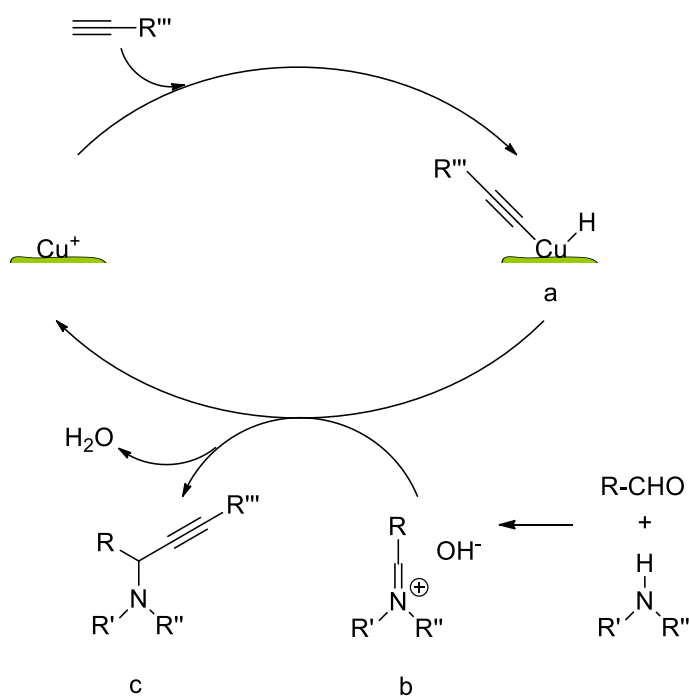


Fig. 4-36 Tentative mechanism of the A<sup>3</sup> coupling. The Cu(I) species activates the C–H bond of the alkyne to give a copper acetylide intermediate (a), which reacts with the immonium ion (b) generated in situ from the aldehyde and secondary amine to give the corresponding propargylamine (c). Reprinted from *Green Chem.*, 15, J. Dulle, et al., Efficient three-component coupling catalysed by mesoporous copper-aluminum based nanocomposite, 1238 – 1243, Copyright (2013), with permission from The Royal Society of Chemistry.

Understanding the structure and the morphology of the catalyst surface is the key to understanding its activity. Therefore, we carried out a series of characterization experiments. Electron microscopy (Fig. 4-37a, c) showed that the initial particles of  $\sim 120 \mu\text{m}$  are broken into  $\sim 40 \mu\text{m}$  pieces after 60 min of sonication. The SEM and TEM images show a porous interfacial layer. Combining this with N<sub>2</sub> adsorption studies (Fig. 4-37d) we confirm the formation of a porous outer surface and modification of the inner structure, increasing the specific surface area to  $34 \text{ m}^2 \text{ g}^{-1}$ . The BET isotherm is type II.[53] We see that the monolayer coverage is completed and multilayer N<sub>2</sub> adsorption starts at a relative pressure of ca. 0.03. This shows that the material has both micropores and mesopores. The meso and micropore areas were  $11.2 \text{ m}^2 \text{ g}^{-1}$  and  $22.8 \text{ m}^2 \text{ g}^{-1}$  and the meso and micropore volumes were  $0.03 \text{ cm}^3 \text{ g}^{-1}$  and  $0.01 \text{ cm}^3 \text{ g}^{-1}$ .

We also examined the inner structure of the material by monitoring the spatial distribution of a fluorescent dye inside the particles. Fig. 4-37b shows a 3D reconstruction of confocal scanning fluorescence microscopy (CSFM) images of a catalyst particle loaded with rhodamine B. Here, too, we can see the porous inner structure.

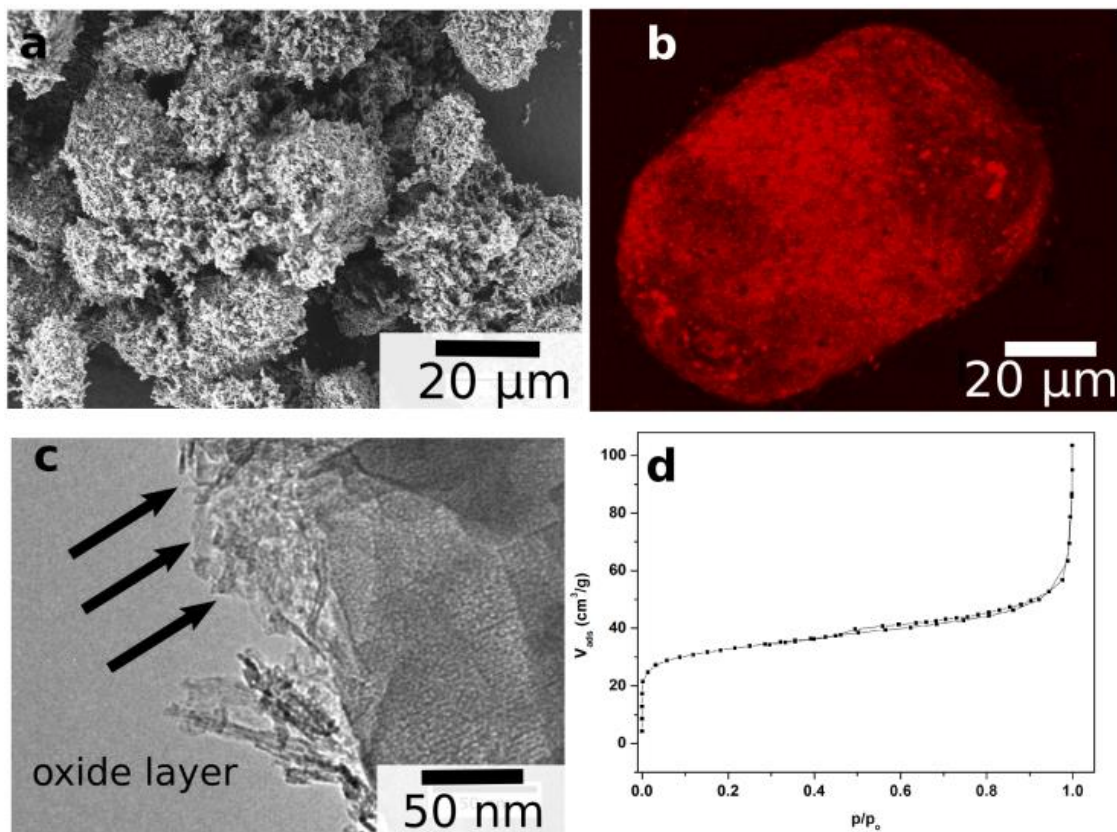


Fig. 4-37 Scanning electron micrograph (a), 3D confocal microscopy reconstruction of the particle loaded with rhodamine B (picture taken in fluorescent mode) showing the porosity throughout the catalyst particle (b), transmission electron micrograph (c), and nitrogen adsorption isotherm (d) of the Cu/Al catalyst, showing the morphology and porous structure. Reprinted from *Green Chem.*, 15, J. Dulle, et al., Efficient three-component coupling catalysed by mesoporous copper-aluminum based nanocomposite, 1238 – 1243, Copyright (2013), with permission from The Royal Society of Chemistry.

The powder X-ray diffraction pattern of the initial alloy showed intense peaks for Al and  $\text{CuAl}_2$  (Fig. 4-38). After sonication, the PXRD reveals the peaks corresponding to highly ordered  $\text{Al}(\text{OH})_3$  (bayerite) crystallites and CuO, thus, partial oxidation of the alloy. The different Cu/Al mixed phases also can be distinguished in the PXRD pattern of the modified particle, indicating an increased interaction between the two metals.

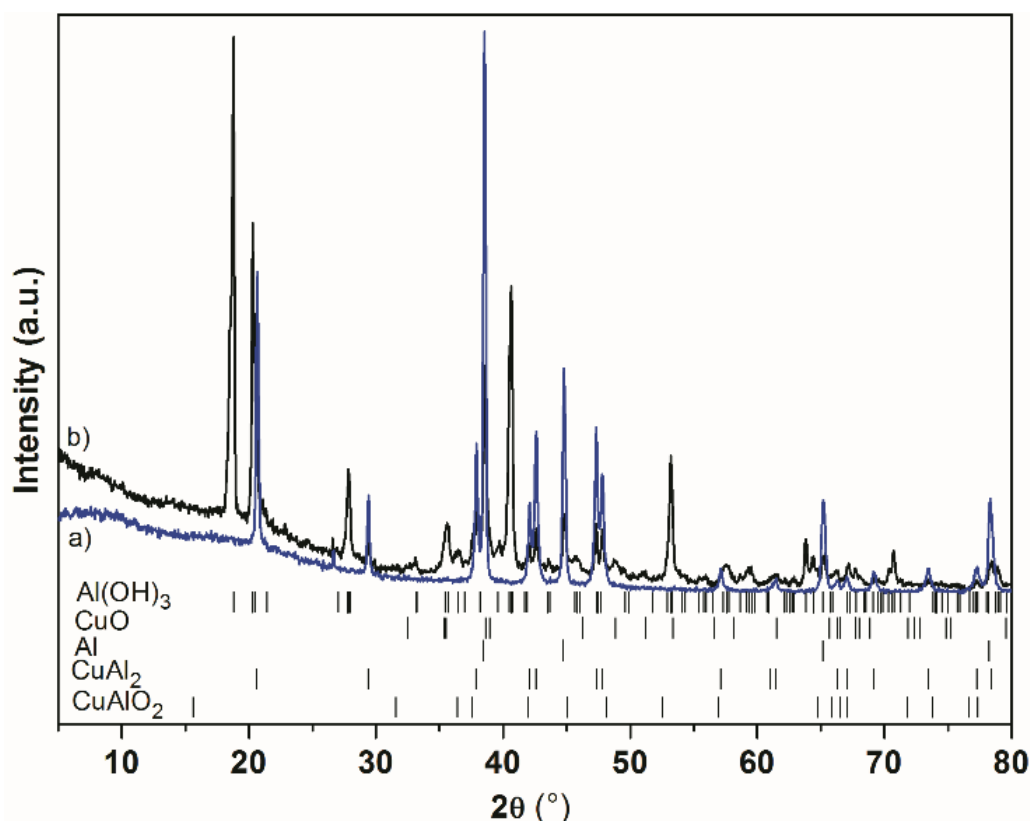


Fig. 4-38 PXRD patterns of the initial particles (a) and particles sonicated for 60 min (b). Reprinted from Green Chem., 15, J. Dulle, et al., Efficient three-component coupling catalysed by mesoporous copper-aluminum based nanocomposite, 1238 – 1243, Copyright (2013), with permission from The Royal Society of Chemistry.

Using XPS, we observed mixed oxidation states for Cu on the catalyst surface (Fig. 4-39 and Table 4-5). The majority (72%) of the copper on the surface was  $\text{Cu}^+$ , with a binding energy (BE) of 932.5 eV. The rest is  $\text{Cu}^{2+}$  (BE - 933.7 eV). Indeed, low intensity satellite features (exclusively due to  $\text{Cu}^{2+}$ ) support the minor contribution from the latter. However, because  $\text{Cu}^0$  and  $\text{Cu}^+$  states have the same BE, we also recorded the X-ray excited Auger electron spectroscopy (XAES) for the Cu LMM region. The Cu LMM peak can be resolved into two distinct peaks (see Fig. 4-39, inset) at 914.2 eV (kinetic energy, KE) and 917.7 eV. These correspond to  $\text{Cu}^+$  and  $\text{Cu}^{2+}$ , respectively. The presence of  $\text{Cu}^{2+}$  was further confirmed by the satellite peaks (denoted by arrows in Fig. 4-39). The absence of an  $\sim 918.5$  eV KE feature in the spectra shows that there is no  $\text{Cu}^0$  in the sample.[54,55] Moreover, the negative shift in the BE of the Al 2p core level (73.7 eV) compared with the Al 2p of the  $\text{Al}_2\text{O}_3$  support alone ( $\sim 74$  eV) indicates a metal-to-support electron transfer process. The interaction between the Cu and the support and consequent modification of the electronic environment may be responsible for the high selectivity of the catalyst, compared to the bulk  $\text{Cu}_2\text{O}$ . Since the PXRD did not show peaks corresponding to  $\text{Cu}_2\text{O}$ , it is either amorphous or highly dispersed on the Al surface.

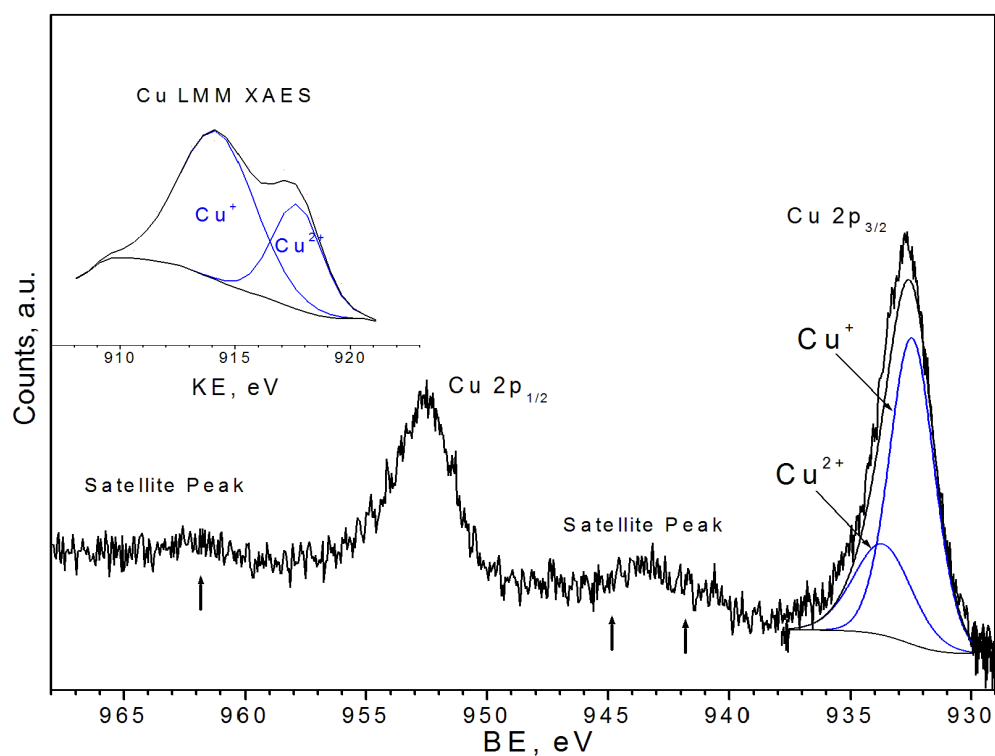


Fig. 4-39 Cu 2p XP spectrum of Cu/Al; the inset shows the Cu LMM XAE spectrum (tabulated data are provided in Table 4-5). Reprinted from Green Chem., 15, J. Dulle, et al., Efficient three-component coupling catalyzed by mesoporous copper-aluminum based nanocomposite, 1238 – 1243, Copyright (2013), with permission from The Royal Society of Chemistry.

Table 4-5 XPS data of the Cu/Al sample. Reprinted from Green Chem., 15, J. Dulle, et al., Efficient three-component coupling catalyzed by mesoporous copper-aluminum based nanocomposite, 1238 – 1243, Copyright (2013), with permission from The Royal Society of Chemistry.

Core level	Binding energy (eV)	FWHM (eV)
Al 2p	73.7	1.87
O 1s	531.3	2.55
Cu 2p (Cu <sup>+</sup> )	932.5 (914.2 <sup>a</sup> )	2.18
Cu 2p (Cu <sup>2+</sup> )	933.7 (917.7 <sup>a</sup> )	2.83

<sup>a</sup> Kinetic energy values of the Cu LMM XAE spectra.

To test catalyst reusability, we ran five consecutive reaction cycles. After each cycle, the catalyst was filtered, washed with acetone and water and dried at 403 K. The results were similar to the original reaction and no significant deactivation was observed, confirming the reusability of our catalyst (Fig. 4-40).

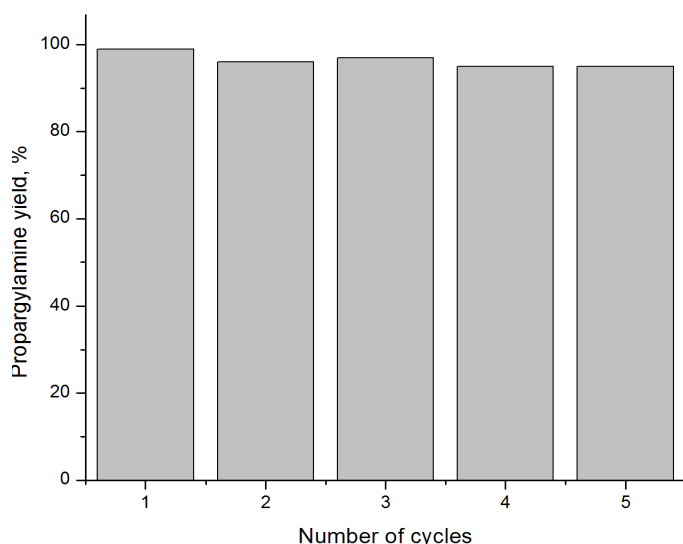


Fig. 4-40 Catalyst recycling studies in the coupling of phenyl acetylene, benzaldehyde and piperidine. Reaction conditions: aldehyde (1.0 mmol), amine (1.2 mmol), and alkyne (1.3 mmol), Cu/Al (0.12 mmol Cu), toluene (1.7 ml), 100 °C, 22 h. After each cycle, the catalyst was filtered, washed with acetone and water and dried at 403 K. Reprinted from Green Chem., 15, J. Dulle, et al., Efficient three-component coupling catalysed by mesoporous copper-aluminum based nanocomposite, 1238 – 1243, Copyright (2013), with permission from The Royal Society of Chemistry.

#### 4.5.5 Conclusion

We showed here that the  $A^3$  coupling reaction can run in the presence of a solid catalyst that contains only copper, aluminum, and oxygen. This catalyst is stable. It is readily recovered after the reaction and can be recycled several times without deactivation. The process is simple and general, giving propargylamines in good to excellent yields for a variety of substrates. Finally, the fact that our catalyst contains neither noble nor heavy or toxic metals opens true opportunities for practical application.

#### 4.5.6 Experimental

##### *Materials and instrumentation*

Aluminum shot (irregular, < 15 mm, 99.9%; metal basis) and copper beads (2 – 8 mm, 99.9995%; trace metals basis) were purchased from Alfa Aesar and Sigma Aldrich, respectively, and used as received. Water was purified using a three-stage Millipore Milli-Q Plus 185 purification system (final resistivity > 18.2 M $\Omega$  cm<sup>-1</sup>).

Transmission and scanning electron microscopes (TEM, Zeiss 922 EFTEM operating at 200 kV and Zeiss 1530 FE-SEM respectively) in combination with an ultra-microtome (Ultracut E Reichert Jung, thickness 50 nm) were applied to characterize the optical response, structure, and size of the Cu/Al powder.

Powder X-ray diffraction data were collected on a Stoe STADI P X-ray diffractometer using Cu K $\alpha_1$  radiation at room temperature. The N<sub>2</sub> adsorption–desorption isotherms were measured at 77 K on a vacuum gas sorption apparatus Surfer (Thermo Scientific), after evacuation at 300 °C for 24 h. The

surface area was calculated by the BET method. X-ray photoelectron spectroscopy measurements were carried out using a multiprobe system (Omicron Nanotechnology, Germany) equipped with a dual Mg/Al X-ray source and a hemispherical analyzer operating in constant analyzer energy (CAE) mode. The spectra were obtained with a pass energy of 50 eV for the survey scan and 20 eV for individual scans. An Mg K $\alpha$  X-ray source was operated at 300 W and 15 kV. The base pressure in the analyzing chamber was maintained a  $1 \times 10^{-10}$  mbar. The data were processed with the Casa XPS program (Casa Software Ltd, UK), and calibrated with reference to the adventitious carbon peak (284.9 eV) in the sample. Peak areas were determined by integration employing a Shirley-type background. Peaks were considered to be a 70:30 mix of Gaussian and Lorentzian functions. The relative sensitivity factors (RSF) provided by the manufacturer were used for quantifying elements.

### ***Procedure for catalyst preparation***

Aluminum and copper were first alloyed using an AM arc melter (Edmund Bühler GmbH, Germany) with a melt stream of 300 A. The reactor was first evacuated to  $10^{-5}$  mbar and then pressurised to 500 mbar argon. For homogenization, the sample was overturned three times and fused each time. The bulk material was cut into pieces and ground using a rotary mill (Pulverisette 14, Fritsch GmbH, Germany) with a sieve ring of 0.12 mm. The resulting powder (typically 30 g alloy, 25.0 wt% Cu) was then sieved by a 150  $\mu$ m sieve.

Five grams of this Cu/Al alloy were then dispersed in 50 ml purified water and sonicated for 60 min with an ultrasound tip (VIP1000hd, Hielscher Ultrasonics GmbH, Germany). The device was operated at 20 kHz with a maximum output power of 1000 W by an ultrasonic horn BS2d22 (head area of 3.8 cm<sup>2</sup>). It was equipped with a booster B2–1.8 for 60 min. The maximum intensity was calculated to be 140 W cm<sup>-2</sup> at a mechanical amplitude of 106  $\mu$ m. To avoid the temperature increase during sonication the experiment was performed in a thermostatic cell. The resulting powder was then dried at 120 °C for 5 h.

### ***General procedure for Cu/Al-catalysed A<sup>3</sup> coupling***

The amine (1.2 mmol), aldehyde (1.0 mmol), alkyne (1.3 mmol), Cu/Al (0.12 mmol based on Cu) and toluene (1.7 ml) were added to a 50 ml round-bottom flask equipped with a magnetic stirring bar and connected to a water-cooled condenser. The mixture was degassed and backfilled with nitrogen, and then stirred for 22 h at 100 °C (oil bath). After the reaction, the mixture was cooled to ambient temperature and the catalyst was filtered. The residue was washed with an additional 5 ml toluene, which was then combined with the filtrate. The samples were analyzed by gas chromatography (VB-1 column, FID), and/or purified by column chromatography (silica gel; hexane: EtOAc 4:1) and analyzed using <sup>1</sup>H NMR spectroscopy and mass spectrometry.

Example: N-(1,3-Diphenyl-2-propynyl)piperidine (Table 4-5, entry 1): Benzaldehyde (1.0 mmol, 106.1 mg), piperidine (1.2 mmol, 102.2 mg), phenylacetylene (1.3 mmol, 132.8 mg), Cu/Al catalyst (0.12 mmol based on Cu, 30 mg), and toluene (1.7 ml) were reacted and analysed as above (258 mg, 94% yield).  $^1\text{H}$  NMR  $\delta$  = 7.00 – 7.65 (m, 10H), 4.80 (s, 1H), 2.40 – 2.60 (m, 4H), 1.56 – 1.69 (m, 4H), 1.30 – 1.50 (m, 2H); MS  $m/z$  (%) 275 ( $\text{M}^+$ , 20), 274 (10), 191 (100), 198 (79), 192 (24), 189 (24), 115 (14), 165 (10), 232 (8).

#### 4.5.7 Acknowledgment

We thank Dr C.S. Gopinath (National Chemical Laboratory, Pune) for his suggestions on XPS measurements and B. Putz (University of Bayreuth) for the PXRD measurements. J. D. and D. A. thank SFB 840 for financial support.

#### References

- [1] K. C. Nicolaou, D. J. Edmonds and P. G. Bulger, *Angew. Chem., Int. Ed.*, 2006, 45, 7134–7186.
- [2] B. M. Trost, *Science*, 1991, 254, 1471–1477.
- [3] M. K. Singh and M. K. Lakshman, *J. Org. Chem.*, 2009, 74, 3079–3084.
- [4] J. W. Lee, T. Y. Kim, Y.-S. Jang, S. Choi and S. Y. Lee, *Trends Biotechnol.*, 2011, 29, 370–378.
- [5] A. A. Boulton, B. A. Davis, D. A. Durden, L. E. Dyck, A. V. Juorio, X.-M. Li, I. A. Paterson and P. H. Yu, *Drug Dev. Res.*, 1997, 42, 150–156.
- [6] M. Miura, M. Enna, K. Okuro and M. Nomura, *J. Org. Chem.*, 1995, 60, 4999–5004.
- [7] T. Naota, H. Takaya and S.-I. Murahashi, *Chem. Rev.*, 1998, 98, 2599–2660.
- [8] L. Zani and C. Bolm, *Chem. Commun.*, 2006, 4263–4275.
- [9] M. E. Jung and A. Huang, *Org. Lett.*, 2000, 2, 2659–2661.
- [10] T. Murai, Y. Mutoh, Y. Ohta and M. Murakami, *J. Am. Chem. Soc.*, 2004, 126, 5968–5969.
- [11] G. Dyker, *Angew. Chem., Int. Ed.*, 1999, 111, 1808–1822.
- [12] C. Wei and C.-J. Li, *J. Am. Chem. Soc.*, 2003, 125, 9584–9585.
- [13] V. K.-Y. Lo, Y. Liu, M.-K. Wong and C.-M. Che, *Org. Lett.*, 2006, 8, 1529–1532.
- [14] C. Wei, Z. Li and C.-J. Li, *Org. Lett.*, 2003, 5, 4473–4475.
- [15] Z. Li, C. Wei, L. Chen, R. S. Varma and C.-J. Li, *Tetrahedron Lett.*, 2004, 45, 2443–2446.
- [16] K. Mohan Reddy, N. Seshu Babu, I. Suryanarayana, P. S. Sai Prasad and N. Lingaiah, *Tetrahedron Lett.*, 2006, 47, 7563–7566.
- [17] Y. Zhang, A. M. Santos, E. Herdtweck, J. Mink and F. E. Kuhn, *New J. Chem.*, 2005, 29, 366–370.
- [18] L. Pin-Hua and W. Lei, *Chin. J. Chem.*, 2005, 23, 1076–1080.
- [19] A. Hoffmann-Roder and N. Krause, *Org. Biomol. Chem.*, 2005, 3, 387–391.
- [20] X. Zhang and A. Corma, *Chem. Commun.*, 2007, 3080–3082.
- [21] X. Zhang and A. Corma, *Angew. Chem., Int. Ed.*, 2008, 47, 4358–4361.

- [22] M. L. Kantam, B. V. Prakash, C. R. V. Reddy and B. Sreedhar, *Synlett*, 2005, 2329–2332.
- [23] W. Yan, R. Wang, Z. Xu, J. Xu, L. Lin, Z. Shen and Y. Zhou, *J. Mol. Catal. A: Chem.*, 2006, 255, 81–85.
- [24] B. M. Choudary, C. Sridhar, M. L. Kantam and B. Sreedhar, *Tetrahedron Lett.*, 2004, 45, 7319–7321.
- [25] A. Fodor, A. Kiss, N. Debreczeni, Z. Hell and I. Gresits, *Org. Biomol. Chem.*, 2010, 8, 4575–4581.
- [26] M. Kidwai, V. Bansal, A. Kumar and S. Mozumdar, *Green Chem.*, 2007, 9, 742–745.
- [27] A. S.-Y. Lee, G.-A. Chen, Y.-T. Chang and S.-F. Chu, *Synlett*, 2009, 441–446.
- [28] V. K. Y. Lo, Y. G. Liu, M. K. Wong and C. M. Che, *Org. Lett.*, 2006, 8, 1529–1532.
- [29] J. V. Madhav, B. S. Kuarm, P. Someshwar, B. Rajitha, Y. T. Reddy and P. A. Crooks, *Synth. Commun.*, 2008, 38, 3215–3223.
- [30] O. P. Pereshivko, V. A. Peshkov and E. V. Van der Eycken, *Org. Lett.*, 2010, 12, 2638–2641.
- [31] C. Wetzel, P. C. Kunz, I. Thiel and B. Spingler, *Inorg. Chem.*, 2011, 50, 7863–7870.
- [32] Z. Xu, X. Yu, X. Feng and M. Bao, *J. Org. Chem.*, 2011, 76, 6901–6905.
- [33] Q. Zhang, J.-X. Chen, W.-X. Gao, J.-C. Ding and H.-Y. Wu, *Appl. Organomet. Chem.*, 2010, 24, 809–812.
- [34] L. Abahmane, J. M. Kohler and G. A. Groß, *Chem.–Eur. J.*, 2011, 17, 3005–3010.
- [35] M. L. Kantam, S. Laha, J. Yadav and S. Bhargava, *Tetrahedron Lett.*, 2008, 49, 3083.
- [36] G. Villaverde, A. Corma, M. Iglesias and F. Sanchez, *ACS Catal.*, 2012, 2, 399–406.
- [37] K. K. R. Datta, B. V. S. Reddy, K. Ariga and A. Vinu, *Angew. Chem., Int. Ed.*, 2010, 49, 5961–5965.
- [38] K. Layek, R. Chakravarti, M. L. Kantam, H. Maheswaran and A. Vinu, *Green Chem.*, 2011, 13, 2878–2887.
- [39] K. M. Reddy, N. S. Babu, I. Suryanarayana, P. S. Sai Prasad and N. Lingaiah, *Tetrahedron Lett.*, 2006, 47, 7563–7566.
- [40] G. Shore, W.-J. Yoo, C.-J. Li and M. G. Organ, *Chem.–Eur. J.*, 2010, 16, 126–133.
- [41] L. Liu, X. Zhang, J. Gao and C. Xu, *Green Chem.*, 2012, 14, 1710–1720.
- [42] V. A. Peshkov, O. P. Pereshivko and E. V. Van der Eycken, *Chem. Soc. Rev.*, 2012, 41, 3790–3807.
- [43] (a) J. Schäferhans, S. Gómez-Quero, D. V. Andreeva and G. Rothenberg, *Chem.–Eur. J.*, 2011, 17, 12254–12256; (b) J. Dulle, S. Nemeth, E. V. Skorb, T. Irrgang, J. Senker, R. Kempe, A. Fery and D. V. Andreeva, *Adv. Funct. Mater.*, 2012, 22, 3128–3135.
- [44] D. V. Andreeva, *Int. J. Mater. Res.*, 2011, 102, 597–598.
- [45] N. Pazos-Peréz, T. Borke, D. V. Andreeva and R. A. Alvarez-Puebla, *Nanoscale*, 2011, 3, 3265–3268.
- [46] E. V. Skorb, D. Fix, D. G. Shchukin, H. Möhwald, D. V. Sviridov, R. Mousa, N. Wanderka, J. Schäferhans, N. Pazos-Pérez, A. Fery and D. V. Andreeva, *Nanoscale*, 2011, 3, 985–993.
- [47] N. Pazos-Pérez, J. Schäferhans, E. V. Skorb, A. Fery and D. V. Andreeva, *Microporous Mesoporous Mater.*, 2011, 154, 164–169.

- [48] C.-J. Li and C. Wei, *Chem. Commun.*, 2002, 268.
- [49] L. T. Shi, Y.-Q. Tu, M. Wang, F.-M. Zhang and C.-A. Fan, *Org. Lett.*, 2004, 6, 1001.
- [50] S. H. H. Zaidi, R. Halder, K. S. Singh, J. Das and J. Iqbal, *Tetrahedron Lett.*, 2002, 43, 6485.
- [51] G. W. Kabalka, L. Wang and R. M. Pagni, *Synlett*, 2001, 676.
- [52] M. J. Albaladejo, F. Alonso, Y. Moglie and M. Yus, *Eur. J. Org. Chem.*, 2012, 3093–3104.
- [53] (a) S. Brunauer, L. S. Deming, W. E. Deming and E. Teller, *J. Am. Chem. Soc.*, 1940, 62, 1723; (b) IUPAC Commission on Colloid and Surface Chemistry Including Catalysis, *Pure Appl. Chem*, 1985, 57, 603–619.
- [54] S. Velu, K. Suzuki, M. Vijayaraj, S. Barman and C. S. Gopinath, *Appl. Catal., B*, 2005, 55, 287.
- [55] M. Vijayaraj and C. S. Gopinath, *J. Catal.*, 2006, 241, 83.

## 4.6 Sononanostructuring of zinc based material

Jana Dulle, Silke Nemeth, Ekaterina V. Skorb and Daria V. Andreeva\*

This work is published in RSC Advances, 2012, 2, 12460 – 1246.

This article is reprinted from RSC Advances, 2, J. Dulle, et al., Sononanostructuring of zinc based material, 12460 – 1246, Copyright (2012), with permission from The Royal Society of Chemistry.

### 4.6.1 Contribution to the joint publication

I wrote the main part of the manuscript and was responsible for the material preparation. I and Silke Nemeth prepared the different zinc samples. Silke Nemeth ran the catalytic experiments under my supervision. Ekaterina V. Skorb performed the XPS material analysis and wrote this part of the manuscript. I evaluated the physisorption measurements, XRD, and TEM data. Daria Andreeva had the supervision for the project. Ekaterina V. Skorb and Daria Andreeva corrected the manuscript.

### 4.6.2 Abstract

We performed the sonochemical nanostructuring (sononanostructuring) of zinc particles into a core-shell “hedgehog” zinc based material by a “green” ultrasound method. The core-shell “hedgehogs” consist of a metallic zinc core covered by zinc oxide nanorods. Due to the “hedgehog” morphology the novel zinc based material exhibit increased surface area, high accessibility for substrate molecules and could be a promising component of sensors, catalysts, active feedback coatings and photovoltaic systems. We demonstrate the results on the photocatalytic performance of the zinc based core-shell “hedgehogs”.

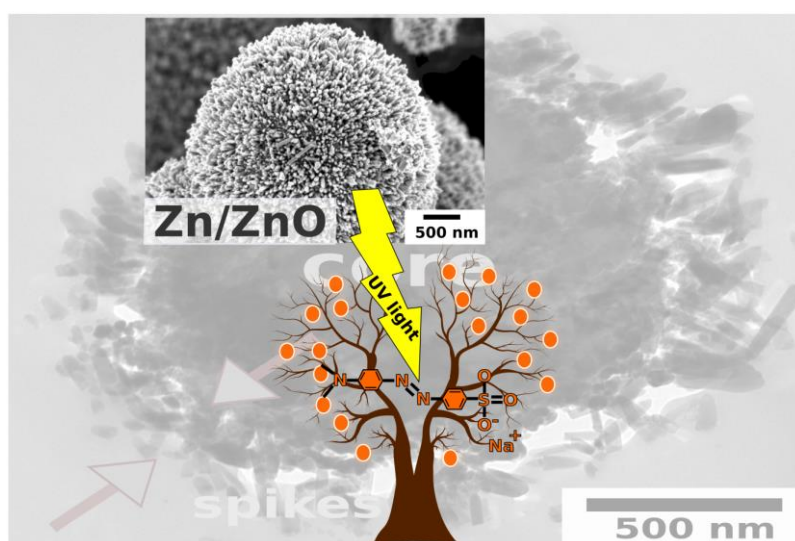


Fig. 4-41 Graphical abstract. Reprinted from RSC Advances, 2, J. Dulle, et al., Sononanostructuring of zinc based material, 12460 – 1246, Copyright (2012), with permission from The Royal Society of Chemistry.

### 4.6.3 Introduction

Ultrasound (US) technology is a green chemistry tool for direct delivery of energy in a chemical reactor. Ultrasound-assisted processes can be carried out in relatively mild conditions and doesn't require aggressive media or harsh chemical additives. The energy is concentrated locally inside and near cavitation bubbles.[1–5] In general, the collapse of acoustic cavitation microbubble (frequency of 20 kHz) in ambient conditions of the bulk solution is characterized by intensive local effects: temperature increase (up to 5000 K), pressure increase (of about 1000 atmospheres), and heating and cooling rates above  $10^9$  degrees per second. The sonochemical effects include the formation of radicals from solvents and the enhancement of reaction rates at ambient temperatures. Thus, ultrasound can be used for fast and effective modification, fragmentation of particles, etching of metal surface, depassivation of metal surface, oxidation, and stimulation growth of a novel metal oxide / hydroxide interfacial layer.

Here we propose an easy ultrasound driven method of modification of zinc particles, so-called sononanostructuring of zinc particles, by using US. The novel US-assisted modification method leads to formation of core-shell "hedgehog" zinc based materials. Wide band gap semiconductor materials like nanostructured zinc oxide (ZnO) are important for several applications such as transparent semiconductors, gas sensors, solar cell windows and photovoltaic devices.[9,10] Thus, ZnO in form of powder,[11–15] nanoparticles,[16–19] nanoplatelets,[20] plates,[21] or thin films[22-24] has gained already an interest as a photocatalyst for the degradation of water pollutants. Photocatalytic materials have become a promising alternative for environmental reprocessing[25] due to their ability to degrade different organic compounds in a more efficient way than other processes, e.g. biodegradation techniques.[26,27] The polluted water contains toxic compounds that are persistent and not biodegradable. Dyes from the textile industry are the examples of such dangerous waste. The degradation of the dyes is a serious problem worldwide.[28–32] In all the cleaning of highly contaminated waste is important for environment and human being. With this in view ZnO is considered as a low cost photocatalyst for photodegradation.[13,16,33–35] The high photocatalytic efficiency of ZnO is attributed to its ability to generate  $H_2O_2$  [36, 37] and to a high number of active sites with high surface reactivity.

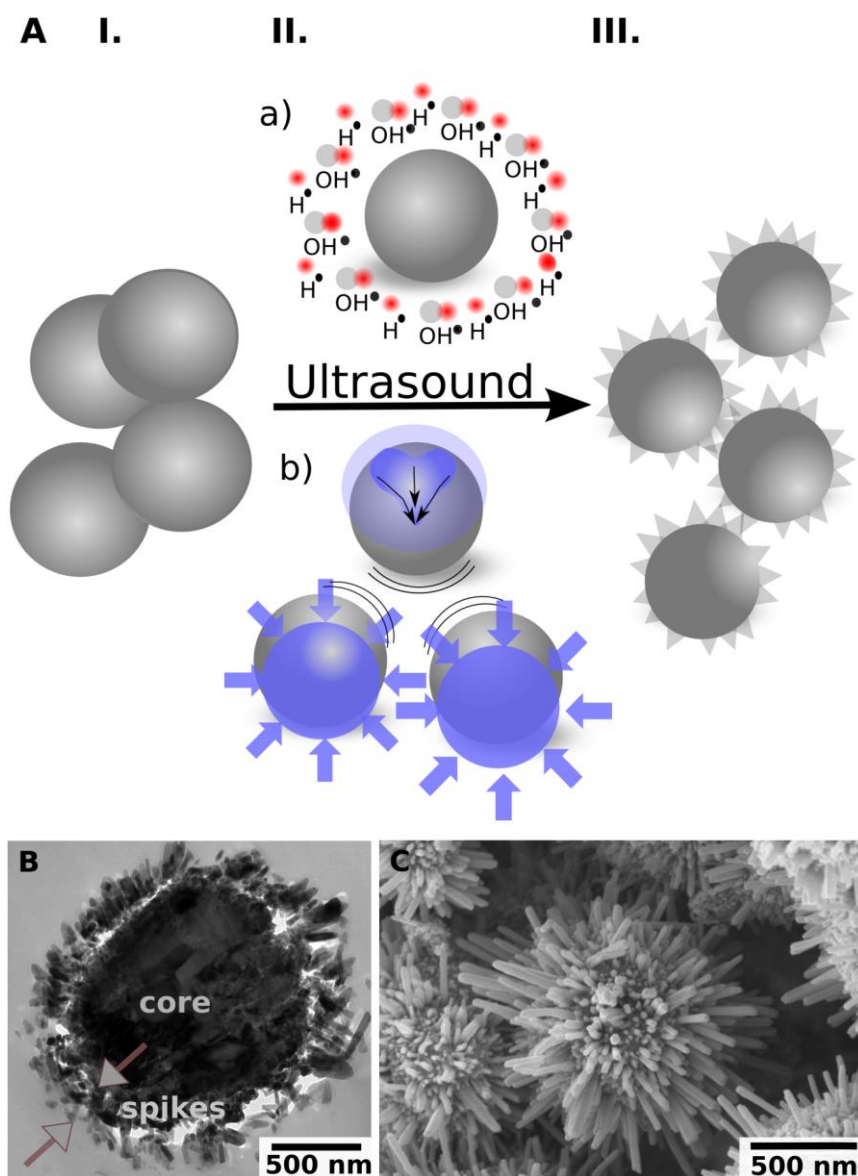


Fig. 4-42 A - Sonochemical modification of zinc particles: (I) initial particles; (II) (a) chemical aspect due to surface oxidation; (b) physical aspects are caused by interparticles collisions and surface impinging by high velocity microjets providing preferable directions of etching; (III) formation of “hedgehog” zinc particles. B, C – TEM (B, 10 min US) and SEM (C, 15 min US) images of core-shell “hedgehog” structure: metal core and the oxide nanorods attached to the core after US treatment. Reprinted from RSC Advances, 2, J. Dulle, et al., Sononanostructuring of zinc based material, 12460 – 12466, Copyright (2012), with permission from The Royal Society of Chemistry.

The formation of zinc oxide nanostructured materials varies from the sol–gel method,[38] the use of a thermal plasma reactor,[16] the chemical vapour deposition method,[39] alkali precipitation,[12] and spray pyrolysis[40] to oriented attachment of preformed ZnO nanoparticles.[41] Here we propose an alternative approach: direct oxidation of zinc surface by using sonochemical approach. The 10 ZnO nanorods form a shell attached to the metal zinc core. The novel approach is based on our previous works.[3,4,6–8] Recently, we demonstrated that mesoporous metal structures stabilized by a metal oxide layer could be formed by using ultrasound. The sononanostructuring of zinc particles requires

relatively mild conditions: aqueous media without any additional oxidants. Production expenses including ultrasound equipment and energy costs of preparing particles are rather low. The US assisted method can be up-scaled by using different sonotrodes or series of sonotrodes.[6] One of the advantage of the proposed here sononanostructuring process is that a wide range of Zn based materials with various morphologies and functionality can be prepared. Photocatalytic performance was demonstrated as one of the potential applications of the sononanostructured Zn. Furthermore, ultrasound-assisted modification was performed at different conditions in order to help understanding the mechanisms of sononanostructuring of Zn.

#### 4.6.4 Results and discussion

##### *Sonication of Zn particles: formation of the Zn based core-shell “hedgehogs”*

Recently we have suggested that surface preferable orientation etching / oxidation of metal particles[4] during their ultrasound modification is an important aspect in nanostructuring of such metals as aluminum and magnesium. In general, the ultrasound driven modification of metals is based on cavitation induced metal depassivation (breakage of initial oxide layer), mechanochemistry, due to particles collision and structure stabilization by sonogenerated oxide layer, sonochemistry. Thus, the sonicated species adopt a number of features attractive for further application: high surface area (more than  $100 \text{ m}^2 \text{ g}^{-1}$  for aluminum-based alloys), narrow pore size distribution in the mesoscopic range. We also demonstrated that long-term (longer than 90 min) ultrasound treatment of Zn particles results in completely conversion of Zn into Zn oxide. Our current research demonstrates that the short-term ultrasound treatment (up to 90 min) of Zn particles gives a Zn-based material with amazing variable core-shell “hedgehog” morphologies depending on initial particle sizes, Zn concentration in the solution and duration of sononanostructuring.

The general concept of ultrasound driven modification of zinc particles is shown in Fig. 4-42. During the US treatment of zinc particles the following phenomena could be observed (Fig. 4-42A): (I) formation of cavitation bubbles in the aqueous suspension of zinc particles; (IIa) the red/ox reactions at interfacial regions; (IIb) interparticle collisions; (III) generation of the core-shell “hedgehog” zinc. Moreover (IV) total oxidation with total conversion to oxide structure is possible (not shown in the sketch).

$\sim 4 \text{ }\mu\text{m}$  and  $\sim 50 \text{ }\mu\text{m}$  Zn particles were used for Zn sononanostructuring. The morphology of the modified Zn based particles was studied by using scanning and transmission electron microscopy (Fig. 4-43). The particles after 10 min of sonication consist on the metallic Zn core covered by ZnO nanorods. The core-shell morphology can be clearly seen in the TEM image of the cross section of the modified Zn particle (Fig. 4-42B). The nanorods are attached perpendicularly to the Zn core. The SEM image (Fig. 4-42C) shows that the nm-long rods homogeneously cover the metal surface forming so-called

“hedgehogs” from Zn particles. We explain the formation of the core-shell “hedgehog” morphology by the oxidation of the surface of Zn particles by free radicals generated during cavitation.

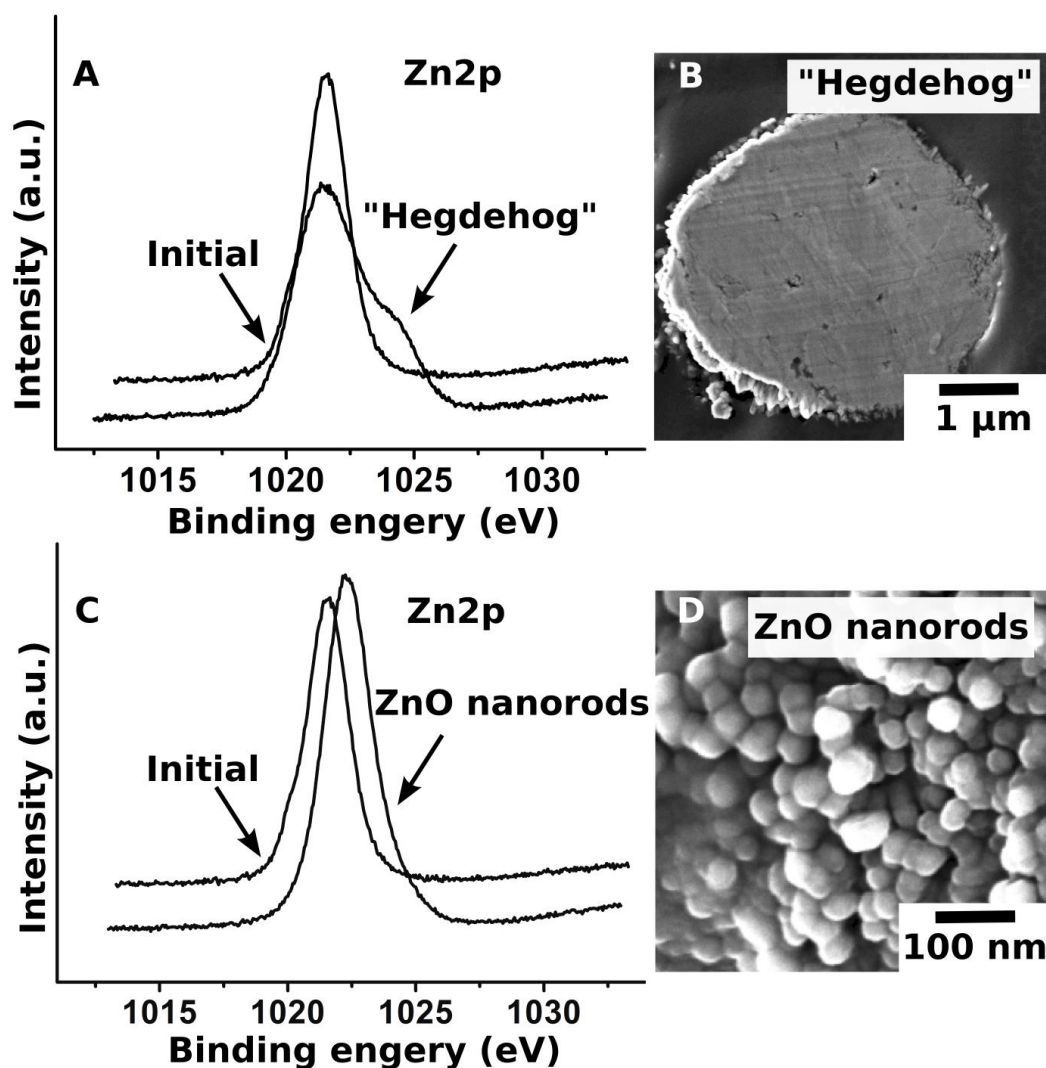


Fig. 4-43 XPS spectra of “hedgehog” zinc particles (A) and the ZnO nanorods (C), and SEM image of the ultramicrotomed Zn/ZnO particle (B) and ZnO nanorods (D) after 15 min of US treatment. Reprinted from RSC Advances, 2, J. Dulle, et al., Sononanostructuring of zinc based material, 12460 – 12466, Copyright (2012), with permission from The Royal Society of Chemistry.

### ***Mechanism of formation of core-shell Zn based “hedgehogs”***

Formation of core-shell Zn based morphology was confirmed by the TEM images (Fig. 4-42B) and the XPS experiments (Fig. 4-43). The XPS spectra (Fig. 4-43A, C) correspond to the Zn 2p<sub>3/2</sub>. It is clear seen that after modification in the case of “hedgehog” structures two peaks correspond to metallic core and oxidized shell. Simultaneous in the case of ZnO nanorods shift of the peak is attribute to change of Zn<sup>0</sup> to Zn<sup>2+</sup>. The growth of ZnO on zinc particles can be controlled by the duration of sonication (Fig. 4-44). The ultrasound-stimulated formation of zinc oxide on the surface of zinc particles (here, ~4 μm initial Zn particles) occurs after short-term sonication. 60 sec US treatment leads to the appearance of

60 nm long ZnO nanorods on the Zn core (Fig. 4-44D). After 10 minutes of sononanostructuring the ZnO nanorods grow up to 160 nm and cover the entire core (Fig. 4-44F). Longer treatment (> 30 min) destroys the relatively long nanorods (Fig. 4-44G). The 160 nm nanorods are removed from the particle surface due to friction forces during interparticle collisions. Then the surface oxidation starts again. The 60-min-sonicated samples are covered by 20 nm nanorods. The powder X-ray diffraction (PXRD) patterns in Fig. 4-44A-G confirm the cycle character of the ultrasound-driven modification of Zn. 10-min ultrasonic treatment leads to the partial conversion of Zn into ZnO, which results in “hedgehog” morphology of the particles. The PXRD pattern of the 10-min-modified samples exhibits the peaks of the both the metallic Zn and ZnO. After 30 min the “hedgehog” structures lose their spikes. Two separate phases, Zn particles and ZnO nanorods, can be distinguished and separated. The PXRD pattern of the Zn after the loss of the ZnO nanorods shell is shown in Fig. 4-44E.

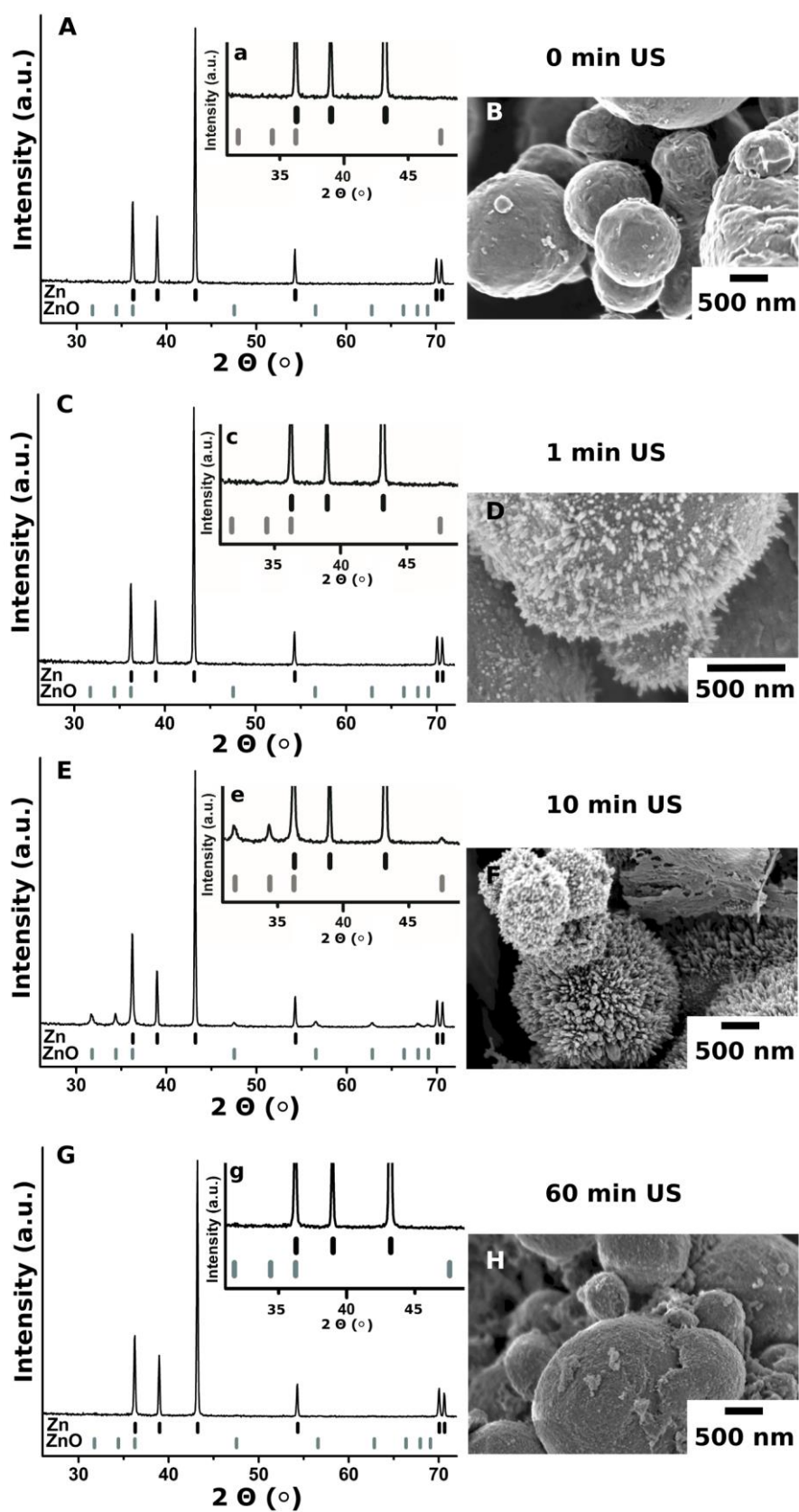


Fig. 4-44 PXRD patterns and SEM images of the initial zinc particles (A, B) and treated for 1 min (C, D), 10 min (E, F) and 60 min (G, H) by ultrasound. The inserts (a, c, e, g) show the magnified part of the PXRD patterns with the ZnO attributed peaks. Reprinted from RSC Advances, 2, J. Dulle, et al., Sononanostructuring of zinc based material, 12460 – 1246, Copyright (2012), with permission from The Royal Society of Chemistry.

The size of the initial Zn particles also affects the modification process and, therefore, the morphology of the modified systems (Fig. 4-45). The modification of the  $\sim 4 \mu\text{m}$  and  $\sim 50 \mu\text{m}$  particles leads to surface oxidation, growth of ZnO nanorods and their detachment. These ZnO nanorods are formed and detached in cyclic manner. The PXRD patterns and the SEM images in Fig. 4-44 showed that the nanorods grow, reach the maximum size, and are detached during sonication then the cycle starts again. However, the character of growth of the metal oxide depends on the particle size. The SEM images (Fig. 4-45) demonstrate that the  $\sim 50 \mu\text{m}$  particles are covered by randomly attached ZnO nanorods (Fig. 4-45A, C, E). The concentration of these nanorods increases with the sonication duration. The increase of the ZnO concentration on the surface of the  $\sim 50 \mu\text{m}$  particles was confirmed by PXRD (not shown here). The  $\sim 4 \mu\text{m}$  Zn particles are covered by the perpendicularly attached ZnO. The surface area of the initial  $\sim 4 \mu\text{m}$  zinc particles is  $0.4 \text{ m}^2 \text{ g}^{-1}$ . The surface area of these particles reaches  $2.6 \text{ m}^2 \text{ g}^{-1}$  after the 10 min sonication. After 30 min of US treatment, the surface of the “hedgehogs” is covered by 20 nm ZnO rods and has the surface area of  $1.3 \text{ m}^2 \text{ g}^{-1}$ . The surface area of the  $\sim 50 \mu\text{m}$  particles can get maximum  $20 \text{ m}^2 \text{ g}^{-1}$  after 10-min sonication due to formation of a thick layer of randomly distributed  $160 \mu\text{m}$  ZnO spikes. After 90 min of modification the surface area of  $\sim 50 \mu\text{m}$  particles is also decreased up to  $12 \text{ m}^2 \text{ g}^{-1}$  due to formation of 100 nm nanorods on the metal surface. Thus, the surface area of the modified particles depends on the character of growth and distribution of ZnO nanorods on the metal core. At the beginning of sonication (10 – 15 min) we observed the formation of the very interesting tubular ZnO nanorods[4] on the surface of the  $\sim 50 \mu\text{m}$  particles that are probably responsible for the increased surface area of such particles. However, as we will demonstrate in the next part of this article, these nanorods don't significantly contribute to the catalytic activity of Zn particles. Probably they are not accessible for the substrate molecules. The 15-min-sonicated  $\sim 4 \mu\text{m}$  Zn particles (Fig. 4-45D) demonstrate the core-shell morphology where the Zn core homogeneously covered by a monolayer of ZnO nanorods. The longer sonication time (the 60-min-sonicated particles in Fig. 4-45F) leads to formation of randomly distributed 100 nm ZnO nanorods similar to the ZnO layer formed on the  $\sim 50 \mu\text{m}$  particles. These particles demonstrate the highest catalytic activity that we will discuss here later.

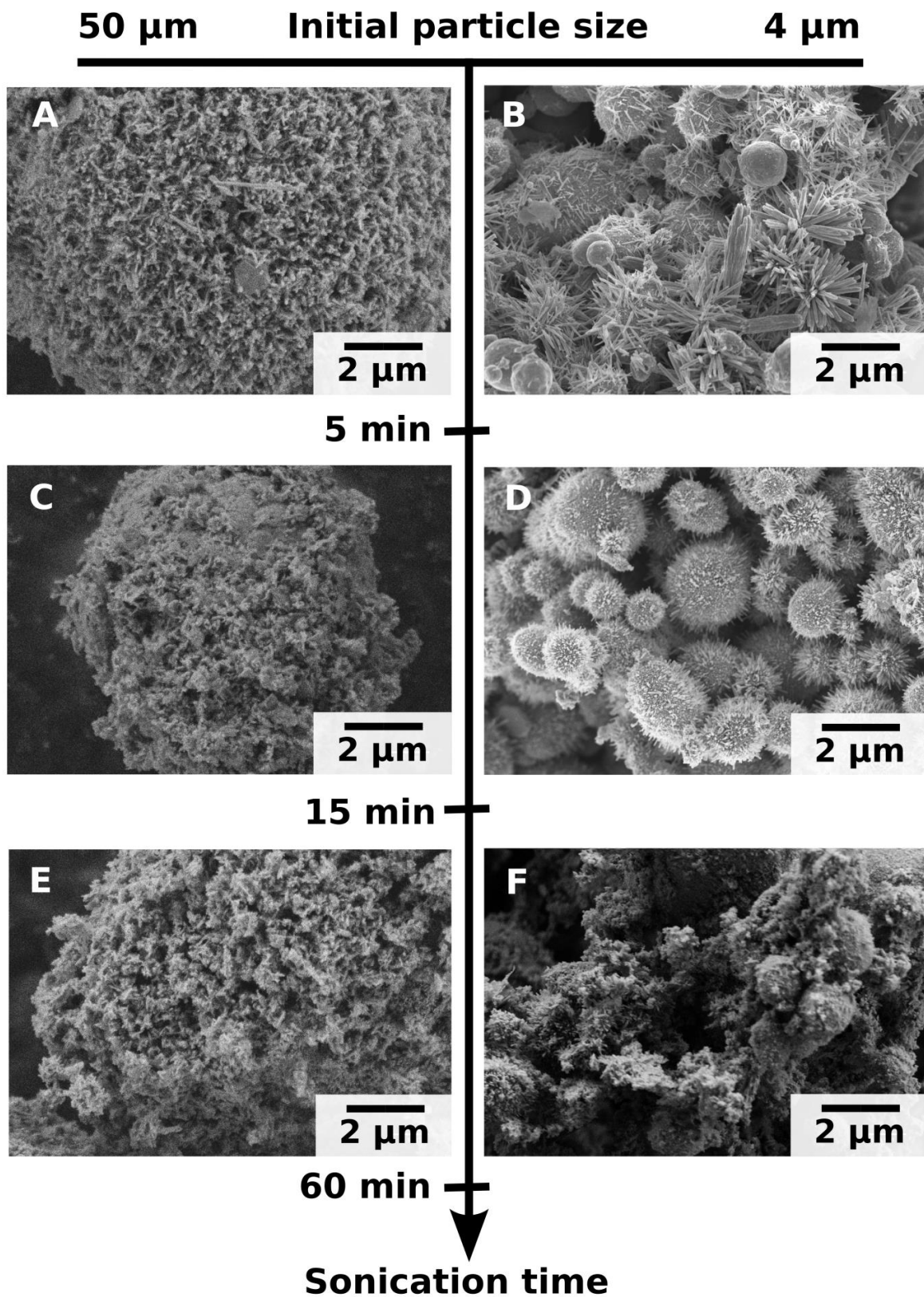


Fig. 4-45 SEM images of  $\sim 4 \mu\text{m}$  and  $\sim 50 \mu\text{m}$  initial particle size after 5 (A, B), 15 (C, D) and 60 min (E, F) ultrasound treatment. Reprinted from RSC Advances, 2, J. Dulle, et al., Sononanostructuring of zinc based material, 12460 – 12466, Copyright (2012), with permission from The Royal Society of Chemistry.

Based on all characterizations performed above we can summarize that the ultrasound modification of Zn particles has a cycle character that depends on sonication time and particle size. The free radicals generated by ultrasound oxidize the surface and the ZnO nanorods rapidly grow on the metallic core. The long nanorods are detached because of interparticle collisions in the sonicated suspensions. We could distinguish two phases: the relatively smooth Zn particles and the ZnO nanorods. Then the oxidation continues and the nanorods grow again on the surface. The size of the nanorods can be controlled by the particle size and the duration of sonication. The short-term sonication (up to 90 min) leads to formation of the core-shell “hedgehogs” with increased surface area.

### ***Photocatalytic activity***

The functionality of the sononanostructured Zn can be related to its properties as a semiconductor. When the modified zinc is illuminated by UV light, the migration of electrons to the zinc core begins (Eq. 1) and positive holes (h<sup>+</sup>) are formed.[42–44] When the semiconductor is immersed in an aqueous medium, spontaneous adsorption of the water molecules in the liquid occurs. Then an electron is transferred to the acceptor molecule and the donor molecule gives an electron to the semiconductor particle. The holes generate OH<sup>•</sup> by reacting with the water molecules (Eq. 2), and the O<sub>2</sub> molecule accepts an electron to form the super-oxide radical O<sub>2</sub><sup>•-</sup> (Eq. 3). These O<sub>2</sub><sup>•-</sup> radicals act as strong oxidizing agents and they also contribute to the formation of hydrogen peroxide (Eqs. 4–7).[45] Thus, as an example of the possible application range of the sononanostructured zinc we tested the photocatalytic activity of the core-shell “hedgehog” in the detoxification of methyl orange (MO). The radicals formed in presence of a semiconductor can react with the dye molecule, disrupting it in its conjugated system which leads to the complete decomposition of the dye.[46, 47]



In Fig. 4-46 are highlighted some results of the detoxification of MO by the core-shell “hedgehog” zinc. The dye degradation was monitored by using UV/VIS spectra. The absorption peaks, corresponding to dye, diminished, and finally disappeared under irradiation, which indicates that the dye is degraded. No new absorption bands appear in either the visible or ultraviolet regions. The spectrum of MO in the visible region exhibits a band with a maximum at 464 nm. The decrease of absorption peaks of MO at

$\lambda_{\text{max}}=464$  nm indicates a rapid degradation of the azo dye. It also indicates that the nitrogen - nitrogen double bond ( $-\text{N}=\text{N}-$ ) of MO is the most active site for oxidation attack. Complete degradation of the dye was observed after 50 min using optimized conditions. The MO without photocatalyst presence in the reaction vessel is stable under UV-irradiation. In the absence of photocatalyst no colour change was observed.

To optimize the ultrasound treatment of Zn particles we tested the catalytic activity of US-Zn prepared at different sonication time. Fig. 4-46 shows the catalytic activity for the samples prepared at different concentration of Zn in water and by using  $\sim 50$   $\mu\text{m}$  and  $\sim 4$   $\mu\text{m}$  initial Zn particles. For all samples we observed the cycle character of reaction rate constant vs. sonication time.

At the beginning of modification up to 10 min sonication we observed increase of the rate constant for all samples. After 10 min of US exposure the activity decreases rapidly and converges to a  $k$  value comparable to the untreated zinc. The observed dependence can be explained by the ultrasound-driven change of particle morphology. During the first 10 min of modification the “hedgehogs” with increased surface area is formed. After long exposure to US, the “hedgehogs” lose their spikes, which results in a loss of photocatalytic activity (Fig. 4-44).

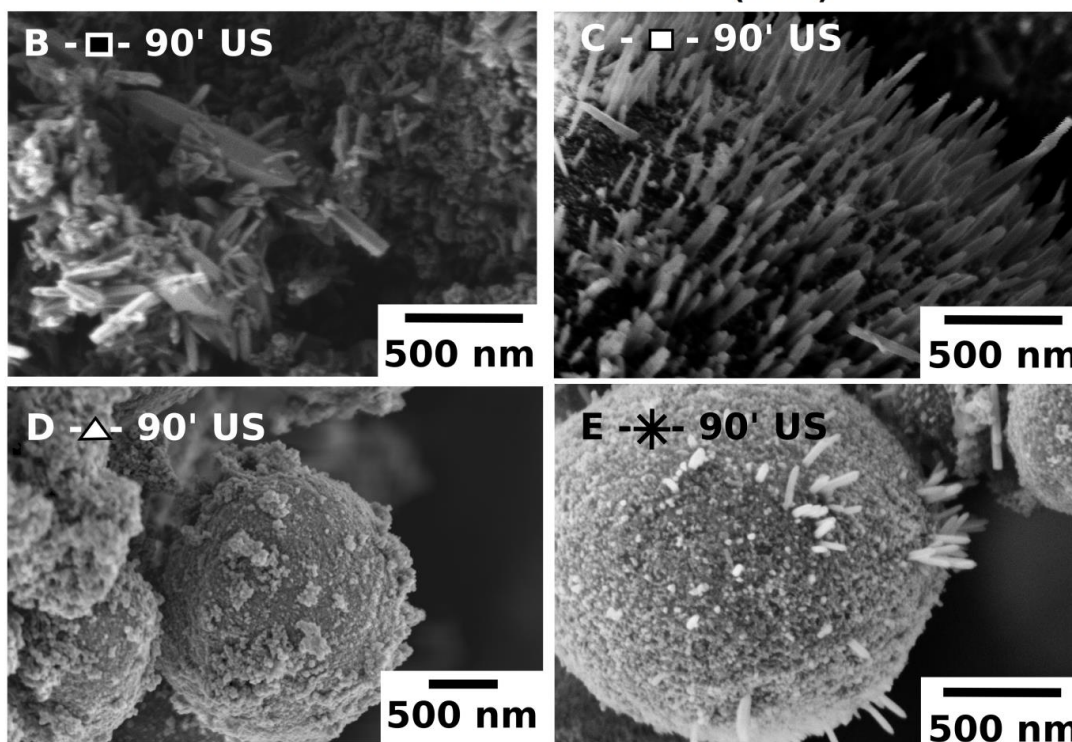
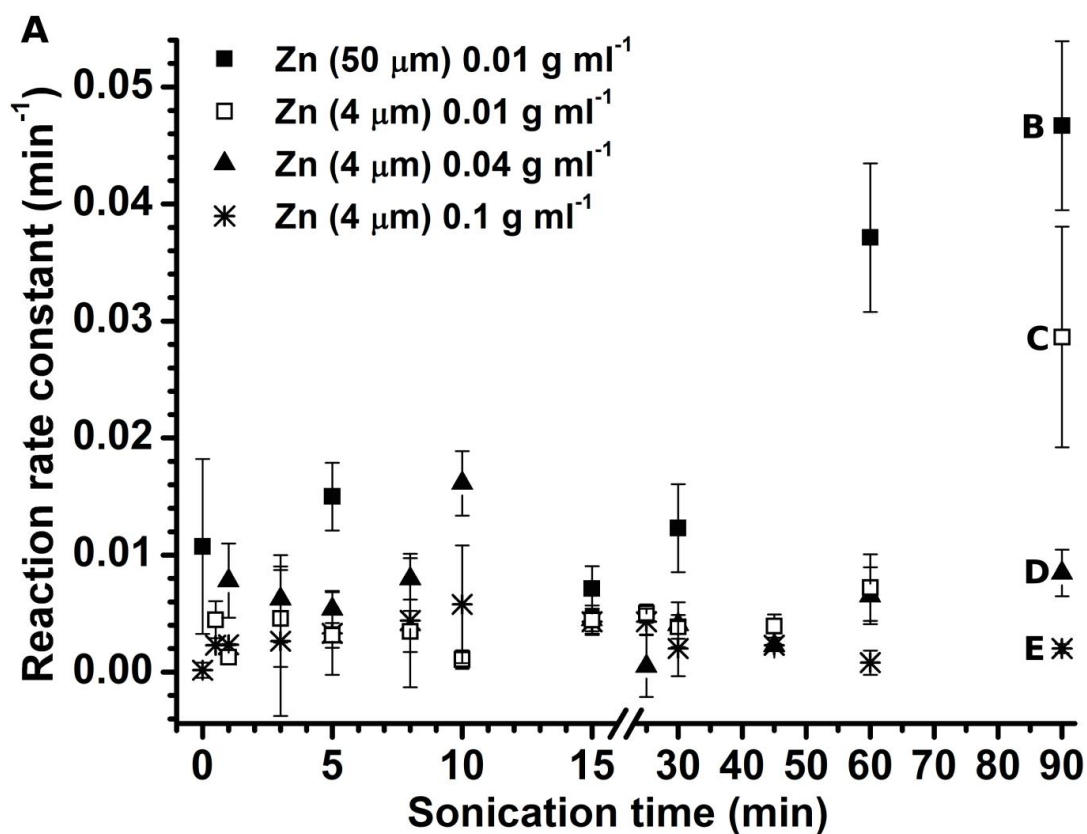


Fig. 4-46 Reaction rate constant  $k$  is shown in dependence of ultrasound treatment duration. We used  $10 \text{ mg}$  of the US-Zn (A). The SEM images of the samples prepared for  $90 \text{ min}$  of sonication:  $0.01 \text{ g ml}^{-1}$   $50 \mu\text{m}$  Zn particles (B),  $0.01 \text{ g ml}^{-1}$   $4 \mu\text{m}$  particles (C),  $0.04 \text{ g ml}^{-1}$   $4 \mu\text{m}$  particles (D) and  $0.1 \text{ g ml}^{-1}$   $4 \mu\text{m}$  particles (E). Reprinted from RSC Advances, 2, J. Dulle, et al., Sononanostructuring of zinc based material, 12460 – 12466, Copyright (2012), with permission from The Royal Society of Chemistry.

The catalytic activity of the sononanostructured Zn prepared at longer sonication time (up to 90 min) strongly depends on concentration of the sonicated particles and initial size of Zn particles.  $\sim 4 \mu\text{m}$  and  $\sim 50 \mu\text{m}$  zinc particles exhibit different photocatalytic activity. We observed, that 90 min US exposure leads to the highest reaction rate constant  $k=0.0490 \text{ min}^{-1}$  for 10 mg of  $\sim 50 \mu\text{m}$  Zn particles, where the same amount of  $\sim 4 \mu\text{m}$  zinc particles reached  $k=0.028 \text{ min}^{-1}$ . The fact that the modified  $\sim 4 \mu\text{m}$  and  $\sim 50 \mu\text{m}$  zinc particles exhibit different activity could be explained by higher concentration of ZnO nanorods randomly attached to the bigger Zn accessible core for the MO molecules. The difference in the surface morphology for the both samples ( $\sim 4 \mu\text{m}$  and  $\sim 50 \mu\text{m}$  Zn particles) can be clearly seen in the SEM images in Fig. 4-46. Additionally, the surface area of the  $\sim 50 \mu\text{m}$  particles is  $12 \text{ m}^2 \text{ g}^{-1}$  and  $1.3 \text{ m}^2 \text{ g}^{-1}$  after 90-min-sonication. This is not the maximum surface area we could achieve for the sononanostructured Zn. However, the 90-min-sonicated Zn based materials exhibit the highest rate of MO conversion probably due to the better accessibility of the ZnO nanorods formed in 90 min modification. The control experiments with commercial ZnO demonstrate the activity similar to US-Zn. The reaction rate constant of the commercial ZnO was estimated  $0.0515 \text{ min}^{-1}$ . In the graph A in Fig. 4-46 we can also see the influence of the concentration of the sonicated particles on the rate constant. The optimal concentration of Zn particles in our experiments was found to be  $0.01 \text{ g ml}^{-1}$ . The higher concentration of Zn particles leads to fast Zn modification but the nanorods might be also rapidly detached from the Zn core surface due to vigorous interparticle collision stimulated by sonication. At the same time, the lower Zn concentration ( $< 0.01 \text{ g ml}^{-1}$ ) leads to reduction of collision events between particles. The particle modification became very slow and we could not achieve the “hedgehog” morphology and comparable catalytic activity.

#### 4.6.5 Conclusion

We showed that the sononanostructuring of zinc is an easy and green method for the production of wide spectrum of interesting zinc based materials with spectacular morphology and functionality e.i. core-shell “hedgehogs” and ZnO nanorods. By using ultrasound the nanostructuring of zinc can be performed in a fairly easy and cost efficient way[7,8] avoiding aggressive media, harsh additives, and oxidants. The Zn/ZnO “hedgehogs” have a Zn metallic core covered by ZnO nanorods. The form and length of these nanorods can be controlled by sonication conditions. The “hedgehogs” demonstrate a good photocatalytic activity due to the semiconductive nature of the ZnO spikes. We do believe that the sonochemical approach to nanostructuring of materials provides a novel methodology for focused construction and functionalizing of solids. The nanostructured semiconductor zinc-based material demonstrated here could be a promising component in construction of a whole range of composite systems for photocatalysis, gas sensing, photovoltaic, etc. The metallic nature of the Zn core could be applied for formation of corrosion protection systems.

#### 4.6.6 Experimental

##### *Formation of core-shell "hedgehogs" from Zn particles*

Zinc powder (Sigma Aldrich,  $\geq 99\%$ , initial size  $\sim 50\ \mu\text{m}$  and  $4\ \mu\text{m}$ ) were dispersed in ultrapure MilliQ-water and sonicated for different durations with an ultrasound tip (VIP1000hd, Hielscher Ultrasonics GmbH, Germany) operated at 20 kHz with a maximum output power of 1000 W ultrasonic horn BS2d22 (head area of  $3.8\ \text{cm}^2$ ) and equipped with a booster B2-1.8. The maximum intensity was calculated to be  $140\ \text{W cm}^{-2}$  at mechanical amplitude of  $106\ \mu\text{m}$ . Concentration of initial powder was varied in the range  $0.01\ \text{g ml}^{-1} - 0.1\ \text{g ml}^{-1}$ . During the treatment the sample was cooled in a thermostatic flow cell. After the treatment, the modified zinc (US-Zn) sample was dried for 24 h.

##### *Characterisation methods*

Transmission and scanning electron microscopy (TEM, Zeiss EM922 Omega, EFTEM operating at 200 kV and SEM, LEO 1530 FE-SEM, Zeiss), in combination with an ultramicrotome (Ultracut E, Reichert Jung, thickness 50 nm) were applied to characterize the optical response, structure, and size of the zinc powder.

The powder X-ray diffraction patterns were collected  $\Theta$ - $\Theta$  mode using a Stoe STADI P X-ray Transmission diffractometer: Cu  $K\alpha_1$ , irradiation, room temperature,  $2^* \Theta = 5^\circ - 90^\circ$ .

Surface area is based on physisorption (adsorption and desorption of gases) and was measured by the BET (Brunauer-Emmett-Teller) [48] method using krypton at 77 K on a vacuum gas sorption Autosorb-1 and Autosorb Degasser apparatus (Quantachrom). Each sample was dried under vacuum for 24 h at  $100\ ^\circ\text{C}$ .

X-ray Photoelectron Spectroscopy was acquired with a SPECS hemispherical energy analyzer (Phoibus 100) and SPECS focus 500 X-ray monochromator using the Al  $K\ \alpha$  with energy of 1486.74 eV.

##### *Photocatalytic experiments*

The photocatalytic activities were used the as-prepared and filtered samples in order to separate the free ZnO nanorods formed by sonication. The core-shell Zn/ZnO particles were used for the degradation of methyl orange (MO, ACS reagent, Sigma-Aldrich) in solution in presence of UV light.

The degradation of MO dye was estimated by the evaluation of the intensity of the absorption band centered at 464 nm, as a function of the illumination time.

The initial pH of these solutions was 5.4. A 450 W UV lamp, equipped with a 420 nm cut-off filter ( $\lambda = 380\ \text{nm}$ ) was used (UV-F 400 F, Dr. Hönle) to irradiate the stirred dispersions. The sample was placed at a distance of 25 cm from the UV lamp, the average light intensity was  $15\ \text{mJ cm}^{-2}$  (measured by tesa® UV

Strip - UV 75 Scan, Fa. Hönle, Germany). 10 mg of zinc modified for different sonication time were dispersed in a 10 mL MO suspension (0.1 mM) and stirred at room temperature. Prior to the irradiation, the suspensions were magnetically stirred in the dark for 30 min to reach an adsorption-desorption equilibrium. At given time intervals, 1  $\mu$ L of the solution samples were collected and analysed by recording the absorption of MO from 190 nm to 800 nm using an Agilent 8453 UV/VIS spectrophotometer with ultrapure water in the reference beam. The degradation percentage was obtained as well as the rate of reaction rate constant  $k$ . This rate of reaction was used to compare the efficiency of the catalysts. For the reusability experiments the catalyst was washed in ultrapure water several times and dried.

The reaction with UV radiation and catalyst follows the first reaction order

$$[A]_t = [A]_0 * e^{-kt}$$

with  $[A]_t$  as the concentration at the time  $t$  and  $[A]_0$  as the starting concentration, with  $k$  ( $\text{min}^{-1}$ ).

#### 4.6.7 Acknowledgments

We thank B. Putz (Uni Bayreuth) for the PXRD measurements and C. Kunert (Uni Bayreuth) for SEM images. We thank C. Hasenöhrl for fruitful discussions. J. D. and D. V. A. thank project A11 SFB 840 for financial support. E. V. S. thanks the Alexander von Humboldt Foundation.

#### References

- [1] K. S. Suslick, *Science*, 1990, 247, 1439-1445.
- [2] K. S. Suslick, D. J. Casadonte, M. L. H. Green and M. E. Thompson, *Ultrasonics*, 1987, 25, 56-59.
- [3] E. V. Skorb, D. G. Shchukin, H. Möhwald and D. V. Andreeva, *Nanoscale*, 2010, 2, 722-727.
- [4] E. V. Skorb, D. Fix, D. G. Shchukin, H. Möhwald, D. V. Sviridov, R. Mousa, N. Wanderka, J. Schäferhans, N. Pazos-Pérez, A. Fery and D. V. Andreeva, *Nanoscale*, 2011, 3, 985-993.
- [5] E. Skorb, D. Shchukin, H. Möhwald and D. Andreeva, *Langmuir*, 2010, 26, 16973-16979.
- [6] D. V. Andreeva, D. V. Sviridov, A. Masic, H. Möhwald and E. V. Skorb, *Small*, 2012, 8, 820-825.
- [7] N. Pazos-Pérez, J. Schäferhans, E. V. Skorb, A. Fery and D. V. Andreeva, *Microporous Mesoporous Mater.*, 2012, 154, 164-169.
- [8] J. Schäferhans, S. Gómez-Quero, D. V. Andreeva and G. Rothenberg, *Chem-Eur J*, 2011, 17, 12254-12256.
- [9] S. J. Pearton, D. P. Norton, K. Ip, Y. W. Heo and T. Steiner, *Prog. Mater. Sci.*, 2005, 50, 293-340.
- [10] H. M. a. Ô. Ôzgür, ed. al, *Zinc Oxide, Fundamentals, Materials and Device Technology*, Wiley-VCH Verlag, Weinheim, 2009.
- [11] B. Dindar and S. İçli, *J. Photochem. Photobiol., A*, 2001, 140, 263-268.

- [12] D. Li and H. Haneda, *Chemosphere*, 2003, 51, 129-137.
- [13] S. K. Kansal, M. Singh and D. Sud, *J. Hazard. Mater.*, 2007, 141, 581-590.
- [14] H. Fu, T. Xu, S. Zhu and Y. Zhu, *Environ. Sci. Technol.*, 2008, 42, 8064-8069.
- [15] N. Daneshvar, D. Salari and A. R. Khataee, *J. Photochem. Photobiol., A*, 2004, 162, 317-322.
- [16] H.-F. Lin, S.-C. Liao and S.-W. Hung, *J. Photochem. Photobiol., A*, 2005, 174, 82-87.
- [17] C. Hariharan, *Appl. Catal., A*, 2006, 304, 55-61.
- [18] K. G. Kanade, B. B. Kale, J.-O. Baeg, S. M. Lee, C. W. Lee, S.-J. Moon and H. Chang, *Mater. Chem. Phys.*, 2007, 102, 98-104.
- [19] R. Ullah and J. Dutta, *J. Hazard. Mater.*, 2008, 156, 194-200.
- [20] C. Ye, Y. Bando, G. Shen and D. Golberg, *J. Phys. Chem. B*, 2006, 110, 15146-15151.
- [21] E. Yassitepe, H. C. Yatmaz, C. Öztürk, K. Öztürk and C. Duran, *J. Photochem. Photobiol., A*, 2008, 198, 1-6.
- [22] B. Pal and M. Sharon, *Mater. Chem. Phys.*, 2002, 76, 82-87.
- [23] J. L. Yang, S. J. An, W. I. Park, G. C. Yi and W. Choi, *Adv. Mater.*, 2004, 16, 1661-1664.
- [24] A. M. Ali, E. A. C. Emanuelsson and D. A. Patterson, *Appl. Catal., B*, 2010, 97, 168-181.
- [25] M. R. Hoffmann, S. T. Martin, W. Choi and D. W. Bahnemann, *Chem. Rev.*, 1995, 95, 69-96.
- [26] P. R. Gogate and A. B. Pandit, *Adv. Environ. Res.*, 2004, 8, 501-551.
- [27] C. Comninellis, A. Kapalka, S. Malato, S. A. Parsons, I. Poullos and D. Mantzavinos, *J. Chem. Technol. Biotechnol.*, 2008, 83, 769-776.
- [28] J. W. Tang, Z. G. Zou, J. Yin and J. H. Ye, *Chem. Phys. Lett.*, 95 2003, 382, 175.
- [29] R. Asahi, T. Morikawa, T. Ohwaki, K. Aoki and Y. Taga, *Science*, 2001, 293, 269.
- [30] X. Tao, W. Ma, T. Zhang and J. Zhao, *Angew. Chem., Int. Ed.*, 2001, 40, 3014.
- [31] W. Ma, J. Li, X. Tao, J. He, Y. Xu, J. C. Yu and J. Zhao, *Angew. Chem., Int. Ed.*, 2003, 42, 1029.
- [32] J. W. Tang, Z. G. Zou, J. Yin and J. H. Ye, *Angew. Chem., Int. Ed.*, 2004, 43, 4463.
- [33] B. Pal and M. Sharon, *Mater. Chem. Phys.*, 2002, 76, 82-87.
- [34] A. A. Aal, S. A. Mahmoud and A. K. Aboul-Gheit, *Mater. Sci. Eng., C*, 2009, 29, 831-835.
- [35] E. Yassitepe, H. C. Yatmaz, C. Öztürk, K. Öztürk and C. Duran, *J. Photochem. Photobiol., A*, 2008, 198, 1-6.
- [36] E. R. Carraway, A. J. Hoffman and M. R. Hoffmann, *Environ. Sci. Technol.*, 1994, 28, 786-793.
- [37] A. J. Hoffman, E. R. Carraway and M. R. Hoffmann, *Environ. Sci. Technol.*, 1994, 28, 776-785.
- [38] S. Liao, H. Donggen, D. Yu, Y. Su and G. Yuan, *J. Photochem. Photobiol., A*, 2004, 168, 7-13.

- [39] J. J. Wu and S. C. Liu, *Adv. Mater.*, 5 2002, 14, 215–218.
- [40] M. Bizarro, *Appl. Catal., B*, 2010, 97, 198–203.
- [41] C. Pacholski, A. Kornowski and H. Weller, *Angew. Chem. Int. Ed.*, 2002, 41, 1188–1191.
- [42] P. V. Kamat, *Pure Appl Chem*, 2002, 74, 1693–1706.
- [43] A. Wood, M. Giersig and P. Mulvaney, *J Phys Chem B*, 2001, 105, 8810–8815.
- [44] F. Han, V. S. R. Kambala, M. Srinivasan, D. Rajarathnam and R. Naidu, *Appl. Catal., A*, 2009, 359, 25–40.
- [45] M. Bizarro, M. A. Tapia-Rodríguez, M. L. Ojeda, J. C. Alonso and A. Ortiz, *Appl. Surf. Sci.*, 2009, 255, 6274–6278.
- [46] J. M. Herrmann, *Top. Catal.*, 2005, 34, 49–65.
- [47] C. A. K. Gouvêa, F. Wypych, S. G. Moraes, N. Durán, N. Nagata and P. Peralta-Zamora, *Chemosphere*, 2000, 40, 433–440.
- [48] S. Brunauer, L. S. Deming, W. E. Deming and E. Teller, *J. Am. Chem. Soc.*, 1940, 62, 1723–1732

## **5 Excerpt of published abstracts at national and international conferences**

### **5.1 COPS 2012 – Poster award**

**Characterization of Porous Solids, Dresden, Germany**

Design of mesoporous metal alloys by ultrasound

J. Schäferhans and D. V. Andreeva

### **5.2 CPM-6 – Poster award**

**6<sup>th</sup> International Workshop: Characterization of Porous Materials: from Angstroms to Millimeters, 2012, Florida, USA**

Design of mesoporous metal alloys by ultrasound

J. Schäferhans and D. V. Andreeva

### **5.3 DPG Frühjahrtagungen**

Deutsche Physikalische Gesellschaft (DPG) -Frühjahrstagung der Sektion Kondensierte Materie (SKM), den Fachverbänden Kristallographie (KR), Strahlen und Medizinphysik (ST), Physik sozio-ökonomischer Systeme (SOE) und des Arbeitskreises Industrie und Wirtschaft (AIW).

**DPG 2010, Regensburg, Germany – Talk**

Mesoporous metal catalysts formed by ultrasound

J. Schäferhans, E. Skorb, N. Pazos Pérez, and D. V. Andreeva

**DPG 2011, Dresden, Germany – Talk**

Ultrasound-driven design of new mesoporous metal catalysts

J. Schäferhans, E. Skorb, N. Pazos Pérez, and D. V. Andreeva

### **5.4 ECIS 2010**

**24<sup>th</sup> Meeting of the European Colloid and Interface Society, Prague, Czech Republic – Poster**

Mesoporous multimetal nanocomposites formed by ultrasound

J. Schäferhans, N. Pazos Pérez, E. Skorb, and D. V. Andreeva

## **5.5 Katalytiker 2011**

**44. Jahrestreffen Deutscher Katalytiker mit Jahrestreffen Reaktionstechnik 2011, Weimar, Germany – Poster**

Catalytically active mesoporous multimetal nanocomposites formed by ultrasound

J. Schäferhans, T. Irrgang, and D. V. Andreeva

## **5.6 EuCheMS 2010**

**3<sup>rd</sup> EuCheMS Chemistry Congress, 2010, Nürnberg, Germany – Poster**

Mesoporous multimetal nanocomposites formed by ultrasound

J. Schäferhans, N. Pazos Pérez, E. Skorb, and D. V. Andreeva

## **Erklärung**

### **(Eidesstattliche) Versicherungen und Erklärungen**

(§ 5 Nr. 4 PromO)

Hiermit erkläre ich, dass keine Tatsachen vorliegen, die mich nach den gesetzlichen Bestimmungen über die Führung akademischer Grade zur Führung eines Doktorgrades unwürdig erscheinen lassen.

(§ 8 S. 2 Nr. 5 PromO)

Hiermit erkläre ich mich damit einverstanden, dass die elektronische Fassung meiner Dissertation unter Wahrung meiner Urheberrechte und des Datenschutzes einer gesonderten Überprüfung hinsichtlich der eigenständigen Anfertigung der Dissertation unterzogen werden kann.

(§ 8 S. 2 Nr. 7 PromO)

Hiermit erkläre ich eidesstattlich, dass ich die Dissertation selbständig verfasst und keine anderen als die von mir angegebenen Quellen und Hilfsmittel benutzt habe.

(§ 8 S. 2 Nr. 8 PromO)

Ich habe die Dissertation nicht bereits zur Erlangung eines akademischen Grades anderweitig eingereicht und habe auch nicht bereits diese oder eine gleichartige Doktorprüfung endgültig nicht bestanden.

(§ 8 S. 2 Nr. 9 PromO)

Hiermit erkläre ich, dass ich keine Hilfe von gewerblichen Promotionsberatern bzw. -vermittlern in Anspruch genommen habe und auch künftig nicht nehmen werde.

Bayreuth, den